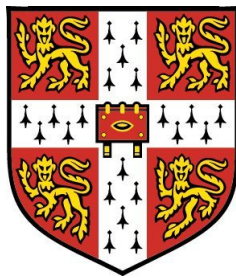


Study of multi-component fuel premixed combustion using direct numerical simulation



Department of Engineering
University of Cambridge

This dissertation is submitted for the degree of:

Doctor of Philosophy

by:

Zacharias M. Nikolaou

Robinson College

April 11, 2014

I would like to dedicate this thesis to the people I love the most in my life, my father Marinos, my mother Eleni, and my brother Christos.

Acknowledgements

I would like to acknowledge my supervisor Prof. N. Swaminathan for all his help and patience during the course of this research. Prof. Swaminathan is by my standards the archetype academic who always has the time to meet and discuss with his students, no matter the triviality of the subject at hand. I would also like to acknowledge Prof. J.Y. Chen of University of California at Berkeley, for all his help in developing the multi-component fuel reduced chemical mechanism. I also acknowledge Prof. S. Cant for providing us with his DNS code SENGA2, without which this work would not have been possible. I also thank Mr. P. Benie for all his help on programming issues. Finally, I thank all my friends at the Hopkinson Lab, including but not limited to Y. Minamoto, I. Ahmed, I. Langella, S. Lombardi and E. Agathokleous for letting me share with them my thoughts and troubles on a daily basis during the course of this research.

I would also like to acknowledge the funding through the Low Carbon Energy University Alliance Programme supported by Tsinghua University, China, and also the educational grant through the A.G. Leventis Foundation.

This work made use of the facilities of HECToR, the UK's national high-performance computing service, which is provided by UoE HPCx Ltd at the University of Edinburgh, Cray Inc and NAG Ltd, and funded by the Office of Science and Technology through EPSRC's High End Computing Programme.

Publications

In chronological order, results from this work have appeared, or are being currently prepared for publication, in:

Journals:

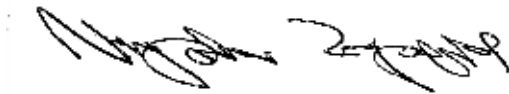
1. Z.M. Nikolaou, J.Y. Chen, N. Swaminathan, *Combust. Flame*, 160 (2013) 56-75. A 5-step reduced mechanism for combustion of CO, H₂, H₂O, CH₄, CO₂ mixtures with low hydrogen/methane and high H₂O content. *Elsevier certificate: (Ranked 4th) in Science Direct top 25 list of most downloaded articles October-December 2012.*
2. Z.M. Nikolaou, N. Swaminathan, *Combust. Flame*, Submitted October (2013)-accepted pending revision. Direct Numerical Simulation of multi-component fuel combustion with detailed chemistry.
3. Z.M. Nikolaou, N. Swaminathan, J.Y. Chen. *Combust. Flame*, Submitted November (2013)-accepted pending revision. Evaluation of a reduced mechanism for turbulent premixed combustion.
4. Z.M. Nikolaou, N. Swaminathan, *Combust. Flame*, Submitted November (2013)-accepted pending revision. Heat release rate markers for premixed combustion.
5. Z.M. Nikolaou, N. Swaminathan. An evaluation of current combustion sub-models in the RANS and LES context. In preparation.
6. Z.M. Nikolaou, N. Swaminathan. Scale-similarity modelling in the context of LES using detailed chemistry DNS data. In preparation.

Conferences:

1. Z.M. Nikolaou, N. Swaminathan. Direct Numerical Simulation (DNS) of wet-CO mixtures. *In: 4th International Forum on Multidisciplinary Education and Research for Energy Science*, Honolulu-Hawaii, December (2011).
2. Z.M. Nikolaou, N. Swaminathan. Direct Numerical simulation (DNS) of wet-CO combustion. *International Conference on Theoretical and Applied Mechanics (ICTAM)*, Beijing-China, August (2012).
3. Z.M. Nikolaou, N. Swaminathan. Direct Numerical Simulation (DNS) of multi-component fuel mixtures. *In: Academy for Co-creative Education of Environment and Energy Science (ACEEES)*, Big Island-Hawaii, December (2012).
4. Z.M. Nikolaou, N. Swaminathan. Direct Numerical Simulations of multi-component fuel mixtures with detailed chemistry. *6th European Combustion Meeting (ECM)*, Lund-Sweden, July (2013).

Declaration

This dissertation is the result of my own work and includes nothing which is the outcome of work done in collaboration except where specifically indicated in the text. The dissertation contains approximately 42273 words, 124 figures and 14 tables.

A handwritten signature in black ink, appearing to read 'Zacharias M. Nikolaou', written in a cursive style.

Zacharias M. Nikolaou, April 11, 2014.

Abstract

Fossil fuel reserves are projected to be decreasing, and emission regulations are becoming more stringent due to increasing atmospheric pollution. Alternative fuels for power generation in industrial gas turbines are thus required able to meet the above demands. Examples of such fuels are synthetic gas, blast furnace gas and coke oven gas. A common characteristic of these fuels is that they are multi-component fuels, whose composition varies greatly depending on their production process. This implies that their combustion characteristics will also vary significantly. Thus, accurate and yet flexible enough combustion sub-models are required for such fuels, which are used during the design stage, to ensure optimum performance during practical operating conditions.

Most combustion sub-model development and validation is based on Direct Numerical Simulation (DNS) studies. DNS however is computationally expensive. This, has so far limited DNS to single-component fuels such as methane and hydrogen. Furthermore, the majority of DNS conducted to date used one-step chemistry in 3D, and skeletal chemistry in 2D only. The need for 3D DNS using skeletal chemistry is thus apparent. In this study, an accurate reduced chemical mechanism suitable for multi-component fuel-air combustion is developed from a skeletal mechanism. Three-dimensional DNS of a freely propagating turbulent premixed flame is then conducted using both mechanisms to shed some light into the flame structure and turbulence-scalar interaction of such multi-component fuel flames.

It is found that for the multi-component fuel flame heat is released over a wider temperature range contrary to a methane flame. This, results from the presence of individual species reactions zones which do not all overlap. The performance of the reduced mechanism is also validated using the DNS data. Results suggest it to be a good substitute of the skeletal mechanism, resulting in significant time and memory savings. The flame markers commonly used to visualize heat release rate in laser diagnostics are found to be inadequate for the multi-component fuel flame, and alternative markers are proposed. Finally, some popular mean reaction rate closures are tested for the multi-component fuel flame. Significant differences are observed between the models' performance at the highest turbulence level considered in this study. These arise from the chemical complexity of the fuel, and further parametric studies using skeletal chemistry DNS would be useful for the refinement of the models.

Contents

Contents	vi
List of Figures	ix
List of Tables	xx
1 Introduction	1
1.1 The need for DNS	1
1.2 Chemistry considerations in reacting flows	2
1.3 Detailed chemistry DNS	4
1.4 Effects of using reduced chemistry	5
1.5 Markers for heat release rate imaging	7
1.6 Mean reaction rate closures	9
1.7 Thesis structure	10
2 Development of skeletal and reduced chemistry for multi-component fuel combustion	11
2.1 Development of skeletal mechanism: Sensitivity analysis	11
2.1.1 CO/H ₂ /H ₂ O-air mixtures	13
2.1.2 CO/CH ₄ /H ₂ O-air mixtures.	16
2.2 Development of reduced chemistry	23
2.3 Reduced mechanism	24
2.4 Validation	26
2.4.1 Premixed flames	29
2.4.2 Autoignition	50

2.5	Speed up times	52
3	Mathematical background: governing equations and numerical method	55
3.1	Governing equations	55
3.2	Transport coefficients	57
3.3	Reaction rates	59
3.3.1	Forward and backward reaction rate evaluation	60
3.3.2	Third body reactions	61
3.3.3	Pressure-dependent reactions	62
3.4	Boundary conditions	63
3.5	Flow configuration	63
3.6	Mixture conditions	64
3.7	Turbulent flame conditions	65
3.8	Computational requirements	65
4	Validation of 5-step reduced mechanism using 3D DNS data	68
4.1	Post-processing method	69
4.2	Comparison of spatial correlations	72
4.3	Comparison of mean profiles	80
4.4	Comparison of flame front structure	83
4.5	Comparison of flame surface statistics	88
5	Flame structure of multi-component fuel flame	93
5.1	Laminar flame structure	93
5.2	Turbulent flame speed	98
5.3	Turbulent kinetic energy spatial profile	99
5.4	Turbulent flame structure	102
5.5	c-space comparison with laminar flame profiles	105
5.6	Surface pdfs and scatter plots	111
5.7	Preferential diffusion	120
5.8	Heat release rate correlations	122

6 Heat release rate markers for premixed combustion	125
6.1 DNS databases	125
6.2 Analysis	125
6.2.1 Fractional influence method	126
6.2.2 Error estimator method	127
6.3 Methane fuel-air mixtures	128
6.4 Multi-component fuel-air mixtures	138
6.5 Proposed HRR markers	145
7 Modelling	148
7.1 RANS	148
7.1.1 SDR model	149
7.1.2 Reaction rate closures	152
7.1.3 c-pdfs model comparison	158
7.2 LES	162
7.2.1 SDR model	164
7.2.2 Reaction rate closures	167
8 Concluding remarks	169
8.1 Conclusions	169
8.2 Future work	170
Appendix A	172
Appendix B	179
References	181

List of Figures

- 2.1 Laminar flame speeds of CO/H₂/H₂O-air mixtures using the reduced (dashed lines) and skeletal (full lines) mechanisms. Open circles: Li et al. [84] mechanism results from Das et al. [39]. Also shown are the predictions using the skeletal mechanism of Boivin et al. (dashed lines with ×) [18]. Filled symbols: experimental results of Das et al. [39]. $T_r = 323$ K, $p = 1$ atm, $f_{H_2} = 5/95$, $X_{N_2}/X_{O_2} = 3.76$ 29
- 2.2 Laminar flame speeds of CO/H₂/H₂O mixtures using the reduced (dashed lines) and skeletal (continuous lines) mechanisms. Filled symbols: experimental results of Singh et al. [40]. $p = 1$ atm, $T_r = 400$ K, $\phi = 1$, oxidiser is O₂, N₂ with $X_{N_2}/X_{O_2} = 3.76$ 30
- 2.3 Laminar flame speeds of syngas mixtures (CO/H₂/CH₄/CO₂/N₂-air) using the reduced (dashed lines) and the skeletal (full lines) mechanisms. Symbols: experimental results of He et al. [79]. $f_{CH_4} = 0.24$ with 11% CO₂ and 42.7% N₂ in the fuel mixture. $T_r = 298$ K, $p = 1$ atm, $X_{N_2}/X_{O_2} = 3.76$. Error bars from He et al. [79] are also shown. 31
- 2.4 Laminar flame speeds of CO/H₂-air mixtures using the reduced (dashed lines) and skeletal (full lines) mechanisms. Symbols: experimental results of Vagelopoulos and Egolfopoulos [99]. $T_r = 298$ K, $p = 1$ atm, $X_{N_2}/X_{O_2} = 3.76$ 32

LIST OF FIGURES

2.5	Laminar flame speeds of CO/H ₂ /O ₂ /N ₂ mixtures using the reduced (dashed lines) and skeletal (continuous lines) mechanisms. Also shown are the results using the 4-step reduced mechanism of Boivin et al. [18] (open squares), the skeletal mechanism of Boivin et al. [18] (open circles) from the same study, and the implementation of the skeletal mechanism of [18] in this study (dashed-dotted lines). Symbols: experimental results of Natarajan et al. [100]. $f_{H_2} = 5/95$ and 1.0, at $p = 1$ atm, $X_{N_2}/X_{O_2} = 3.76$, for $T_r = 400, 500, 600$ and 700 K.	33
2.6	Laminar flame speeds of CO/H ₂ mixtures using the reduced (dashed lines) and skeletal (continuous lines) mechanisms. Filled symbols: experimental results of Singh et al. [40]. $p = 1$ atm, oxidizer is air.	34
2.7	Laminar flame speeds of CO/H ₂ /CO ₂ /O ₂ /N ₂ mixtures using the reduced (dashed lines) and skeletal (continuous lines) mechanisms . Symbols: experimental results of Natarajan et al. [100]. $f_{H_2} = 5/95$ and 1.0, at $p = 1$ atm, $X_{N_2}/X_{O_2} = 3.76$ with 10% and 20% CO ₂ dilution.	35
2.8	Laminar flame speeds of CO/H ₂ mixtures using the reduced (dashed lines) and skeletal (continuous lines) mechanisms. Symbols: experimental results of Hongyan et al. [86]. At $p = 1$ atm the oxidizer is O ₂ , N ₂ with $X_{N_2}/X_{O_2} = 3.76$. At $p = 5, 10, 20$ atm the oxidizer is O ₂ and He with $X_{He}/X_{O_2} = 7.0$. Open symbols: experimental results of Singh et al. [40].	36
2.9	Laminar flame mass burning rate for CO/H ₂ /O ₂ /Ar mixtures using the reduced (dashed lines) and skeletal (continuous lines) mechanisms. Filled symbols: experimental data of Burke et al. [87]. $T_r = 295$ K, $\phi = 2.5$, $X_{Ar}/X_{O_2} = 10.95$	37
2.10	Laminar flame speeds of CO/H ₂ /CH ₄ /CO ₂ /O ₂ /N ₂ mixtures using the reduced (dashed lines) and skeletal (continuous lines) mechanisms. Symbols: experimental results of Park et al. [101], $p = 1$ atm, $T_r = 298$ K.	38

LIST OF FIGURES

2.11 Laminar flame speeds of CO/H ₂ /CH ₄ /H ₂ O/CO ₂ /O ₂ /N ₂ mixtures using the reduced (dashed lines) and skeletal (continuous lines) mechanisms. Symbols: GRI- 3.0 results. $f_{H_2} = 5/95$, $f_{CH_4} = 5/95$, $f_{CO_2} = 0.5$, $T_r = 600$ K at $p = 1$ and 10 atm.	39
2.12 Laminar flame speeds of CO/H ₂ /H ₂ O/CO ₂ /O ₂ /N ₂ mixtures using the reduced (dashed lines) and skeletal (continuous lines) mechanisms. Symbols: GRI-3.0 results. $f_{H_2} = 5/95$, $f_{CO_2} = 0.5$, $T_r = 600$ K at $p = 1$ and 10 atm.	40
2.13 Laminar flame speeds of CO/H ₂ /H ₂ O/O ₂ /N ₂ mixtures using the reduced (dashed lines) and skeletal (continuous lines) mechanisms. Symbols: GRI-3.0 predictions. $f_{H_2} = 5/95$, $T_r = 600$ K at $p = 1$ and 10 atm.	42
2.14 Laminar flame speeds of CO/CH ₄ /H ₂ O/O ₂ /N ₂ mixtures using the reduced (dashed lines) and skeletal (continuous lines) mechanisms. Symbols: GRI-3.0 predictions. $f_{CH_4} = 5/95$, $T_r = 600$ K at $p = 1$ and 10 atm.	43
2.15 Flame structure for CO/H ₂ /O ₂ /N ₂ . $\phi = 0.8$, $f_{H_2} = 5/95$, $T_r = 400$ K, $p = 1$ atm. (conditions as in Fig. 2.5 top).	44
2.16 Flame structure for CO/H ₂ /O ₂ /N ₂ . $\phi = 0.8$, $f_{H_2} = 5/95$, $T_r = 700$ K, $p = 1$ atm. (conditions as in Fig. 2.5 top).	45
2.17 Flame structure for CO/H ₂ /O ₂ /He. He/O ₂ = 7.0, $\phi = 2.0$, $f_{H_2} = 1.0$, $T_r = 298$ K, $p = 5$ atm. (conditions as in Fig. 2.8 top). . . .	46
2.18 Flame structure for CO/H ₂ /O ₂ /He. He/O ₂ = 7.0, $\phi = 2.0$, $f_{H_2} = 1.0$, $T_r = 298$ K, $p = 10$ atm. (conditions as in Fig. 2.8 top). . . .	47
2.19 Flame structure for CO/H ₂ /CH ₄ /H ₂ O/CO ₂ /O ₂ /N ₂ with 25% H ₂ O. $\phi = 1.0$, $f_{H_2} = 5/95$, $f_{CH_4} = 5/95$, $f_{CO_2} = 0.5$, $T_r = 600$ K, $p = 1$ atm. (conditions as in Fig. 2.11).	48
2.20 Flame structure for CO/H ₂ /CH ₄ /H ₂ O/CO ₂ /O ₂ /N ₂ with 25% H ₂ O. $\phi = 1.0$, $f_{H_2} = 5/95$, $f_{CH_4} = 5/95$, $f_{CO_2} = 0.5$, $T_r = 600$ K, $p = 10$ atm. (conditions as in Fig. 2.11).	49

LIST OF FIGURES

2.21 Ignition delay times of CO/H ₂ /O ₂ /N ₂ mixtures ($X_{N_2}/X_{O_2} = 3.76$) for $\phi = 0.5$ using the reduced (dashed lines) and skeletal (continuous lines) mechanisms. Symbols: experimental results of Kalitan et al. [102]. Also shown for comparison are the results with the skeletal mechanism of Boivin et al. [18] (dashed lines with \times) for the $f_{H_2} = 20/80$ case.	52
2.22 Ignition delay times of CO/H ₂ /CO ₂ /O ₂ /N ₂ mixtures using the reduced (dashed lines) and skeletal (continuous lines) mechanisms. Symbols: experimental data of Vasu et al. [81]. Mixture composition: 8.91%H ₂ + 11.58%CO + 24.44%CO ₂ + 10.25%O ₂ + 44.83%N ₂	53
2.23 Ignition delay times of CO/H ₂ /H ₂ O/CH ₄ /O ₂ /N ₂ mixtures using the reduced (dashed lines) and skeletal (continuous lines) mechanisms. Symbols: experimental data of Gurentsov [107]. $\phi = 1$, $p = 5$ atm. Mixture: 3H ₂ + CO + H ₂ O + 4O ₂ + CH ₄ + 16N ₂	54
3.1 Sketch of the computation domain. Periodic boundary conditions are applied in the y, z directions. Grey area indicates laminar flame used for initialization.	64
3.2 The inlet turbulence parameters for the three cases on the turbulent combustion diagram.	66
4.1 Consumption speed s_c for cases A (thick line) and B (thin line), using the skeletal (continuous line) and reduced (dashed line) mechanisms.	69
4.2 Instantaneous heat release rate \dot{Q}^+ in the $x-y$ plane at different z locations. The top row is for the skeletal mechanism and the bottom row is for the reduced mechanism, for case A at $t/t_{fl}=4.0$	73
4.3 Instantaneous heat release rate \dot{Q}^+ in the $x-y$ plane at different z locations. The top row is for the skeletal mechanism and the bottom row is for the reduced mechanism, for case B at $t/t_{fl}=1.6$	74
4.4 Correlation coefficient r across the z direction for the heat release rate and species mass fractions, for case A (left) and case B (right).	75
4.5 Correlation coefficient r across the z direction for the heat release rate and species mass fractions, for the laminar unstrained case.	76

LIST OF FIGURES

4.6	Species rate-related QSSA error e_α , for case A (left) at $t/t_{fl}=4.0$, and case B (right) at $t/t_{fl}=1.6$. Grey bars show the laminar flame result.	77
4.7	Local QSSA error for the OH radical. Grey continuous line: conditional average in bins of c , and time averaged. Grey dashed line: laminar flame result.	79
4.8	Local QSSA error for HO ₂ . Grey continuous line: conditional average in bins of c , and time averaged. Grey dashed line: laminar flame result.	79
4.9	Local QSSA error for O. Grey continuous line: conditional average in bins of c , and time averaged. Grey dashed line: laminar flame result.	80
4.10	H and CO mean mass fractions. Thick lines-case A, thin lines-case B. Continuous lines-skeletal mechanism, dashed lines-reduced mechanism. Grey lines-laminar unstrained flame result.	81
4.11	H ₂ O and H ₂ O ₂ mean mass fractions. Lines as in Fig. 4.10.	82
4.12	H and CO mean net rates. Lines as in Fig. 4.10.	83
4.13	H ₂ O and H ₂ O ₂ mean net rates. Lines as in Fig. 4.10.	83
4.14	Mean progress variable and mean heat release rate against normalized distance. Lines as in Fig. 4.10.	84
4.15	H and CO mass fractions conditionally averaged in bins of c , and time-averaged for case B, using the skeletal (black continuous lines) and the reduced (dashed continuous lines) mechanisms. Grey lines show the laminar unstrained flame result.	84
4.16	H ₂ O and H ₂ O ₂ mass fractions conditionally averaged in bins of c , and time-averaged for case B. Lines as in Fig. 4.15.	85
4.17	H ₂ mass fraction conditionally averaged in bins of c , and time-averaged for case B. Lines as in Fig. 4.15.	85
4.18	Heat release rate conditionally averaged in bins of c , and time-averaged for case B. Lines as in Fig. 4.15.	86
4.19	Surface displacement speed pdfs. Thick lines-case A, thin lines-case B. Continuous lines-skeletal mechanism, dashed lines-reduced mechanism.	89

LIST OF FIGURES

4.20	Surface stretch rate pdf. Lines as in Fig. 4.19.	89
4.21	Surface generalized FSD ($=\chi$) pdf. Lines as in Fig. 4.19.	90
4.22	Scatter plots of normalized heat release rate and displacement speed against normalized surface curvature using the skeletal (black dots) and reduced (grey dots) mechanisms, for case B at $t/t_{fl}=1.6$	91
4.23	Scatter plots of normalized heat release rate and displacement speed against normalized surface tangential strain rate using the skeletal (black dots) and reduced (grey dots) mechanisms, for case B at $t/t_{fl}=1.6$	91
5.1	Heat release and main species normalized reaction rates comparison. Continuous lines: stoichiometric multi-component flame, dashed lines: stoichiometric methane flame (left) and stoichiometric hydrogen flame (right).	94
5.2	Species reaction zone thickness normalized by the heat release zone thickness. Index α as in Table 3.1. Filled circles: multi-component flame. Open circles: methane flame. Squares: hydrogen flame. Due care is required in DNS to ensure that the minimum species reaction zone thickness is well resolved.	94
5.3	Different progress variables definitions against c based on temperature. Continuous lines: multi-component flame. Green dashed line: methane flame c_{CH_4} . Blue dashed line: hydrogen flame c_{H_2}	97
5.4	Consumption speeds for the two turbulence levels.	98
5.5	The variation of normalised \tilde{k} with $\hat{x}=x/L_x$. The mean leading flame front position is marked using vertical lines corresponding to $\tilde{c} = 0.05$ in the respective cases.	99
5.6	Variation of u_{rms} normalized using its value at the inlet across the flame brush for cases A and C. Vertical lines show the location of the leading flame front ($\tilde{c}=0.05$).	101

LIST OF FIGURES

5.7	The combustion diagram. Circles: case A. Squares: case C. Black symbols/lines indicate location using δ , and grey symbols/lines using δ_l (note that the Da number lines remain unchanged). Filled symbols show turbulence parameters at the inlet and open symbols at the leading flame front ($\tilde{c}=0.05$).	101
5.8	Heat release rate contours $\dot{Q}/\max(\dot{Q}_{lam})$ for case A at $t/t_{fl}=4.0$. . .	102
5.9	Heat release rate contours $\dot{Q}/\max(\dot{Q}_{lam})$ for case C at $t/t_{fl}=1.0$. . .	103
5.10	Heat release rate contours $\dot{Q}/\max(\dot{Q}_{lam})$ for case C at $t/t_{fl}=2.0$. . .	104
5.11	Variation of normalized species mass fractions and heat release rate with c for case C at $t/t_{fl}=2$. Continuous grey line shows the conditional average and dashed line shows the laminar flame result.	106
5.12	Variation of normalized species mass fractions and heat release rate with c for case C at $t/t_{fl}=2$. Continuous grey line shows the conditional average and dashed line shows the laminar flame result.	107
5.13	Net rates of CH ₃ -associated reactions from the set in Table 2.3 in molm ⁻³ s ⁻¹ for an unstrained laminar flame.	108
5.14	Pdf of generalized FSD for case A (left) and case C (right).	111
5.15	Displacement speed pdfs for case A (left) and case C (right).	112
5.16	Curvature pdfs for case A (left) and case C (right). Lines as in Fig. 5.15.	112
5.17	Tangential strain rate pdfs for case A (left) and case C (right). Lines as in Fig. 5.15.	113
5.18	Stretch rate pdfs for case A (left) and case C (right). Lines as in Fig. 5.15.	113
5.19	Displacement speed against curvature for cases A (left) at $t/t_{fl}=4.0$, and case C (right) at $t/t_{fl}=2.0$, for $c^*=0.32$	115
5.20	Displacement speed against tangential strain rate for case A (left) at $t/t_{fl}=4.0$, and case C (right) at $t/t_{fl}=2.0$, for $c^*=0.32$	115
5.21	Heat release against curvature for case A (left) at $t/t_{fl}=4.0$, and case C (right) at $t/t_{fl}=2.0$, for $c^*=0.32$	116
5.22	Heat release rate against tangential strain rate for case A (left) at $t/t_{fl}=4.0$, and case C (right) at $t/t_{fl}=2.0$, for $c^*=0.32$	116

LIST OF FIGURES

5.23	Displacement speed against heat release rate for case A (left) at $t/t_{fl}=4.0$, and case C (right) at $t/t_{fl}=2.0$, for $c^*=0.32$	117
5.24	Tangential strain rate against curvature for case A (left) at $t/t_{fl}=4.0$, and case C (right) at $t/t_{fl}=2.0$, for $c^*=0.32$	117
5.25	Displacement speed against stretch rate for case A (left) at $t/t_{fl}=4.0$, and case C (right) at $t/t_{fl}=2.0$, for $c^*=0.32$. Grey continuous line shows the conditional average for case C.	118
5.26	H and OH mass fractions against curvature for case C at $t/t_{fl}=2.0$, for $c^*=0.32$	120
5.27	CO consumption rate against curvature, and heat release rate against H mass fraction for case C at $t/t_{fl}=2.0$, for $c^*=0.32$	121
5.28	Heat release rate normalized by its instantaneous maximum value, against the forward rate of the reaction $\text{OH} + \text{CH}_2\text{O} = \text{HCO} + \text{H}_2\text{O}$, for case A (left) at $t/t_{fl}=4$, and case C (right) at $t/t_{fl}=2$. Grey lines show the laminar unstrained flame result using GRI-3.0.	123
6.1	Methane-air, $\phi=0.5$, $T_r=800$ K, $p=1$ atm.	129
6.2	Methane-air, $\phi=1.0$, $T_r=800$ K, $p=1$ atm.	129
6.3	Methane-air, $\phi=0.5$, $T_r=800$ K, $p=1$ atm.	130
6.4	Methane-air, $\phi=1.0$, $T_r=800$ K, $p=1$ atm.	130
6.5	Methane-air, $\phi=0.5$, $T_r=800$ K, $p=1$ atm.	131
6.6	Methane-air, $\phi=1.0$, $T_r=800$ K, $p=1$ atm.	132
6.7	ϕ -averaged $Z(\dot{w}_r)$ across $\phi=0.5-1.0$ in steps of 0.1, using GRI-3.0 (left) and San Diego (right) mechanisms.	133
6.8	$Z(\dot{w}_r)^+$ of the top six reactions in Fig. 6.7 against ϕ	133
6.9	Scatter plot of heat release rate against the rates of $\text{OH} + \text{CH}_2\text{O} \Rightarrow \text{HCO} + \text{H}_2\text{O}$ (grey dots) and $\text{H} + \text{CH}_2\text{O} \Rightarrow \text{HCO} + \text{H}_2$ (black dots) for case C in [143], using the rate constants from Smooke's mechanism [109].	135
6.10	Scatter plot of heat release rate against the rates of $\text{OH} + \text{CH}_2\text{O} \Rightarrow \text{HCO} + \text{H}_2\text{O}$ (grey dots) and $\text{H} + \text{HO}_2 = \text{O}_2 + \text{H}_2$ (black dots) for case C in [143], using the rate constants from Smooke's mechanism [109].	135

LIST OF FIGURES

6.11 Scatter plot of heat release rate against the rates of $\text{OH} + \text{CH}_2\text{O} \Rightarrow \text{HCO} + \text{H}_2\text{O}$ (grey dots) and $\text{H} + \text{CH}_2\text{O} \Rightarrow \text{HCO} + \text{H}_2$ (black dots), for mild combustion case B in [143], using the rate constants from Smooke’s mechanism [109]. 137

6.12 A comparison of the top HRR-correlating reactions using GRI-3.0 [73] (continuous lines) and Smooke [109] (dashed lines) mechanisms. The results are for a stoichiometric methane-air laminar flame. 137

6.13 Multi-component fuel mixture, $\phi=0.5$, $T_r=800$ K, $p=1$ atm. 138

6.14 Multi-component fuel mixture, $\phi=1.0$, $T_r=800$ K, $p=1$ atm. 139

6.15 Multi-component fuel mixture, $\phi=0.5$, $T_r=800$ K, $p=1$ atm. 139

6.16 Multi-component fuel mixture, $\phi=1.0$, $T_r=800$ K, $p=1$ atm. 140

6.17 Multi-component fuel mixture, $\phi=0.5$, $T_r=800$ K, $p=1$ atm. 141

6.18 Multi-component fuel mixture, $\phi=1.0$, $T_r=800$ K, $p=1$ atm. 141

6.19 ϕ -averaged $Z(\dot{w}_r)$ across $\phi=0.5-1.0$ in steps of 0.1, using GRI-3.0 (left) and Li et al. (right) mechanisms. 142

6.20 $Z(\dot{w}_r)^+$ of the top three reactions in Fig. 6.19 against ϕ 142

6.21 Normalised rate of $\text{H} + \text{O}_2 + \text{M} = \text{HO}_2 + \text{M}$ and Eq. 6.5 (dashed line) across the flame brush. 144

6.22 Scatter plot of heat release rate for case A (left), and case C (right), against the rate of $\text{OH} + \text{CH}_2\text{O} \Rightarrow \text{HCO} + \text{H}_2\text{O}$ (grey dots) and using Eq. 6.5 (black dots). 144

6.23 Scatter plot of heat release rate for case A (left) and case C (right), against the rate of $\text{OH} + \text{CH}_2\text{O} \Rightarrow \text{HCO} + \text{H}_2\text{O}$ (grey dots) and the rate of $\text{O} + \text{HO}_2 \Rightarrow \text{OH} + \text{O}_2$ (black dots). 145

6.24 A comparison of the top HRR-correlating reactions using GRI-3.0 [73] (continuous lines) and Nikolaou et al. [38] (dashed lines) mechanisms. 146

7.1 $g = \widetilde{c}''^2 / \widetilde{c}(1 - \widetilde{c})$ for cases A and C. Note that g is much less than unity for both cases. 150

LIST OF FIGURES

7.2	Scalar dissipation rate comparison with the model's prediction (Eq. 7.2) for cases A (left) and C (right) . Case A: $\beta=6.70$. Case C: $\beta=9.49$	151
7.3	Density-weighted displacement speed pdfs, $\rho s_d/\rho_r s_t$, for case A (left) and case C (right).	155
7.4	EBU model, and Bray's model using $\tilde{\epsilon}_{cm}$ (Bray-1) and $\tilde{\epsilon}_c$ (Bray-2). Case A (left) and case C (right). Case A: $C_{ebu}=3.26$. Case C: $C_{ebu}=2.43$	157
7.5	Unstrained flamelet model (UF), FSD model and strained flamelet model (SF). Case A (left) and case C (right).	157
7.6	$\tilde{c}=0.1$ case A (left) and case C (right).	160
7.7	$\tilde{c}=0.3$ case A (left) and case C (right).	160
7.8	$\tilde{c}=0.5$ case A (left) and case C (right).	161
7.9	$\tilde{c}=0.7$ case A (left) and case C (right).	161
7.10	$\tilde{c}=0.9$ case A (left) and case C (right).	162
7.11	Progress variable filtered reaction rate $\overline{w_c^+}$, normalized using the maximum laminar value, for case C at $t/t_{fl}=2.0$. Filter widths (bottom to top): $\Delta^+=0.2, 1.0$ and 2.0	165
7.12	Scalar dissipation rate \tilde{N}^+ conditionally averaged in bins of \tilde{c} , and time-averaged, from the DNS (continuous lines) and estimated using Eq. 7.12 (dashed lines), for different filter widths Δ^+ , for cases A (left) and C (right). Case A: $\beta_c=9.4$. Case C: $\beta_c=7.5$	166
7.13	Mean reaction rate \bar{w}_c^+ conditionally averaged in bins of \tilde{c} , and time-averaged, from the DNS (continuous lines) and estimated using Eq. 7.4 (dashed lines) (and using \tilde{N} instead of $\tilde{\epsilon}_c$), for different filter widths Δ^+ , for cases A (left) and C (right). Case A: $\beta_c=9.4$. Case C: $\beta_c=7.5$	167
7.14	Mean reaction rate \bar{w}_c^+ conditionally averaged in bins of \tilde{c} , and time-averaged, from the DNS (continuous lines) and estimated using Eq. 7.13 (dashed lines), for different filter widths Δ^+ , for cases A (left) and C (right). Case A: $C_{ebu}=15.88$. Case C: $C_{ebu}=4.83$	168

LIST OF FIGURES

1	$T_r=323$ K, $p=1$ atm, $\phi=0.9$, $f_{H_2} = 5/95$ with $H_2O=0\%$ (left), 20% (right).	173
2	$T_r=323$ K, $p=1$ atm, $\phi=0.9$, $f_{H_2} = 1.0$ with $H_2O=0\%$ (left), 20% (right).	173
3	$T_r=323$ K, $p=1$ atm, $\phi=2.0$, $f_{H_2} = 5/95$ with $H_2O=0\%$ (left), 20% (right).	174
4	$T_r=600$ K, $p=10$ atm, $\phi=0.9$, $f_{H_2} = 5/95$ with $H_2O=0\%$ (left), 20% (right).	174
5	$T_r=1000$ K, $p=10$ atm, $\phi=0.9$, $f_{H_2} = 5/95$ with $H_2O=0\%$ (left), 20% (right).	175
6	$T_r=600$ K, $p=20$ atm, $\phi=0.9$, $f_{H_2} = 5/95$ with $H_2O=0\%$ (left), 20% (right).	175
7	$T_r=323$ K, $p=1$ atm, $\phi=0.9$, $f_{CH_4} = 5/95$ with $H_2O=0\%$ (left), 20% (right).	176
8	$T_r=323$ K, $p=1$ atm, $\phi=0.9$, $f_{CH_4} = 1.0$ with $H_2O=0\%$ (left), 20% (right).	176
9	$T_r=323$ K, $p=1$ atm, $\phi=2.0$, $f_{CH_4} = 5/95$ with $H_2O=0\%$ (left), 20% (right).	177
10	$T_r=600$ K, $p=10$ atm, $\phi=0.9$, $f_{CH_4} = 5/95$ with $H_2O=0\%$ (left), 20% (right).	177
11	$T_r=1000$ K, $p=10$ atm, $\phi=0.9$, $f_{CH_4} = 5/95$ with $H_2O=0\%$ (left), 20% (right).	178
12	$T_r=600$ K, $p=20$ atm, $\phi=0.9$, $f_{CH_4} = 5/95$ with $H_2O=0\%$ (left), 20% (right).	178

List of Tables

2.1	The first 40 most sensitive reactions from GRI-3.0. The sensitivity analysis was conducted at $T_r=323$ K, $\phi=0.9$, $f_{H_2} = 5/95$ with $H_2O\%=20\%$	15
2.2	The first 40 most sensitive reactions from GRI-3.0. The sensitivity analysis was conducted at $T_r=323$ K, $\phi=0.9$, $f_{CH_4} = 5/95$ with $H_2O\%=20\%$	17
2.3	The skeletal mechanism. Units are in cm, s, mol, cal, K.	21
2.4	The range of fuel composition and operating conditions tested. . .	28
2.5	Time in s of the run for each condition using PREMIX [96] with thermal and multi-component diffusion.	54
3.1	Species Lewis numbers. The species in parentheses are in steady-state using the 5-step reduced mechanism.	58
3.2	Fuel mixture composition (molar percentages) used in the DNS. Note that the oxidizer is atmospheric air.	65
3.3	Turbulent flame parameters for the DNS. The total run time of the simulations is t_{total} . Cases in parentheses denote DNS also contacted using the 5-step reduced mechanism.	65
3.4	Computational domain size and resolution.	66
3.5	Computational requirements for the DNS.	66
5.1	Comparison of the turbulent flame parameters for the DNS at the inlet and at the mean leading flame front position ($\tilde{c}=0.05$). . . .	100
5.2	Mean μ and standard deviation σ calculated using the respective flame surface variable pdfs.	109

LIST OF TABLES

6.1	The range of equivalence ratios where the respective reactions show improved correlations with the HRR (for the methane and diluted methane mixtures) as opposed to the commonly used marker, using GRI -3.0 [73]. The San Diego [106] and Li et al. [84] mechanisms were also used to confirm these results (see Figs. 6.7 and 6.19). For the multi-component fuel two alternative correlations are proposed.	147
7.1	Mean μ and standard deviation σ calculated using the respective flame surface variable pdfs.	154
A1	Conditions for sensitivity analysis.	172

Chapter 1

Introduction

1.1 The need for DNS

Direct Numerical Simulation (DNS) studies of turbulent reacting flows are a very useful tool in Computational Fluid Dynamics (CFD) simulations. Although DNS itself involves many assumptions and is thus not directly comparable to experimental data, it is currently the next best thing to an experiment. This is because all scales down to the smallest dissipative scales of turbulence i.e. the Kolmogorov length scale η_k are resolved, in contrast for example with Reynolds Averaged Navier-Stokes (RANS), and Large Eddy Simulations (LES), which resolve only part of the energy spectrum. DNS is widely used to gain physical insight into the complex processes governing turbulent combustion, since it provides a lot of useful information which experiments cannot, such as instantaneous distributions of species mass fractions, temperature, heat release rate, and the velocity field. DNS studies are widely used to develop and validate combustion sub-models, the majority of which are now used in commercial CFD codes.

DNS however is computationally expensive. On one part, this arises from the very fine numerical grid required to resolve the Kolmogorov length scale. DNS of reacting flows is even more expensive since additional balance equations for all the species concentrations need to be solved for, which add to the computational workload. In fact, chemistry requirements can in some cases be more stringent than turbulence requirements, and thus alternative methods are required to re-

duce the computational complexity associated with chemical effects. This very important topic is further discussed in section 1.2, which forms the backbone and at the same time the motivation behind the work in this thesis.

1.2 Chemistry considerations in reacting flows

The dwindling amounts of the naturally found hydrocarbon based fuels, and at the same time the more stringent emission regulations imposed due to the increasing levels of CO₂ in the atmosphere, are leading major manufacturers to the development of gas-turbine combustors for industrial power generation using alternative fuels [1]. These fuels may be Synthetic Gas which is commonly known as Syngas, Coke Oven Gas (COG) and Blast Furnace Gas (BFG) or suitable combinations of these gases [1].

The constituents of and the relative species proportions in these gases however vary considerably. The Syngas obtained by coal gasification is mostly composed of hydrogen and carbon monoxide with varying levels of carbon dioxide, water and other trace species [2, 3]. The relative proportions of the predominant gases vary widely depending on the gasification process and the ratio of hydrogen to carbon monoxide mole fractions in the fuel, $f_{\text{H}_2} = X_{\text{H}_2}/X_{\text{CO}}$, is typically larger than 0.1 and it can be as high as 3 [1, 2, 4, 5, 6, 7, 8]. The industrial COG includes a considerable amount of CH₄ in addition to these species with f_{H_2} as high as 11 and $f_{\text{CH}_4} \approx 5$ [9], whereas BFG has f_{H_2} and f_{CH_4} ranging from 0 to 0.15 [1, 5, 9]. In terms of calorific values, BFG has the lowest value of about 2.95 MJ/m³N compared to 40 MJ/m³N (where N stands for normal cubic meter) for the standard natural gas used in gas turbines [1]. BFG is produced in large quantities in the steel industry and it is the fuel of interest in this study.

The design of combustors operating efficiently, and in an environmentally-friendly manner to burn such fuels in turbulent flows is challenging. An integral part of the modern design process involves CFD simulations of turbulent reactive flows. Three-dimensional DNS of turbulent reactive flows of practical interest, are still expensive despite the development of faster and efficient computers. This is primarily due to two issues: (1) as previously stated, accurate description of the flow field requires to resolve the smallest dissipative scales, i.e. the Kolmogorov

length scale η_k , which requires an extremely prohibitive fine numerical grid, and (2) accurate description of the chemistry requires the use of a very large detailed reaction set. A detailed reaction set usually involves more than hundreds of reactions and tens of species, even for the combustion of a single-component fuel such as CH_4 with air, and the requirement for multi-component fuel-air combustion is even larger. Furthermore, the time scales associated with each species can be very disparate, thus requiring the use of an extremely small time-step. All of these factors, make such simulations impractical even on the fastest super-computer available to date. Robust and accurate models for combustion chemistry and its interaction with turbulence are thus required for the design and development of gas turbines intended to operate with the aforementioned multi-component fuels.

RANS and LES approaches tackle the first issue on numerical and computational requirements. The second issue on the required chemical complexity, can be tackled in a variety of ways, using tabulated chemistry approaches, [10, 11], and chemistry reduction involving quasi-steady state assumptions (QSSA), combined with partial equilibrium assumptions [12, 13]. In schemes with QSSA, the computational effort is reduced considerably by introducing steady state and partial equilibrium assumptions for particular species and reactions respectively. This reduces the number of species to be carried in simulations, and the stiffness of the system, by removing species with relatively short lifetimes. The wide variation in fuel mixture composition noted above, offers a considerable challenge to construct a reliable, robust, and computationally efficient chemical kinetic scheme. The computational efficiency is specifically of high importance from the view point of turbulent combustion calculation. Reduced mechanisms thus offer a convenient way to achieve this objective, and yet maintain an acceptable level of accuracy for important attributes such as laminar flame speed, flame structure, ignition delay time, extinction limits e.t.c. There have been many developments of such reduced mechanisms for the most commonly used single-component fuels [14, 15, 16, 17]. Generally, these mechanisms were developed systematically by introducing steady-state and/or partial equilibrium assumptions respectively for some species and reactions involved in a skeletal mechanism. Sensitivity analyses were typically used to obtain a skeletal mechanism from a full comprehensive

set of elementary reactions. As noted earlier, these strategies have been used in many past studies to obtain reduced kinetic mechanisms for single-component fuels, and there has not been an attempt to obtain a reduced mechanism for the combustion of a multi-component fuel, such as the BFG, to the best of our knowledge.

The range of validity of a reduced mechanism strongly depends on the fuel composition and operating condition used to develop it. The hydrogen content is low in the BFG as noted earlier, and one may like to mix it with small amounts of H_2 , CH_4 and H_2O or other gases containing high fractions of these species in order to enhance the BFG combustion characteristics. The need of a reduced mechanism for such multi-component fuels then becomes imperative. Most of the attempts in the past to get reduced mechanisms for a multi-component fuel were for syngas and were validated only for relatively high f_{H_2} values and very low water vapour content [18, 19]. More importantly, the effect of CH_4 was not considered, since it was generally taken that the CH_4 content in such fuels was too low to affect the combustion characteristics which might not be entirely correct. For example, it is later shown in Chapter 2 that small amounts of CH_4 in a CO, CH_4, H_2O -air mixture directly affect the flame speed response to water content in the fuel mixture.

It is thus apparent that combustion sub-model development for the multi-component fuel which is of interest in this study, has to begin with the development of sufficiently accurate, detailed, and yet fast chemical kinetic mechanisms which will be used in DNS of turbulent combustion of such fuels.

1.3 Detailed chemistry DNS

DNS studies using skeletal mechanisms although still expensive, provide a compromise between the conflicting demands on chemical detail and computational expenses. Skeletal chemistry also provides more accurate information than 1-step or reduced chemistry schemes. The first study using a skeletal mechanism was by Baum et al. [20, 21] over fifteen years ago. Turbulent premixed hydrogen-air flames interacting with two-dimensional turbulence were simulated. It was concluded that when using more realistic chemistry and transport models, the flame

structure correlated more with tangential strain rate than curvature [20, 21], a result which was used in subsequent combustion sub-model development.

Since then, there have been a lot of DNS studies of turbulent premixed combustion employing skeletal chemistry, predominantly examining the role of chemical mechanism, turbulence level, equivalence ratio and flow configuration. For example, hydrogen flames using a skeletal mechanism, have been extensively simulated in 2D [20, 21, 22, 23, 24]. More recently such flames have also been simulated in 3D [25, 26, 27]. Methane flames have also been extensively studied in 2D [28, 29, 30, 31, 32, 33] and in 3D [34, 35, 36]. It is thus apparent that the vast majority of DNS conducted to date using a skeletal mechanism for the chemical kinetics modelling are two-dimensional, which is not very realistic.

Direct simulations of other fuels such as syngas, specifically fuels of future interest, involving a multi-component fuel has rarely been done, except in the case of non-premixed combustion only, where a CO/H₂-air mixture has been simulated [37]. Understanding turbulent combustion of these fuels is very much required, especially in the current energy climate. Details of these fuels were examined in section 1.2. The water vapour can alter the chemical pathway depending on its concentration, and in doing so enhance combustion leading to an increase in the flame speed [38, 39, 40]. The carbon dioxide on the other hand has mainly a thermal effect, increasing the specific heat capacity of the reactant mixture thus reducing the flame temperature and speed. The hydrogen content can also enhance combustion through preferential diffusion effects when it is in large amounts [41]. All of these effects play key roles in determining the flame response to turbulence, and its combustion characteristics.

Despite this fact, most combustion sub-models currently employed for reacting flow calculations were developed based on DNS studies of simple single-component fuels as noted earlier. Thus, one can clearly see the need to directly simulate turbulent combustion of multi-component fuels.

1.4 Effects of using reduced chemistry

Usually, reduced mechanisms obtained using the approximations explained in section 1.2, are validated against laminar one-dimensional measurements such as

the flame speed and ignition delay time. Following this validation procedure, such reduced mechanisms have been used in past DNS [35, 42, 43] to gain insight for combustion sub-model development. This step entails a major assumption: that the reduced mechanism retains the same flame front structure and turbulence-flame interaction thereby yielding the same statistics as one would obtain using a detailed or a skeletal mechanism. This may or may not be correct and has not been validated yet in three dimensions, since most of the DNS studies in the past used either a single irreversible reaction or reduced chemical kinetics in three-dimensional turbulence. Skeletal chemical kinetic mechanisms on the other hand were predominantly used in two-dimensional simulations only, due to the high computational demand for three-dimensional simulations with detailed chemical complexity.

These investigations have been reviewed in many past studies [44, 45] helping us to understand the role of chemical detail in turbulent combustion simulations. The role of simulation dimensions was examined in detail in [46] where 2D simulations yielded much broader displacement speed pdfs in comparison with 3D simulations, with the discrepancies being proportional to the turbulence level. While the 3D simulations revealed the displacement speed to be strongly negatively correlated with curvature, the 2D data showed a much weaker correlation [46]. Since the displacement speed strongly depends on the flow field and mixture transport properties, it is expected that the type of chemical mechanism used will also affect this correlation and the respective pdfs. This is particularly important from a modelling point of view, since the displacement speed is involved in the G-equation and in the FSD modelling approaches. Furthermore, preferential diffusion effects of light species are not accurately described when a 1-step chemistry is used. The comparison of LES results with experimental data to assess the accuracy of the reduced chemistry models [47], suffers from many additional assumptions introduced for the sub-grid scale modelling. As a result, the exact influence of the chemical model employed, cannot be isolated unambiguously.

DNS studies are ideal to isolate the influence of chemical kinetics modelling on the flame structure and turbulence chemistry interaction, and to test the performance of a particular chemical scheme for turbulent combustion. However, in the past, DNS studies of premixed combustion in simple canonical configurations

with skeletal chemistry and archetypical configurations with reduced chemistry were predominantly used to gain insights on turbulence-chemistry interaction and model validation. These studies have been reviewed in [44], which suggests that 3D DNS with adequate detail of chemical kinetics will be required to make general strides on the development of combustion sub-models for optimal design of future engines and fuels. The DNS of combusting flows in archetypical configurations with detailed chemistry and molecular transport for multi-component fuels is expected to be beyond the reach of even exa-scale computing. The use of skeletal or reduced mechanisms seems a plausible choice at this time.

1.5 Markers for heat release rate imaging

Heat release rate (HRR) is another very important quantity in the study of laminar and turbulent reacting flows. HRR imaging is widely used to experimentally investigate the reacting flow field and to evaluate the performance of the combustor. From a practical view point, the spatial distribution of heat release is useful to discern flames and their locations. This spatial distribution directly influences important physical processes such as flame-turbulence interaction, sound generation [48] and its interaction with flames resulting in combustion instabilities [49, 50], determining the behaviour of practical devices such as industrial or aero gas turbines. Although a quantitative measurement of HRR is of great importance from both theoretical and practical view points, it is a challenging task as it involves accurate measurement of the order of 50 or more scalar concentrations and temperature simultaneously, since the local heat release rate is given by:

$$\dot{Q} = \sum_{\alpha=1}^N \dot{\omega}_{\alpha} h_{f,\alpha}^0 \quad (1.1)$$

where $N \geq 50$ is the number of species involved, $h_{f,\alpha}^0$ is the standard enthalpy of formation for species α and $\dot{\omega}_{\alpha}$ is its reaction rate. A quantitative measurement of HRR is a daunting task at this time and has been attempted rarely. However, useful correlations for qualitative estimates of local HRR have been proposed in past studies [51, 52, 53]. The primary aims of those studies [51, 52, 53], were to identify a scalar having good, possibly linear correlation with the local heat release rate.

It was observed by Najm and his co-workers [51, 52, 53] that the formyl radical, HCO, showed a good correlation with the local heat release rate for stoichiometric and slightly rich (equivalence ratio, ϕ , of 1.2) methane and dimethylether-air laminar flames. This correlation was also found to be insensitive to flame stretch (strain and curvature) effects resulting from flame-vortex interaction. As Eq. 1.1 suggests, the chemical kinetics model used in the computations of laminar flames would also impart due influences on this correlation. Thus, two chemical mechanisms, one involving 46 reactions and 16 species [54], and GRI Mech 1.2 involving 177 reactions and 32 species, were tested, and it was concluded that the correlation of HCO with local HRR was not disturbed. This reasonably robust correlation, at least for the conditions tested in [51, 52, 53], was attributed to the following two reasons: (1) HCO is a major intermediate species in the oxidation of CH₄ to CO₂ and (2) the production of HCO from formaldehyde, CH₂O, is directly dependent on the rate of the reaction $O + CH_3 = H + CH_2O$, which was found to have the largest fractional contribution to the local HRR. The production of HCO from CH₂O occurs through $OH + CH_2O = HCO + H_2O$ and $H + CH_2O = HCO + H_2$. Since the formyl radical is produced in these elementary reactions, and the signal to noise ratio for laser induced fluorescence of HCO is generally low compared to OH and CH₂O, the product of OH and CH₂O signals was proposed to be an indicator for HRR. However, a recent study [55], showed that these correlations involving the formyl radical and, the formaldehyde and hydroxyl radicals, are inadequate for fuel-rich mixtures of unsaturated hydrocarbons and for oxygenated fuels. Also, it was suggested [55] that the formaldehyde-based correlation is adequate when the major chemical path for fuel oxidation involves the methyl, CH₃ radical, and correlations involving ketyle, HCCO radicals, become more appropriate if the major oxidation route bypasses the methyl radical. Of course, it is imperative that a validation step for these correlations would be required if the flame conditions change from those investigated in the above studies. It is also worth to note that the formaldehyde-based correlation, i.e. $[OH][CH_2O]$, where [A] indicates the molar concentration of species A, has been used in a number of studies [56, 57] as the de facto standard to infer heat release rate related information in laminar and turbulent premixed flames, irrespective of the fuel mixture composition and stoichiometry.

The validity of the current flame markers for multi-component fuel-air combustion remains an open question.

1.6 Mean reaction rate closures

The design of combustors requires not only accurate chemical kinetics schemes, but also accurate combustion sub-models. These models are used to close the relevant governing equations solved for during the design process using CFD.

RANS simulations are still a work-horse for industry use, and also form a basis for development of LES combustion sub-models. Furthermore, RANS methodology is widely used in hybrid RANS/LES codes to minimize computational costs, since there exist regions in a flow-field where RANS would give similar if not identical results to LES at reduced computational costs. In the context of reacting RANS simulations one is required to solve a transport equation for the mean progress variable, \tilde{c} , in addition to the conservation equations for mass, momentum, and energy. For high Reynolds numbers, Re , this equation is [58]:

$$\frac{\partial \bar{\rho} \tilde{c}}{\partial t} + \frac{\partial \bar{\rho} \tilde{u}_i \tilde{c}}{\partial x_i} = - \frac{\partial \overline{\rho u_i'' c''}}{\partial x_i} + \overline{\dot{w}_c} \quad (1.2)$$

The above equation however has two unclosed terms requiring modelling. These are the progress variable mean reaction rate, $\overline{\dot{w}_c}$, and the turbulent scalar flux, $\overline{\rho u_i'' c''}$. There exist a variety of modelling approaches for turbulent premixed flames [59]. Flamelet-based methods include the G-equation [60], flame surface density (FSD) [61, 62, 63, 64, 65], thickened flamelets and laminar flamelets. Non-flamelet methods include pdf methods [66, 67, 68] and conditional moment closure (CMC) [69]. DNS databases are primarily used to derive and validate closures for the progress variable mean reaction rate, $\overline{\dot{w}_c}$, whether in RANS or LES context. These models were predominantly developed using DNS data of single-component fuel combustion often using 1-step chemistry for the chemical kinetics modelling. These studies are reviewed in [44, 70].

As noted earlier, the future fuels are more likely to be multi-component including light and heavy gases. As a result, it is thus not clear how the current combustion sub-models will perform for a multi-component fuel flame.

1.7 Thesis structure

In Chapter 2, accurate skeletal and reduced chemical kinetic mechanisms are developed suitable for the combustion of multi-component fuel mixtures containing CO, H₂, H₂O, CO₂ and CH₄, with low f_{H_2} and f_{CH_4} . These mechanisms are validated for laminar flame speed and its structure, and ignition delay times, for pressure and temperature conditions relevant to ground-based, heavy weight, gas-turbines with typical overall pressure ratios of about 20.0 or smaller [3, 5, 59], and combustor inlet temperature not exceeding 1000.0 K [3, 59]. To the best of our knowledge, this is the first attempt to obtain a reduced mechanism for a multi-component fuel mixture with a good accuracy over a wide range of thermo-chemical conditions.

The computational details, governing equations, and the DNS parameters are given in Chapter 3. In Chapter 4 the performance of the reduced mechanism developed in Chapter 2 is evaluated under turbulent conditions by comparing the flame statistics obtained using the reduced mechanism with those obtained using the skeletal chemistry DNS data. In Chapter 5 the flame structure of the multi-component fuel flame is analysed, and the performance of the commonly used markers for the HRR is evaluated using the DNS data. In Chapter 6, the validity of the commonly used flame markers for the HRR is re-examined. This is done both for the more conventional methane flame, and for the multi-component flame, and alternative HRR flame markers are proposed. The performance of some commonly used mean reaction rate closures is evaluated using the DNS data in Chapter 7, and conclusions are drawn in Chapter 8.

Chapter 2

Development of skeletal and reduced chemistry for multi-component fuel combustion

2.1 Development of skeletal mechanism: Sensitivity analysis

The chemical kinetics of CO/H₂ mixture oxidation have been investigated by numerous studies in the past, and a sustained interest on the combustion of Syngas in gas turbines for power generation has led to publication of a dedicated volume on this topic in the Combustion Science and Technology journal in 2008. The reviews by Chaos and Dryer [3], and by Sung and Law [4], clearly identified that the important reactions for CO oxidation are $\text{CO} + \text{OH} = \text{CO}_2 + \text{H}$ and $\text{CO} + \text{HO}_2 = \text{CO}_2 + \text{OH}$, with the second reaction becoming important at elevated pressures. Comprehensive kinetic mechanisms for dry and moist CO oxidation have been proposed in the past [71, 72], and have been updated in a number of later studies as has been noted by Sung and Law [4]. The interested readers are referred to [4] for further details.

Out of these many available comprehensive mechanisms, a set of 22-reactions suggested by Wang and Rogg [19] as a guideline along with the GRI-3.0 [73] dataset is used to obtain a skeletal mechanism in this study. This choice is

mainly for the following two reasons. (1) The stiffness of the reduced mechanism, signified by the non-linear coupled equations for steady-state species, strongly depends on the skeletal mechanism used. Wang and Rogg [19] produced a non-stiff and working mechanism for moist CO oxidation using their 22 reactions. (2) The interest in this study also includes the effects of CH₄ on moist CO and thus the GRI-3.0 dataset is used, since this mechanism is widely validated using experimental data for methane, H₂O-diluted and oxygen enriched methane [74], moist H₂/CO mixtures at elevated temperature [40] and 323 K [39]. This mechanism was also observed to give reasonable results for flame speeds and ignition delay times for multi-species fuel mixtures over a wide range of pressure, temperature and fuel composition. Burke et al. [75] noted that the measured mass burning rate of laminar premixed flames of H₂/CH₄/O₂/He mixture of equivalence ratios from 0.3 to 1.0 at pressures from 1 to 25 atmosphere can be obtained using GRI-3.0, but some of the rate constants need to be adjusted empirically. Kuznetsov et al. [76] concluded that GRI-3.0 is reasonable to compute the laminar burning velocity of a stoichiometric flame of H₂/O₂/H₂O for pressures ranging from 10 to 72 bar, but the mechanism of Lutz [77] is better for 1 to 72 bar. The burning velocities calculated by Boushaki et al. [78] for CH₄/H₂/H₂O/air atmospheric flames over a wide range of equivalence ratio with 0-30% H₂, dry (0% H₂O) and wet (100% relative humidity) conditions using GRI-3.0, compares acceptably well with measurements. He et al. [79] concluded that the laminar flame speeds calculated using GRI-3.0 and USC-II [80] mechanisms agreed well with their measurements using PLIF techniques for lean flames, and that the USC-II mechanism gives better agreement for flames with equivalence ratio of 0.8 and 0.9. Vasu et al. [81] noted that GRI-3.0 is able to capture the trends and magnitudes of the measured ignition delays at temperatures 974-1160 K and pressures 1.1-2.6 atmosphere for stoichiometric H₂/CO/CO₂/air mixtures. The analysis of ignition data by Petersen et al. [82] for syngas/air at 600-1148 K and 10-30 atmosphere suggested that the available kinetic mechanisms are reasonable if the temperature is larger than 1000 K, even up to 450 atmosphere as shown in [83]. Two points become clear from this brief survey; the BFG like fuel mixture was not considered in earlier studies and the use of GRI-3.0 is reasonable as long as the fuel mixture contains molecules such as CO, H₂, CH₄, CO₂ and H₂O.

The mechanism of Wang and Rogg [19] contains reactions that can also be found in the GRI-3.0 dataset which is very convenient. This is in contrast to the 31-reaction C1/O2 subset of Li et al. [84] for example, where reactions 30 ($\text{HCO} + \text{HO}_2 = \text{CO}_2 + \text{OH} + \text{H}$) and 31 ($\text{HCO} + \text{HCO} = \text{H}_2 + \text{CO} + \text{CO}$) do not appear in the GRI-3.0 set.

2.1.1 CO/H₂/H₂O-air mixtures

In order to identify the most sensitive reactions for fuel mixtures involving both H₂ and CH₄, sensitivity analyses are performed using the GRI-3.0 [73] reaction set and, its thermodynamic and transport databases. In this procedure, the most sensitive reactions will be identified as the ones which influence the most the burning characteristics of the mixtures. The least sensitive reactions will be disregarded assuming that low sensitivities do not affect the combustion process in any way. It has to be noted at this point that this procedure has been used extensively in the literature to obtain skeletal mechanisms. In this procedure the effect of the reactions having low sensitivities is not accounted for in the final derived skeletal mechanism which in principle should affect the combustion process. The justification of this subtle point is unclear a priori, and can only come a posteriori provided the agreement of the derived skeletal mechanism with experimental data is good.

In this section, flame speed sensitivity analyses are conducted using GRI-3.0 [73], at high (20%) and zero water vapour content in the fuel mixture in order to obtain a suitable skeletal mechanism for CO/H₂/H₂O mixtures. The skeletal mechanism must be as detailed as possible involving a possibly minimum number of species. This is because the number of species involved is the most important factor affecting the computational time especially in direct numerical simulation studies of turbulent combustion. The first 40 most sensitive reactions for CO/H₂/H₂O fuel mixture at an equivalence ratio of $\phi = 0.9$ and reactant temperature of $T_r = 323$ K with $f_{\text{H}_2} = 0.053$ and 20% water vapour content are given in Table 2.1. The sensitivity coefficients are normalised as $S_v^{k_i} = \left| \frac{k_i}{v} \frac{\partial v}{\partial k_i} \right| / \left| \frac{k_i}{v} \frac{\partial v}{\partial k_i} \right|_{\max}$ where k_i is the specific rate constant for reaction i and v is the flame speed.

Consistent with the findings of [19], the majority of their 22 reactions have

the highest sensitivities, but some reactions which are not present in [19] have appeared in Table 2.1 with higher sensitivities and they must be included. In order of decreasing sensitivity these are reactions 120, 2, 12, 5, 14, and 47. Reactions 35, 36, and 34 do appear in [19] through $\text{H} + \text{O}_2 + \text{M} = \text{HO}_2 + \text{M}$, but in the GRI-3.0 set there are separate reactions for some of the third body species and should be included. This is also the case for reactions 41, 42 and 40 through $2\text{H} + \text{M} = \text{H}_2 + \text{M}$ and reaction 166 through $\text{HCO} + \text{M} = \text{H} + \text{CO} + \text{M}$. These reactions are shown in bold letters in Table 2.1. Reactions involving atomic N are neglected since they have low sensitivities in general. Also, note that reactions appearing twice in Table 2.1 are duplicate reactions (D) in the GRI-3.0 set.

Considering all of the above changes, 22 from [19], 3 duplicate and 13 additional, a 38-reaction skeletal mechanism is obtained for CO/H₂/H₂O-air mixtures with large H₂O percentage.

Further parametric sensitivity analyses were conducted at various thermochemical conditions examining the effects of pressure, temperature and equivalence ratio. Figs. A1 to A6 in Appendix A show these results. After a careful examination of Figs. A1 to A6, the following points can be deduced:

1. When the water vapour is added the sensitivity to the three body recombination reaction $\text{H} + \text{O}_2 + \text{H}_2\text{O} = \text{HO}_2 + \text{H}_2\text{O}$ becomes significantly large, while the sensitivity of the corresponding three body reactions involving N₂ and M are reduced. The reaction $\text{H} + \text{HO}_2 = 2\text{OH}$ increases the flame speed being the biggest OH-radical provider as noted by Das et al. [39]. It is also observed that the sensitivity of the reaction $2\text{OH} = \text{O} + \text{H}_2\text{O}$ increases significantly when the moisture content in the fuel mixture is increased thereby increasing OH radical production [40, 39]. This provides an extra source of OH radicals for CO oxidation through the most dominant reaction $\text{OH} + \text{CO} = \text{H} + \text{CO}_2$. Also, the sensitivity of chain propagation reaction $\text{OH} + \text{H}_2 = \text{H} + \text{H}_2\text{O}$ at 20% of water vapour content is reduced. However, as one can see an increase in H₂O concentration shifts the equilibrium of this reaction to the left resulting in more OH which makes fuel mixtures with low H₂ content to be more sensitive to H₂O addition as observed in [40, 39].

$S_v^{k_1}$	No. in GRI-3.0 set	Reaction
3.54E-05	209	$\text{NNH} + \text{H} = \text{H}_2 + \text{N}_2$
3.76E-05	40	$2\text{H} + \text{H}_2 = 2\text{H}_2$
1.13E-04	208	$\text{NNH} + \text{O} = \text{NH} + \text{NO}$
2.21E-04	42	$2\text{H} + \text{CO}_2 = \text{H}_2 + \text{CO}_2$
3.30E-04	48	$\text{H} + \text{H}_2\text{O}_2 = \text{OH} + \text{H}_2\text{O}$
3.57E-04	47	$\text{H} + \text{H}_2\text{O}_2 = \text{HO}_2 + \text{H}_2$
4.33E-04	116(D)	$2\text{HO}_2 = \text{O}_2 + \text{H}_2\text{O}_2$
5.68E-04	168	$\text{HCO} + \text{O}_2 = \text{HO}_2 + \text{CO}$
6.85E-04	14	$\text{O} + \text{HCO} = \text{H} + \text{CO}_2$
7.97E-04	88(D)	$\text{OH} + \text{H}_2\text{O}_2 = \text{HO}_2 + \text{H}_2\text{O}$
8.65E-04	100	$\text{OH} + \text{HCO} = \text{H}_2\text{O} + \text{CO}$
9.79E-04	1	$2\text{O} + \text{M} = \text{O}_2 + \text{M}$
1.12E-03	5	$\text{O} + \text{H}_2\text{O}_2 = \text{OH} + \text{HO}_2$
1.43E-03	12	$\text{O} + \text{CO}(+\text{M}) = \text{CO}_2(+\text{M})$
1.62E-03	89(D)	$\text{OH} + \text{H}_2\text{O}_2 = \text{HO}_2 + \text{H}_2\text{O}$
1.96E-03	2	$\text{O} + \text{H} + \text{M} = \text{OH} + \text{M}$
2.31E-03	120	$\text{HO}_2 + \text{CO} = \text{OH} + \text{CO}_2$
2.33E-03	115(D)	$2\text{HO}_2 = \text{O}_2 + \text{H}_2\text{O}_2$
2.40E-03	55	$\text{H} + \text{HCO} = \text{H}_2 + \text{CO}$
2.83E-03	166	$\text{HCO} + \text{H}_2\text{O} = \text{H} + \text{CO} + \text{H}_2\text{O}$
3.44E-03	41	$2\text{H} + \text{H}_2\text{O} = \text{H}_2 + \text{H}_2\text{O}$
3.64E-03	39	$2\text{H} + \text{M} = \text{H}_2 + \text{M}$
5.12E-03	167	$\text{HCO} + \text{M} = \text{H} + \text{CO} + \text{M}$
8.38E-03	287(D)	$\text{OH} + \text{HO}_2 = \text{O}_2 + \text{H}_2\text{O}$
1.10E-02	34	$\text{H} + 2\text{O}_2 = \text{HO}_2 + \text{O}_2$
1.51E-02	85	$2\text{OH}(+\text{M}) = \text{H}_2\text{O}_2(+\text{M})$
1.75E-02	44	$\text{H} + \text{HO}_2 = \text{O} + \text{H}_2\text{O}$
2.14E-02	4	$\text{O} + \text{HO}_2 = \text{OH} + \text{O}_2$
3.36E-02	84	$\text{OH} + \text{H}_2 = \text{H} + \text{H}_2\text{O}$
5.23E-02	43	$\text{H} + \text{OH} + \text{M} = \text{H}_2\text{O} + \text{M}$
5.96E-02	86	$2\text{OH} = \text{O} + \text{H}_2\text{O}$
8.27E-02	33	$\text{H} + \text{O}_2 + \text{M} = \text{HO}_2 + \text{M}$
9.48E-02	36	$\text{H} + \text{O}_2 + \text{N}_2 = \text{HO}_2 + \text{N}_2$
9.66E-02	38	$\text{H} + \text{O}_2 = \text{O} + \text{OH}$
9.72E-02	87(D)	$\text{OH} + \text{HO}_2 = \text{O}_2 + \text{H}_2\text{O}$
1.43E-01	3	$\text{O} + \text{H}_2 = \text{H} + \text{OH}$
1.69E-01	35	$\text{H} + \text{O}_2 + \text{H}_2\text{O} = \text{HO}_2 + \text{H}_2\text{O}$
2.12E-01	45	$\text{H} + \text{HO}_2 = \text{O}_2 + \text{H}_2$
3.18E-01	46	$\text{H} + \text{HO}_2 = 2\text{OH}$
1.00E+00	99	$\text{OH} + \text{CO} = \text{H} + \text{CO}_2$

Table 2.1: The first 40 most sensitive reactions from GRI-3.0. The sensitivity analysis was conducted at $T_r=323$ K, $\phi=0.9$, $f_{\text{H}_2} = 5/95$ with $\text{H}_2\text{O}\%=20\%$.

2. The chain branching reactions $\text{O} + \text{H}_2 = \text{H} + \text{OH}$, $\text{H} + \text{O}_2 = \text{O} + \text{OH}$ show increased sensitivities, while the chain carrier reaction $\text{OH} + \text{H}_2 = \text{H} + \text{H}_2\text{O}$ shows positive sensitivity consistent with the results of [40] when the H_2 fraction in the fuel mixture is increased. Also, the recombination reaction $\text{H} + \text{O}_2 + \text{H}_2\text{O} = \text{HO}_2 + \text{H}_2\text{O}$ becomes significant in the dry mixture due to an increased H radical level resulting from the increased H_2 fraction in the mixture. The addition of water vapour in this case does not affect the reaction sensitivities as much for the mixture with low H_2 fraction. This

implies that the positive chemical effect of water vapour addition will be less pronounced as observed by Das et al. [39]. The effects are similar to these when the equivalence ratio of the fuel mixture is increased.

3. From a practical point of view in using BFG-like gases, lean mixtures with low H₂ content is of interest. Thus, the effects of reactant temperature and pressure on the reaction sensitivity are also investigated in Appendix A. It is well known (see for example [3]) that HO₂ chemistry becomes important at high pressures and thus the CO consuming reaction HO₂ + CO = OH + CO₂ has large sensitivities for both dry and wet mixtures and OH + CO = H + CO₂ remains as the most important reaction with sensitivity nearly five times larger than for the HO₂ reaction for CO consumption. As one would expect, the sensitivities of three-body recombination reactions are increased at high pressures with the sensitivity of H + O₂ + H₂O = HO₂ + H₂O moving up the sensitivity coefficient ranking for wet mixtures as noted for atmospheric conditions. The chain branching reaction H + O₂ = O + OH becomes the second most dominant reaction for both the dry and the wet mixture at high pressures.

Although there is a shift in the ranking of the reactions the more dominant reactions remain the same. Hence it is noted that the reaction make up for the H₂/CO chemistry is unaffected for the range of conditions studied here.

2.1.2 CO/CH₄/H₂O-air mixtures.

The flame speed sensitivity analyses for CO/CH₄/H₂O-air mixtures are discussed in this section. This analysis helps one to identify the most important reactions involving CH₄. The normalised flame speed sensitivity coefficients are shown in Table 2.2 for the first 40 most sensitive reactions from the GRI-3.0 set. In this case, the most important reactions involving only CH₄, CH₃ and CH₂O were considered. As a result, in order of decreasing sensitivity, reactions 52, 11, 98, 284, 10, 15, 53, 58, 101 shown in bold letters in Table 2.2 are added to the 38 reactions identified above. These 9 reactions identified here are also consistent with the study of Cherian et al. [85] although no mechanism was presented in their case for mixtures with high water vapour content, or with CH₄.

$S_v^{k_i}$	No. in GRI-3.0 set	Reaction
2.15E-03	115	$2\text{HO}_2 = \text{O}_2 + \text{H}_2\text{O}_2$
2.69E-03	120	$\text{HO}_2 + \text{CO} = \text{OH} + \text{CO}_2$
3.07E-03	41	$2\text{H} + \text{H}_2\text{O} = \text{H}_2 + \text{H}_2\text{O}$
3.10E-03	14	$\text{O} + \text{HCO} = \text{H} + \text{CO}_2$
3.18E-03	39	$2\text{H} + \text{M} = \text{H}_2 + \text{M}$
3.37E-03	168	$\text{HCO} + \text{O}_2 = \text{HO}_2 + \text{CO}$
3.39E-03	144	$\text{CH}_2(\text{S}) + \text{O}_2 = \text{H} + \text{OH} + \text{CO}$
3.59E-03	126	$\text{CH} + \text{H}_2 = \text{H} + \text{CH}_2$
3.71E-03	100	$\text{OH} + \text{HCO} = \text{H}_2\text{O} + \text{CO}$
4.16E-03	290	$\text{CH}_2 + \text{O}_2 \Rightarrow 2\text{H} + \text{CO}_2$
4.33E-03	95	$\text{OH} + \text{CH}_3(+\text{M}) = \text{CH}_3\text{OH}(+\text{M})$
5.36E-03	97	$\text{OH} + \text{CH}_3 = \text{CH}_2(\text{S}) + \text{H}_2\text{O}$
5.81E-03	12	$\text{O} + \text{CO}(+\text{M}) = \text{CO}_2(+\text{M})$
7.23E-03	101	$\text{OH} + \text{CH}_2\text{O} = \text{HCO} + \text{H}_2\text{O}$
7.63E-03	58	$\text{H} + \text{CH}_2\text{O} = \text{HCO} + \text{H}_2$
7.99E-03	119	$\text{HO}_2 + \text{CH}_3 = \text{OH} + \text{CH}_3\text{O}$
8.36E-03	44	$\text{H} + \text{HO}_2 = \text{O} + \text{H}_2\text{O}$
8.91E-03	287	$\text{OH} + \text{HO}_2 = \text{O}_2 + \text{H}_2\text{O}$
1.01E-02	34	$\text{H} + 2\text{O}_2 = \text{HO}_2 + \text{O}_2$
1.10E-02	55	$\text{H} + \text{HCO} = \text{H}_2 + \text{CO}$
1.17E-02	84	$\text{OH} + \text{H}_2 = \text{H} + \text{H}_2\text{O}$
1.42E-02	53	$\text{H} + \text{CH}_4 = \text{CH}_3 + \text{H}_2$
1.59E-02	85	$2\text{OH}(+\text{M}) = \text{H}_2\text{O}_2(+\text{M})$
1.59E-02	15	$\text{O} + \text{CH}_2\text{O} = \text{OH} + \text{HCO}$
2.09E-02	10	$\text{O} + \text{CH}_3 = \text{H} + \text{CH}_2\text{O}$
2.56E-02	284	$\text{O} + \text{CH}_3 \Rightarrow \text{H} + \text{H}_2 + \text{CO}$
4.46E-02	86	$2\text{OH} = \text{O} + \text{H}_2\text{O}$
4.53E-02	98	$\text{OH} + \text{CH}_4 = \text{CH}_3 + \text{H}_2\text{O}$
4.72E-02	11	$\text{O} + \text{CH}_4 = \text{OH} + \text{CH}_3$
4.86E-02	43	$\text{H} + \text{OH} + \text{M} = \text{H}_2\text{O} + \text{M}$
5.50E-02	52	$\text{H} + \text{CH}_3(+\text{M}) = \text{CH}_4(+\text{M})$
7.38E-02	87	$\text{OH} + \text{HO}_2 = \text{O}_2 + \text{H}_2\text{O}$
7.74E-02	33	$\text{H} + \text{O}_2 + \text{M} = \text{HO}_2 + \text{M}$
9.20E-02	3	$\text{O} + \text{H}_2 = \text{H} + \text{OH}$
9.44E-02	36	$\text{H} + \text{O}_2 + \text{N}_2 = \text{HO}_2 + \text{N}_2$
1.64E-01	45	$\text{H} + \text{HO}_2 = \text{O}_2 + \text{H}_2$
1.73E-01	35	$\text{H} + \text{O}_2 + \text{H}_2\text{O} = \text{HO}_2 + \text{H}_2\text{O}$
1.99E-01	38	$\text{H} + \text{O}_2 = \text{O} + \text{OH}$
2.50E-01	46	$\text{H} + \text{HO}_2 = 2\text{OH}$
1.00E+00	99	$\text{OH} + \text{CO} = \text{H} + \text{CO}_2$

Table 2.2: The first 40 most sensitive reactions from GRI-3.0. The sensitivity analysis was conducted at $T_r=323$ K, $\phi=0.9$, $f_{\text{CH}_4} = 5/95$ with $\text{H}_2\text{O}\%=20\%$.

As for the $\text{CO}/\text{H}_2/\text{H}_2\text{O}$ mixtures, additional sensitivity analyses were also conducted for $\text{CO}/\text{CH}_4/\text{H}_2\text{O}$ mixture with high and no water vapour. The conditions for this analysis and the raw sensitivity coefficients for the top 20 reactions are shown in Table A1 and Figs. A7 to A12 in Appendix A. The following points, in addition to those noted for $\text{CO}/\text{H}_2/\text{H}_2\text{O}$ mixtures in section 2.1.1, can be summarised:

1. It is obvious to expect some reactions involving CH_4 , CH_3 , CH_2 , HCO and CH_2O to show up for the CH_4 mixture. This is because CH_4 readily reacts

with OH and O decomposing to CH₃ which in turn decomposes to carbon-containing species having fewer H atoms.. More importantly, the chain branching reaction $\text{H} + \text{O}_2 = \text{O} + \text{OH}$ moves from 9th rank for CO/H₂/H₂O mixture to 3rd rank for the methane containing mixture and this reaction becomes the most dominant for mixtures with $f_{\text{CH}_4} = 1$. This is because of increased level of H resulting from CH₄. Close examination of the net reaction rates of reactions 41-49 (for the methane-containing mixtures), has shown that they are all positive i.e. their net reaction rates proceed from the left of the equality symbol to the right. This means that originally, CH₄ decomposes to CH₃ through reactions 41 and 42. In turn CH₃ decomposes to H through reactions 43 and 44. Thus, addition of methane to a CO mixture results in increased H radical production rate through the above decomposition process. In turn increased H radical production rate causes increased sensitivities of $\text{H} + \text{O}_2 = \text{O} + \text{OH}$ and $\text{H} + \text{CH}_3 + \text{M} = \text{CH}_4 + \text{M}$. The sensitivity of $\text{H} + \text{O}_2 + \text{H}_2\text{O} = \text{HO}_2 + \text{H}_2\text{O}$ is also increased (absolute value) as a result, and this explains why CO/CH₄ mixtures are chemically less sensitive to water vapour addition.

2. Another important difference observed is the decrease of the sensitivity of the chain propagation $\text{OH} + \text{H}_2 = \text{H} + \text{H}_2\text{O}$, moving down from 7th rank to 14th in the top 20 reactions. In the H₂ containing mixtures this reaction can be seen as the fuel attacking step, but for CH₄ containing mixture the fuel attack is signified by reactions involving CH₄ and thus these reactions involving methane take precedence (see Fig. A7). In the wet methane containing mixtures the above chain carrier reaction moves further down in the list.
3. The reaction $\text{O} + \text{CH}_3 = \text{H} + \text{H}_2 + \text{CO}$ becomes one of the top 7 reactions for dry and wet mixtures with $f_{\text{CH}_4} = 1$ at atmospheric pressure. This reaction moves out of the top 20 reactions when the pressure becomes 10 atmosphere.
4. At high pressures (10, 20 atm.), the reaction $\text{O} + \text{CH}_2\text{O} = \text{OH} + \text{HCO}$ appear in the top 20 reactions but moves out of this set when water vapour

is added to the fuel mixture or the pressure is atmospheric.

5. For a relatively high methane concentration in the fuel mixture, reactions with CH_2 and CH_3O become important. For a lower methane content these species are not important for all the conditions tested, hence the reaction make up in the skeletal mechanism is sufficient to describe the methane chemistry of such fuel mixtures. Thus, the effect of small CH_4 amounts in the fuel mixture is adequately captured by the extra 9 reactions noted above, something which was neglected while developing reduced mechanism in a previous study [18].

In order to account for the He, Ar diluted experimental conditions of Hongyyan et al. [86] and of Burke et al. [87], the reactions $\text{H} + \text{O}_2 + \text{Ar} = \text{HO}_2 + \text{Ar}$ and $\text{H} + \text{O}_2 + \text{He} = \text{HO}_2 + \text{He}$ are also included in the set assuming that He has the same kinetic parameters as Ar. Slight modifications were made to some of the reaction rate parameters with respect to their values in the GRI-3.0 set to improve the agreement with experimental results. These modifications are as follows: (1) The pre-exponential factor of the dominant CO-consuming reaction $\text{OH} + \text{CO} = \text{H} + \text{CO}_2$ was reduced by 1.5%, and the pre-exponential factor of the OH-producing reaction $\text{H} + \text{HO}_2 = 2\text{OH}$ was reduced by 1% for better agreement with the experimental data on the flame speeds at high water vapour conditions. (2) The rate of the chain-terminating reaction $\text{H} + \text{O}_2 + \text{N}_2 = \text{HO}_2 + \text{N}_2$ was reduced by increasing the absolute value of the temperature exponent n by 8% (from $n=-1.24$ to $n=-1.339$) and by reducing the pre-exponential factor by 2.5%. This was found to be necessary since the original GRI-3.0 parameters resulted in slight over-estimation of the ignition delay time at low pressure, low temperature conditions. (3) The activation energy of the CO-consuming reaction $\text{HO}_2 + \text{CO} = \text{OH} + \text{CO}_2$ was increased by 4%. This was done for better agreement in the high pressure and high temperature regime of the measured ignition delay times since the original GRI-3.0 parameters under-estimated the ignition delay times slightly for these conditions. All the changes made are thus minor, and will not de-optimize the set of original GRI-3.0 reactions. These modifications are as per the common practice [75, 88, 89], since they are within the uncertainties of the rate parameters for the above reactions.

Based on the above analysis, the final skeletal mechanism for this study includes 38 reactions suggested in section 2.1.1, 9 reactions for methane mixtures and 2 three body recombination reaction involving Ar and He identified in this section. Hence, there are 49 reactions involving 15 species in total and this set is given in Table 2.3 along with the kinetic rate parameters.

	Reaction	A	n	Ea
1	H + O ₂ = O + OH	2.650E+16	-0.6707	17041.0
2	O + H ₂ = H + OH	3.870E+04	2.7	6260.0
3	OH + H ₂ = H + H ₂ O	2.160E+08	1.51	3430.0
4	2OH = O + H ₂ O	3.570E+04	2.4	-2110.0
5 ^a	H + O ₂ + M = HO ₂ + M	2.800E+18	-0.86	0.0
6	H + O ₂ + H ₂ O = HO ₂ + H ₂ O	1.126E+19	-0.76	0.0
7	H + O ₂ + N ₂ = HO ₂ + N ₂	2.535E+19	-1.3392	0.0
8	H + O ₂ + He => HO ₂ + He	7.000E+17	-0.8	0.0
9	H + O ₂ + Ar => HO ₂ + Ar	7.000E+17	-0.8	0.0
10	H + 2O ₂ = HO ₂ + O ₂	2.080E+19	-1.24	0.0
11	H + HO ₂ = 2OH	8.316E+13	0	635.0
12	H + HO ₂ = O ₂ + H ₂	4.480E+13	0	1068.0
13(D)	OH + HO ₂ = O ₂ + H ₂ O	1.450E+13	0	-500.0
14(D)	OH + HO ₂ = O ₂ + H ₂ O	5.000E+15	0	17330.0
15	H + HO ₂ = O + H ₂ O	3.970E+12	0	671.0
16	O + HO ₂ = OH + O ₂	2.000E+13	0	0.0
17(D)	2HO ₂ = O ₂ + H ₂ O ₂	1.300E+11	0	-1630.0
18(D)	2HO ₂ = O ₂ + H ₂ O ₂	4.200E+14	0	12000.0
19 ^b	2OH(+M) = H ₂ O ₂ (+M)	7.400E+13	-0.37	0.0
20	H + H ₂ O ₂ = OH + H ₂ O	1.000E+13	0	3600.0
21(D)	OH + H ₂ O ₂ = HO ₂ + H ₂ O	1.700E+18	0	29410.0
22(D)	OH + H ₂ O ₂ = HO ₂ + H ₂ O	2.000E+12	0	427.0
23	H + H ₂ O ₂ = HO ₂ + H ₂	1.210E+07	2	5200.0
24	O + H ₂ O ₂ = OH + HO ₂	9.630E+06	2	4000.0
25 ^c	2H + M = H ₂ + M	1.000E+18	-1	0.0
26	2H + H ₂ = 2H ₂	9.000E+16	-0.6	0.0
27	2H + CO ₂ = H ₂ + CO ₂	5.500E+20	-2	0.0
28	2H + H ₂ O = H ₂ + H ₂ O	6.000E+19	-1.25	0.0
29 ^d	H + OH + M = H ₂ O + M	2.200E+22	-2	0.0
30 ^e	2O + M = O ₂ + M	1.200E+17	-1	0.0
31 ^f	O + H + M = OH + M	5.000E+17	-1	0.0
32	OH + CO = H + CO ₂	4.689E+07	1.228	70.0
33	HO ₂ + CO = OH + CO ₂	1.500E+14	0	24544.0
34 ^g	O + CO(+M) = CO ₂ (+M)	1.800E+10	0	2385.0
35	H + HCO = H ₂ + CO	7.340E+13	0	0.0
36	OH + HCO = H ₂ O + CO	5.000E+13	0	0.0
37	HCO + O ₂ = HO ₂ + CO	1.345E+13	0	400.0
38 ^h	HCO + M = H + CO + M	1.870E+17	-1	17000.0
39	HCO + H ₂ O = H + CO + H ₂ O	1.500E+18	-1	17000.0
40	O + HCO = H + CO ₂	3.000E+13	0	0.0
41	O + CH ₄ = OH + CH ₃	1.020E+09	1.5	8600.0
42	OH + CH ₄ = CH ₃ + H ₂ O	1.000E+08	1.6	3120.0
43	O + CH ₃ = H + CH ₂ O	5.060E+13	0	0.0
44	O + CH ₃ => H + H ₂ + CO	3.370E+13	0	0.0
45	O + CH ₂ O = OH + HCO	3.900E+13	0	3540.0
46 ⁱ	H + CH ₃ (+M) = CH ₄ (+M)	1.390E+16	-0.534	536.0
47	H + CH ₄ = CH ₃ + H ₂	6.600E+08	1.62	10840.0
48	H + CH ₂ O = HCO + H ₂	5.740E+07	1.9	2742.0
49	OH + CH ₂ O = HCO + H ₂ O	3.430E+09	1.18	-447.0

Table 2.3: The skeletal mechanism. Units are in cm, s, mol, cal, K.

^a: O₂/0.0, H₂O/0.0, CO/0.75, CO₂/1.5, N₂/0.0, Ar/0.0, He/0.0

^b: Low:2.300E+18/-0.900/-1700.00, Troe: 0.7346/94.00/1756.00/5182.00, H₂/2.0, H₂O/6.0, CH₄/2.0, CO/1.5, CO₂/2.0, Ar/0.7, He/0.7

-
- ^c H₂/0.0, H₂O/0.0, CH₄/2.0, CO₂/0.0, Ar/0.63, He/0.63
- ^d H₂/0.73, H₂O/3.65, CH₄/2.0, Ar/0.38, He/0.38
- ^e: H₂/2.4, H₂O/15.4, CH₄/2.0, CO/1.75, CO₂/3.6, Ar/0.83, He/0.83
- ^f H₂/2.0, H₂O/6.0, CH₄/2.0, CO/1.5, CO₂/2.0, Ar/0.7, He/0.7
- ^g: Low: 6.020E+14/0.0/3000.00, H₂/2.0, O₂/6.0, H₂O/6.0, CH₄/2.0, CO/1.5, CO₂/3.5, Ar/0.5, He/0.5
- ^h: H₂/2.0, H₂O/0.0, CH₄/2.0, CO/1.5, CO₂/2.0
- ⁱ: Low: 2.620E+33/-4.760/2440.00, Troe: 0.7830/74.00/2941.00/6964.00, H₂/2.0, H₂O/6.0, CH₄/3.0, CO/1.5, CO₂/2.0, Ar/0.7, He/0.7

2.2 Development of reduced chemistry

From a numerical standpoint, the time advancement of the species composition corresponds to the solution of a system of stiff ordinary differential equations (ODEs). Without transport phenomena, there are N_s ODEs describing the net rate of change of these species as:

$$\frac{\partial C_i}{\partial t} = \omega_{i,p} - \omega_{i,d}, \quad i = 1 \dots N_s \quad (2.1)$$

where C_i is the concentration of species i , with a production rate of $\omega_{i,p}$, and a destruction rate of $\omega_{i,d}$. By removing certain intermediate species from the detailed mechanism, the computational effort is reduced as the number of ODEs that must be solved is decreased. For a restricted regime of interest, many intermediate species can be removed from the ODE system without losing the solution accuracy. Intermediate species can be systematically identified and removed from the ODE system via two major sequential steps. First, a skeletal mechanism is generated from the original detailed mechanism using sensitivity analysis as discussed in Section 2.1. Second, further reduction of the skeletal mechanism results in a reduced mechanism. In the second step, the Quasi-Steady State Assumption (QSSA) (e.g. [13, 15, 90, 91, 92, 93]) can be applied to certain intermediate species. Such a reduced mechanism with QSSA can be described as:

For non-QSS species:

$$\frac{\partial C_i}{\partial t} = \omega_{i,p} - \omega_{i,d}, \quad i = 1 \dots N_{s, \text{reduced}} \quad (2a)$$

For QSS species:

$$0 = \omega_{j,p} - \omega_{j,d}, \quad j = 1 \dots (N_{s, \text{skeletal}} - N_{s, \text{reduced}}) \quad (2b)$$

QSSA is applicable to an intermediate species when its production rate, $\omega_{j,p}$ is nearly equal in magnitude to the destruction rate $\omega_{j,d}$ resulting in a very small net change in concentration.

Concentrations of QSS species are solved by the non-linear algebraic system described in Eq. (2b), without any truncation, and identified using a relative error $100(\dot{\omega}_{j,p} - \dot{\omega}_{j,d})/\max(\dot{\omega}_{j,p}, \dot{\omega}_{j,d})$ [16], whereas non-QSS species concentrations are

resolved in the usual manner using Eq. (2a). Computational time saving results from the further decrease in system size from $N_{s,skeletal}$ to $N_{s,reduced}$. Furthermore, the stiffness of the system is also decreased further as species with small life times are removed using a targeted search algorithm (TSA) of Tham et al. [16]. For fast development of reduced chemistry, the interactive Computer Assisted Reduction Mechanism (CARM) algorithm [93, 94] was used for the automatic generation of reduced chemistry with the ability to produce source codes needed for computing the chemical sources. Numerical solutions of the zero-dimensional Perfectly-Stirred Reactor (PSR) with the 49-reaction skeletal mechanism in Table 2.3 were used as input to CARM. The CARM runs were conducted by Prof. J.Y. Chen after providing him the skeletal mechanism.

2.3 Reduced mechanism

The reduced mechanism is derived from the 49-reaction, 15 species (H, O₂, H₂O, CO, CO₂, H₂, H₂O₂, OH, HO₂, HCO, O, CH₄, CH₃, CH₂O, N₂/He/Ar) skeletal mechanism shown in Table 2.3. For the He-diluted mixtures the inert N₂ is simply replaced by He along with the different third body efficiencies and the corresponding reaction rate constants. The same would apply in cases where Ar is the inert. During the development, it was found that retaining H₂O₂ instead of HO₂ in the reduced mechanism provides a more robust reduced chemistry. Also, for fine tuning of the reduced chemistry, the activation energy of reaction 2 in Table 2.3 was increased by 27.5%, a procedure similar to the correction factor employed by [18] to correctly predict the ignition delay times. This is done because the introduction of steady-state assumptions for some of the species results in over-estimation of their reaction rates. As a result an over-estimation in the reaction rate of the OH radical results in an increased CO consumption rate through the most dominant reaction $\text{CO} + \text{OH} = \text{CO}_2 + \text{H}$, leading to an over-estimation of the flame speed. By increasing the activation energy of the chain branching reaction $\text{O} + \text{H}_2 = \text{H} + \text{OH}$, the production rates of OH and H radicals are reduced leading to the correct nominal values for the flame speeds. Subsequently, steady-state assumptions are introduced for HO₂, HCO, CH₃, CH₂O, OH, and O. The resulting 5-step reduced mechanism involving 9 species is as follows:

-
- (1) $\text{O}_2 + \text{H}_2\text{O} + 3\text{CO} = 2\text{H} + 3\text{CO}_2$
 - (2) $\text{CO}_2 + \text{H}_2 = \text{H}_2\text{O} + \text{CO}$
 - (3) $2\text{H} + \text{CO}_2 = \text{H}_2\text{O} + \text{CO}$
 - (4) $\text{O}_2 + 2\text{H}_2\text{O} + 2\text{CO} = 2\text{H} + 2\text{CO}_2 + \text{H}_2\text{O}_2$
 - (5) $2\text{H} + 4\text{CO}_2 + \text{CH}_4 = 3\text{H}_2\text{O} + 5\text{CO}$

The global net rates \dot{w}_k of the non steady-state species involved in the above 5 steps are then given by:

$$\dot{w}_k = \sum_{j=1}^{Nr} (\nu'' - \nu')_{kj} \dot{w}_{kj}$$

where Nr is the total number of reactions in the skeletal mechanism, ν'' and ν' are the molar stoichiometric coefficients of species k in reaction j on the product and reactant side respectively, and \dot{w}_{kj} is the net rate of species k in reaction j of Table 2.3. The rate expressions for the 15 species involved in the above 5 steps are given in Appendix B.

The steady-state relationships include non-linear terms and are solved by point iteration. The steady-state relationships can be written as:

$$\frac{dC_A}{dt} = \psi_A(ss, ss') - g_A(ss, ss')C_A = 0,$$

where $\psi_A(ss, ss')$ and $g_A(ss, ss')$ are functions of species both in steady-state, denoted by ss , and non steady-state, denoted by ss' . Here, ψ_A denotes the sum of the rates of reactions producing A and g_A is the sum of the rates of reactions consuming A . The simple point iterative scheme of the following form is used:

$$C_A^{n+1} = \frac{\psi_A(ss, ss')^n}{g_A(ss, ss')^n},$$

where n denotes the iteration number and the iteration procedure is applied sequentially to all steady-state species. The difference $|C_A^{n+1} - C_A^n|$ is monitored and the iteration is considered to be converged for a given species A if $|C_A^{n+1} - C_A^n| \leq A_{\text{tol}}$ where A_{tol} is the tolerance limit defined as $A_{\text{tol}} = \max(C_A \cdot \text{Rel}_{\text{tol}}, \text{Abs}_{\text{tol}})$, $\text{Rel}_{\text{tol}} = 10^{-5}$, $\text{Abs}_{\text{tol}} = 10^{-15}$. For reduced chemistry with strongly coupled QSS species, a combined point iteration and matrix inversion [95] can be

used. Since the current QSS species are not strongly coupled, the point iteration scheme is found to be sufficient for the present case.

2.4 Validation

Both the skeletal and reduced mechanisms are validated over wide range of conditions shown in Table 2.4, by comparing laminar flame speeds, ignition delay times and the flame structure with experimental results and/or the computational results obtained using the GRI-3.0 [73]. In the following figures, $f_A = X_A/X_{CO}$ is the ratio of mole fractions of species A to CO. The flame speeds are calculated using the PREMIX [96] code of the CHEMKIN package [97] including the thermal diffusion and multi-component formulation for the species' diffusivities. In the cases where no experimental data are available, the skeletal and the reduced mechanisms are validated against the predictions of the GRI-3.0 set, and so readers are cautioned while interpreting this particular comparison. In these cases only the mixture-averaged formulation for diffusion is used in order to reduce the computational time for the GRI-3.0 calculations, since a qualitative comparison between the different mechanisms is of interest here, hence the use of multi-component diffusion formulation is less essential.

Ignition delay times are calculated using a constant volume reactor solver of the CHEMKIN package [97]. The ignition delay time was defined as the instant, t_{ign} , corresponding to the maximum temperature gradient with respect to time, dT/dt . In calculating the ignition delay times with the reduced mechanism, the correction factor used in the study of [18] is employed. This correction factor was originally developed in [98] from an analysis of the autoignition eigenvalue under lean conditions. This correction is necessary because the steady-state assumptions for O and OH do not hold during autoignition events leading to under-predictions of the ignition delay times as noted by [18]. The species reaction rates \dot{W}_k are thus corrected by multiplying ($\dot{W}'_k = \dot{W}_k \cdot \Lambda$) with the correction factor Λ given by:

$$\Lambda = \frac{\{(1 + 2B)^{0.5} - 1\}}{B} \quad (3)$$

where B is given by:

$$B = \frac{2 k_{f1} C_{O_2} (k_{f1} C_{O_2} + k_{f2} C_{H_2} + k_{f3} C_{H_2})}{k_{f2} k_{f3} C_{H_2}^2}. \quad (4)$$

In this study the factor 2, rather than 4 used in [18], in the expression for B is used giving improved agreement with the experimental data. In cases where the steady-states apply such as for example premixed flames, the correction factor is $\Lambda = 1$.

Fuel	Oxidizer	f_{H_2}	f_{CH_4}	f_{CO_2}	H ₂ O%	p (atm)	T_r (K)	ϕ	Source
Flame speed:									
CO/H ₂ /H ₂ O ¹	Air	5/95	0	0	0-36	1	323	0.6-0.9	[39], Fig. 2.1
CO/H ₂ /H ₂ O ¹	Air	5/95	0	0	0-40	1	400	0.6-0.9	[40], Fig. 2.2
CO/H ₂ /CH ₄ /CO ₂ /N ₂	Air	Vary	0.24	11%	0	1	298	1.0,0.9,0.8	[79], Fig. 2.3
CO/H ₂	Air	Vary	0	0	0	1	303	-	[99], Fig. 2.4
CO/H ₂	Air	5/95	0	0	0	1	400-700	0.2-1.1	[100], Fig. 2.5
CO/H ₂	Air	1	0	0	0	1	400-700	0.2-1.1	[100], Fig. 2.5
CO/H ₂	Air	1	0	0	0	1	298-500	0.7-3.0	[40], Fig. 2.6
CO/H ₂ /CO ₂	Air	5/95	0	0.117	0	1	298	0.5-1.2	[100], Fig. 2.7
CO/H ₂ /CO ₂	Air	1	0	0.5	0	1	298	0.5-1.2	[100], Fig. 2.7
CO/H ₂	Air	5/95	0	0	0	1	298	0.5-1.2	[100], Fig. 2.7
CO/H ₂	Air	1	0	0	0	1	298	0.5-1.2	[86], Fig. 2.8
CO/H ₂	Air	1/99	0	0	0	1	298	0.5-5.0	[86], Fig. 2.8
CO/H ₂	Air	5/95	0	0	0	1	298	0.5-5.0	[86], Fig. 2.8
CO/H ₂	Air	25/75	0	0	0	1	298	0.5-5.0	[86], Fig. 2.8
CO/H ₂	Air	50/50	0	0	0	1	298	0.5-5.0	[86], Fig. 2.8
CO/H ₂	Air	75/25	0	0	0	1	298	0.5-5.0	[40], Fig. 2.8
CO/H ₂ ²	O ₂ /He	10/30	0	0	0	5,10,20	298	0.5-5.0	[86], Fig. 2.8
CO/H ₂	O ₂ /He	1	0	0	0	5,10	298	0.5-5.0	[86], Fig. 2.8
CO/H ₂	O ₂ /Ar	10/90	0	0	0	1-20	295	2.5	[87], Fig. 2.9
CO/H ₂ /CH ₄	Air	0.55	0.17	0	0	1	298	0.4-1.2	[101], Fig. 2.10
CO/H ₂ /CH ₄	Air	6	3	0	0	1	298	0.4-1.2	[101], Fig. 2.10
CO/H ₂ /CH ₄ /CO ₂ ³	Air	4.9	2.27	0.91	0	1	298	0.5-1.2	[101], Fig. 2.10
CO/H ₂ /CH ₄ /H ₂ O/CO ₂	Air	5/95	5/95	0.5	0-70	1,10	600	0.7,1.0	[73], Fig. 2.11
CO/H ₂ /H ₂ O/CO ₂	Air	5/95	0	0.5	0-70	1,10	600	0.7,1.0	[73], Fig. 2.12
CO/H ₂ /H ₂ O	Air	5/95	0	0	0-70	1,10	600	0.7,1.0	[73], Fig. 2.13
CO/CH ₄ /H ₂ O	Air	0	5/95	0	0-70	1,10	600	0.7,1.0	[73], Fig. 2.14
Flame structure:									
CO/H ₂	Air	5/95	0	0	0	1	400	0.8	[73], Fig. 2.15
CO/H ₂	Air	5/95	0	0	0	1	700	0.8	[73], Fig. 2.16
CO/H ₂	O ₂ /He	1	0	0	0	5	298	2	[73], Fig. 2.17
CO/H ₂	O ₂ /He	1	0	0	0	10	298	2	[73], Fig. 2.18
CO/H ₂ /CH ₄ /CO ₂ /H ₂ O	Air	5/95	5/95	0.5	25	1	600	1	[73], Fig. 2.19
CO/H ₂ /CH ₄ /CO ₂ /H ₂ O	Air	5/95	5/95	0.5	25	10	600	1	[73], Fig. 2.20
Ignition delay times:									
CO/H ₂	Air	4	0	0	0	1.1	900-1340	0.5	[102], Fig. 2.21
CO/H ₂	Air	1.5	0	0	0	1.1	900-1340	0.5	[102], Fig. 2.21
CO/H ₂	Air	0.67	0	0	0	1.1	900-1340	0.5	[102], Fig. 2.21
CO/H ₂	Air	0.25	0	0	0	1.2,15.4	900-1340	0.5	[102], Fig. 2.21
CO/H ₂ ⁴	Air	0.11	0	0	0	1.1,14.9	900-1340	0.5	[102], Fig. 2.21
CO/H ₂ /CO ₂	Air	0.77	0	2.1	0	1.24-2.36	900-1340	1.0	[81], Fig. 2.22
CO/H ₂ /H ₂ O/CH ₄	Air	3	1	0	10%	5	1017-1197	1.0	[81], Fig. 2.23

Table 2.4: The range of fuel composition and operating conditions tested.

2.4.1 Premixed flames

Comparisons of computed flame speeds, s_L , against available experimental data for the mixtures listed in Table 2.4 are presented in Figs. 2.1-2.10. The above comparisons show that overall both the skeletal and the reduced mechanism give good agreement with the experimental data and the computations with GRI-3.0.

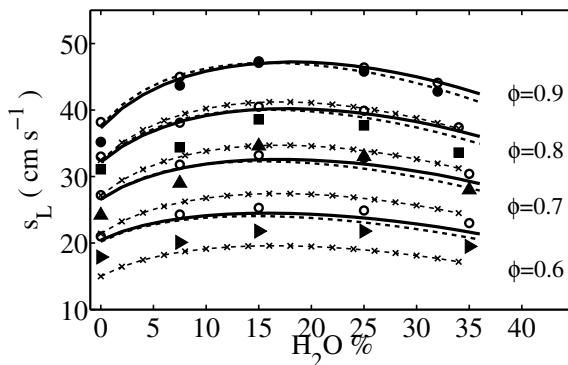


Figure 2.1: Laminar flame speeds of CO/H₂/H₂O-air mixtures using the reduced (dashed lines) and skeletal (full lines) mechanisms. Open circles: Li et al. [84] mechanism results from Das et al. [39]. Also shown are the predictions using the skeletal mechanism of Boivin et al. (dashed lines with ×) [18]. Filled symbols: experimental results of Das et al. [39]. $T_r = 323$ K, $p = 1$ atm, $f_{H_2} = 5/95$, $X_{N_2}/X_{O_2} = 3.76$.

Figure 2.1 presents results for fuel mixtures with $f_{H_2} = 5/95$ and H₂O content up to 36%. Although the experimental data in Fig.1 were not a target of [18], the skeletal mechanism of [18] as implemented in this study, under-predicts the flame speeds for all equivalence ratios and the level of under-prediction increases with the H₂O content in the fuel mixture. The skeletal mechanism in Table 2.3 of this work gives good agreement with the experimental results and is slightly more accurate than the mechanism of Li et al. [84] for $\phi = 0.6$. The reduced mechanism also shows a good agreement with the experimental data and captures the increase in flame speed with water content in the fuel. The increase in the flame speed with the addition of water vapour essentially comes from an increase in the OH radical production through the reaction $O + H_2O = 2OH$ identified in section 2.1 and as suggested by Das et al. [39]. Consequently, this increases CO

consumption rate through the most dominant reaction $\text{CO} + \text{OH} = \text{CO}_2 + \text{H}$ as shown by the sensitivity analyses in section 2.1.

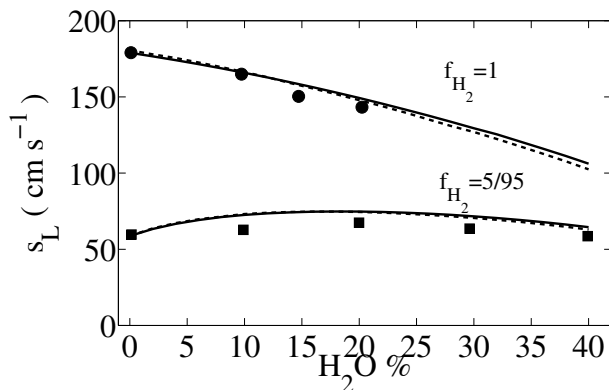


Figure 2.2: Laminar flame speeds of CO/H₂/H₂O mixtures using the reduced (dashed lines) and skeletal (continuous lines) mechanisms. Filled symbols: experimental results of Singh et al. [40]. $p = 1$ atm, $T_r = 400$ K, $\phi = 1$, oxidiser is O₂, N₂ with $X_{\text{N}_2}/X_{\text{O}_2} = 3.76$.

Figure 2.2 compares computational results with the experimental data of [40] for a stoichiometric mixture at 400 K containing low and high hydrogen fractions in the fuel mixture. The agreement is very good for the entire range of water vapour content considered. The inhibiting effect of increased hydrogen fraction in the fuel mixture is clearly seen; for $f_{\text{H}_2} = 5/95$ water vapour addition has a net positive chemical effect on the flame speed up to about 15% whereas the water vapour addition yields a monotonic decrease of the flame speed for $f_{\text{H}_2} = 1$. As discussed in [40], this is because of the reaction $\text{OH} + \text{H}_2 = \text{H} + \text{H}_2\text{O}$. For low f_{H_2} the reverse rate is sufficiently large resulting in high total OH production yielding an increased CO consumption rate through $\text{OH} + \text{CO} = \text{H} + \text{CO}_2$. This results in a net positive chemical effect on increasing the flame speed. For high f_{H_2} , the forward rate is sufficiently high resulting in OH consumption. This combined with the negative dilution effect of water vapour reduces the flame speed. All of these effects are captured clearly by the reduced mechanism proposed in this study. It is to be noted that updating the heat of formation value for OH from its default

value of 9.4 to 8.9 kcal/mol as suggested in [103, 104], yields a maximum over prediction of about 10% for $\phi = 0.9$ case in Fig. 2.1 when the moisture content is about 18%. This level of over prediction can be reduced by re-optimising the rate parameters for the GRI-3.0 set, which is not the focus of this study. Thus, the default value of 9.4 kcal/mol is used in this study as it gives good agreement for the experimental conditions tested in this study.

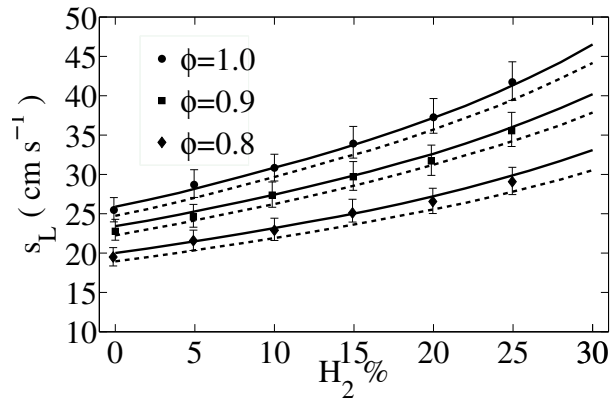


Figure 2.3: Laminar flame speeds of syngas mixtures (CO/H₂/CH₄/CO₂/N₂-air) using the reduced (dashed lines) and the skeletal (full lines) mechanisms. Symbols: experimental results of He et al. [79]. $f_{CH_4} = 0.24$ with 11% CO₂ and 42.7% N₂ in the fuel mixture. $T_r = 298$ K, $p = 1$ atm, $X_{N_2}/X_{O_2} = 3.76$. Error bars from He et al. [79] are also shown.

Figure 2.3 compares results with typical syngas mixtures from [79]. The value of f_{CH_4} is kept constant at 0.24 approximately with 11% CO₂ and 42.7% N₂ in the fuel mixture. The skeletal mechanism gives a very good agreement with the experimental results. The reduced mechanism yields a slightly lower values as the hydrogen fraction in the fuel mixture increases but remains within the experimental errors as shown in Fig. 2.3.

Figure 2.4 compares the computational results using the skeletal and reduced mechanisms with the experimental results of [99] for CO/H₂-air mixtures. The values of $(X_{CO} + X_{H_2})$ is kept constant while the hydrogen molar fraction, X_{H_2} , in the fuel mixture is varied. For this case, the maximum f_{H_2} value in the fuel is

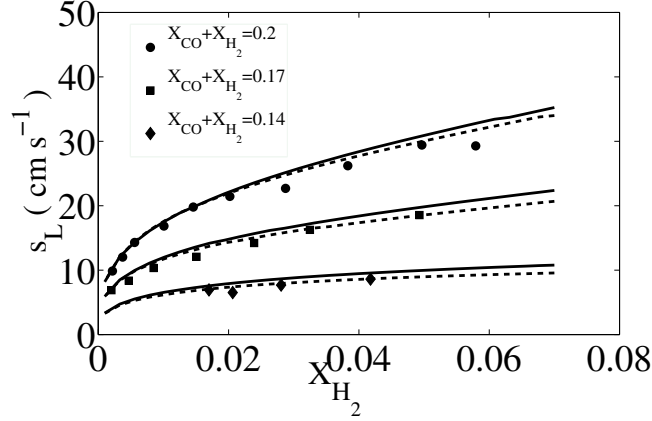


Figure 2.4: Laminar flame speeds of CO/H₂-air mixtures using the reduced (dashed lines) and skeletal (full lines) mechanisms. Symbols: experimental results of Vagelopoulos and Egolfopoulos [99]. $T_r = 298$ K, $p = 1$ atm, $X_{N_2}/X_{O_2} = 3.76$.

about 0.43. The agreement in Fig. 4 is observed to be good for the entire range of X_{H_2} values considered.

Figure 2.5 shows the variation of computed flame speeds with equivalence ratio for CO/H₂/O₂/N₂ mixtures for reactant temperature ranging from 400 to 700 K. It is to be noted that there is no H₂O vapour in the fuel mixture. The results are shown for low (top figure) and high (bottom figure) hydrogen fractions in Fig. 2.5. The experimental data of Natarajan et al. [100] are shown for comparison. The computational results obtained with the 4-step reduced mechanism, and the skeletal mechanism of Boivin et al. [18] as reported in [18] are shown. The skeletal mechanism of Boivin et al. [18] as implemented in this study is also shown. The 4-step mechanism [18] over-predicts the flame speed by a large factor for the entire range of equivalence ratio shown in Fig. 2.5. The flame speeds computed using the skeletal and 5-step reduced mechanisms proposed in this study agree quite well with the experimental measurements for the range of equivalence ratio, reactant temperature and the hydrogen fraction shown in Fig. 2.5.

Figure 2.6 shows the computed flame speeds for CO/H₂/O₂/N₂ mixture for equivalence ratios larger than in Fig. 2.5 for $f_{H_2} = 1$. The experimental data shown in Fig. 2.6 are from Singh et al. [40]. The results in Fig. 2.6 serve

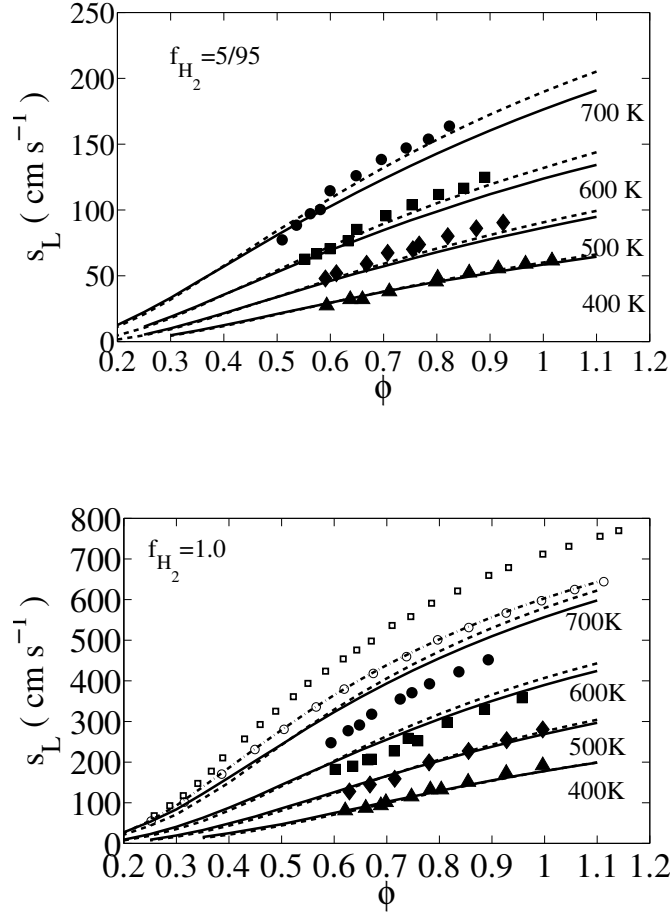


Figure 2.5: Laminar flame speeds of CO/H₂/O₂/N₂ mixtures using the reduced (dashed lines) and skeletal (continuous lines) mechanisms. Also shown are the results using the 4-step reduced mechanism of Boivin et al. [18] (open squares), the skeletal mechanism of Boivin et al. [18] (open circles) from the same study, and the implementation of the skeletal mechanism of [18] in this study (dashed-dotted lines). Symbols: experimental results of Natarajan et al. [100]. $f_{H_2} = 5/95$ and 1.0, at $p = 1$ atm, $X_{N_2}/X_{O_2} = 3.76$, for $T_r = 400, 500, 600$ and 700 K.

as the additional validation for the mechanisms proposed in this study. At low temperatures the agreement is very good for the entire range of equivalence ratios considered. At higher temperatures the skeletal and reduced mechanisms slightly over-predict the flame speed. This is not surprising since it was shown in [40]

that all of the tested mechanisms (GRI-3.0 [73], Davis [105], San Diego [106]) over predicted the flame speed for the range of conditions tested in Fig. 2.6. The sensitivity analysis by Singh et al. [40] suggested that further studies into the rate constants of the elementary reactions $\text{O} + \text{H}_2 = \text{H} + \text{OH}$, $\text{OH} + \text{H}_2 = \text{H} + \text{H}_2\text{O}$ and $\text{H} + \text{O}_2 + \text{M} = \text{HO}_2 + \text{M}$ were required. These reactions are expected to be in the top 10 reactions for rich mixture as shown in Fig. 3 in Appendix A.

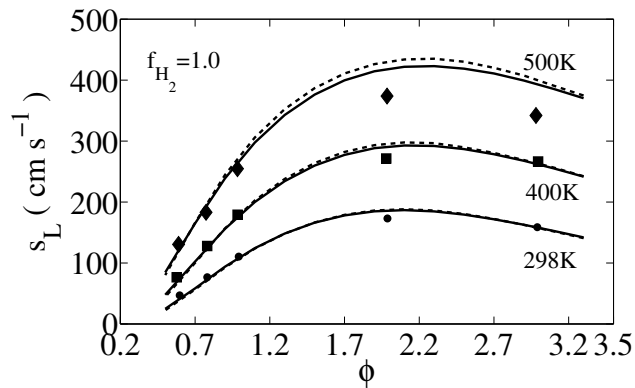


Figure 2.6: Laminar flame speeds of CO/H₂ mixtures using the reduced (dashed lines) and skeletal (continuous lines) mechanisms. Filled symbols: experimental results of Singh et al. [40]. $p = 1$ atm, oxidizer is air.

The effect of CO₂ dilution on the flame speed for the Syngas mixture is shown in Fig. 2.7. The comparisons show that the results computed using the current skeletal and reduced mechanisms are in good agreement with the experimental measurements of Natarajan et al. [100], and these mechanisms capture the CO₂ dilution effects well.

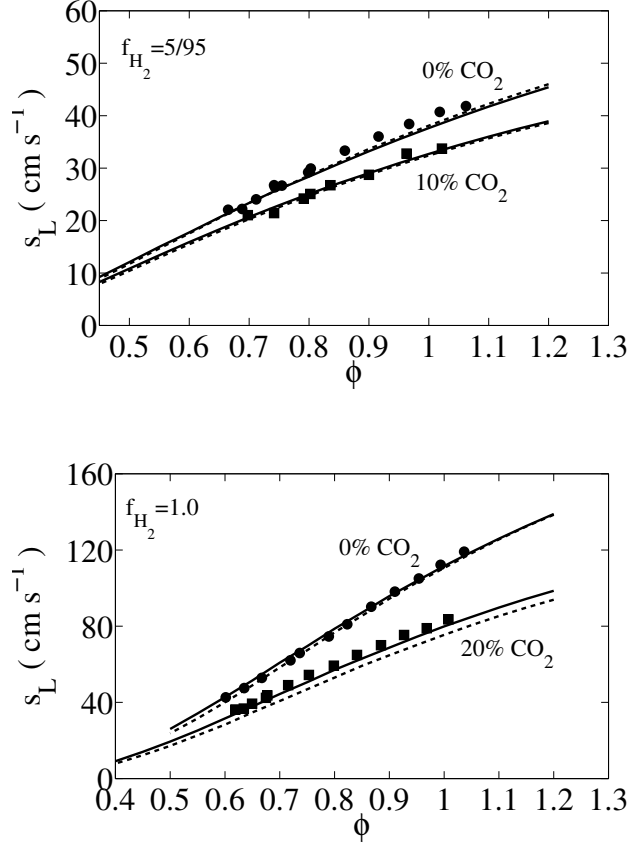


Figure 2.7: Laminar flame speeds of CO/H₂/CO₂/O₂/N₂ mixtures using the reduced (dashed lines) and skeletal (continuous lines) mechanisms. Symbols: experimental results of Natarajan et al. [100]. $f_{H_2} = 5/95$ and 1.0, at $p = 1$ atm, $X_{N_2}/X_{O_2} = 3.76$ with 10% and 20% CO₂ dilution.

The laminar flame speeds computed using the skeletal and reduced mechanisms at elevated pressures for a range of f_{H_2} values and a wide range of equivalence ratios are compared to the experimental measurements of Hongyan et al. [86] in Fig. 2.8. The experimental measurements of Singh et al. [40] at atmospheric pressure are also included in Fig. 2.8 for further comparison. The agreement observed in this figure is encouraging and indeed very good. Figure 2.9 compares the variation of mass burning rate with pressure for a rich ($\phi = 2.5$) Ar diluted mixture for $f_{H_2} = 10/90$ measured by Burke et al. [87] to the values computed in this study using the skeletal and reduced mechanisms. The agree-

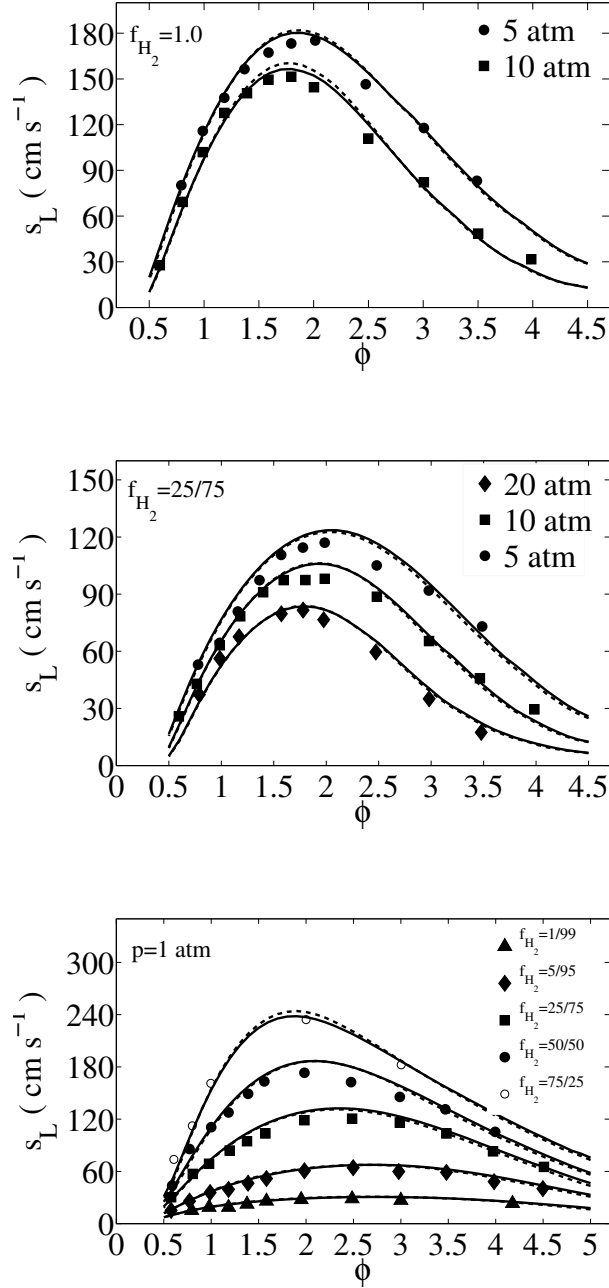


Figure 2.8: Laminar flame speeds of CO/H₂ mixtures using the reduced (dashed lines) and skeletal (continuous lines) mechanisms. Symbols: experimental results of Hongyan et al. [86]. At $p = 1$ atm the oxidizer is O₂, N₂ with $X_{\text{N}_2}/X_{\text{O}_2} = 3.76$. At $p = 5, 10, 20$ atm the oxidizer is O₂ and He with $X_{\text{He}}/X_{\text{O}_2} = 7.0$. Open symbols: experimental results of Singh et al. [40].

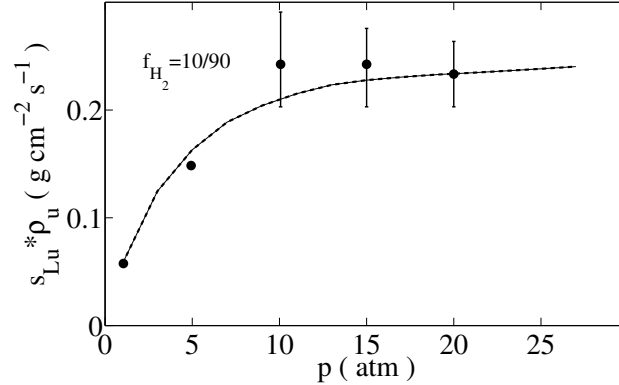


Figure 2.9: Laminar flame mass burning rate for CO/H₂/O₂/Ar mixtures using the reduced (dashed lines) and skeletal (continuous lines) mechanisms. Filled symbols: experimental data of Burke et al. [87]. $T_r = 295$ K, $\phi = 2.5$, $X_{Ar}/X_{O_2} = 10.95$.

ment is very good for pressures up to about 5 atm. and for higher pressures in the range of 15-20 atm. There is a slight under prediction of the mass burning rate for 5-15 atm. but it is within the experimental errors as one can see in Fig. 2.9. In the same study [87] it was shown that there is a maximum in mass burning flux with pressure which is more pronounced as the f_{H_2} ratio increases. However, none of the skeletal mechanisms tested captured this effect satisfactorily, especially in the high pressure regime, and significant deviations were observed between the different mechanisms. In the same study [87] it was concluded that major modifications to the rate parameters may be required for the high pressure regime, as well as the inclusion of additional reactions. Such a reaction was suggested to be $O + OH + M = HO_2 + M$ which is not included in most skeletal mechanisms.

The flame speeds of some multi-species fuel mixtures from the study of [101] are computed and compared in Fig. 2.10. The highest f_{H_2} value for these cases is 6.0 (bottom figure) and the lowest is 0.55 (top figure), and the corresponding f_{CH_4} values are 3.0 and 0.17 respectively. The middle figure also includes the effect of CO₂ dilution. As one can observe in Fig. 2.10, both the skeletal and reduced mechanisms show good agreement with the experimental data for all equivalence ratios considered despite the high methane content in the bottom two plots. However, the ratio f_{H_2}/f_{CH_4} is greater than or equal to 2 and thus

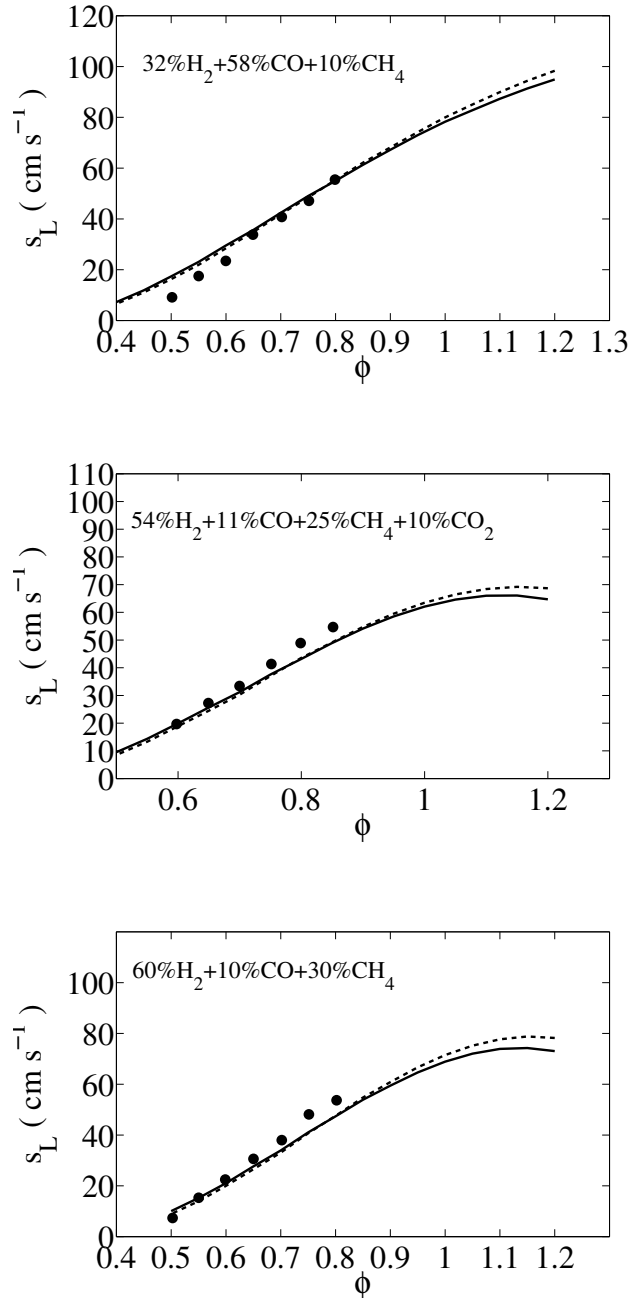


Figure 2.10: Laminar flame speeds of $\text{CO}/\text{H}_2/\text{CH}_4/\text{CO}_2/\text{O}_2/\text{N}_2$ mixtures using the reduced (dashed lines) and skeletal (continuous lines) mechanisms. Symbols: experimental results of Park et al. [101], $p = 1 \text{ atm}$, $T_r = 298 \text{ K}$.

the H_2 chemical kinetics become more dominant than the methane kinetics. For the mixture with $f_{CH_4} > 1$ however, one observes a slight under prediction of the flame speed for $\phi \geq 0.7$ since extra species such as CH , CH_2 , CH_3O , CH_3OH , etc., identified in section 2.1 (see Table 2.2) through the sensitivity analyses are required for improved description of the methane chemistry.

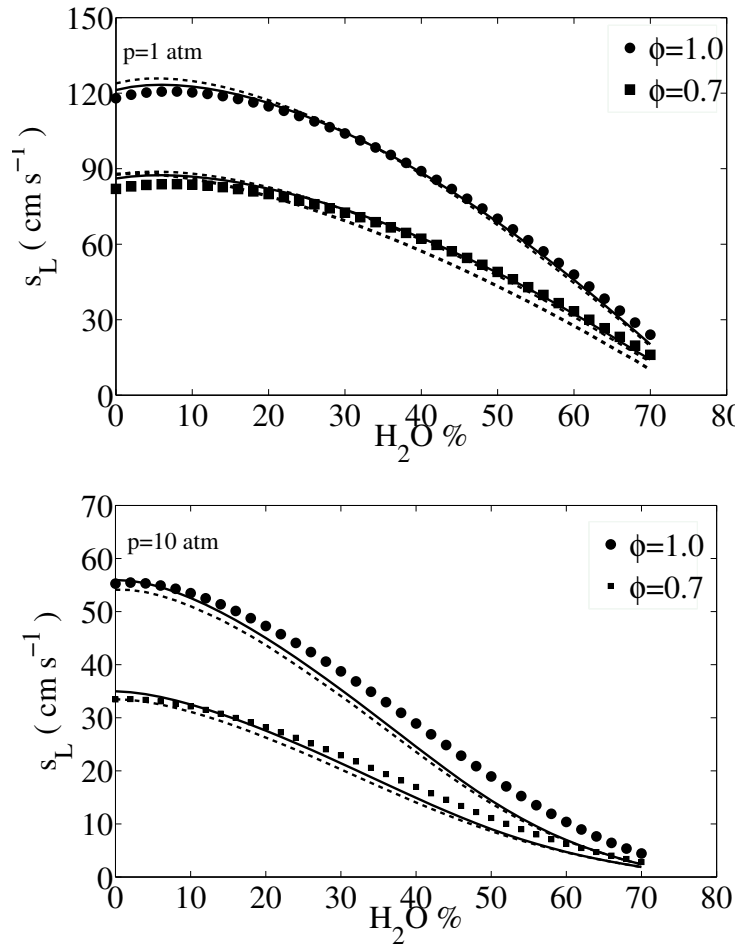


Figure 2.11: Laminar flame speeds of $CO/H_2/CH_4/H_2O/CO_2/O_2/N_2$ mixtures using the reduced (dashed lines) and skeletal (continuous lines) mechanisms. Symbols: GRI- 3.0 results. $f_{H_2} = 5/95$, $f_{CH_4} = 5/95$, $f_{CO_2} = 0.5$, $T_r = 600$ K at $p = 1$ and 10 atm.

The flame speeds computed using the skeletal and reduced mechanism are compared to the results of the GRI-3.0 mechanism in Fig. 2.11, since no exper-

imental data are found for this mixture, not only for the pressure and temperature noted in this figure but also for atmospheric conditions. The fuel mixture is composed of CO, H₂, H₂O, CH₄ and CO₂ with $f_{H_2} = 5/95$, $f_{CH_4} = 5/95$ and $f_{CO_2} = 0.5$. It is clear that both the reduced and skeletal mechanism give good agreement even with a high water vapour content in the mixture for both low and high pressures.

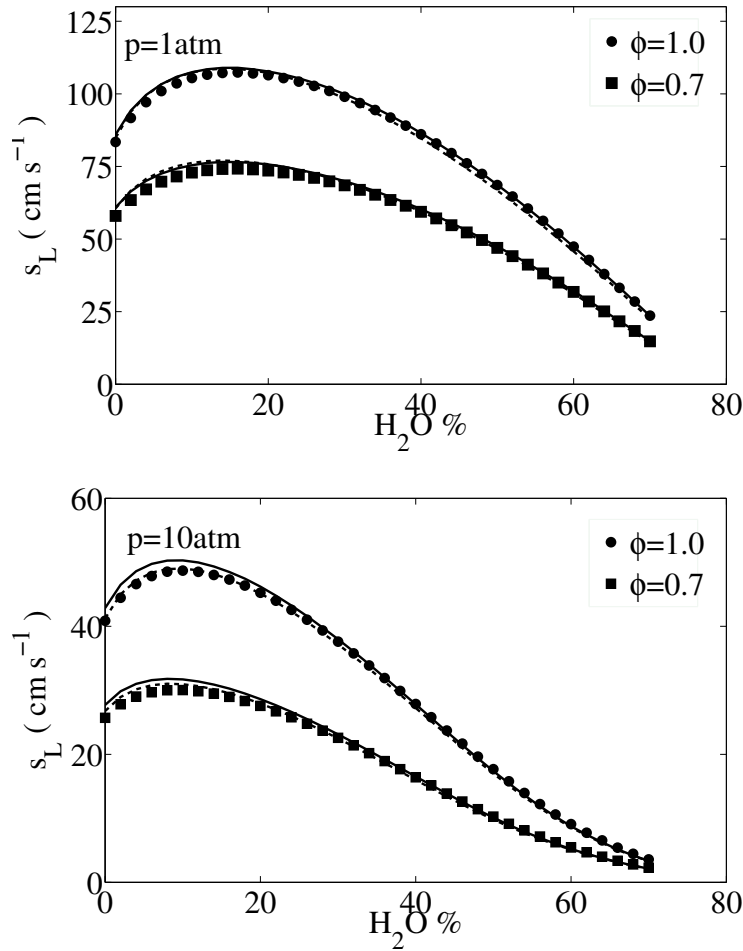


Figure 2.12: Laminar flame speeds of CO/H₂/H₂O/CO₂/O₂/N₂ mixtures using the reduced (dashed lines) and skeletal (continuous lines) mechanisms. Symbols: GRI-3.0 results. $f_{H_2} = 5/95$, $f_{CO_2} = 0.5$, $T_r = 600$ K at $p = 1$ and 10 atm.

Figure 2.12 shows a similar comparison with the same fuel proportions as in Fig. 2.11 with $f_{CH_4} = 0$ in order to elucidate the effect of CH₄ on the dependence

of flame speed on water vapour content. For the case presented in Fig. 2.11, the methane content is $f_{CH_4} = 5/95$, which is quite small and corresponds to about 2.5% by volume in the fuel mixture. In comparison to Fig. 2.12 this small addition of CH_4 to the fuel mixture significantly alters the chemical and thermal effect of water vapour. That is, the small amount of CH_4 causes the flame to become chemically less sensitive to water vapour addition since the gradient of s_L with respect to H_2O content is less steep. The reason for this is that less OH radicals are available for CO oxidation through the reaction $OH + CO = H + CO_2$ which is the most important path for CO consumption and the most important reaction as one may see from the sensitivity plots in the Appendix A. The OH radicals are now directly consumed in the oxidation of CH_4 through $OH + CH_4 = CH_3 + H_2O$ giving more water vapour. This makes the mixture chemically less sensitive to further addition of H_2O , but also thermally more sensitive since H_2O production through the direct oxidation of CH_4 above will increase the product specific heat capacity. All these effects are captured properly by both the reduced and skeletal mechanisms since they include CH_4 , in contrast to any existing skeletal or reduced mechanisms for multi-species fuel mixtures.

For the fuel mixture considered in Fig. 2.13, there is no CH_4 or CO_2 . Again there is a good agreement with the full GRI-3.0 mechanism and it is somewhat improved in the high pressure case, compared to the predictions of the methane-containing fuel mixture in Fig. 2.11. Figure 2.14 shows a similar comparison but with no H_2 or CO_2 . By comparing Figs. 2.12 and 2.13 one can see the effect of CO_2 – the flame speeds are reduced considerably.

The flame structure computed using the skeletal and reduced mechanisms are compared to those using GRI-3.0 in Figs. 2.15-2.20 over a range of operating conditions including the effects of reactant temperature, pressure and fuel composition. The progress variable, c , in these figures is based on temperature with $c = 0$ denoting the unburned reactant and $c = 1$ denoting the burnt products. Both the reduced and the skeletal mechanisms show overall good agreement for the major species mass fractions, temperature and heat release rate with the predictions using GRI-3.0. The thermochemical and thermodynamic conditions chosen for Figs. 2.15 to 2.20 correspond to those considered for the flame speed comparisons discussed earlier. These results demonstrate the robustness of the

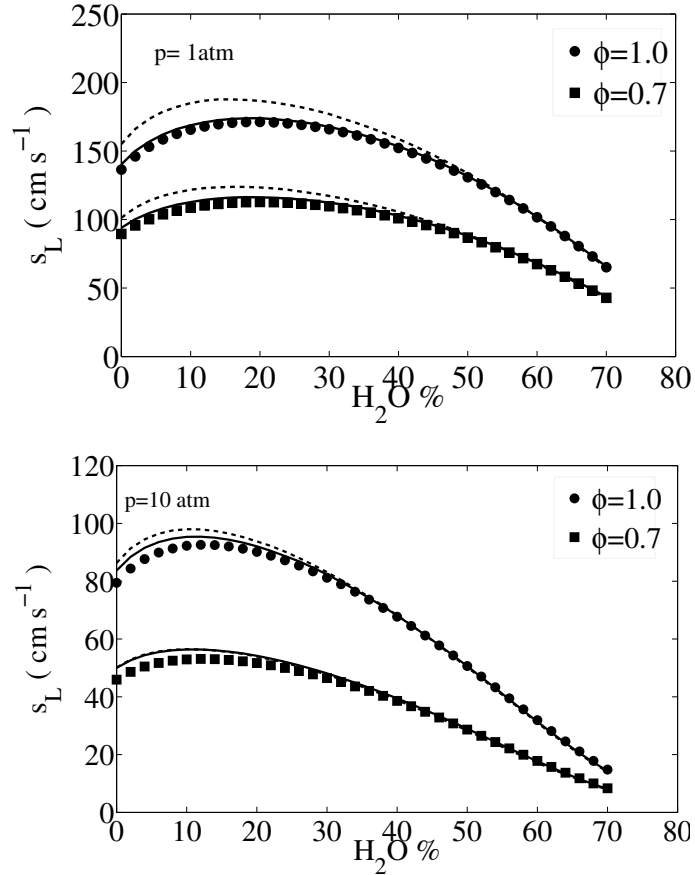


Figure 2.13: Laminar flame speeds of CO/H₂/H₂O/O₂/N₂ mixtures using the reduced (dashed lines) and skeletal (continuous lines) mechanisms. Symbols: GRI-3.0 predictions. $f_{H_2} = 5/95$, $T_r = 600$ K at $p = 1$ and 10 atm.

skeletal and reduced mechanisms to get the flame structure and its laminar burning velocity over the range of conditions considered in this study.

Although there are no experimental data available for the conditions tested using GRI-3.0, these comparisons serve to show that (i) the reduced mechanism derived in this study agrees well with the GRI-3.0 results and (ii) the small modifications made to some of the reaction rate parameters as discussed in section 2.1 do not "de-optimize" the skeletal mechanism.

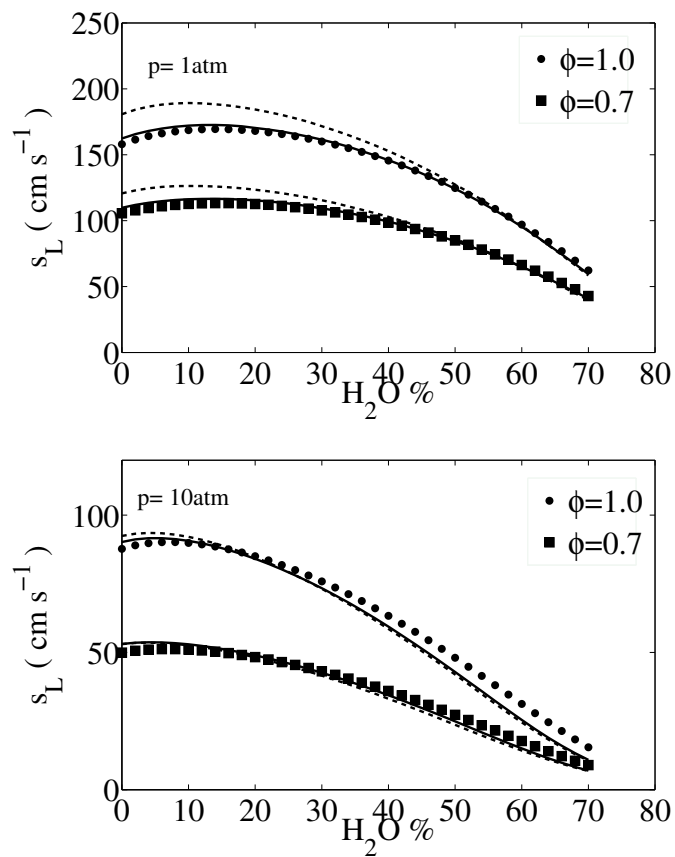


Figure 2.14: Laminar flame speeds of CO/CH₄/H₂O/O₂/N₂ mixtures using the reduced (dashed lines) and skeletal (continuous lines) mechanisms. Symbols: GRI-3.0 predictions. $f_{CH_4} = 5/95$, $T_r = 600$ K at $p = 1$ and 10 atm.

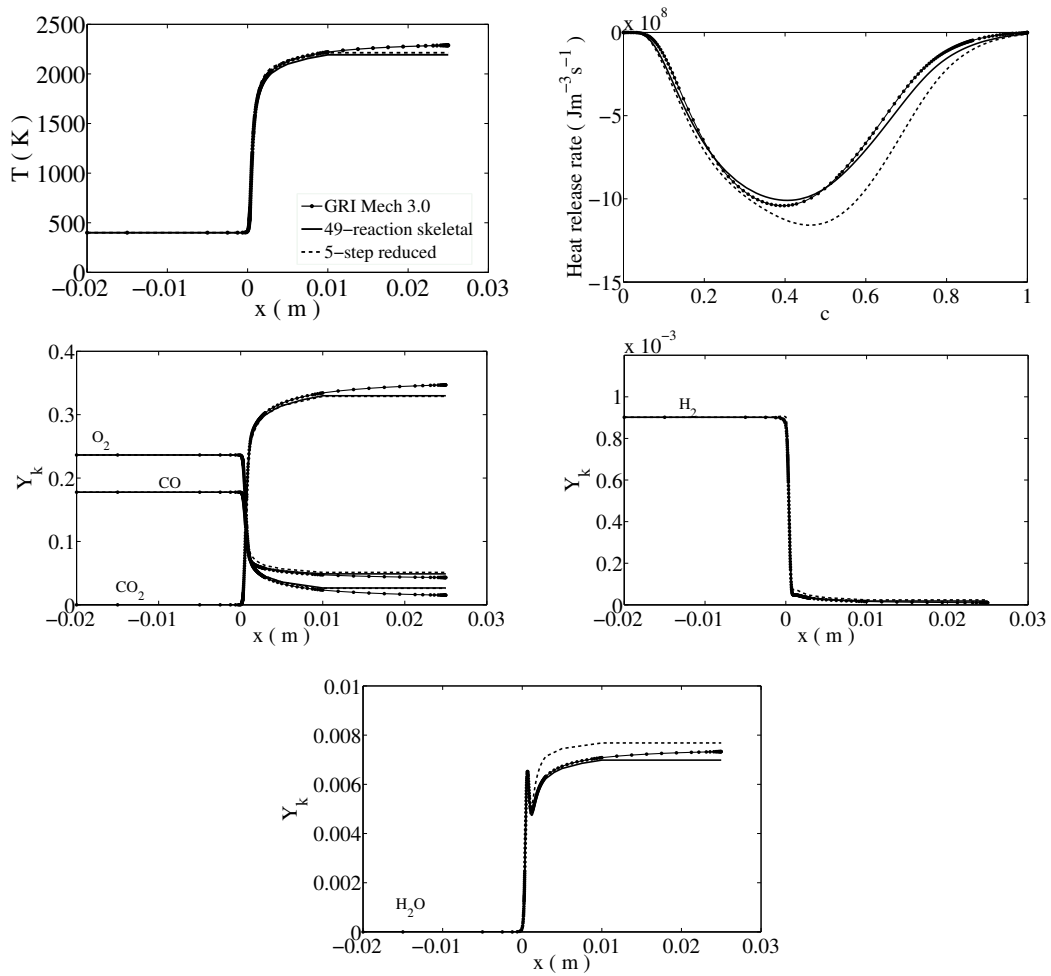


Figure 2.15: Flame structure for CO/H₂/O₂/N₂. $\phi = 0.8$, $f_{H_2} = 5/95$, $T_r = 400$ K, $p = 1$ atm. (conditions as in Fig. 2.5 top).

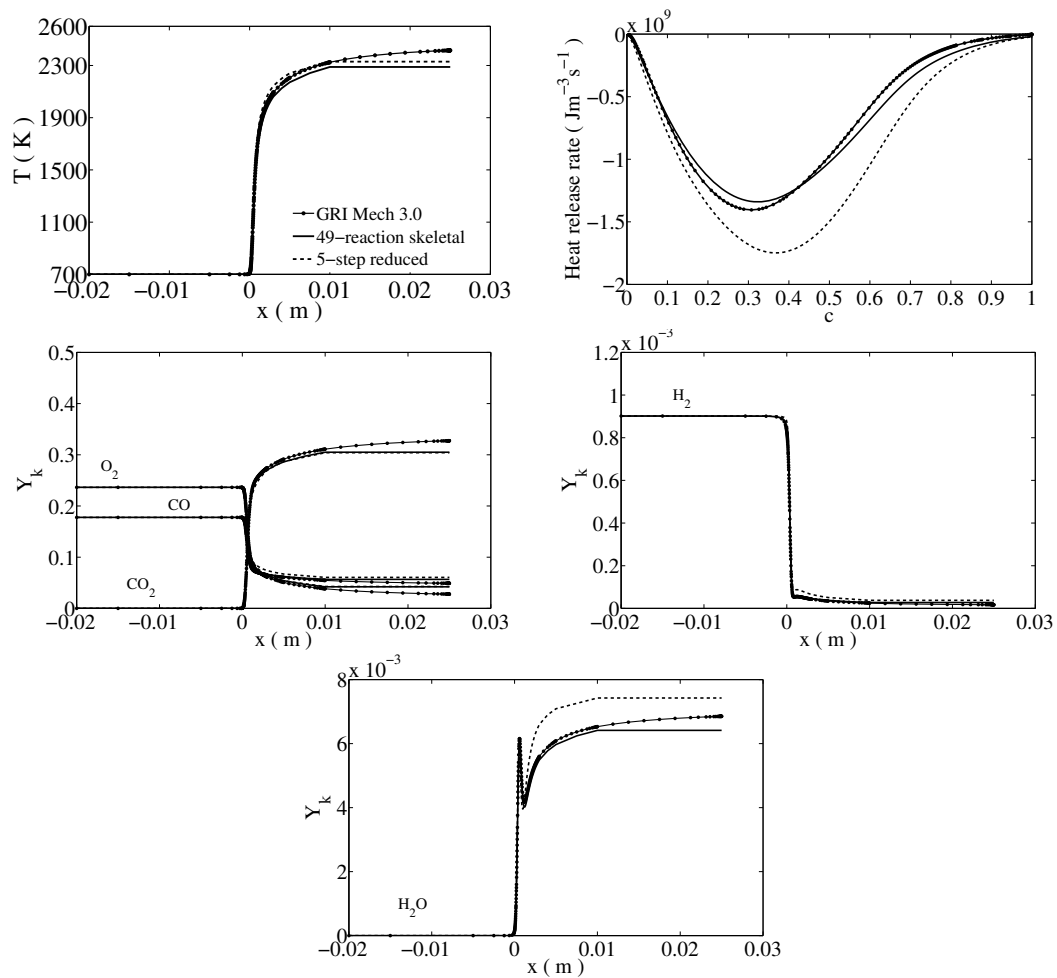


Figure 2.16: Flame structure for CO/H₂/O₂/N₂. $\phi = 0.8$, $f_{\text{H}_2} = 5/95$, $T_r = 700$ K, $p = 1$ atm. (conditions as in Fig. 2.5 top).

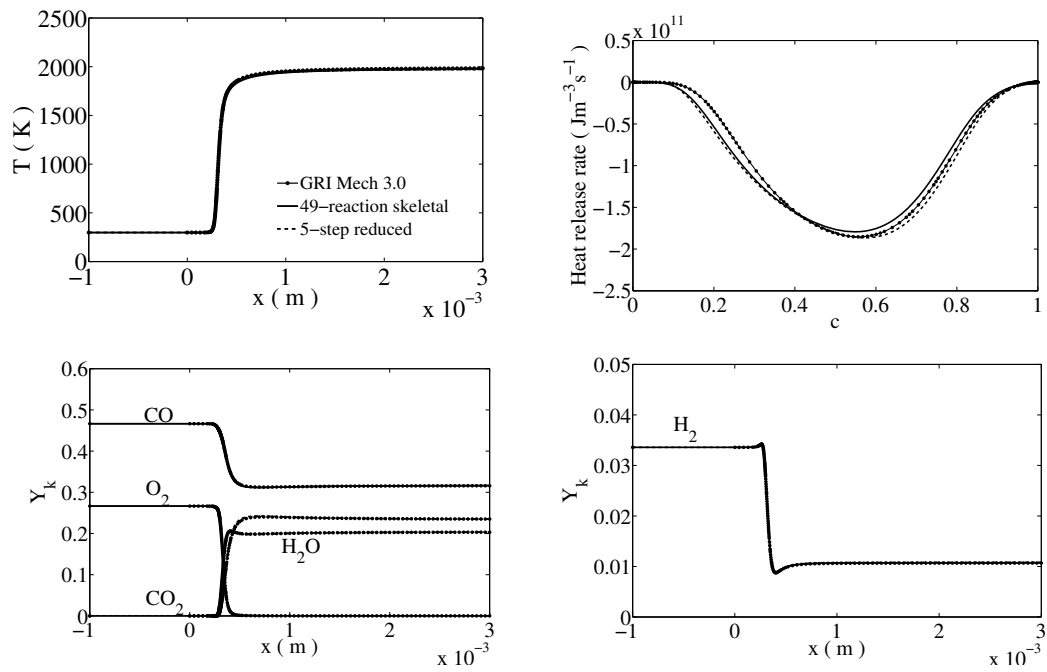


Figure 2.17: Flame structure for CO/H₂/O₂/He. He/O₂ = 7.0, $\phi = 2.0$, $f_{\text{H}_2} = 1.0$, $T_r = 298$ K, $p = 5$ atm. (conditions as in Fig. 2.8 top).

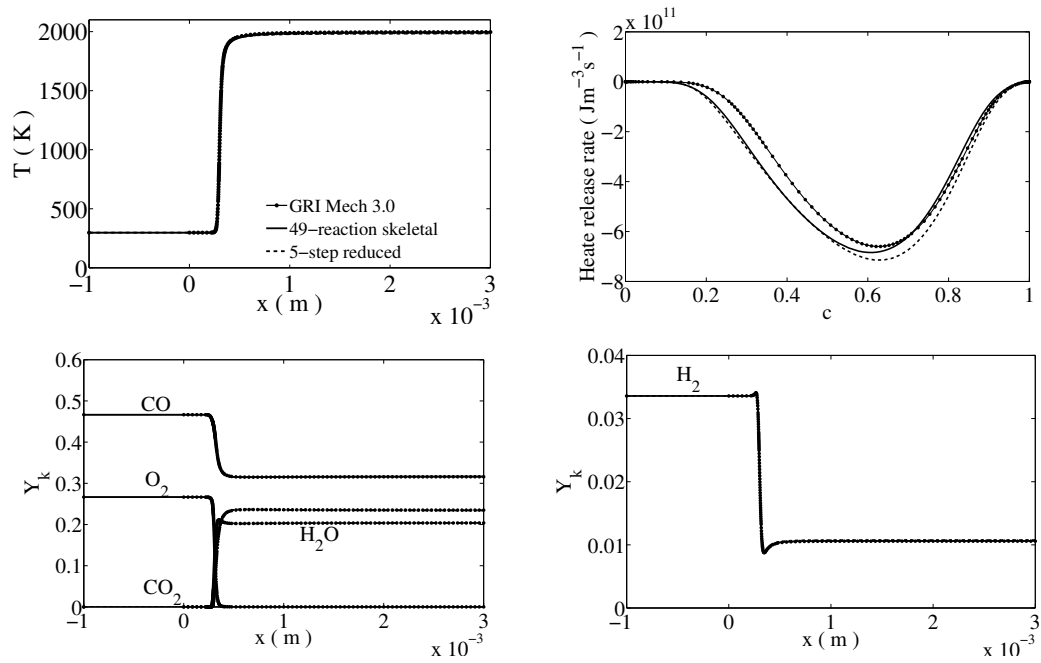


Figure 2.18: Flame structure for CO/H₂/O₂/He. He/O₂ = 7.0, $\phi = 2.0$, $f_{H_2} = 1.0$, $T_r = 298$ K, $p = 10$ atm. (conditions as in Fig. 2.8 top).

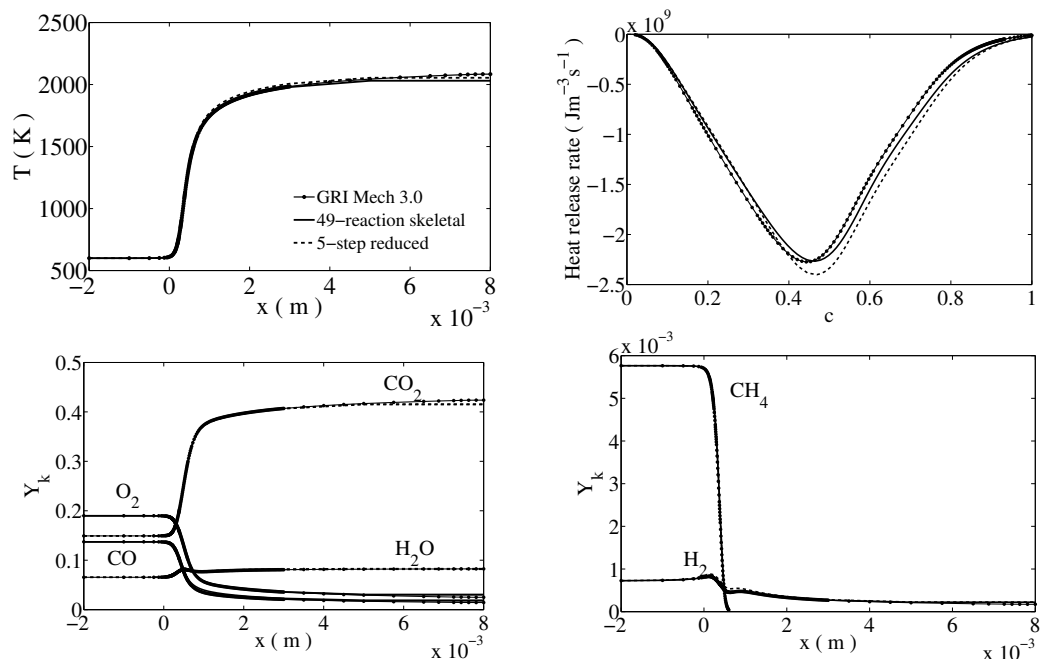


Figure 2.19: Flame structure for $\text{CO}/\text{H}_2/\text{CH}_4/\text{H}_2\text{O}/\text{CO}_2/\text{O}_2/\text{N}_2$ with 25% H_2O . $\phi = 1.0$, $f_{\text{H}_2} = 5/95$, $f_{\text{CH}_4} = 5/95$, $f_{\text{CO}_2} = 0.5$, $T_r = 600$ K, $p = 1$ atm. (conditions as in Fig. 2.11).

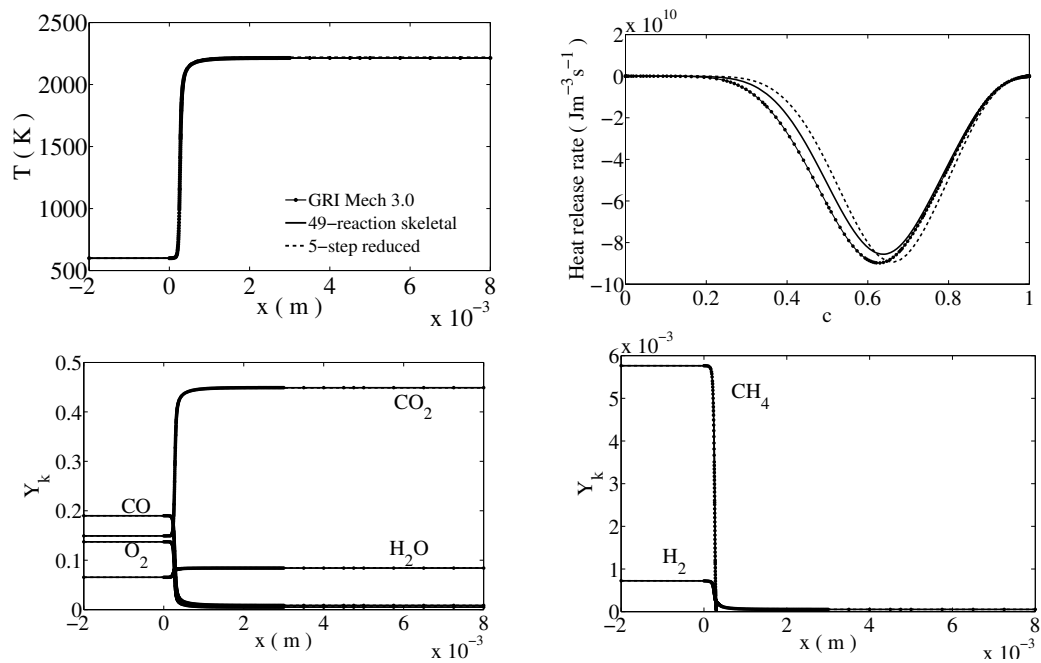


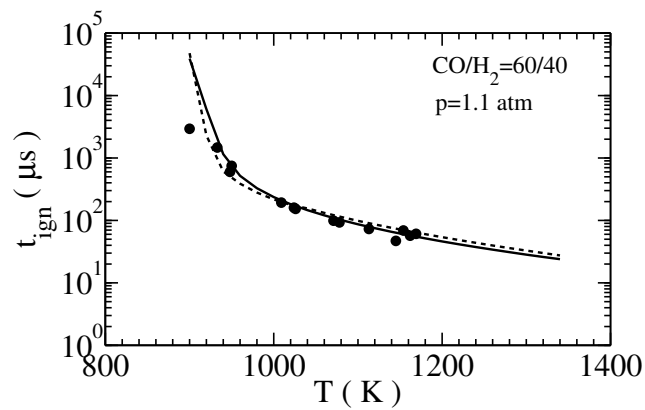
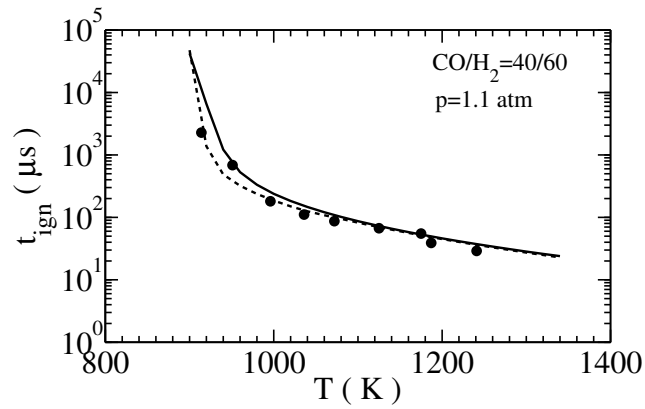
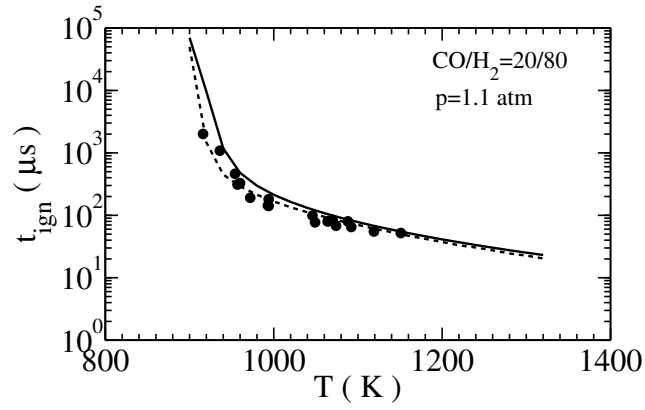
Figure 2.20: Flame structure for CO/H₂/CH₄/H₂O/CO₂/O₂/N₂ with 25% H₂O. $\phi = 1.0$, $f_{\text{H}_2} = 5/95$, $f_{\text{CH}_4} = 5/95$, $f_{\text{CO}_2} = 0.5$, $T_r = 600$ K, $p = 10$ atm. (conditions as in Fig. 2.11).

2.4.2 Autoignition

Figure 2.21 compares the computed ignition delay times (with the correction factor in Eq. 3 applied) with the experimental results of Kalitan et al. [102] for CO/H₂ mixtures over a range of conditions listed in Table 2.4. Overall, the agreement is very good for both low and high pressures and for the entire range of temperatures considered. In the high pressure regime, the values computed in this study give slightly better agreement for higher temperatures than the skeletal mechanism of Boivin et al. [18] as can be seen for the $f_{H_2} = 20/80$ case at 15.4 atm. Also, one may like to recall that the expression for B in Eq. 4 is modified as noted earlier to yield the agreement shown here and the correction factor is applied over the whole of the integration period.

Figure 2.22 compares ignition delay times computed for a CO₂-diluted mixture to the measured values of Vasu et al. [81] at different pressures. The reduced mechanism shows good agreement with the experimental data for the entire temperature range. The skeletal mechanism also shows a good agreement but seems to slightly over predict the ignition delay times as the pressure is increased. As noted in [81] using sensitivity analysis, the most important reactions at the conditions tested were the chain-branching reactions and the three body recombination reaction $H + O_2 + CO_2 = HO_2 + CO_2$. In the same study it was concluded that the rate of this recombination reaction used in GRI-3.0 was ideal to be used for kinetic modelling for the temperature range of 800-1305 K and 1-8 atm. Thus, a small reduction in the rate of the chain-branching reactions would certainly improve the agreement for higher pressures but this would only be minor.

Figure 2.23 shows the computed variation of ignition delay time with mixture temperature for a stoichiometric CO/H₂/CH₄/H₂O/O₂/N₂ mixture at 5 atm. The computational results obtained using the skeletal and reduced mechanisms are compared to the experimental data of Gurentsov [107]. It is clear that the reduced mechanism is able to give accurate ignition delay times for such complex multi-species fuel mixture including the effect of water vapour.



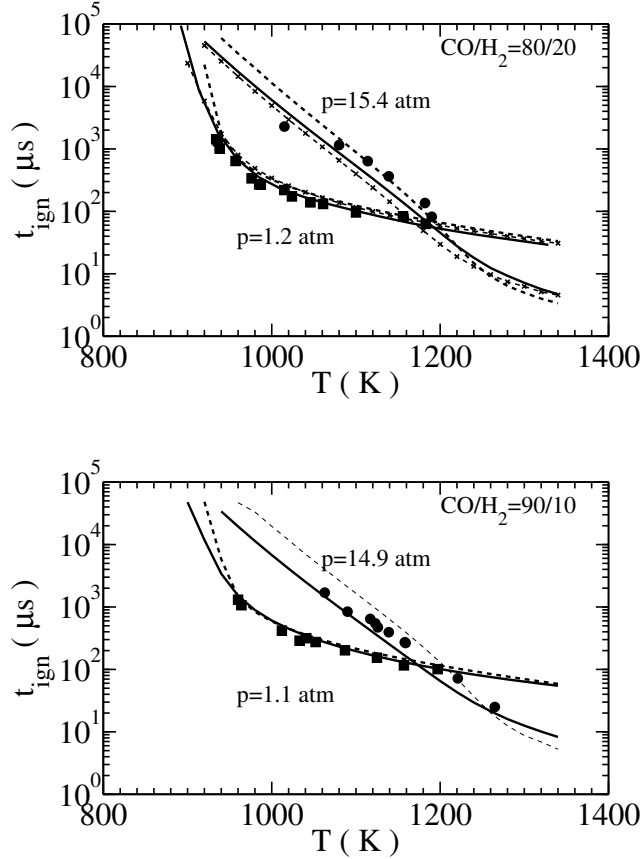


Figure 2.21: Ignition delay times of CO/H₂/O₂/N₂ mixtures ($X_{N_2}/X_{O_2} = 3.76$) for $\phi = 0.5$ using the reduced (dashed lines) and skeletal (continuous lines) mechanisms. Symbols: experimental results of Kalitan et al. [102]. Also shown for comparison are the results with the skeletal mechanism of Boivin et al. [18] (dashed lines with \times) for the $f_{H_2} = 20/80$ case.

2.5 Speed up times

Table 2.5 shows the time in seconds taken for each run for each of the conditions shown in Table 4. The flame speeds were calculated using the PREMIX code with thermal diffusion and a multi-component formulation for the species' diffusivities, in a 2.5 cm domain with adaptive grid. It is clear that both the skeletal and reduced mechanisms reduced the computational time significantly compared to

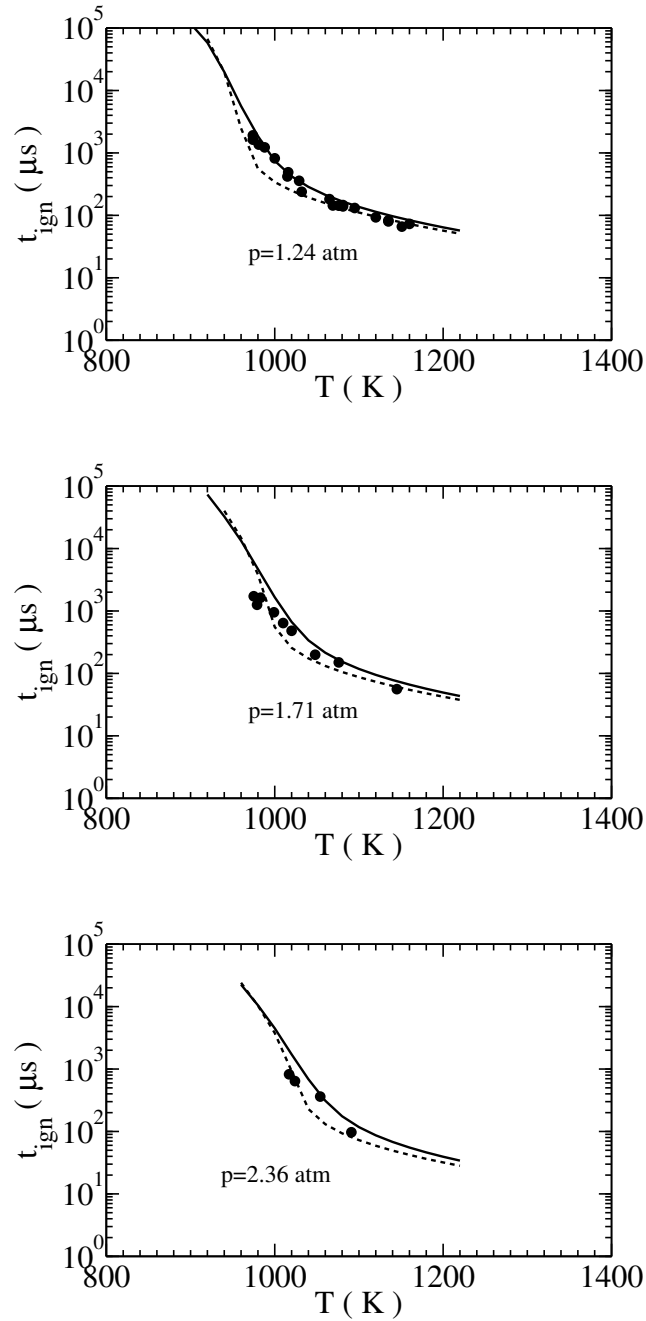


Figure 2.22: Ignition delay times of $\text{CO}/\text{H}_2/\text{CO}_2/\text{O}_2/\text{N}_2$ mixtures using the reduced (dashed lines) and skeletal (continuous lines) mechanisms. Symbols: experimental data of Vasu et al. [81]. Mixture composition: $8.91\%\text{H}_2 + 11.58\%\text{CO} + 24.44\%\text{CO}_2 + 10.25\%\text{O}_2 + 44.83\%\text{N}_2$.

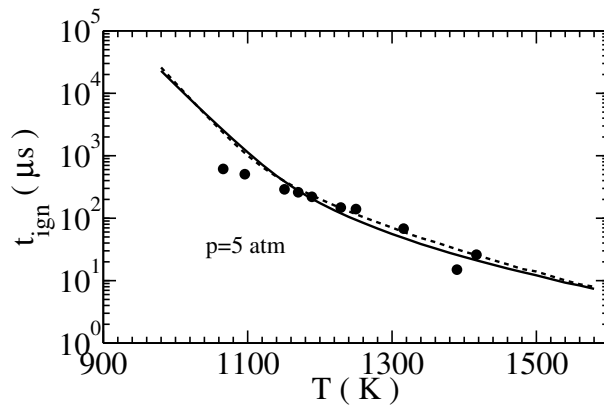


Figure 2.23: Ignition delay times of $\text{CO}/\text{H}_2/\text{H}_2\text{O}/\text{CH}_4/\text{O}_2/\text{N}_2$ mixtures using the reduced (dashed lines) and skeletal (continuous lines) mechanisms. Symbols: experimental data of Gurentsov [107]. $\phi = 1$, $p = 5$ atm. Mixture: $3\text{H}_2 + \text{CO} + \text{H}_2\text{O} + 4\text{O}_2 + \text{CH}_4 + 16\text{N}_2$.

GRI-3.0, while maintaining the same level of accuracy. In particular for case 3 the skeletal mechanism is about 50 times faster and the reduced mechanism about 300 times faster.

Case	Conditions	GRI-3.0	49r-skeletal	5-step
1	$\text{H}_2\text{O}\%=20$, $\phi=0.9$	1415.099	47.559	5.941
2	$p=20\text{atm}$, $\phi=5.0$	7956.458	284.573	29.179
3	$\phi=1.2$	2903.111	51.992	9.044

Table 2.5: Time in s of the run for each condition using PREMIX [96] with thermal and multi-component diffusion.

Chapter 3

Mathematical background: governing equations and numerical method

The purpose of this chapter is to present the governing equations of reacting flows and details of the numerical implementation. The chemical mechanisms developed in the previous chapter are subsequently used to conduct DNS of multi-component fuel combustion with atmospheric air, the conditions of which are given in this chapter.

3.1 Governing equations

The direct numerical simulations have been conducted using the SENGA2 code [108] which is a fully compressible code. The equations solved are those for the conservation of mass (Eq. 3.1), momentum (Eq. 3.2), specific energy (Eq. 3.3), and of species α mass fraction (Eq. 3.4):

$$\frac{\partial \rho}{\partial t} + \frac{\partial \rho u_k}{\partial x_k} = 0, \quad (3.1)$$

$$\frac{\partial \rho u_i}{\partial t} + \frac{\partial \rho u_k u_i}{\partial x_k} = -\frac{\partial p}{\partial x_i} + \frac{\partial \tau_{ki}}{\partial x_k}, \quad (3.2)$$

$$\frac{\partial \rho E}{\partial t} + \frac{\partial \rho u_k E}{\partial x_k} = -\frac{\partial p u_k}{\partial x_k} - \frac{\partial q_k}{\partial x_k} + \frac{\partial \tau_{km} u_m}{\partial x_k}, \quad (3.3)$$

$$\frac{\partial \rho Y_\alpha}{\partial t} + \frac{\partial \rho u_k Y_\alpha}{\partial x_k} = \dot{w}_\alpha - \frac{\partial \rho V_{\alpha,k} Y_\alpha}{\partial x_k}. \quad (3.4)$$

Mass conservation implies that the species mass fractions, Y_α , must obey:

$$\sum_{\alpha=1}^N Y_\alpha = 1 \quad (3.5)$$

where N is the total number of species in the mixture.

The pressure, p , is calculated using the thermal equation of state:

$$p = \rho R^0 T \sum_{\alpha=1}^N \frac{Y_\alpha}{W_\alpha} \quad (3.6)$$

In the equation above, R^0 is the universal gas constant, T is the absolute temperature, and W_α is the species α molecular weight. The specific energy, E , at a point in the domain is defined as the sum of the mixture's specific internal energy $\left(\sum_{\alpha=1}^N Y_\alpha h_\alpha - \frac{p}{\rho}\right)$ and specific kinetic energy as follows:

$$E = \sum_{\alpha=1}^N Y_\alpha h_\alpha - \frac{p}{\rho} + \frac{1}{2} u_k u_k \quad (3.7)$$

The enthalpy, h_α , of species α is defined as:

$$h_\alpha = \int_{T_0}^T C_{p\alpha} dT + h_{f,\alpha}^0, \quad (3.8)$$

$C_{p\alpha}$ is the mass-based specific heat capacity of species α . and it is a function of temperature which is given for each species in terms of a polynomial function. The polynomial coefficients are listed in the chemical mechanism's thermodynamic database which in this case is the same as that of GRI-3.0 [73]. $h_{f,\alpha}^0$ is the species formation enthalpy at the reference temperature T_0 , while the first term on the right-hand side of the above equation is the sensible enthalpy contribution. Further details of the numerical evaluation of thermodynamic quantities can be found in the SENG2 User Guide [108].

The viscous stress tensor, τ_{ki} , is given by:

$$\tau_{ki} = \mu \left(\frac{\partial u_k}{\partial x_i} + \frac{\partial u_i}{\partial x_k} \right) - \frac{2}{3} \mu \frac{\partial u_m}{\partial x_m} \delta_{ki}, \quad (3.9)$$

In the case of constant density (incompressible) flow $\partial u_m / \partial x_m = 0$, and shear stresses arise solely from velocity gradients. In the case of reacting flows heat release causes density changes in the flow i.e. $\partial u_m / \partial x_m$ can be non-zero and must be accounted for.

The heat flux vector is given by:

$$q_k = -\lambda \frac{\partial T}{\partial x_k} + \sum_{\alpha=1}^N \rho V_{\alpha,k} Y_{\alpha} h_{\alpha} \quad (3.10)$$

where λ is the mixture's thermal conductivity, the calculation of which is explained in section 3.2. $V_{\alpha,k}$ is the diffusion velocity of species α which by definition must satisfy:

$$\sum_{\alpha=1}^N V_{\alpha,k} Y_{\alpha} = 0. \quad (3.11)$$

The first term in Eq. 3.10 is Fourier's law of conduction. The second term is included to describe the heat flux occurring as a result of species diffusion which carry with them a certain amount of energy in the form of enthalpy.

3.2 Transport coefficients

The mixture's thermal conductivity, λ , is estimated using [109]:

$$\frac{\lambda}{C_p} = A_{\lambda} \left(\frac{T}{T_0} \right)^r \quad (3.12)$$

where C_p is the mixture's specific heat capacity, $A_{\lambda} = 2.6246 \times 10^{-5} \text{ kgm}^{-1}\text{s}^{-1}$ and $r = 0.6859$. The dynamic viscosity, μ , of the mixture is then estimated by assuming a constant mixture Prandtl number, Pr:

$$\mu = \frac{\lambda}{C_p} \text{Pr} \quad (3.13)$$

From laminar unstained flame calculations it is found that the Prandtl number is equal to 0.7. The species diffusion velocities are calculated assuming Fickian diffusion:

$$\rho V_{\alpha,k} Y_{\alpha} = -\rho D_{\alpha} \frac{\partial Y_{\alpha}}{\partial x_k}. \quad (3.14)$$

and the diffusion coefficient, D_{α} , is calculated by assuming a constant but different Lewis number, Le , for each species [109]:

$$D_{\alpha} = \frac{\lambda}{\rho C_p Le_{\alpha}} \quad (3.15)$$

The species Lewis numbers are calculated by taking the average Le_{α} for each species across the flame front from a laminar unstrained flame calculation, and are shown in Table 3.1.

Index	Species	Le
1	H	0.156
2	O ₂	0.996
3	H ₂ O	0.756
4	CO	0.991
5	CO ₂	1.311
6	H ₂	0.264
7	H ₂ O ₂	1.005
8	(OH)	0.650
9	(HO ₂)	0.998
10	(HCO)	1.149
11	(O)	0.637
12	CH ₄	0.896
13	(CH ₃)	0.891
14	(CH ₂ O)	1.159
15	N ₂	0.922

Table 3.1: Species Lewis numbers. The species in parentheses are in steady-state using the 5-step reduced mechanism.

The constant Lewis number assumption used to calculate D_{α} however when used in Fick's law does not ensure mass conservation as per Eq. 3.1. If Eq. 3.14 is used in Eq. 3.4 and Eq. 3.4 is then summed over all species then:

$$\frac{\partial \rho}{\partial t} + \frac{\partial \rho u_k}{\partial x_k} = \sum_{\alpha=1}^N \frac{\partial \rho D_\alpha}{\partial x_k} \frac{\partial Y_\alpha}{\partial x_k}. \quad (3.16)$$

It is also important to note that Eqs. 3.5 and 3.20 (to be discussed later) have also been used for the above derivation. Clearly, mass conservation is not ensured since the right-hand side of the above equation is not zero. To ensure mass conservation a correction velocity, $V_k^{(c)}$, is added to the species diffusion velocity as follows:

$$\rho V_{\alpha,k} Y_\alpha = -\rho D_\alpha \frac{\partial Y_\alpha}{\partial x_k} + \rho V_k^{(c)} Y_\alpha \quad (3.17)$$

where the correction velocity is given by:

$$\rho V_k^{(c)} = \sum_{\alpha=1}^N \rho D_\alpha x_k \frac{\partial Y_\alpha}{\partial x_k}. \quad (3.18)$$

The above ensures that when Eq. 3.11 is applied, mass is conserved as per Eq. 3.1.

3.3 Reaction rates

The mass rate of production of species α is calculated by summing up the contribution to the species rate from all M reactions in the chemical mechanism set:

$$\dot{w}_\alpha = W_\alpha \sum_{m=1}^M \bar{w}_{\alpha,m} \quad (3.19)$$

$\bar{w}_{\alpha,m}$ is the molar production rate of species α in reaction m . The species rates must satisfy the condition:

$$\sum_{\alpha=1}^N \dot{w}_\alpha = 0. \quad (3.20)$$

The evaluation of the species molar rate, $\bar{w}_{\alpha,m}$, in reaction m depends however on the type of the reaction in the chemical mechanism set. This is discussed in the following section.

3.3.1 Forward and backward reaction rate evaluation

A reaction step m involving N species can be denoted by:



\mathcal{M}_{α} is the particular species taking part in the reaction, and $\nu'_{\alpha,m}$ and $\nu''_{\alpha,m}$ are the species stoichiometric coefficients in the reactants and products respectively. The net molar rate of a species in such a reaction is given by:

$$\bar{w}_{\alpha,m} = (\nu''_{\alpha,m} - \nu'_{\alpha,m}) \left[k_{f,m}(T) \prod_{\beta=1}^N c_{\beta}^{\nu'_{\beta,m}} - k_{r,m}(T) \prod_{\beta=1}^N c_{\beta}^{\nu''_{\beta,m}} \right]. \quad (3.22)$$

where $k_{f,m}$ and $k_{r,m}$ are the forward and reverse rate constants of reaction m respectively. c_{β} is the molar concentration of a species given by $c_{\beta} = \rho Y_{\beta} / W_{\beta}$. Assuming Arrhenius kinetics, the forward rate constant is given by:

$$k_{f,m} = A_m T^{n_m} \exp\left(-\frac{E_m}{R^0 T}\right) \quad (3.23)$$

where A_m , n and E_m are the pre-exponential factor, temperature exponent and activation energy of reaction m respectively. Usually, the forward rate coefficients only are supplied for a reaction, and it becomes necessary to calculate the reverse rate using the equilibrium constant $K_{c,m}$:

$$K_{c,m} = \prod_{\alpha=1}^N c_{\alpha}^{(\nu''_{\alpha,m} - \nu'_{\alpha,m})} = \frac{k_{r,m}}{k_{f,m}} \quad (3.24)$$

The equilibrium constant, $K_{c,m}$, depends on temperature and on the change in Gibbs function of a reaction. In particular:

$$K_{c,m} = K_{p,m}^0 \left(\frac{p_0}{R^0 T}\right)^{\Delta \nu_m} \quad (3.25)$$

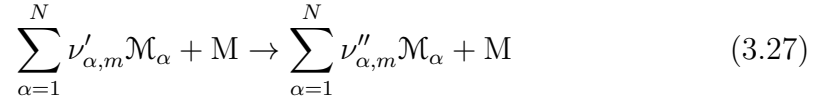
where p_0 is a reference pressure, and $\Delta \nu_m = \sum_{\alpha=1}^N (\nu''_{\alpha,m} - \nu'_{\alpha,m})$. $K_{p,m}^0$ is given by:

$$R^0 T \ln K_{p,m}^0 = \Delta \hat{G}_m = \sum_{\alpha=1}^N \bar{g}_\alpha (\nu''_{\alpha,m} - \nu'_{\alpha,m}) \quad (3.26)$$

where $\Delta \hat{G}_m$ is the change in the molar Gibbs function of reaction m and $\bar{g}_\alpha = (\bar{h}_\alpha - T\bar{s}_\alpha)$ is the molar Gibbs function of species α . s_α is the molar entropy of species α and is evaluated in a similar way like \bar{h}_α further details of which can be found in [108].

3.3.2 Third body reactions

Third body reactions are reactions of the form:



where M stands for the third body. An example of a third body reaction is the reaction $\text{H} + \text{O}_2 + \text{M} = \text{HO}_2 + \text{M}$. In this reaction, H and O₂ are too energetic for the recombination step to occur. As a result, a third body (any other species in the mixture) is required to remove some of the excess energy by colliding with the reacting molecules thus allowing the recombination to occur. As a result, such reactions usually have a negative temperature exponent n since higher temperatures imply more energetic molecules. The molar production rate of a species in such reactions is given by:

$$\bar{w}_{\alpha,m} = (\nu''_{\alpha,m} - \nu'_{\alpha,m}) k_m(T) c_M \prod_{\beta=1}^N c_\beta^{\nu'_{\beta,m}}. \quad (3.28)$$

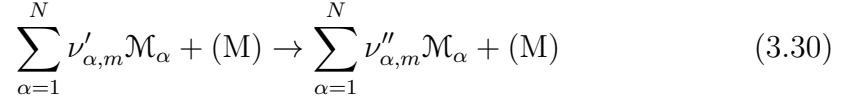
where c_M is the third body concentration:

$$c_M = \sum_{\alpha=1}^N \eta_{\alpha,M} c_\alpha \quad (3.29)$$

$\eta_{\alpha,M}$ are the third-body efficiencies for each species M.

3.3.3 Pressure-dependent reactions

Third-body and pressure dependent reactions are denoted as:



where the rate constant is now a function of pressure also. The molar production rate of a species α in this case is calculated using:

$$\bar{w}_{\alpha,m} = (\nu''_{\alpha,m} - \nu'_{\alpha,m}) k'(T) \prod_{\beta=1}^N c_\beta^{\nu'_{\beta,m}}. \quad (3.31)$$

For Lindemann form pressure dependent reactions, the reaction rate constant $k'(T)$ is expressed as:

$$k'(T) = k_L(T) = k_\infty \frac{P_r}{1 + P_r} F \quad (3.32)$$

where the reduced pressure P_r is proportional to the third body concentration:

$$P_r = \frac{k_0 c_M}{k_\infty} \quad (3.33)$$

k_∞ is the rate constant at the high pressure limit, k_0 is the low pressure limit rate constant, $F = F_L = 1$, and c_M is the third body concentration as defined in the previous section. A more accurate description of a pressure dependent reaction is obtained when Troe form is used, which is basically the same as the Lindemann form the only difference being that the parameter F is not constant. In Troe form the parameter $F = F_{Troe}$ is given by:

$$\log F = \frac{\log Fc}{1 + \left[\frac{\log P_r + c}{n - d(\log P_r + c)} \right]^2} \quad (3.34)$$

where:

$$c = -0.4 - 0.67 \log F_c \quad (3.35)$$

$$n = 0.75 - 1.67 \log F_c \quad (3.36)$$

$$d = 0.14 \tag{3.37}$$

$$F_c = (1 - \alpha^*) \exp^{-\frac{T}{T_1}} + \alpha^* \exp^{-\frac{T}{T_2}} + \exp^{-\frac{T_3}{T}} \tag{3.38}$$

with the parameters α^*, T_1, T_2, T_3 depending on the reaction.

3.4 Boundary conditions

Periodic boundary conditions are applied in the homogeneous (y and z) directions marked in Fig. 3.1. Subsonic constant density reflecting inflow boundary conditions are applied at the inflow boundary, and partially-reflecting boundary conditions at the outflow boundary, based on characteristic analysis [110, 111], later extended to the NSCBC (Navier-Stokes Characteristic Boundary Conditions) formulation [112, 113, 114]. Transverse convective terms are also included [115, 116], in order to correctly estimate the wave amplitude variations at both the inflow and outflow boundaries. This was found to be an essential component of the simulations ensuring numerical stability, especially for the highest turbulence level. The computational domain is discretised in space using a structured and uniform Cartesian mesh. Each of the spatial derivatives in the conservation equations is discretised using a 10th order centred finite difference scheme for all interior points. The order of this centred differencing scheme is reduced gradually to 4th order as the boundaries are approached. The time advancement of the solution is carried out using a low-storage fourth-order Runge-Kutta method [117].

3.5 Flow configuration

A sketch of the computational domain is given in Fig. 3.1, to simulate a freely propagating multi-component fuel turbulent premixed flame. At the inlet $u_{in} = \bar{u} + u'$ where \bar{u} is the constant mean inlet velocity and u' are the turbulence fluctuations. The fluctuations are calculated from a previous cold run using periodic boundary conditions and a Batchelor-Townsend energy spectrum [118]. The pre-computed

velocity fluctuations are then saved and added to the mean flow at the inlet for every time step. A scanning plane runs through the saved velocity field and Fourier interpolation is used to correctly update the inlet boundary. The turbulence at the inlet is homogeneous and isotropic and it decays downstream. The dissipation rate is high because of the intense turbulence, with the flame interacting with a weaker turbulence than at the inlet. u_{rms} and l_{int} only serve to characterize the turbulence at the inlet. This cannot be avoided in simulations of this kind [25, 26, 36, 35], unless the Re is sufficiently low or if forced turbulence schemes are used which are usually computationally very expensive.

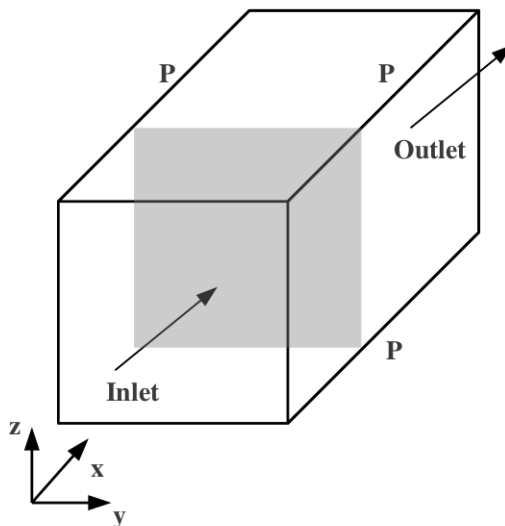


Figure 3.1: Sketch of the computation domain. Periodic boundary conditions are applied in the y, z directions. Grey area indicates laminar flame used for initialization.

3.6 Mixture conditions

The scalar field is initialised using steady-state laminar flame solutions obtained using the PREMIX code of the CHEMKIN package [96, 97]. The fuel mixture is at 800 K and 1 atm, with the equivalence ratio of $\phi=1$ and it is composed of CO, H₂, H₂O, CO₂ and CH₄. The mole fraction percentages of these species

are given in Table 3.2 and this composition is typical of a BFG mixture [1], or a low hydrogen content syngas mixture [6, 7, 8]. The flame thickness $\delta_l=(T_p - T_r)/\max(dT/dx)$ where T_r is the reactant temperature and T_p is the product temperature, and $\delta = \nu_r/s_l$ where ν_r is the kinematic viscosity of the reactant mixture.

T_r/K	ϕ	p/atm	CO	H ₂	H ₂ O	CO ₂	CH ₄	s_l (ms ⁻¹)	δ_l (m)	δ (m)
800.0	1.0	1.0	62.687	1.881	16.000	18.806	0.627	2.5	0.75E-3	3.26E-5

Table 3.2: Fuel mixture composition (molar percentages) used in the DNS. Note that the oxidizer is atmospheric air.

3.7 Turbulent flame conditions

Table 5.1 shows the turbulence parameters of the DNS: u_{rms} is the rms value of fluctuating incoming velocity, with an integral length scale l_{int} on the reactant side. The turbulence Reynolds number is $\text{Re}=u_{rms}\cdot l_{int}/\nu_r$, the Damkohler number is $\text{Da}=(l_{int}/u_{rms})/(\delta/s_l)$ and the Karlovitz number is $\text{Ka}=(\delta/\eta_k)^2$. Figure 3.2 shows the location of these conditions in the combustion diagram. The flame time is defined as $t_{fl}=\delta_l/s_l$, and the eddy turn-over time $t_e=l_{int}/u_{rms}$.

Case	u_{rms}/s_l	l_{int}/δ	$\text{Re}t$	Da	Ka	\bar{u}_{in}/s_l	t_{total}/t_{fl}	t_{total}/t_e
(A)	3.18	16.54	52.66	5.19	1.39	2.6	9.76	33.92
(B)	9.00	16.66	150.05	1.85	6.62	3.6	4.16	51.98
C	14.04	16.43	230.69	1.17	12.97	4.8	4.05	80.06

Table 3.3: Turbulent flame parameters for the DNS. The total run time of the simulations is t_{total} . Cases in parentheses denote DNS also contacted using the 5-step reduced mechanism.

3.8 Computational requirements

Table 3.4 gives the computational domain size and resolution for each case. The resolution is dictated by the turbulence scale in cases B and C, giving $\delta_r=2.5\eta_k$,

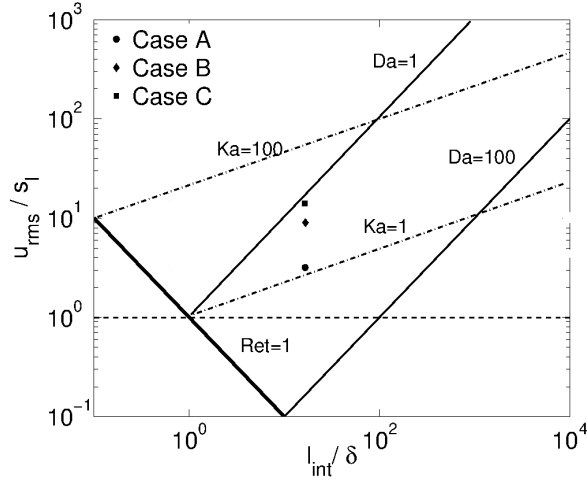


Figure 3.2: The inlet turbulence parameters for the three cases on the turbulent combustion diagram.

Case	$L_x(m)$	$L_y(m)$	$L_z(m)$	N_x	N_y	N_z
A	14.0E-3	7.0E-3	7.0E-3	768	384	384
A-red	14.0E-3	7.0E-3	7.0E-3	432	216	216
B	14.0E-3	7.0E-3	7.0E-3	768	384	384
C	21.0E-3	7.0E-3	7.0E-3	1632	544	544

Table 3.4: Computational domain size and resolution.

Case	Memory (GB)	Cores	Wall clock time (h)	t_{out}/t_{fl}	N_{tot}	δ_t (ns)
A	304.1	24^3	180	0.08	122	15
(A)	98.9	6^3	240	0.08	122	15
B	304.1	24^3	72	0.08	53	15
(B)	167.9	24^3	36	0.08	53	15
C	1066.3	32^3	156	0.09	95	8

Table 3.5: Computational requirements for the DNS.

where δ_r is the diagonal distance in a computational unit cell. For case A, the resolution is dictated by the minimum reaction zone thickness of all species present. These conditions ensure that there are approximately 20 grid points inside the minimum reaction zone thickness. It was observed during the course of the simulations that resolutions less than this resulted in severe numerical instabilities causing the simulation to crash. Using the 5-step reduced mechanism however

for case A the minimum number of grid points required for numerical stability was found to be 10 hence the lower resolution observed for case (A) in Table 3.4. The simulations were run on the UKs super-computer facility HECTOR. The computational details such as total memory requirements, number of cores used, output frequency t_{out} , total number of data sets saved N_{tot} , and time step δ_t are given in Table 3.5.

Chapter 4

Validation of 5-step reduced mechanism using 3D DNS data

A reduced mechanism is preferred for obvious computational reasons. However, the reduced mechanism must retain the essential features of flame structure, the relative role of various fuel species and important radicals, and their interactions with turbulence. The former aspects are usually verified using laminar flame measurements and quantities computed using detailed or skeletal chemistry. The turbulence-flame interaction aspects are usually presumed to hold. In this chapter, an attempt has been made to verify the ability of the 5-step reduced mechanism developed in Chapter 2 to capture the turbulence-flame interaction and flame front structure compared to a skeletal mechanism, using the DNS data of cases A and B described in Chapter 3. This ability is evaluated: (1) by comparing the spatial distribution of heat release rate and species mass fractions (2) by comparing the respective statistics of mass fractions, reaction rates e.t.c. obtained using these two mechanisms and (3) by examining the flame statistics, specifically pdfs of flame curvature, displacement speed, tangential strain rate, stretch rate and generalised flame surface density (FSD).

4.1 Post-processing method

The global flame behaviour is analysed through the calculation of the consumption speed defined as:

$$s_c = \frac{1}{\rho_r A} \int_V \frac{-\sum_{\alpha} h_{\alpha} \dot{w}_{\alpha}}{C_p (T_p - T_r)} dV \quad (4.1)$$

where A is the total area in the homogeneous direction and the integral is taken over the volume V of the computational domain. Figure 4.1 shows the temporal evolution of s_c/s_l for the two cases. Time is normalized using the flame time t_{fl} which is common for both cases. Initially, s_c is approximately equal to the laminar flame speed for both cases, indicating that s_c is a good measure of global flame behaviour. After about one flame time, the flame reaches a statistically stationary state for case B, and remains there up to 2.56 flame times where the simulation is stopped. Case A on the other hand shows a more delayed evolution: the consumption speed keeps increasing up to about 3 flame times, and remains in a more or less statistically stationary state up to about 5 flame times after which the consumption speed drops.

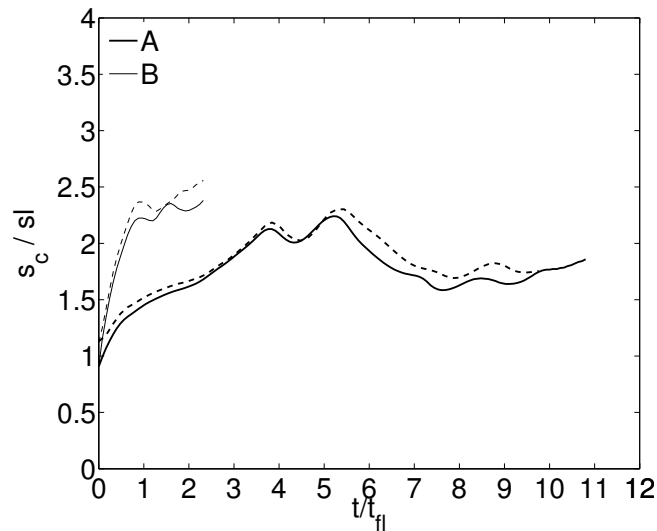


Figure 4.1: Consumption speed s_c for cases A (thick line) and B (thin line), using the skeletal (continuous line) and reduced (dashed line) mechanisms.

The DNS data have been post-processed using the same spatial differencing scheme as used in the DNS. Averaging is done both in space (in the homogeneous y , z directions) and in time, and by combining adjacent spatial points in order to increase the statistical accuracy. Five neighbouring points (symmetrically about i for interior points) are combined, after ensuring that the statistics such as the x -wise averages, and the pdfs of c are not affected. The average value of a quantity V at point i in the x direction is calculated according to:

$$\bar{V}(i) = \frac{1}{N_t N_y N_z N_p} \sum_{t=t_1}^{t=t_2} \sum_{k=1}^{N_z} \sum_{j=1}^{N_y} \sum_{p=1}^{N_p} V(i-3+p, j, k, t) \quad (4.2)$$

where $N_p=5$. The $i-3$ indicates that for points well away from the boundaries the averaging is symmetric about point i , using the 4 neighbouring grid points. Due care is taken at the boundaries. For case A, time averaging is performed between 3.5 and 5.6 flame times, and for case B time averaging is performed between 1.0 and 2.0 flame times. During these two intervals the flames in both cases seem to be in a statistically quasi-steady state at least as far as s_c is concerned, as shown in Fig. 4.1. This averaging procedure forms one part of the evaluation procedure of the reduced mechanism. The aim is to compare quantities such as the heat release, progress variable and species mass fraction variations across the flame brush between the two mechanisms. Conditional averages are taken over the entire volume in bins of c , and time-averaged over the above time intervals, and form another part of the evaluation process enabling to discern whether any differences arise in progress variable space between the two mechanisms.

The flame surface except where stated otherwise is defined as the temperature iso-surface using $c=(T - T_r)/(T_p - T_r)=c^*=0.32$, corresponding to the location of maximum heat release in the unstrained planar laminar flame. This choice is justified by the fact that the maximum discrepancies in the statistics between the two mechanisms will be observed close to this location of maximum heat release. Furthermore, mass fraction based progress variable definitions are found (Chapter 5) to vary substantially among different reactant species. The normal to the flame surface is given by:

$$n_i = -\frac{1}{\chi} \frac{\partial c}{\partial x_i} \quad (4.3)$$

where $\chi^2 = (\partial c / \partial x_i)(\partial c / \partial x_i)$. The generalized flame surface density (FSD) Σ is then $\Sigma = \bar{\chi}$, where the overbar denotes an LES filtering operation [65]. In the limit of zero filter width and using a Gaussian filter, LES becomes DNS, and $\Sigma = \bar{\chi} = \chi$. As a result χ which is called the surface density function (SDF) can in this regard be considered as being equivalent to the generalized FSD.

The flame stretch Φ is given by [119]:

$$\Phi = (\delta_{ij} - n_i n_j) \frac{\partial u_i}{\partial x_j} + s_d \frac{\partial n_i}{\partial x_i} = a_t + s_d \cdot K_m \quad (4.4)$$

where a_t is the tangential strain rate, K_m is the surface curvature, and s_d the displacement speed. The displacement speed, neglecting compressible terms which are expected to be small, is calculated on all points on the flame surface using [120]:

$$\chi s_d|_{c^*} = \frac{dc}{dt}|_{c^*} = \left[\frac{1}{\rho C_p} \frac{\partial}{\partial x_i} \left(\lambda \frac{\partial c}{\partial x_i} \right) - \frac{\partial c}{\partial x_i} \sum_a \frac{C_{pa} Y_a V_{ai}}{C_p} + \frac{\dot{Q}}{\rho C_p (T_p - T_r)} \right] |_{c^*} \quad (4.5)$$

where the heat release rate $\dot{Q} = -\sum_{\alpha} h_{\alpha} \dot{\omega}_{\alpha}$ (sensible enthalpy contribution was observed to be negligible based on laminar unstrained flame solutions). Normalized flame surface quantities are as follows: $a_t^+ = a_t \cdot t_{fl}$, $K_m^+ = K_m \cdot \delta_l$ and $\Phi^+ = \Phi \cdot t_{fl}$.

Probability density functions of displacement speed, curvature, tangential strain and stretch are extracted from the flame surface calculated using the samples collected over the entire sampling period as for the mean quantities. These quantities are analysed to address the third objective of this study, but not all of these quantities are shown here.

4.2 Comparison of spatial correlations

Figures 4.2 and 4.3 show the instantaneous heat release rate in x - y planes for cases A and B respectively. Slices are shown for four different z^+ spanning the entire length of the physical domain in the z direction. The top row shows the results using the skeletal mechanism, and the bottom row is for the reduced mechanism. The heat release rate \dot{Q} in both figures is normalized using the maximum heat release rate in the laminar case using the skeletal mechanism i.e. $\dot{Q}^+ = \dot{Q} / \max(\dot{Q}_{lam,skel})$ in order to highlight differences with the reduced mechanism.

For case A the general shape of the flame front is captured well by the reduced mechanism for all z . In both cases heat release is observed to peak in regions with negative curvature (convex towards the products), indicating that the same physical behaviour is recovered. Some differences are observed with respect to the maximum heat release rate values obtained, with the reduced mechanism reaching slightly higher maximum heat release values. Furthermore, heat release regions behind the main flame like the one for the third location, although captured with the reduced mechanism, are found to burn faster. For case B the differences between the two mechanisms are more pronounced: the skeletal mechanism shows a more patchy and distributed flame front, giving an overall thicker flame. The reduced mechanism on the other hand has a thinner flame front with a more continuous heat release zone. The difference though in the maximum heat release rate between the two mechanisms is reduced in comparison with case A, implying that turbulence is more dominant than chemical kinetics to the flame evolution.

The two-dimensional spatial cross-correlation function r , can be used to better quantify the difference between the two mechanisms for a given heat release x^+ - y^+ plane. This can be calculated for each z^+ from:

$$r(z_k) = \frac{\sum_i \sum_j (V_{ijk}^r - \overline{V^r})(V_{ijk}^s - \overline{V^s})}{\sqrt{\sum_i \sum_j (V_{ijk}^r - \overline{V^r})^2 \sum_i \sum_j (V_{ijk}^s - \overline{V^s})^2}} \quad (4.6)$$

In the above equation i , j and k are indices for the x^+ , y^+ and z^+ directions respectively, and the superscripts s and r stand for the skeletal and reduced mechanisms respectively. $\overline{V^r}$ is the average of a quantity V over a given x^+ -

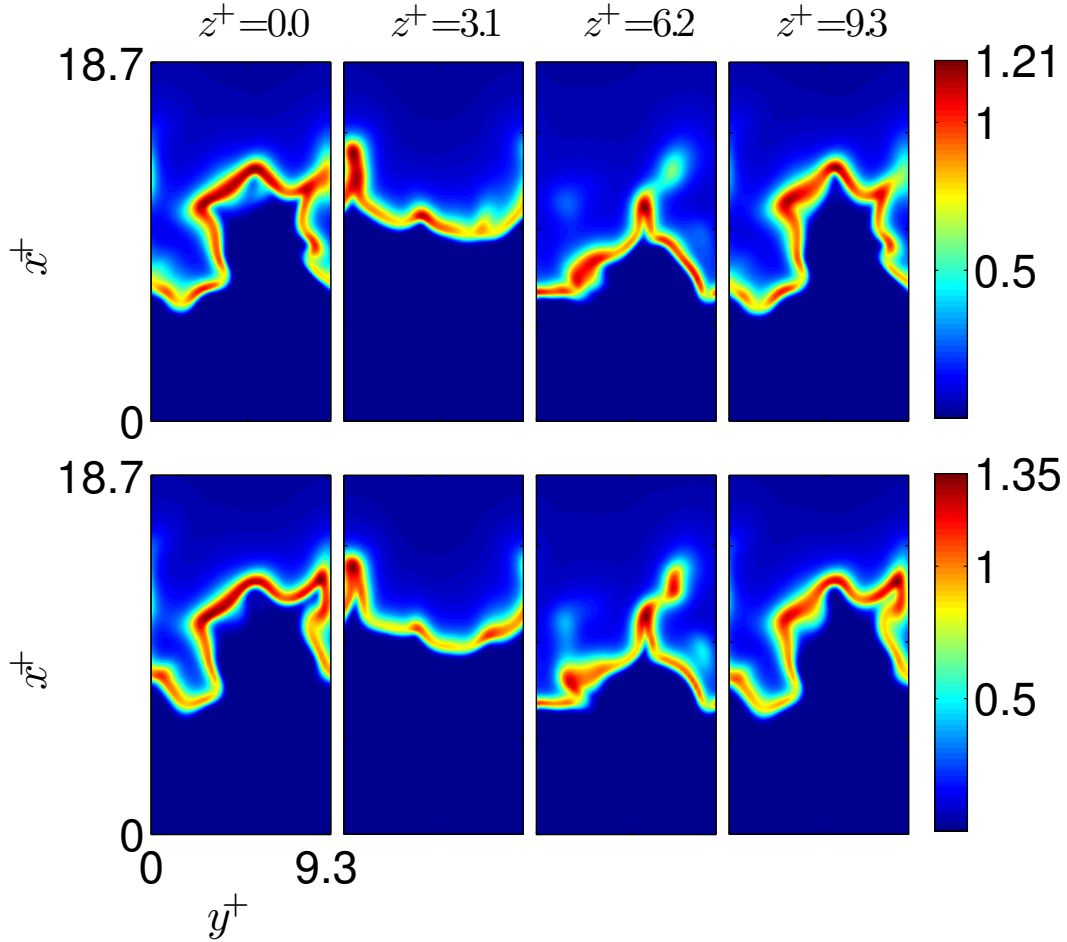


Figure 4.2: Instantaneous heat release rate \dot{Q}^+ in the x - y plane at different z locations. The top row is for the skeletal mechanism and the bottom row is for the reduced mechanism, for case A at $t/t_{fl}=4.0$.

y^+ plane using the reduced mechanism and $\overline{V^s}$ using the skeletal mechanism. The cross-correlation $r(z_k)$ is also time-averaged as discussed in the previous section, and is calculated for the heat release rate and species mass fractions. The function $r(z_k)$ is essentially a measure of the similarity of a given x^+ - y^+ plane between the two mechanisms. In the case where $V = \dot{Q}$ for example, it tells us how similar each pair of the heat release rate pictures shown in Fig. 4.3 are, with $r(z_k)=1$ implying identical pairs and hence a perfect correlation, and with $r(z_k)=0$ suggesting very dissimilar pairs of pictures. The results are shown in Fig. 4.4 for cases A and B respectively. The correlation for the heat release rate

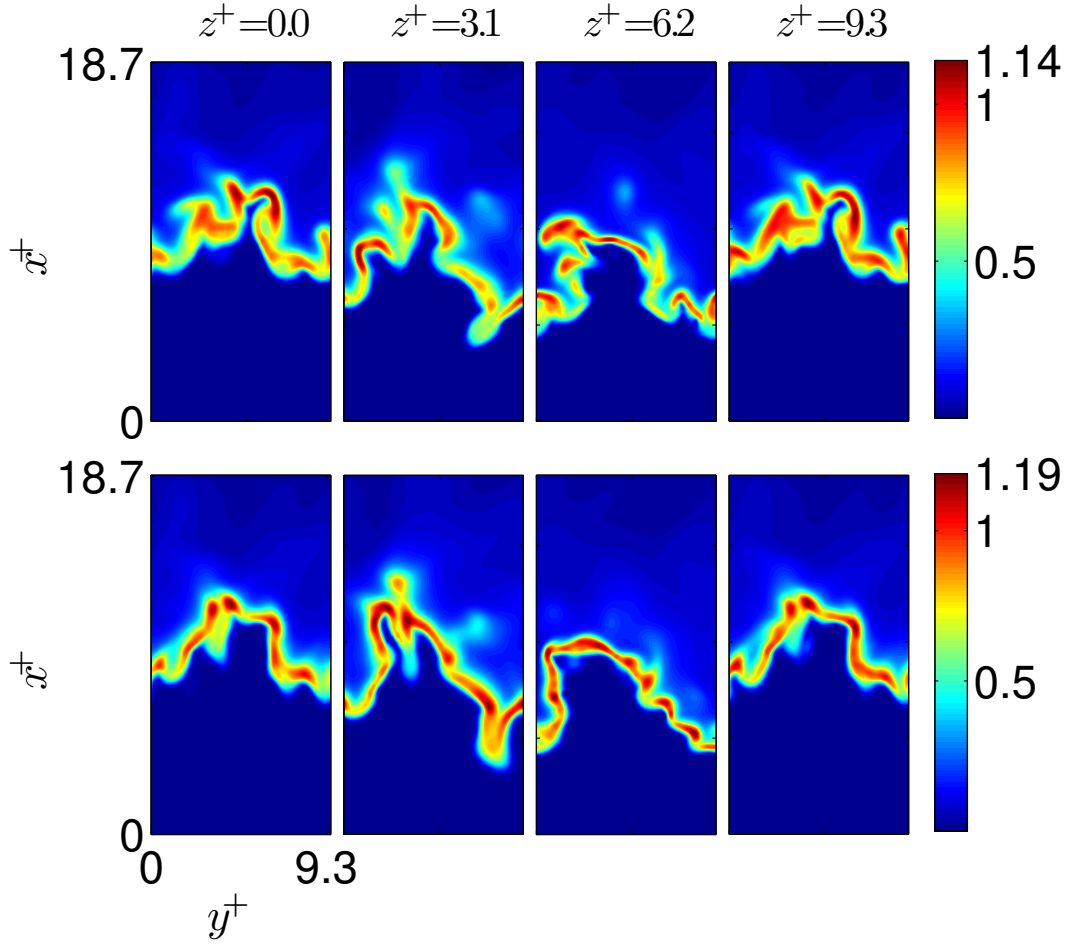


Figure 4.3: Instantaneous heat release rate \dot{Q}^+ in the x - y plane at different z locations. The top row is for the skeletal mechanism and the bottom row is for the reduced mechanism, for case B at $t/t_{fl}=1.6$.

is high for case A across all z , with the minimum falling only slightly below 0.8, something which is consistent with the visual comparison seen in the heat release contours in Fig. 4.2. For case B the heat release correlation is not as strong and is found to drop to about 0.6 in the middle of the domain, something which is also in agreement with Fig. 4.3. Comparison of the corresponding correlations for the species mass fractions reveals strong correlations for H, O₂, CO, CO₂ and CH₄ with near 1 values. Furthermore, the species CO, CO₂ and O₂ have almost identical correlation distributions. Less strong correlations are observed for H₂, and the least strong correlations are observed for H₂O and H₂O₂. The same

pattern is found to be true for case B, with the difference that the correlations are in general weaker, except for H_2 whose correlation coefficient is less sensitive to the turbulence level.

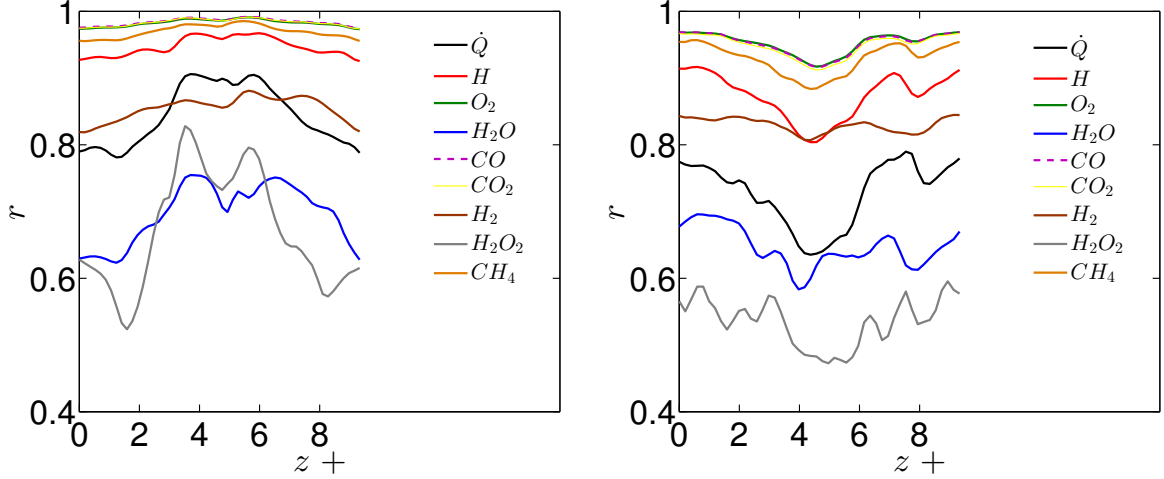


Figure 4.4: Correlation coefficient r across the z direction for the heat release rate and species mass fractions, for case A (left) and case B (right).

In order to help elucidate the effect of the turbulence on the spatial correlations, Fig. 4.5 shows the correlation coefficients for the unstrained laminar flame. The correlation coefficients in the laminar case are all high contrary to the turbulent cases, reaching values larger than 0.9 both for the heat release and the species mass fractions. This result signifies the importance of using three-dimensional DNS data for validating a reduced mechanism's performance, in contrast to laminar one-dimensional validations. Thus, turbulence reduces the spatial correlation coefficients. The 5-step mechanism was developed using numerical solutions of the Perfectly Stirred Reactor (PSR) to ease the numerical implementation, as input to CARM [93, 94]. A species α was identified as being in steady-state if:

$$100 \cdot \frac{|\dot{w}_{\alpha p} - \dot{w}_{\alpha d}|}{\max(\dot{w}_{\alpha p}, \dot{w}_{\alpha d})} \leq e \quad (4.7)$$

where $\dot{w}_{\alpha p}$ and $\dot{w}_{\alpha d}$ are the species production and destruction rates respectively, and the error e was taken to be less than 1%. Thus, are the poorer correlation coefficients observed in Fig. 4.4 in the turbulent case a result of the failure of

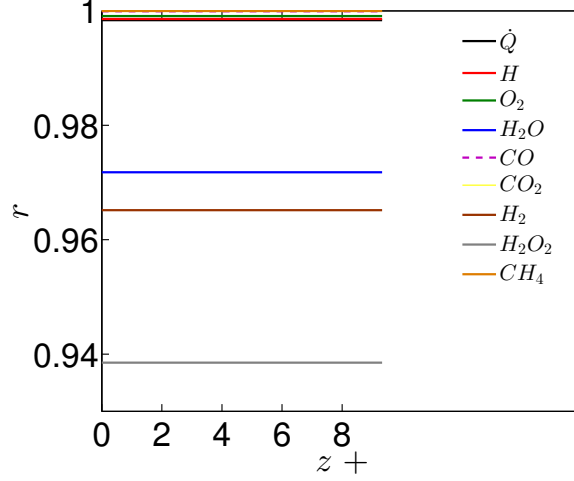


Figure 4.5: Correlation coefficient r across the z direction for the heat release rate and species mass fractions, for the laminar unstrained case.

the above QSS assumption related to the species rates? In order to establish the validity of this in the turbulent case, one can compute the maximum species rate-related QSSA error e_α from the skeletal chemistry DNS data using:

$$e_\alpha = \max_{gl} \left[100 \cdot \frac{|\dot{w}_{\alpha p} - \dot{w}_{\alpha d}|}{\max_{loc}(\dot{w}_{\alpha p}, \dot{w}_{\alpha d})} \right] \quad (4.8)$$

where the denominator is chosen based on the local maximum, \max_{loc} , between the species production and destruction rates, while the outer global maximum, \max_{gl} , is taken over the entire volume of the domain. Furthermore, in order to ensure that there are significant production or destruction rates for species α at the spatial point where the error is calculated, the denominator is subject to the following conditions: if the local production rate is larger than the local destruction rate i.e. for $(\dot{w}_{\alpha p} - \dot{w}_{\alpha d}) \geq 0$, then

$$\max_{loc}(\dot{w}_{\alpha p}, \dot{w}_{\alpha d}) = \begin{cases} \dot{w}_{\alpha p}, & \text{if } \dot{w}_{\alpha p} \geq 0.01 \times \max_{gl}(\dot{w}_{\alpha p}) \\ \infty, & \text{otherwise} \end{cases} \quad (4.9)$$

If the local destruction rate is higher i.e. for $(\dot{w}_{\alpha d} - \dot{w}_{\alpha p}) > 0$, then

$$max_{loc}(\dot{w}_{\alpha p}, \dot{w}_{\alpha d}) = \begin{cases} \dot{w}_{\alpha d}, & \text{if } \dot{w}_{\alpha d} \geq 0.01 \times max_{gl}(\dot{w}_{\alpha d}) \\ \infty, & \text{otherwise} \end{cases} \quad (4.10)$$

Figure 4.6 shows the instantaneous e_α as obtained from the DNS using Eqs. 4.8, 4.9, 4.10 for species 1-14 in the skeletal mechanism (see Table 3.1), for cases A and B. A similar trend was observed at different time-steps. Also shown in the same figures in grey bars is the laminar flame result. It is important to remind ourselves at this point that species 8, 9, 10, 11, 13 and 14 i.e. OH, HO₂, HCO, O, CH₃ and CH₂O are put in steady-state while developing the reduced mechanism [38]. Figure 4.6 shows that the errors for the laminar flame are larger than the 1% limit set in the PSR computations. Despite this, the use of the reduced mechanism is justified as the correlations in Fig. 4.5 are high. For cases A and B the error is reduced in comparison to the laminar flame for HCO only, and increased for OH, HO₂, O, CH₃ and CH₂O. Of these species, the steady-state assumptions introduced for OH, O, CH₃ and CH₂O are expected to primarily affect the CH₄ correlations, since these species readily interact with CH₄ through reactions 41-49 of Table 2.3. The spatial mass fraction correlations of CH₄ however in Fig. 4.4 are as high as in the laminar case, implying that CH₄ is relatively insensitive to the QSSA for the aforementioned species.

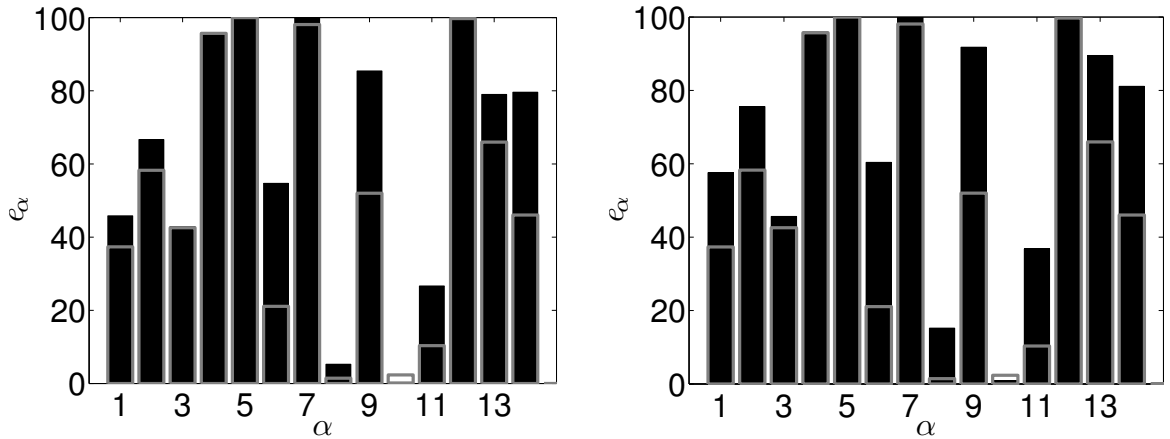


Figure 4.6: Species rate-related QSSA error e_α , for case A (left) at $t/t_{fl}=4.0$, and case B (right) at $t/t_{fl}=1.6$. Grey bars show the laminar flame result.

In order to understand how the QSSA error is affected by the turbulence,

the local error, i.e. without the global maximum operation in Eq. 4.8 can be analysed. Figures 4.7-4.9 show e_{OH} , e_{HO_2} and e_O against c for case B. These species readily react with H_2O and H_2O_2 in the majority of the reactions listed in Table 2.3, and are thus expected to influence the most the spatial correlations of these species. Also shown in grey continuous lines is the conditionally averaged QSSA error, in bins of c , and time-averaged as explained in section 4.1. The grey dashed line shows the laminar flame result to elucidate the turbulence effect. In the laminar case, the QSSA error peaks for OH at $c \simeq 0.5$, for HO_2 at $c \simeq 0.01$ and for O at $c \simeq 0.3$. The local QSSA error for the turbulent case on the other hand peaks for all of these species at much lower c values i.e. in the preheat zone of the flame. This is expected since the turbulence is stronger in the preheat zone of the flame thus affecting the most the species rates. As previously stated, the reduced mechanism was developed using PSR solutions as input to CARM, and as a result diffusion effects are not accounted for. Hence strong turbulence in the preheat zone of the flame invalidates the QSSA through enhanced turbulent diffusion. On the burnt side the QSSA error is generally less since the turbulence is weaker. In particular, the conditional error is less than the laminar flame error for $c > \simeq 0.2$ for OH and O, and for $c > \simeq 0.1$ for HO_2 . Also, for all of these species the majority of points fall below the laminar flame result which implies that QSSA holds, on average, better in the turbulent case than in the laminar case. In the following sections it is shown that the mass fraction of H_2O is over-estimated at relatively larger c values. Since the QSSA errors in the turbulent case are larger than the laminar flame for relatively lower c values, the low correlation observed for H_2O cannot be a result of the QSSA.

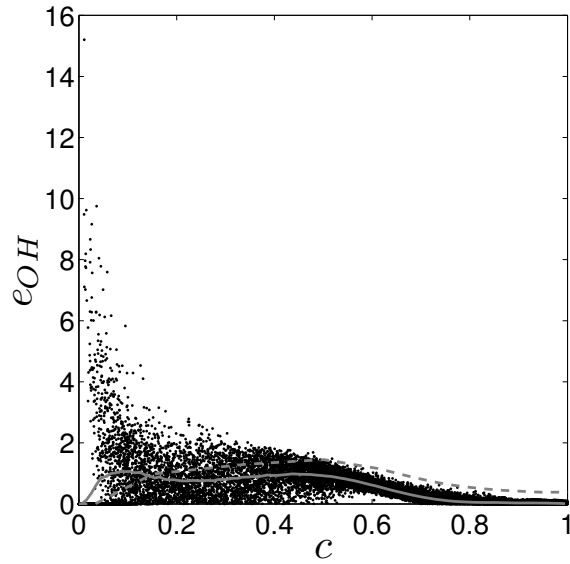


Figure 4.7: Local QSSA error for the OH radical. Grey continuous line: conditional average in bins of c , and time averaged. Grey dashed line: laminar flame result.

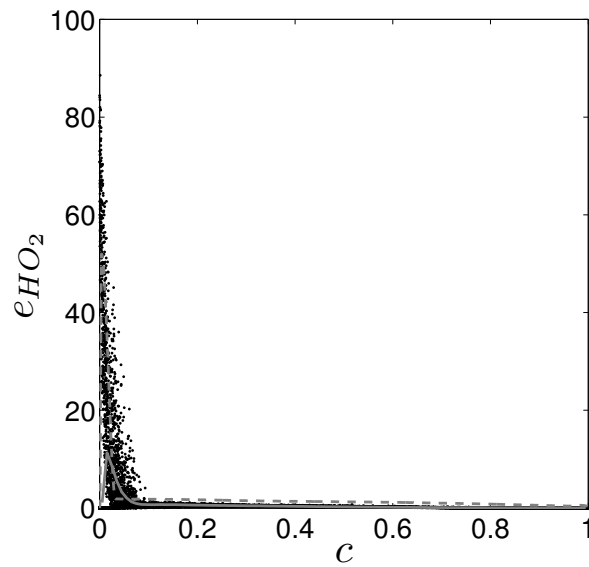


Figure 4.8: Local QSSA error for HO_2 . Grey continuous line: conditional average in bins of c , and time averaged. Grey dashed line: laminar flame result.

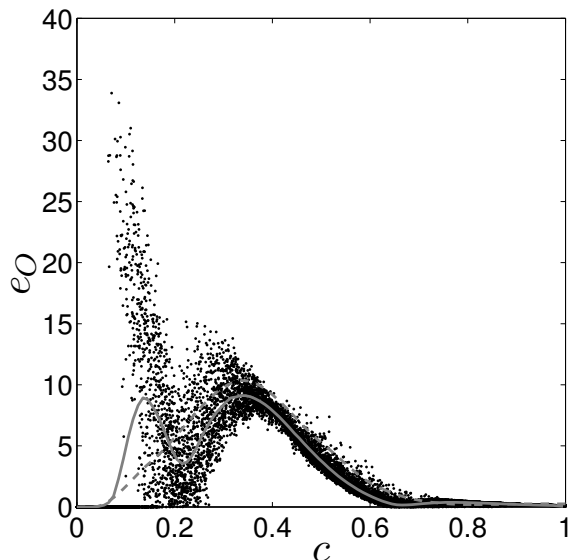


Figure 4.9: Local QSSA error for O. Grey continuous line: conditional average in bins of c , and time averaged. Grey dashed line: laminar flame result.

4.3 Comparison of mean profiles

In this section the mean profiles of important species mass fractions and net rates, heat release rate, and progress variable across the flame brush are examined, to test the performance of the 5-step reduced mechanism. The results are shown in Figs. 4.10-4.13. As noted earlier, the quantities are normalized with respect to the maximum laminar value of the skeletal mechanism. Figure 4.10 shows that the H mean mass fraction is slightly under-estimated by the reduced mechanism as one moves towards the products, and close examination of Fig. 4.12 reveals that this is owing to the slight under-estimation of the H production rate over the same region. Nevertheless, taking into account that H is a highly diffusive species, the overall agreement with the skeletal mechanism is good. The CO mean mass fraction, which is the main fuel constituent, is well captured and similar results were found for the species O_2 , CO_2 and CH_4 . The mean mass fractions of H_2O and H_2O_2 are over-estimated for both turbulence levels, and the same was observed for the mean mass fraction of H_2 , which explains the lower

spatial correlations observed for these species in the previous section. Careful examination of Fig. 4.11 reveals that H_2O and H_2O_2 are over-estimated in the unstrained laminar case also. H_2O in particular is over-estimated mainly in the product side while H_2O_2 is over-estimated across the entire flame brush. Careful examination of Fig. 4.13 reveals that the over-estimation of the H_2O mass fraction is owing to the over-estimation of its production rate in the same region. Similar arguments apply for H_2O_2 also, the only difference being that its consumption rate is instead over-estimated in the product side, which helps to explain why the reduced mechanism's estimation for the H_2O_2 mass fraction approaches that of the skeletal mechanism for large x^+ .

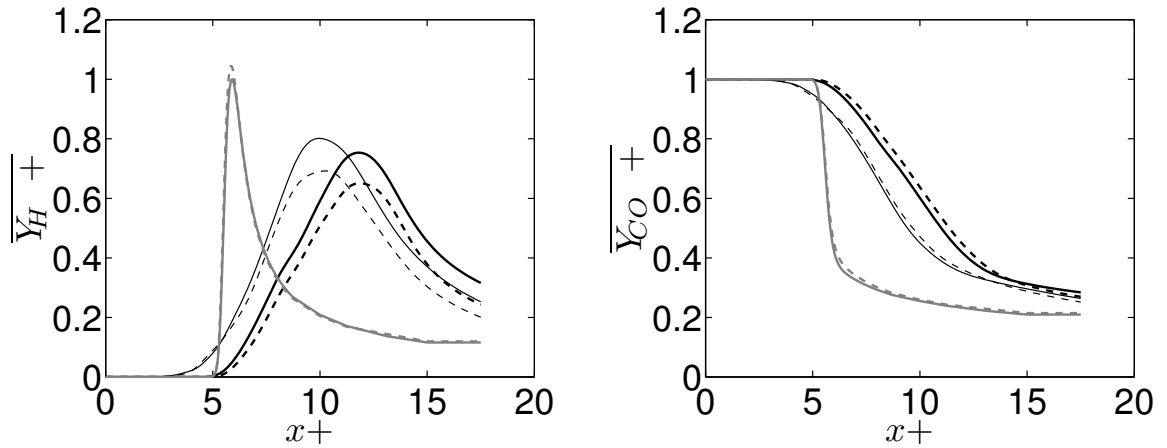


Figure 4.10: H and CO mean mass fractions. Thick lines-case A, thin lines-case B. Continuous lines-skeletal mechanism, dashed lines-reduced mechanism. Grey lines-laminar unstrained flame result.

As discussed in Chapter 2, these effects may be alleviated through the adjustment of the activation energy of one of the most dominant reactions, namely the chain-branching reaction $\text{O} + \text{H}_2 = \text{H} + \text{OH}$. Increasing the activation energy of this reaction would reduce the production rates of the OH and H radicals. This in turn would have a direct effect on the production rates and mass fractions of H_2O , H_2 , and H_2O_2 , since they readily interact with OH and H radicals. However, at the same time the flame speed would also decrease, since less OH radicals would be available for CO oxidation through the main heat releasing reaction $\text{OH} + \text{CO} = \text{H} + \text{CO}_2$. Since there is no way to pre-estimate the increase factor

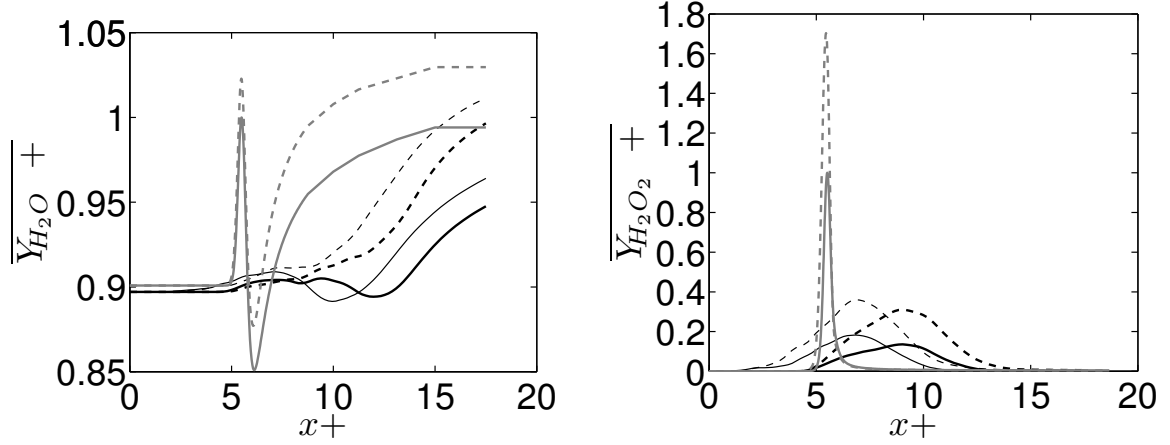


Figure 4.11: H_2O and H_2O_2 mean mass fractions. Lines as in Fig. 4.10.

for the activation energy, this has to be based on one-dimensional laminar flame data. Thus as was indicated in [38], an increase of the activation energy of the reaction $\text{O} + \text{H}_2 = \text{H} + \text{OH}$ by 27.5%, reproduces the correct flame speed despite the small over-estimation of the aforementioned species mass fractions. Furthermore, species such as CO_2 (not shown here) relating to atmospheric pollution are estimated with excellent accuracy. Also, despite the discrepancies observed for the mean mass fractions of H_2O and H_2O_2 , as one may see from Fig. 4.14 the reduced mechanism captures very well the mean progress variable and heat release rate variation across the entire flame brush. For both turbulence levels the reduced mechanism predicts the heat release rate to drop and spread out due to flame thickening and consistent with the laminar flame result, the maximum heat release rate occurs around $\bar{c}=0.32$ also.

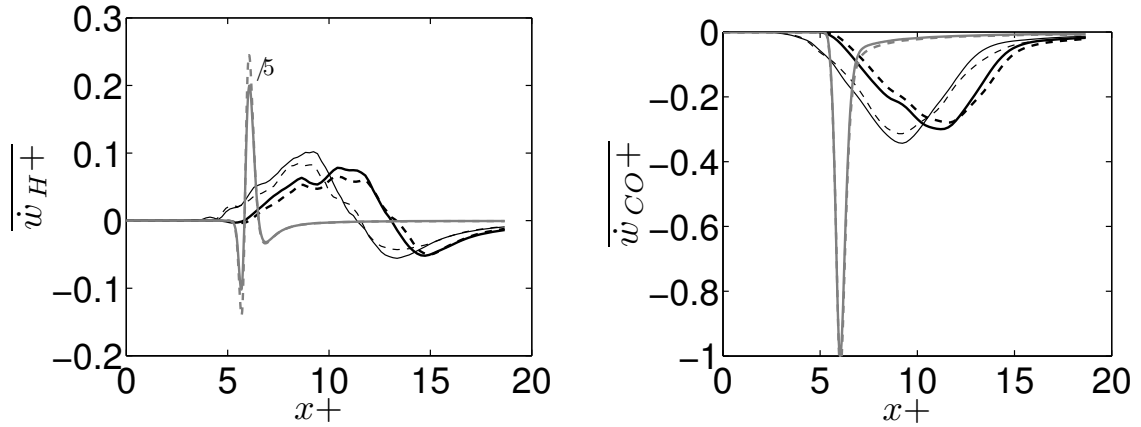


Figure 4.12: H and CO mean net rates. Lines as in Fig. 4.10.

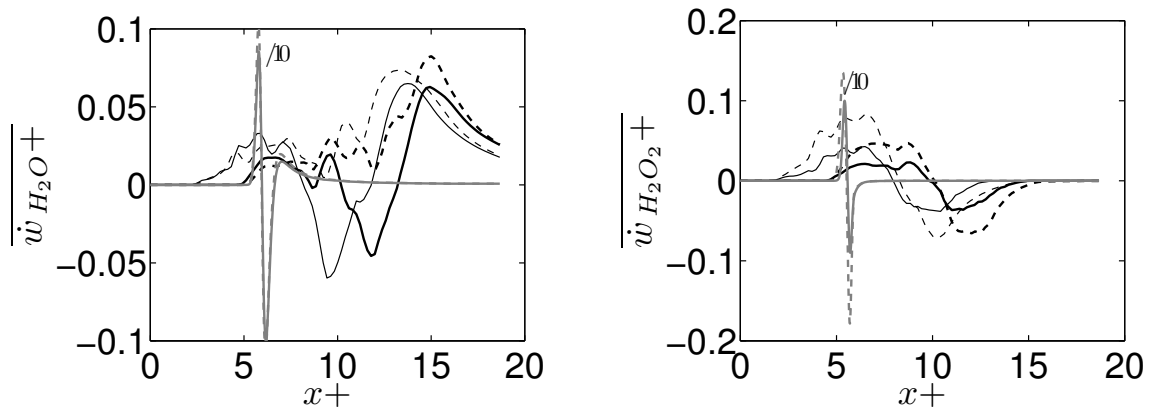


Figure 4.13: H_2O and H_2O_2 mean net rates. Lines as in Fig. 4.10.

4.4 Comparison of flame front structure

The 5-step reduced mechanism was found in the previous section to give an overall good agreement with the majority of species mass fractions and heat release rate in the mean sense. From a modelling point of view though one would use the reduced mechanism DNS data not only to save computational time but also to develop combustion sub-models many of which are based on the flamelet

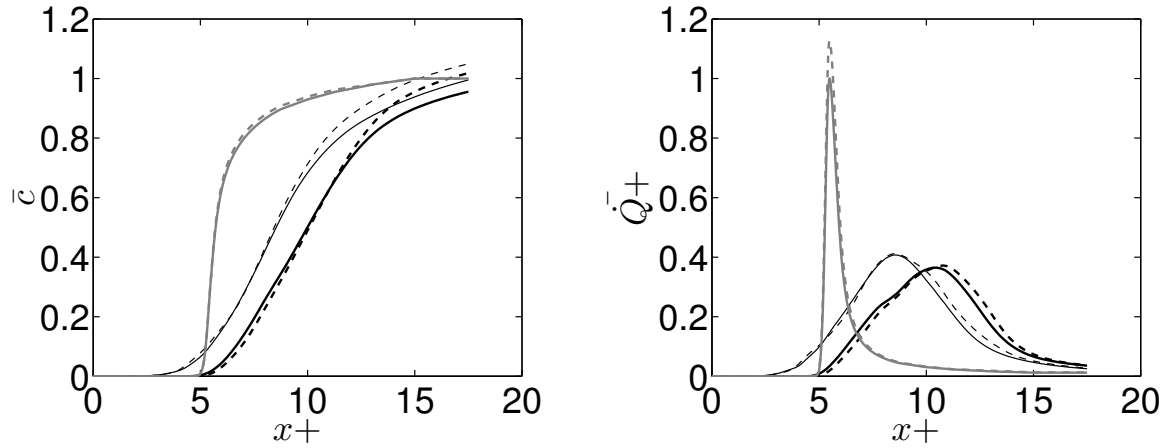


Figure 4.14: Mean progress variable and mean heat release rate against normalized distance. Lines as in Fig. 4.10.

assumption. The conditional average of a quantity with respect to c gives an estimate of the flamelet nature of the flame. Thus in this section we test whether the reduced mechanism is able to reproduce the statistics across the flame brush for the conditionally averaged values obtained for the skeletal mechanism.

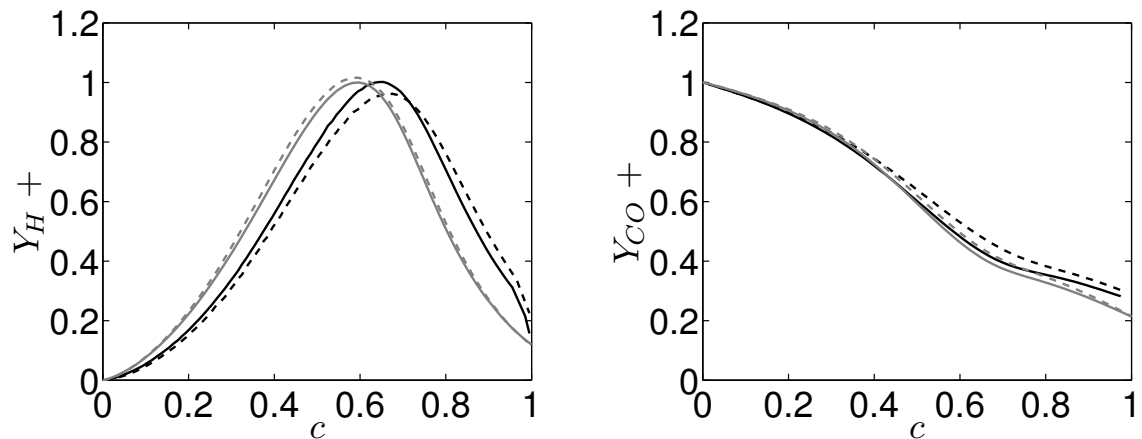


Figure 4.15: H and CO mass fractions conditionally averaged in bins of c , and time-averaged for case B, using the skeletal (black continuous lines) and the reduced (dashed continuous lines) mechanisms. Grey lines show the laminar unstrained flame result.

Figures 4.15-4.18 show conditional averages in bins of c for the species mass fractions and heat release rate for the highest turbulence level i.e. case B. Similar

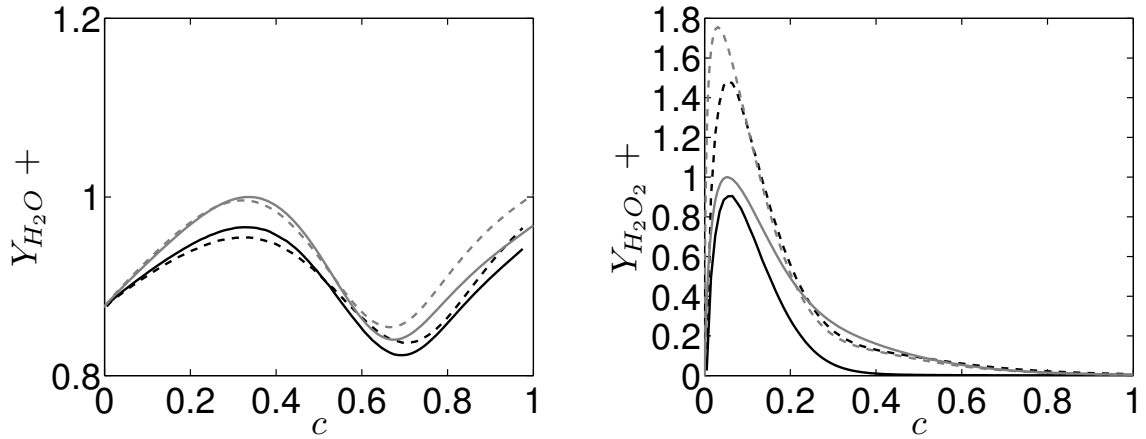


Figure 4.16: H_2O and H_2O_2 mass fractions conditionally averaged in bins of c , and time-averaged for case B. Lines as in Fig. 4.15.

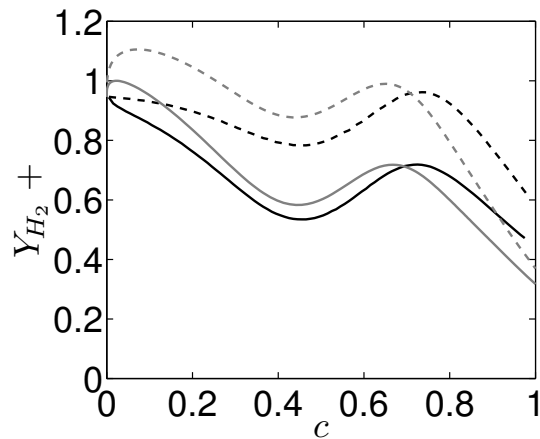


Figure 4.17: H_2 mass fraction conditionally averaged in bins of c , and time-averaged for case B. Lines as in Fig. 4.15.

results were obtained for case A. The continuous black lines show the results using the skeletal mechanism, and the dashed black lines show the results using the reduced mechanism. Also shown in grey is the laminar flame result which helps to elucidate the effect of the turbulence. Figure 4.15 shows that the conditionally averaged mass fractions of H and CO are well captured by the reduced mechanism and a similar good agreement was also found for the conditional averages of O_2 , CO_2 and CH_4 . These results imply that the distribution of the aforemen-

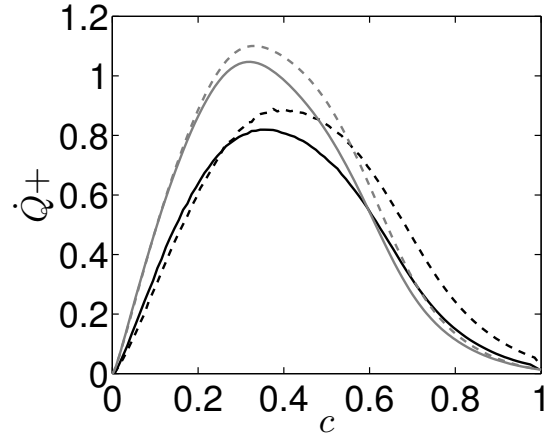


Figure 4.18: Heat release rate conditionally averaged in bins of c , and time-averaged for case B. Lines as in Fig. 4.15.

tioned species over the temperature field calculated with the reduced mechanism is similar to that using the skeletal mechanism. Figure 4.16 shows that the conditional average of the H_2O mass fraction is estimated equally well as the H mass fraction. Nevertheless, for high c which are expected to occur for large x , the conditionally averaged mass fraction of H_2O is slightly over-estimated. This happens both for the laminar and the turbulent cases which explains the associated over-estimation of its mean spatial value for large x . Careful examination of the reactions involving H_2O shows that one of the most important reactions affecting H_2O concentration is the reaction $\text{OH} + \text{H}_2 = \text{H} + \text{H}_2\text{O}$. Furthermore, this reaction was found to become more important as one moves towards the products side and actually produces H_2O for large c [38, 39, 40, 121].

Figure 4.17 shows that the conditionally averaged mass fraction of H_2 is also over-estimated, and for all c even in the laminar case. Both the H_2O and the H_2 over-estimation for the laminar flame are interlinked: the reaction $\text{O} + \text{H}_2 = \text{H} + \text{OH}$ affects the H_2 concentration significantly and throughout the flame brush. The QSSA for O and OH, causes higher reverse rates through this step, reducing the H_2 consumption, and increasing its concentration throughout. At the same time, the QSSA combined with the higher levels of H_2 enhances the forward rate of the reaction $\text{OH} + \text{H}_2 = \text{H} + \text{H}_2\text{O}$ at large c , producing more

H_2O , and causing an over-estimation in its concentration in this region. However, as explained in section 4.2, despite this fact the correlations in the laminar flame remain high. Furthermore, the H_2O over-estimation occurs at large c and as shown in section 4.2 the QSSA (for the species expected to affect the most the H_2O concentration) in the turbulent case, holds on average better in this region than in the laminar flame. Hence the lower spatial correlations for H_2O observed in Fig. 4.4 in the turbulent case, are owing primarily to the different scalar-turbulence interaction rather than failure of the QSSA.

Figure 4.16 also shows the conditional average of H_2O_2 , which in comparison to H_2O peaks at lower c values. This explains the much lower spatial correlations observed for H_2O_2 in Figs. 4.4 and 4.5, since this species exhibits strong mass fraction gradients in a more intense turbulence region. As previously stated, the QSSA errors also peak in the preheat zone of the flame. One would therefore expect perhaps the H_2O_2 over-estimation seen in Fig. 4.16 to be associated with failure of the QSSA. However, when compared to the laminar flame result, the over-estimation using the reduced mechanism, for the turbulent case at low c is approximately of the same magnitude, implying that it is not a result of the QSSA. Another important observation which may help to justify the above point is the following: for $c \gtrsim 0.2$ where the H_2O_2 gradients (and hence diffusive effects) are high, the difference with the skeletal mechanism result is small for the laminar case but large for the turbulent case. Figures 4.7-4.9 show that for $c \gtrsim 0.2$ the conditionally averaged QSSA error for OH, HO_2 and O is lower than for the laminar case. As a result, the over-estimation of the H_2O_2 mass fraction using the reduced mechanism, in this regime, cannot be attributed to the failure of the QSSA.

Figure 4.18 shows the conditionally averaged heat release rate. For small c the 5-step reduced mechanism gives a good agreement with the skeletal mechanism while for large c the reduced mechanism slightly over-estimates the conditionally averaged heat release rate. This is consistent with the slightly higher maximum heat release rate values observed in Fig. 4.3. Since most of the heat release comes from the enthalpy of formation of H_2O whose mass fraction as previously discussed is over-estimated for large c , this causes the associated slight over-estimation of the heat release rate in the same region. Nevertheless, in the section which follows

it is shown that the correct flame surface statistics are recovered in the case of the reduced mechanism.

4.5 Comparison of flame surface statistics

Figures 4.19-4.21 show the pdfs of the displacement speed, flame stretch and generalized FSD. These quantities are obtained on the $c^*=0.32$ iso-surface where the heat release rate peaks in the laminar flame. The pdfs of curvature and tangential strain rate using the reduced mechanism were indistinguishable with the skeletal mechanism results and thus they are not shown here. As one may see from Fig. 4.19 the reduced mechanism produces almost identical displacement speed pdfs with the skeletal mechanism both for the low and high turbulence levels. This implies that the flame structure computed using the reduced mechanism has the same dependency on strain and curvature effects as with that computed using the skeletal mechanism. Thus the flame stretch is also almost identical for the reduced and skeletal mechanisms as one can observe in the flame stretch pdf shown in Fig. 4.20. The generalized FSD pdf shown in Fig. 4.21 suggests some differences. The generalized FSD from the calculation using the reduced mechanism has a higher mean value for both turbulence levels. Since $\Sigma=\chi=\sqrt{(\partial c/\partial x_i)(\partial c/\partial x_i)}$, it is a measure of the flame brush thickness and thus the reduced mechanism has a slightly smaller flame brush. The reduced mechanism is thus less sensitive to the turbulence, a result consistent with previous studies [20, 21, 122]. The quantitative difference however is found to be small (less than 12%).

Figure 4.22 shows scatter plots for the heat release rate and displacement speed against curvature for case B. Similar results were observed for case A. The black dots show the skeletal mechanism results and the grey dots show the reduced mechanism results. For both turbulence levels the correct physical behaviour is recovered by the reduced mechanism i.e. heat release rate and displacement speed correlate strongly with curvature with peak values reached in negatively curved regions. In regions of positive curvature the results for both mechanisms are found to be nearly identical. For negative values of curvature the reduced mechanism slightly over-estimates the maximum heat release rate and

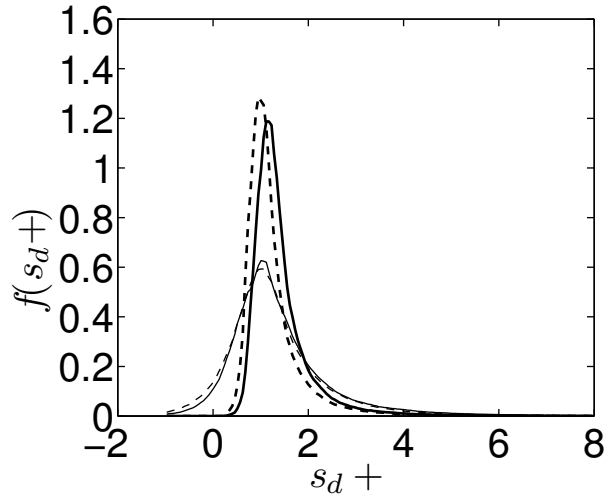


Figure 4.19: Surface displacement speed pdfs. Thick lines-case A, thin lines-case B. Continuous lines-skeletal mechanism, dashed lines-reduced mechanism.

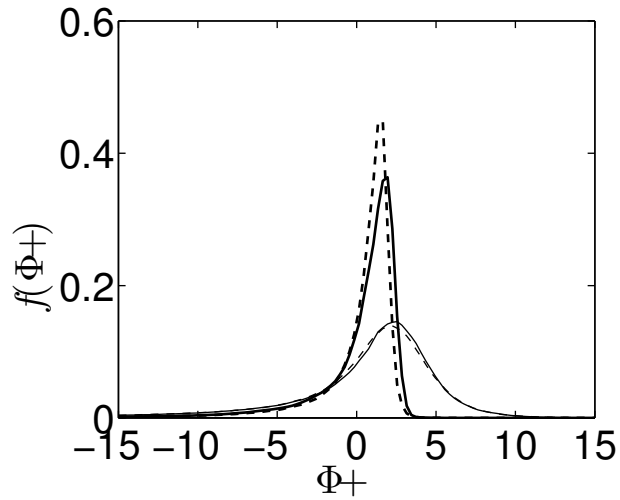


Figure 4.20: Surface stretch rate pdf. Lines as in Fig. 4.19.

the displacement speed, which is consistent with the slightly higher heat release rates observed in Figs. 4.2 and 4.3. Figure 4.23 shows the corresponding scatter plots for the tangential strain rate. Although some correlation is observed for the heat release rate, with generally positively strained regions showing a higher heat release rate, the influence of curvature is much more dominant. In the case of

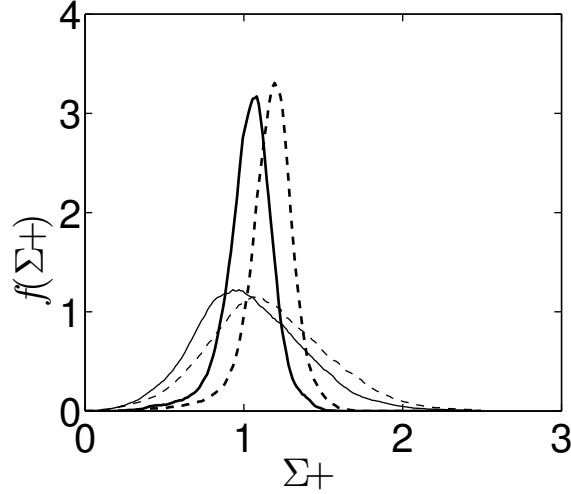


Figure 4.21: Surface generalized FSD ($=\chi$) pdf. Lines as in Fig. 4.19.

the displacement speed the correlation with the strain rate is not as strong as for the heat release rate. The displacement speed is observed to reach a maximum for a positive value of strain rate. For large strain rates the displacement speed drops down to the laminar flame speed, and shows the same dependence as for negatively strained regions.

All of these effects are well captured by the reduced mechanism for both turbulence levels, indicating that it is an acceptable substitute for the skeletal mechanism. However, one should bear in mind that the results of this study are specific to the turbulence and mixture conditions tested here, i.e. a premixed flame at a maximum turbulence level $u_{rms,in}/s_l$ of 9.0. For the lower turbulence level case considered in this study, the reduced mechanism is shown to perform better. Therefore one would expect the reduced mechanism to perform better for larger Da numbers and poorer for lower Da numbers. Since the QSS assumptions hold better in the PSR limit where the reduced mechanism was developed from, it is expected that there is a regime between the PSR limit and the flamelet limit of combustion where this mechanism may not perform equally well. Thus, further DNS at higher turbulence levels is required to establish the upper limit of applicability of the reduced mechanism. Although without such DNS results to establish this upper limit, the Da number for case B is 1.85. Thus, one would

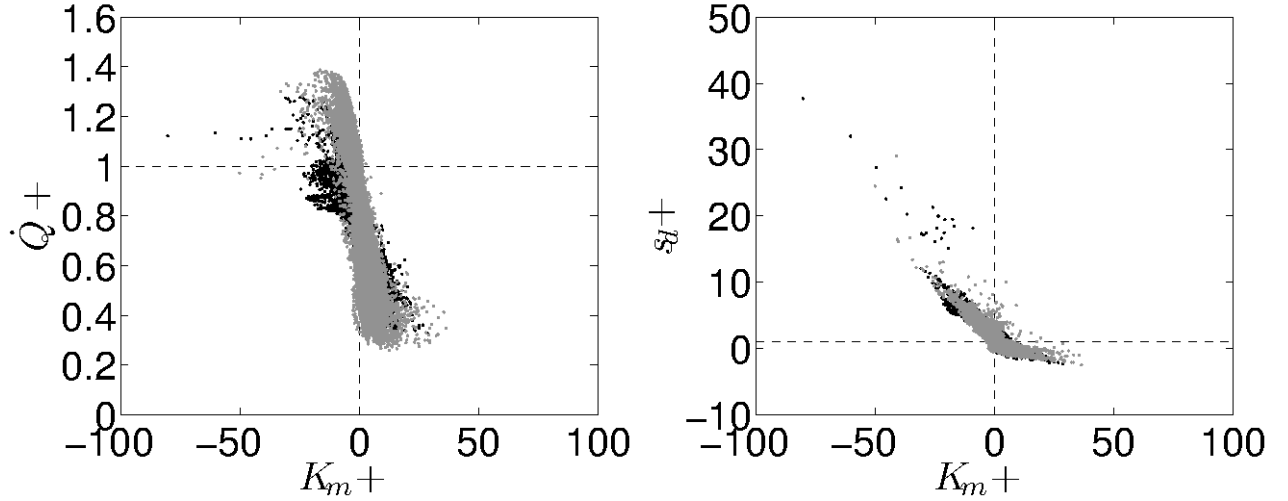


Figure 4.22: Scatter plots of normalized heat release rate and displacement speed against normalized surface curvature using the skeletal (black dots) and reduced (grey dots) mechanisms, for case B at $t/t_{fl}=1.6$.

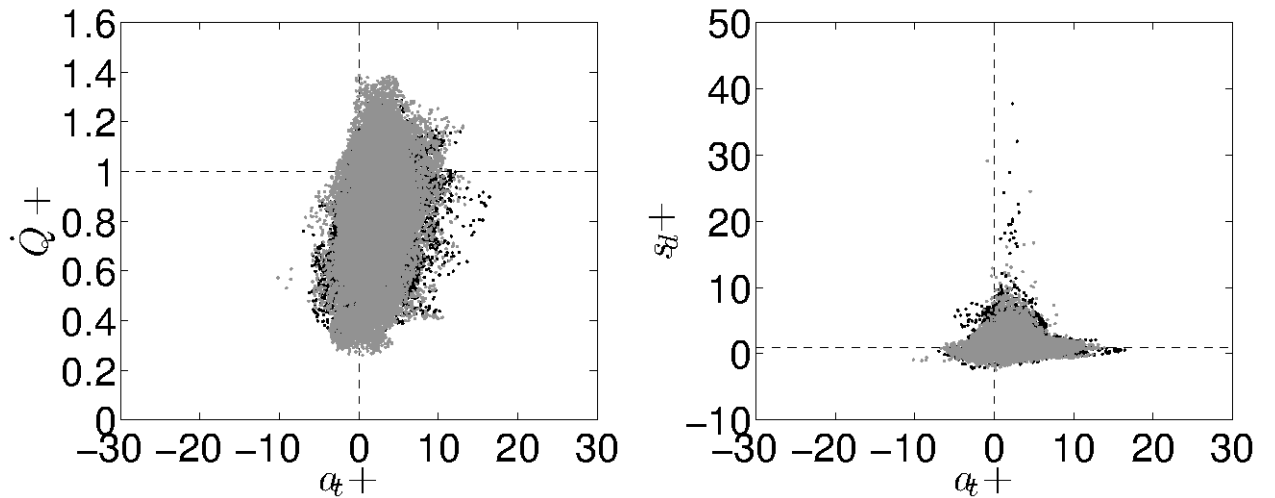


Figure 4.23: Scatter plots of normalized heat release rate and displacement speed against normalized surface tangential strain rate using the skeletal (black dots) and reduced (grey dots) mechanisms, for case B at $t/t_{fl}=1.6$.

expect the reduced mechanism not to perform as well once $Da < 1$ because the heat release zone will be heavily influenced by the turbulence. Additional DNS in non-premixed combustion with extinction and re-ignition, would be useful in

evaluating the performance of the reduced mechanism over a broader range of conditions.

Chapter 5

Flame structure of multi-component fuel flame

In this chapter, the DNS data of the low and high turbulence cases i.e. cases A and C in Table 5.1, using the skeletal mechanism derived in Chapter 2, are used to examine the flame structure of the multi-component fuel flame. Furthermore, the validity of the rate of the reaction $\text{OH} + \text{CH}_2\text{O} = \text{HCO} + \text{H}_2\text{O}$ which is commonly used in laser diagnostics for heat release rate imaging, is assessed for the multi-component flame.

5.1 Laminar flame structure

In order to understand how the multi-component fuel flame differs from the typical methane and hydrogen flames, unstrained premixed laminar flame computations have been performed for all of the three mixtures. The computations have been performed using the PREMIX code of the CHEMKIN package [96, 97] with GRI-3.0 [73]. All of these computations have been performed at the same thermo-chemical conditions as for the DNS i.e. $T_r=800$ K, $p=1$ atm and $\phi=1.0$, and a mixture-averaged formulation is used for the species' diffusivities. It has to be emphasized here that under these conditions the flame speeds of the multi-component and of the methane flames are almost the same (2.47 ms^{-1} for the multi-component flame and 2.48 ms^{-1} for the methane flame), while the flame

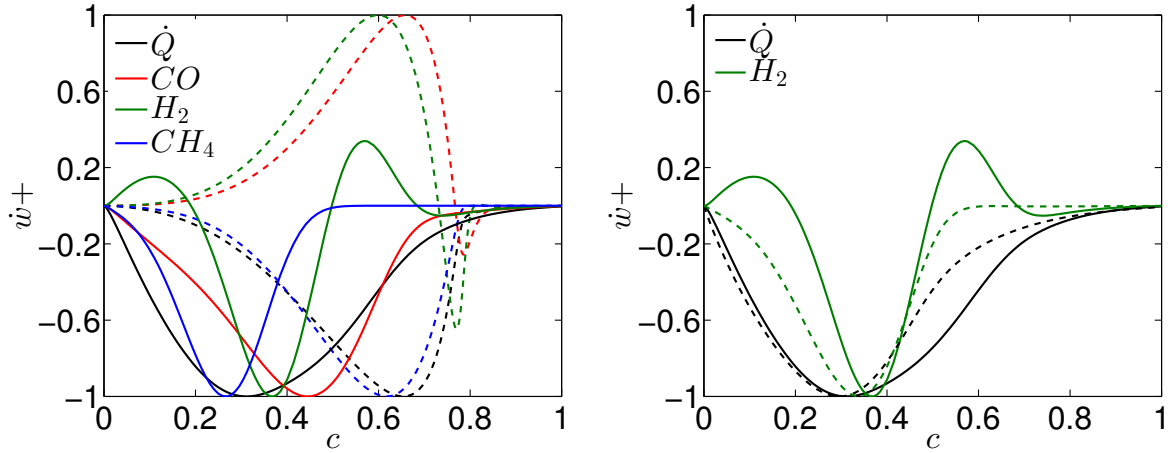


Figure 5.1: Heat release and main species normalized reaction rates comparison. Continuous lines: stoichiometric multi-component flame, dashed lines: stoichiometric methane flame (left) and stoichiometric hydrogen flame (right).

speed of the hydrogen-air flame is significantly larger (14.2 ms^{-1}).

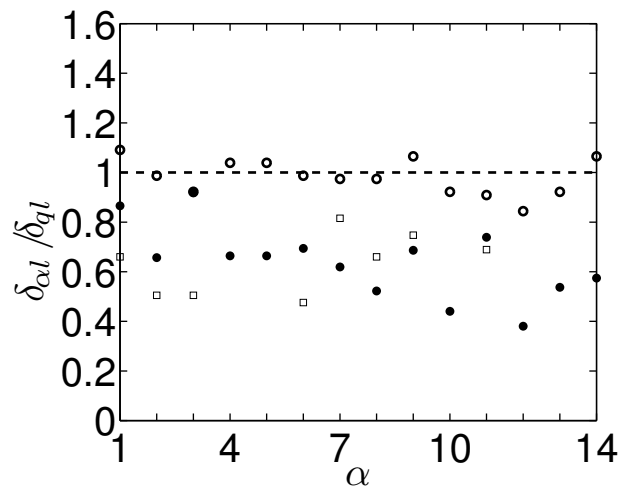


Figure 5.2: Species reaction zone thickness normalized by the heat release zone thickness. Index α as in Table 3.1. Filled circles: multi-component flame. Open circles: methane flame. Squares: hydrogen flame. Due care is required in DNS to ensure that the minimum species reaction zone thickness is well resolved.

Figure 5.1 shows a comparison between the main fuel species net rates and

the heat release rate in each flame. The symbol + indicates quantities normalized with respect to their maximum laminar values. The species' net rates are superimposed in the same plot as the heat release rate, for all mixtures, in order to highlight important differences. Here the progress variable is based on temperature i.e. $c=(T - T_r)/(T_p - T_r)$ (for reasons that will become apparent later). Some very distinct differences are observed between the multi-component fuel flame and the methane flame. The maximum heat release rate for the methane flame occurs around $c=0.68$, whereas for the multi-component fuel flame it is around $c=0.3$. A similar trend is observed for the hydrogen flame shown in Fig. 5.1 on the right. Defining the heat release zone thickness, δ_{ql} , as the spatial distance over which the heat release drops to 5% of its maximum value on either side, then for the multi-component fuel flame $\delta_{ql}=10.8$ mm, for the methane flame $\delta_{ql}=5.3$ mm, and for the hydrogen flame $\delta_{ql}=4.9$ mm. Thus, the heat release zone of the multi-component fuel flame is much broader than either the methane or hydrogen flames giving an overall thicker flame. For the methane flame the net reaction rates of CO, H₂ and CH₄ are found to coincide with the heat release zone and to have approximately the same width. For the multi-component fuel flame on the other hand, there are clearly distinct reaction zones: CH₄ consumption peaks first, close but earlier than peak heat release, followed by peak H₂ consumption again close but later than peak heat release, while peak CO consumption comes last and much later than the peak heat release. H₂ on the other hand is consumed across all c for the hydrogen flame as one would expect, but in the multi-component fuel flame there is a production around $c=0.1$ and around $c=0.6$.

Another important point is that the reaction zone width of each species in the multi-component fuel flame is different. In order to quantify this more clearly, the species reaction zone thickness, δ_{al} , and the heat release thickness are calculated and are shown in Fig. 5.2. δ_{al} is defined as the thickness over which the respective reaction rate falls to 5% of its maximum value on either side of the flame. As one can see from Fig.5.2, all the major species in the methane flame have a reaction zone thickness almost equal to the heat release thickness. This is in contrast to the multi-component fuel and hydrogen flames, where the majority of species are found to have a much smaller reaction zone thickness than the heat release

thickness. For the multi-component fuel flame, CH₄ has the smallest reaction zone thickness which is less than half of the heat release thickness. H₂O on the other hand has the thickest reaction zone for both the methane and multi-component flames. Thus it is clear that in such DNS studies, due care has to be taken in order to ensure that there are enough points to capture the minimum reaction zone thickness.

Figure 5.3 shows different progress variable definitions based on fuel species mass fractions, plotted against c . In particular, $c_{CO}=(Y_{CO,r} - Y_{CO})/(Y_{CO,r} - Y_{CO,p})$, $c_{CH_4}=(Y_{CH_4,r} - Y_{CH_4})/(Y_{CH_4,r} - Y_{CH_4,p})$, and $c_{H_2}=(Y_{H_2,r} - Y_{H_2})/(Y_{H_2,r} - Y_{H_2,p})$. Continuous lines indicate progress variable definitions for the multi-component fuel flame while the green dashed line indicates the progress variable definition c_{CH_4} for the methane flame, and the dashed blue line indicates c_{H_2} for the hydrogen flame. Consistent with the results depicted in Figs. 5.1 and 5.2, CH₄ is consumed early on at relatively low temperatures resulting in a sharp increase in c_{CH_4} both for the multi-component and methane flames. The difference is that by about $c=0.4$, all the methane has been consumed in the multi-component flame in contrast with the methane flame where CH₄ consumption is complete later on at around $c=0.8$.

The consumption of CO is slower and is enhanced after CH₄ consumption is complete. c_{H_2} shows a non-monotonic behaviour: for low c increased production causes a higher H₂ value, resulting in negative c_{H_2} . Careful examination of the H₂-related reactions, revealed the dominant reactions to be: 2, 3, 12, 44, 47 and 48 given in Table 2.3. Of these, reaction 2 is the only H₂-consuming reaction across the flame brush. The CH₄-related reactions 44, 47 and 48 produce H₂ through the consumption of methane in the preheat zone of the flame, which explains the positive production rate observed in Fig. 5.1 around $c=0.1$. Reaction 3 however has a double nature: in the preheat zone of the flame its net rate is positive thus consuming H₂, while in the product zone its net rate is negative which produces H₂. This is because across the flame H₂ is overall consumed and its concentration drops, allowing the reverse rate of reaction 3 to overcome the forward rate [38, 40]. Hence the observed slight increase in H₂ concentration around $c=0.6$ and the corresponding slight drop in H₂O concentration. Careful examination of the reaction set in Table 2.3, reveals that CH₄ consumption occurs

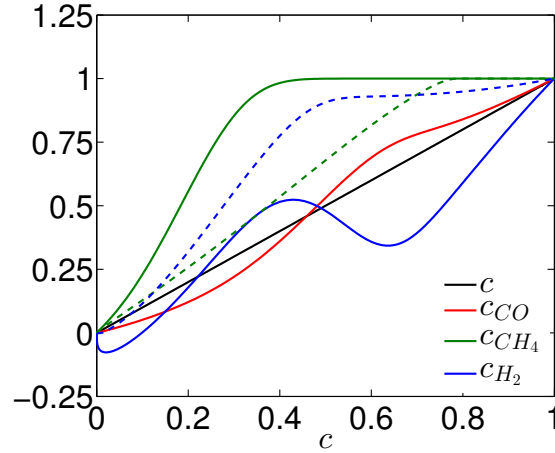


Figure 5.3: Different progress variables definitions against c based on temperature. Continuous lines: multi-component flame. Green dashed line: methane flame c_{CH_4} . Blue dashed line: hydrogen flame c_{H_2} .

through reactions 41, 42 and 47. Of these, the reaction $\text{OH} + \text{CH}_4 = \text{CH}_3 + \text{H}_2\text{O}$ has the lowest activation energy and is found to have the highest net rate at lower temperatures. This is primarily a result of the increased OH radical production rate through the reaction $2\text{OH} = \text{O} + \text{H}_2\text{O}$ due to the presence of water vapour in the reactant mixture [38, 39, 40]. These two mechanisms make the reaction $\text{OH} + \text{CH}_4 = \text{CH}_3 + \text{H}_2\text{O}$ the major CH_4 consumption pathway at low temperatures, thus resulting in a sharp increase in c_{CH_4} in the preheat zone of the flame. This is not the case in a pure methane flame, where OH radicals can come only through the direct decomposition of CH_4 and O_2 thus requiring relatively higher temperatures. The above also help to explain the sharp increase in c_{CO} once CH_4 consumption is complete: the major CO consumption pathway is the reaction $\text{OH} + \text{CO} = \text{H} + \text{CO}_2$ [38, 39, 40]. Thus once CH_4 consumption is complete at about $c = 0.4$, more OH radicals are available for CO oxidation through the above reaction, resulting in a sudden increase in c_{CO} as one may see from Fig. 5.3.

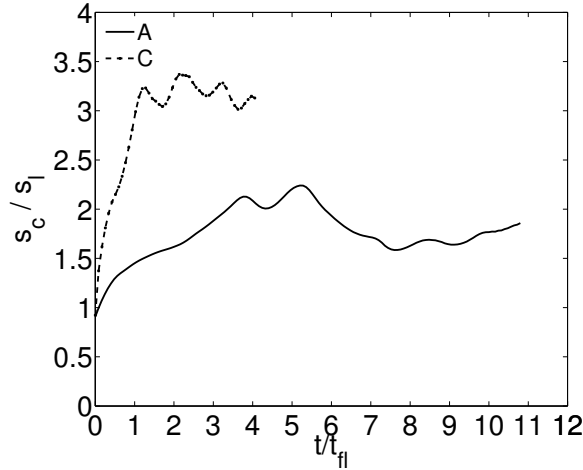


Figure 5.4: Consumption speeds for the two turbulence levels.

5.2 Turbulent flame speed

Figure 5.4 shows the evolution of s_c/s_l for the two cases, and the time is normalized by the flame time t_{fl} which is common for both cases. Initially, s_c is approximately equal to the laminar flame speed for both cases. After about one flame time, the flame reaches a quasi-steady state for case C and almost remains there for up to 4 flame times when the simulation is stopped. Case A on the other hand shows a slower evolution: the consumption speed keeps increasing up to about 3 flame times and remains in a more or less quasi-steady state up to about 5 flame times. After 5 flame times the consumption speed drops as the flame is observed to slowly start moving out of the computational domain.

For case A, time averaging is performed between 3.52 and 5.6 flame times, and for case C time averaging is performed between 1.0 and 3.0 flame times as per the results in Fig. 5.4. During these two intervals the flames in both cases seem to be in a quasi-steady state at least as far as s_c is concerned. Conditional averages to be discussed later, are taken over the entire volume in bins of c , and time-averaged over the above time intervals.

5.3 Turbulent kinetic energy spatial profile

As discussed in Chapter 2 turbulence decays with downstream distance x . The Favre-averaged kinetic energy, \tilde{k} , decay rate is shown for cases A and C in Fig. 5.5. \tilde{k} is time-averaged as explained in the previous section and normalised by its value at the inlet boundary. The leading flame front locations in the two cases corresponding to $\tilde{c}=0.05$, are also marked in Fig. 5.5. Although the flame-brush introduces anisotropy and inhomogeneity, the decay of \tilde{k} follows a power law with an exponent of $n = -1.46$ for case A and $n = -1.52$ for case C and, these values of n are close to experimental values observed for (non-reacting) grid turbulence [123, 124]. This occurs up to about $\tilde{c}=0.05$, after which the linear relation is somewhat distorted as a result of flow dilatation due to the heat release.

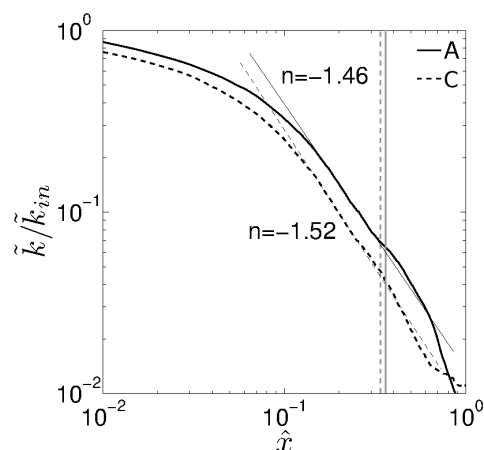


Figure 5.5: The variation of normalised \tilde{k} with $\hat{x}=x/L_x$. The mean leading flame front position is marked using vertical lines corresponding to $\tilde{c} = 0.05$ in the respective cases.

Figure 5.6 shows u_{rms} against distance x . Also shown is the location of the $\tilde{c}=0.05$ surface indicating the mean position of the leading edge of the flame during the statistically quasi-steady-state. Since turbulence is decaying, the leading edge of the flame interacts, on average, with a weaker turbulence than at the inlet. Table 5.1 also gives the turbulence parameters at $\tilde{c}=0.05$. Figure 5.7 shows the location of these conditions in the combustion diagram along with their

Case	u_{rms}/s_l	l_{int}/δ	Re_t	Da	Ka
A, inlet	3.18	16.54	52.66	5.19	1.39
A, $\tilde{c}=0.05$	0.76	17.41	13.25	22.85	0.16
C, inlet	14.04	16.43	230.69	1.17	12.97
C, $\tilde{c}=0.05$	2.87	36.81	105.61	12.82	0.80

Table 5.1: Comparison of the turbulent flame parameters for the DNS at the inlet and at the mean leading flame front position ($\tilde{c}=0.05$).

corresponding location when δ_l is used for normalization instead of δ . When δ ($=\nu_r/s_l$) is used for normalization, the corresponding Re, Da and Ka relations are given by:

$$\frac{u_{rms}}{s_l} = Re \left(\frac{l_{int}}{\delta} \right)^{-1} \quad (5.1)$$

$$\frac{u_{rms}}{s_l} = Da^{-1} \left(\frac{l_{int}}{\delta} \right) \quad (5.2)$$

$$\frac{u_{rms}}{s_l} = Ka^{2/3} \left(\frac{l_{int}}{\delta} \right)^{1/3} \quad (5.3)$$

When on the other hand the laminar flame thickness δ_l is used for normalization the corresponding Re, Da_l and Ka_l relations are given by:

$$\frac{u_{rms}}{s_l} = Re \left(\frac{l_{int}}{\delta_l} \right)^{-1} \left(\frac{\delta}{\delta_l} \right) \quad (5.4)$$

$$\frac{u_{rms}}{s_l} = Da_l^{-1} \left(\frac{l_{int}}{\delta_l} \right) \quad (5.5)$$

$$\frac{u_{rms}}{s_l} = Ka_l^{2/3} \left(\frac{l_{int}}{\delta_l} \right)^{1/3} \left(\frac{\delta}{\delta_l} \right)^{1/3} \quad (5.6)$$

Hence it is clear that the Ka and Re numbers lines change. These lines change by a factor of $(\delta/\delta_l)^{1/3}$ and by (δ/δ_l) for Ka and Re respectively. The Da number line however remains unchanged as the corresponding equations suggest. Also shown is the mean trajectory from the inlet up to the leading edge of the flame i.e. at $\tilde{c}=0.05$. Consistent with the values given in Table 5.1, at $\tilde{c}=0.05$ the Da

number increases to 22.85 for case A and to 12.82 for case C. The Ka on the other hand decreases for both cases to less than 1 values.

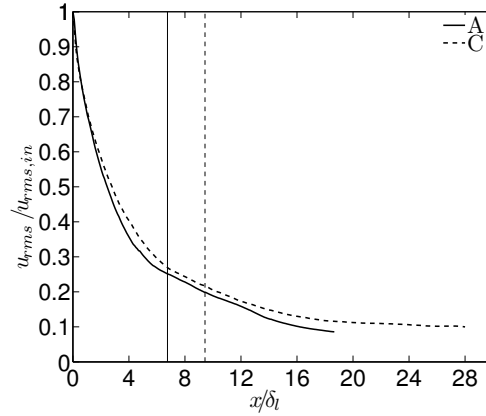


Figure 5.6: Variation of u_{rms} normalized using its value at the inlet across the flame brush for cases A and C. Vertical lines show the location of the leading flame front ($\tilde{c}=0.05$).

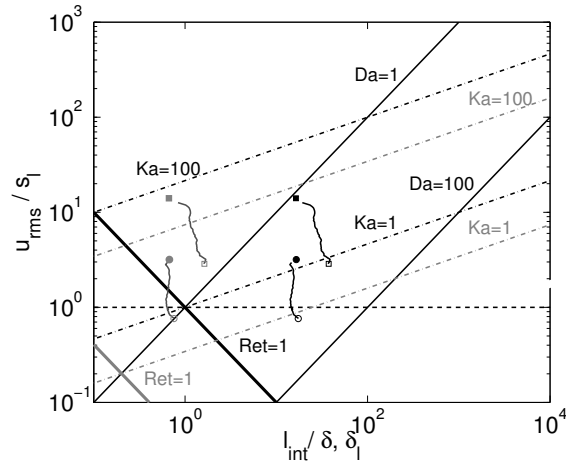


Figure 5.7: The combustion diagram. Circles: case A. Squares: case C. Black symbols/lines indicate location using δ , and grey symbols/lines using δ_l (note that the Da number lines remain unchanged). Filled symbols show turbulence parameters at the inlet and open symbols at the leading flame front ($\tilde{c}=0.05$).

5.4 Turbulent flame structure

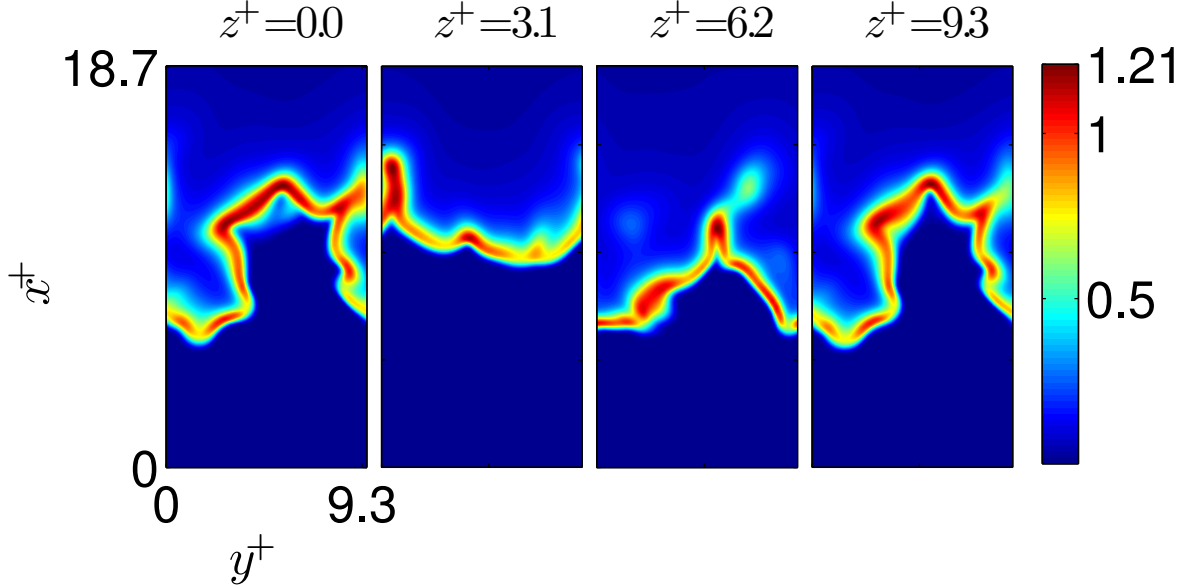


Figure 5.8: Heat release rate contours $\dot{Q}/\max(\dot{Q}_{lam})$ for case A at $t/t_{fl}=4.0$.

Figures 5.8, 5.9 and 5.10 show for cases A and C respectively instantaneous heat release rate contours, $\dot{Q}/\max(\dot{Q}_{lam})$, taken at different z^+ locations in x - y planes. The distance is normalized using δ_l . For case A the flame structure shown in Fig. 5.8 resembles that of a laminar flame wrinkled by the large-scale turbulence, with localized thickening and thinning of the flame front. Furthermore, the heat release along the flame surface is observed to vary significantly reaching values around 20% higher than the laminar flame, and a similar trend was observed at different times during the statistically quasi-steady state. For case C the heat release rate field is much different and more erratic: there is not any more a continuous flame surface, but rather localized pockets of hot spots surrounded by regions of less intense heat release, as one can see from Fig. 5.9. There is excessive diffusion and local break up of the heat release surface, primarily resulting from flame-flame interactions, allowing occasional movement of reactants into the product zone which form local hot spots behind the “main” reaction zone, as one may see from the second frame of Fig. 5.10. At the same

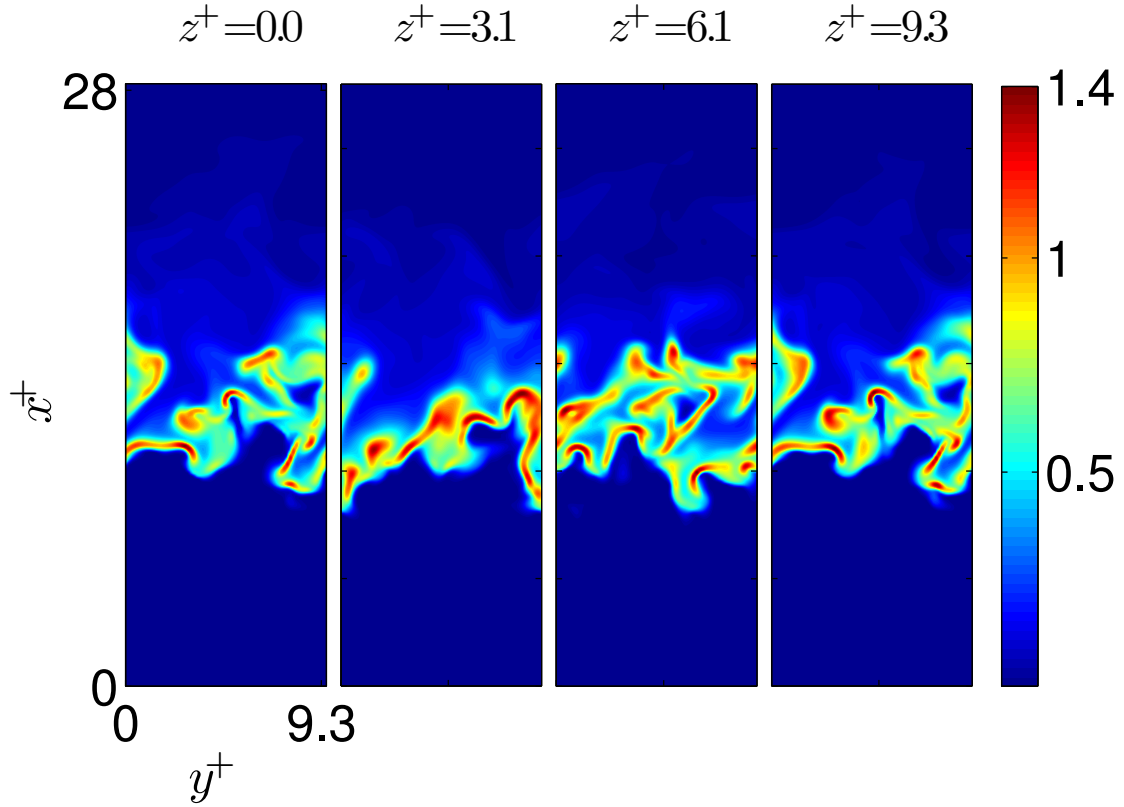


Figure 5.9: Heat release rate contours $\dot{Q}/\max(\dot{Q}_{lam})$ for case C at $t/t_{fl}=1.0$

time, there are regions of high positive curvature (convex to reactant side), trying to move into the reactants (second frame of Fig. 5.10) which finally break apart due to excessive conductive heat losses. Nevertheless, it is found that the heat release is maximised in negatively curved regions for both cases, consistent with previous studies of methane-air [125] and hydrogen-air [25] combustion.

In comparison, in the study of Tanahashi et al. [126] a stoichiometric hydrogen flame was simulated using a detailed mechanism at $u_{rms,in}/s_l=3.41$, $l_{int,in}/\delta_l=0.85$ and $T_r=700$ K. These conditions are similar to the conditions for case A, and thus offer a good standard of comparison. It was observed [126] that high heat release rate regions were unconnected and isolated in space, results which are consistent with case A of this study. Similar results were obtained in Fig. 1 in the study of Bell et al. [34], where a lean ($\phi=0.8$) methane flame was simulated,

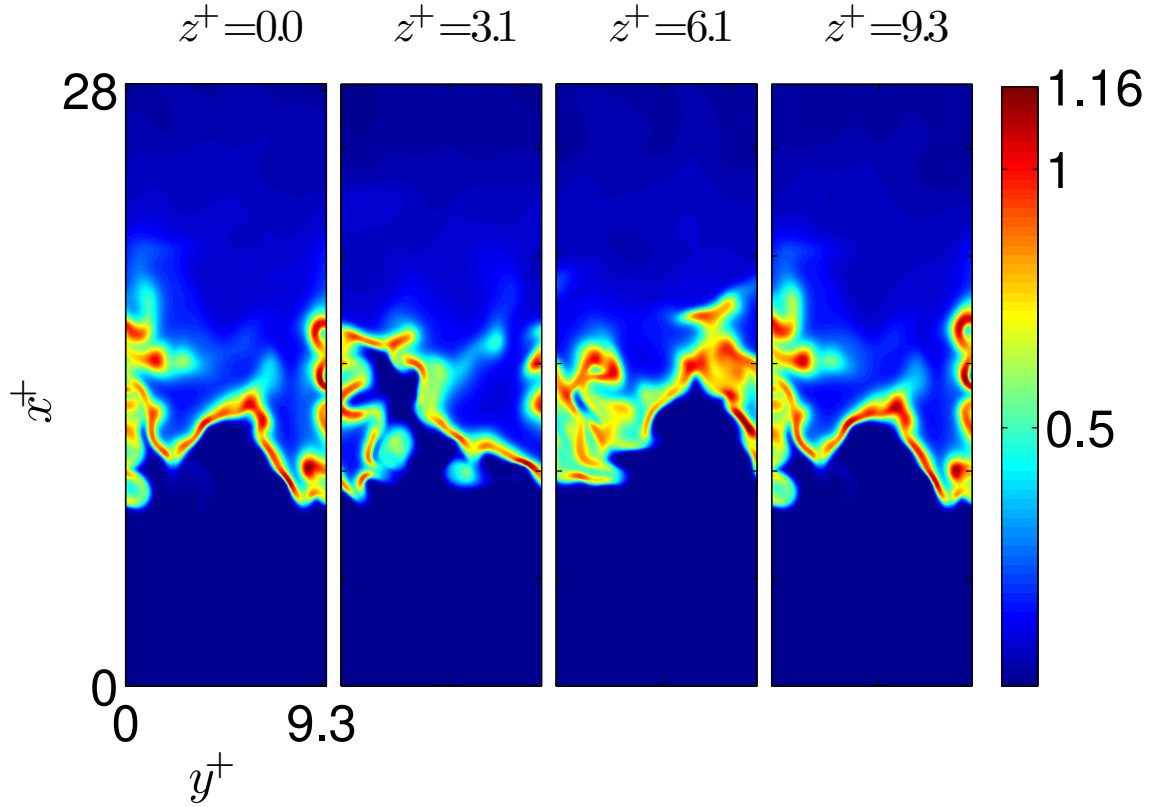


Figure 5.10: Heat release rate contours $\dot{Q}/\max(\dot{Q}_{lam})$ for case C at $t/t_{fl}=2.0$

also using a detailed mechanism at $u_{rms,in}/s_l=1.7$. This sort of flame structure resembles that of a corrugated flamelet in the classical combustion diagram [127]. In this regime, $Ka < 1$ and $u_{rms}/s_l > 1$. Figure 5.7 shows that this regime is best described by the filled black circle, which denotes the turbulence parameters for the inlet turbulence and using δ for normalization. Case C on the other hand has a flame structure resembling that of distributed reactions zones since it is more difficult to identify a clear flame front. In the distributed reaction zones regime $Ka > 1$ and $Da > 1$ [127], conditions best described by the filled black square in Fig. 3.2 also denoting the inlet turbulence parameters and using δ for normalization. Using δ_l for normalization and the inlet conditions gives according to the classical combustion diagram [127] flames in the well-stirred reactor regime something which does not apply for either case A or C. Using δ_l and the turbulence

conditions at the leading flame front on the other hand, does not recover for case A a flame in the corrugated flamelets regime, and does not recover for case C a flame in the distributed reaction zones regime. Thus although turbulence is decaying and the leading flame front experiences less intense turbulence, the flame structure seems to be best described by the inlet turbulence parameters (and using δ for normalization).

5.5 c-space comparison with laminar flame profiles

Figures 5.11 and 5.12 show in progress variable space, scatter plots of the heat release rate and species mass fractions for case C (similar results but with less scatter were obtained for case A and are thus not shown here). The superscript + indicates quantities normalized with respect to their maximum laminar values. The continuous grey line shows the conditional average and the dashed grey line shows the unstrained laminar flame result.

The scatter in the heat release rate is maximum for $0.0 < c < 0.6$ approximately, and especially around $c=0.2$. This is to be expected since turbulence in this region is stronger. As a result, the heat release fluctuates significantly above and below the laminar value with local drop occurring relatively frequently. For $c=0.1$ and below, the heat release rate is observed dropping to zero, implying that local extinction is taking place near the leading edge of the flame. A similar behaviour is observed in the same regime for the mass fractions of the intermediates H, OH, HCO and O, which helps to explain the large variations in the heat release rate. The OH mass fraction for example drops to zero, and since the majority of the heat release rate comes from the reaction $\text{OH} + \text{CO} = \text{H} + \text{CO}_2$, local extinction occurs.

The variation of normalized mass fractions of O_2 , H_2O , CO , CO_2 , H_2 and CH_4 , which compose the fuel, show minimal scatter for both cases considered, and a very good agreement with the laminar flame result is seen. Large deviations from the laminar flame are observed for the intermediates CH_2O and CH_3 . The laminar profiles under-predict the CH_2O and CH_3 mass fractions considerably for low c .

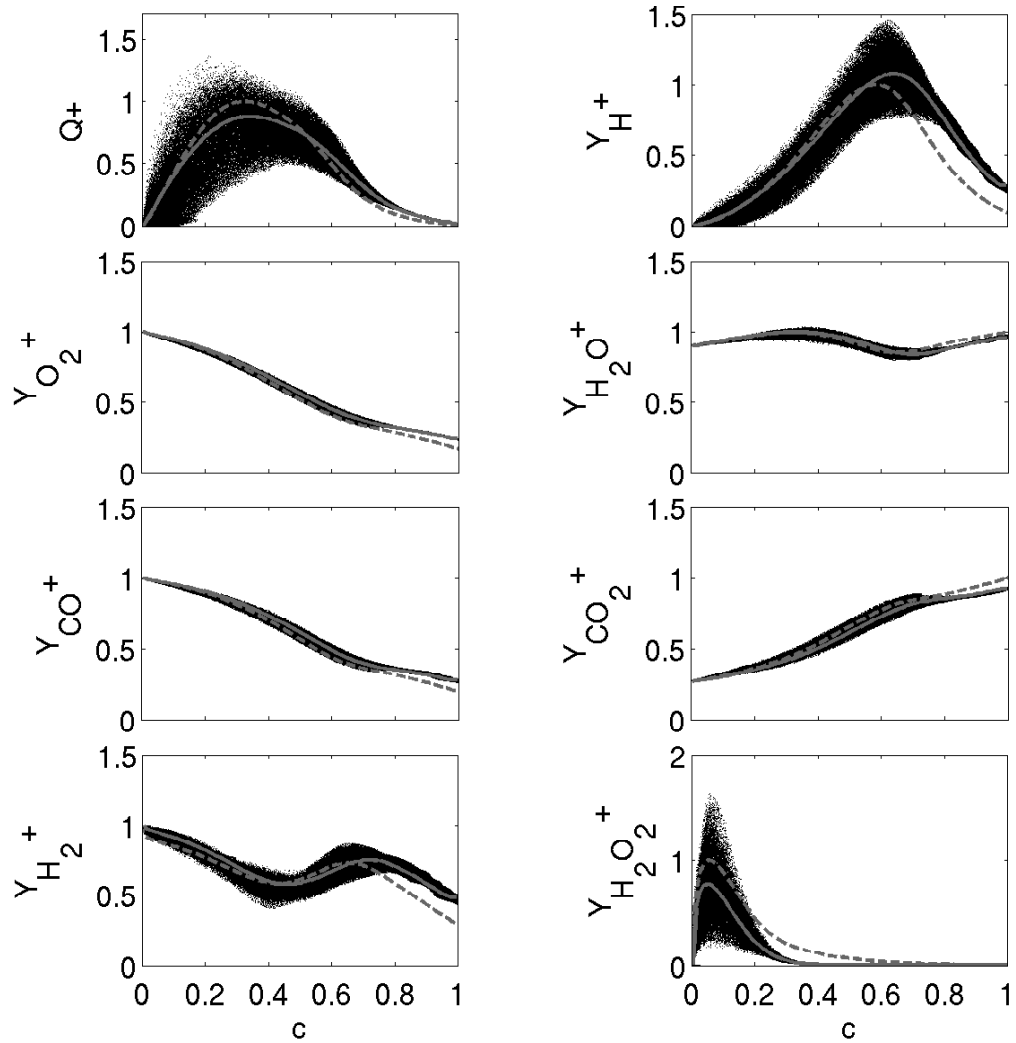


Figure 5.11: Variation of normalized species mass fractions and heat release rate with c for case C at $t/t_{fl}=2$. Continuous grey line shows the conditional average and dashed line shows the laminar flame result.

These species peak early on well before the maximum heat release, which for the laminar flame occurs at $c=0.32$. As a result, it is expected that turbulence-scalar interaction will be stronger in this regime. This leads to increased transport into

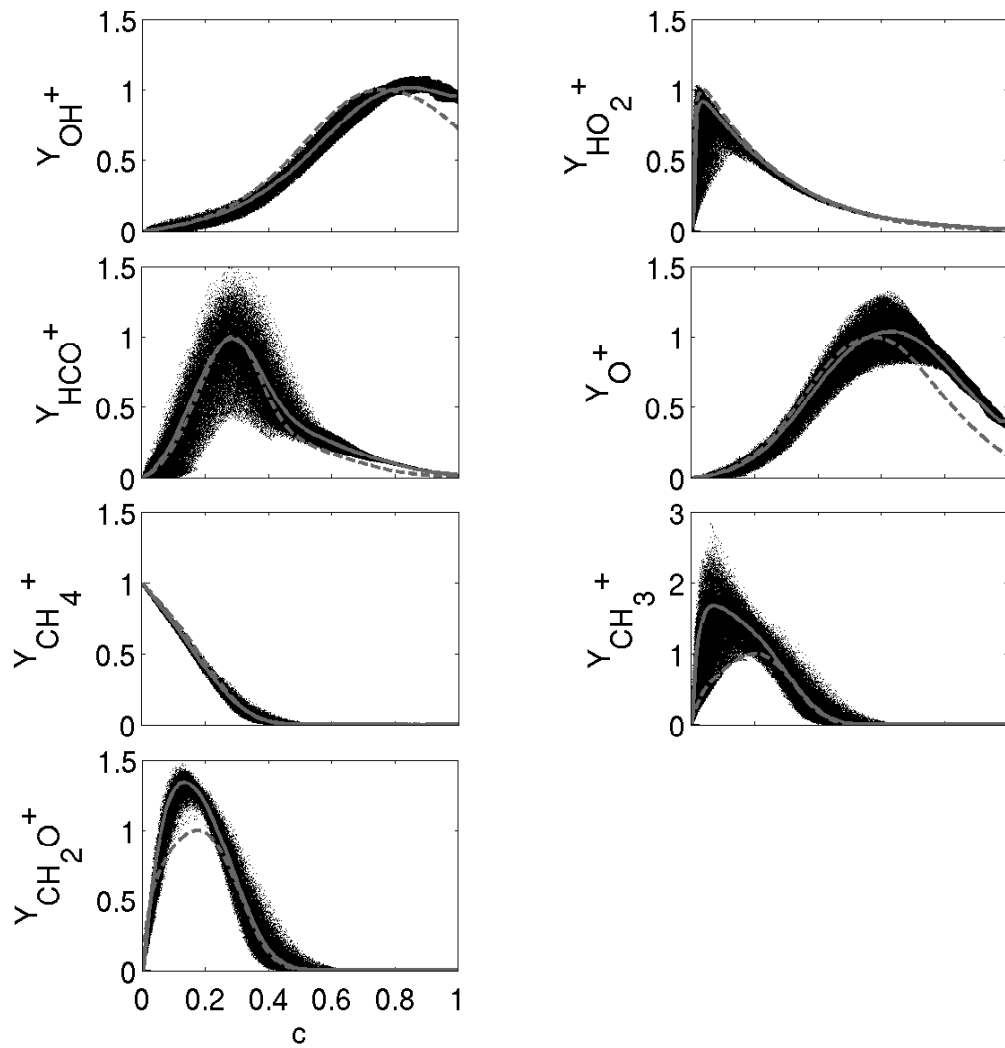


Figure 5.12: Variation of normalized species mass fractions and heat release rate with c for case C at $t/t_{fl}=2$. Continuous grey line shows the conditional average and dashed line shows the laminar flame result.

the preheat zone of the flame, thus raising the concentration of these species. At the same time, analysis of the reaction rates revealed the production of CH_2O and CH_3 to be significantly higher than the laminar value in the preheat zone

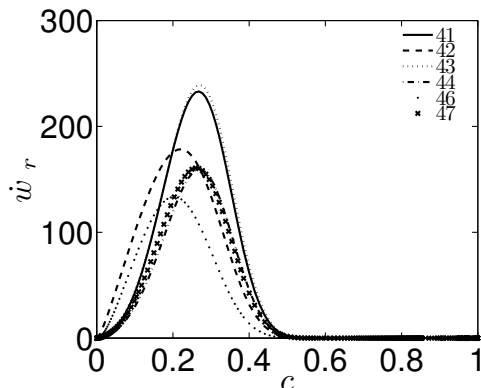


Figure 5.13: Net rates of CH_3 -associated reactions from the set in Table 2.3 in $\text{molm}^{-3}\text{s}^{-1}$ for an unstrained laminar flame.

of the flame, which helps to explain the enhanced mass fraction distributions. A similar trend was observed for low c in the lean methane DNS of Bell et al. [34] for CH_3O , which is mainly produced from CH_3 reacting with HO_2 . However, in [34] the increased concentration of CH_3O was found to occur primarily in negatively curved regions, where the concentrations of CH_3 and HO_2 also peaked. This is in contrast to the results of this study where the concentrations of both CH_3 and CH_2O showed no significant correlations with either curvature or strain. A careful examination of the reaction set in Table 2.3, shows that CH_3 is involved in the reactions 41-44, 46 and 47. In order to understand the contribution of these reactions to the production of CH_3 , the net rates of these reactions are computed for an unstrained laminar flame. The results are shown in Fig. 5.13. It is clear that CH_3 is produced through reactions 41, 42 and 47 and consumed in 43, 44 and 46. Furthermore, reaction 41 is balanced by reaction 43 and reaction 47 is balanced by reaction 44. Hence the dominant reactions are 42: $\text{OH} + \text{CH}_4 = \text{CH}_3 + \text{H}_2\text{O}$ and 46: $\text{H} + \text{CH}_3(+\text{M}) = \text{CH}_4 + (\text{M})$. Since the OH radical peaks in the product zone it is expected that OH will diffuse towards the reactants i.e. lower c values thus increasing the net rate of reaction 42, and the concentration of CH_3 in this region. This in turn will also give rise to higher CH_2O concentrations through the decomposition of CH_3 . The same argument is also true for the H radical which will also raise the rate of the CH_3 -consuming reaction 46. However, as one may see from Fig. 5.13, reaction 42 is more dominant in the region of low c values of

the flame than reaction 46. In addition to this, the effect of reaction 46 is not only to consume CH_3 but to also produce CH_4 which will in turn be consumed by reaction 42. As a result, the production rate of CH_3 is enhanced for low c and so does the production rate of CH_2O , leading to higher than the laminar concentrations.

Case A	s_d^+		K_m^+		a_t^+		Φ^+		Σ^+	
c^*	μ	σ	μ	σ	μ	σ	μ	σ	μ	σ
0.1	1.123	0.555	-0.090	2.484	0.743	0.771	0.033	3.571	0.962	0.168
0.32	1.421	0.672	-0.026	1.981	0.789	0.732	0.007	3.579	1.033	0.155
0.5	1.667	0.859	0.040	1.768	0.727	0.665	-0.019	3.668	1.207	0.200
0.7	2.063	1.098	0.160	1.865	0.489	0.496	-0.116	4.310	1.570	0.372
Case C	s_d^+		K_m^+		a_t^+		Φ^+		Σ^+	
c^*	μ	σ	μ	σ	μ	σ	μ	σ	μ	σ
0.1	1.282	1.182	-0.341	4.636	2.390	3.721	-0.087	6.956	0.885	0.387
0.32	1.657	1.389	-0.431	3.960	2.241	3.184	-0.042	6.687	1.014	0.385
0.5	1.912	1.628	-0.174	3.604	1.889	2.831	0.116	6.861	1.187	0.459
0.7	2.118	1.956	0.487	3.423	1.347	2.302	1.055	7.065	1.364	0.559

Table 5.2: Mean μ and standard deviation σ calculated using the respective flame surface variable pdfs.

Overall, there is a good agreement between the conditional average with the unstrained laminar flame for the majority of species mass fractions and for the heat release rate. This implies that an unstrained flamelet model should give good results for the mean heat release rate and for the mean species mass fractions. In order to understand this better, pdfs of the generalized FSD, $\Sigma=\chi$, for $c^*=0.1, 0.32, 0.5$ and 0.7 , are calculated and are shown in Fig. 5.14. The mean μ and standard deviation σ are given in Table 5.2 (other quantities in the table will be discussed later). The FSD on each iso-surface is normalized according to $\Sigma^+=\Sigma(c^*)/\Sigma_{lam}(c^*)$ i.e. based on the FSD value of the laminar flame on the same iso-surface. Thus, Σ^+ becomes a measure of the thinning and/or thickening of the c^* iso-surfaces, values larger than 1 indicating thinning, and values less than 1 indicating thickening. For both cases, the $c^*=0.1$ iso-surface has a less than 1 mean, indicating that the leading edges are on average thickened by the turbulence. The $c^*=0.32$ iso-surface does not thicken or thin and remains in the mean sense close to a laminar flame. Of all iso-surfaces considered, it also has the lowest standard deviation indicating that it is less affected by the turbulence.

As one moves towards the product side, the mean value of the FSD increases above 1, a result which implies thinning of the iso-surfaces takes place. Thus turbulence acts to bring iso-surfaces together in the products side, while at the same time turbulence acts to move iso-surfaces apart in the reactants away from the heat release zone. In this context by heat release zone we mean the c^* value where heat release is maximum in the laminar flame. This means that the flame front broadens for low c^* and thins for high c^* , consistent with previous 1-step chemistry DNS in 3D [128, 129, 130]. A similar analysis using 1-step chemistry in 3D was done by Kim and Pitsch [131] at almost the same turbulence level as for case C of this study ($u_{rms,in}/s_l=13.8$). A similar behaviour was observed in that high c^* iso-surfaces have generally larger means and thus thin under turbulence. In agreement with the results of this study, Σ^+ pdfs for low c^* values were found to be skewed towards $\Sigma^+ < 1$, with the skewness disappearing towards the product side. A noticeable difference with the 1-step results of [131], is that the variance of the pdfs was found to decrease towards the product side, in contrast with the results of this study where in general there is an increase instead. This can be attributed to the wide region of heat release for the multi-component flame, as one may see from Fig. 5.11: the presence of individual species reaction zones each peaking at different c values results in a production of c gradients spanning $0 < c < 0.8$. Thus, up to $c=0.7$ there is still significant heat release which produces c gradients.

The Σ^+ pdfs can also be used to infer the flamelet nature of turbulent combustion. For both cases on the $c^*=0.32$ iso-surface the mean is close to 1, however it is clear that case C is less flamelet-like than case A. This is reflected in the standard deviation of Σ^+ : the less the standard deviation, the flame is more flamelet-like, and a standard deviation of zero indicates a laminar flame. The results in Table 5.2 show that case A is in general more flamelet-like than case C. At the same time we also find that the $c^*=0.32$ iso-surface is more flamelet-like than all the other iso-surfaces.

From a modelling point of view, Σ^+ pdfs of a laminar unstrained flame on any c^* surface are delta functions situated at 1 i.e. $f(\Sigma^+; c^*)=\delta(\Sigma^+ - 1)$. Clearly in the turbulent case $f(\Sigma^+; c^*)$ is some function which depends on c^* and the turbulence parameters. Thus we may say that a flame is strictly flamelet-like if

$f(\Sigma^+; c^*) = \delta(\Sigma^+ - 1)$, or that $\lim_{u_{rms} \rightarrow 0} f(\Sigma^+; c^*) = \delta(\Sigma^+ - 1)$. For extremely high turbulence on the other hand, one would expect: $\lim_{u_{rms} \rightarrow \infty} f(\Sigma^+; c^*) = \delta(\Sigma^+)$. This is so because as u_{rms}/s_l increases c gradients are likely to be very low, and the probability of $\Sigma^+ = 0$ becomes increasingly larger. Hence in the PSR limit it is expected that $f(\Sigma^+; c^*) = \delta(\Sigma^+)$. All these effects are represented by $f(\Sigma^+; c^*)$ for case C, which shows increased probabilities of having $\Sigma^+ < 1$ for all c^* iso-surfaces as compared to case A. Further DNS at higher turbulence levels will help in this regard to establish limits on the flamelets regime.

5.6 Surface pdfs and scatter plots

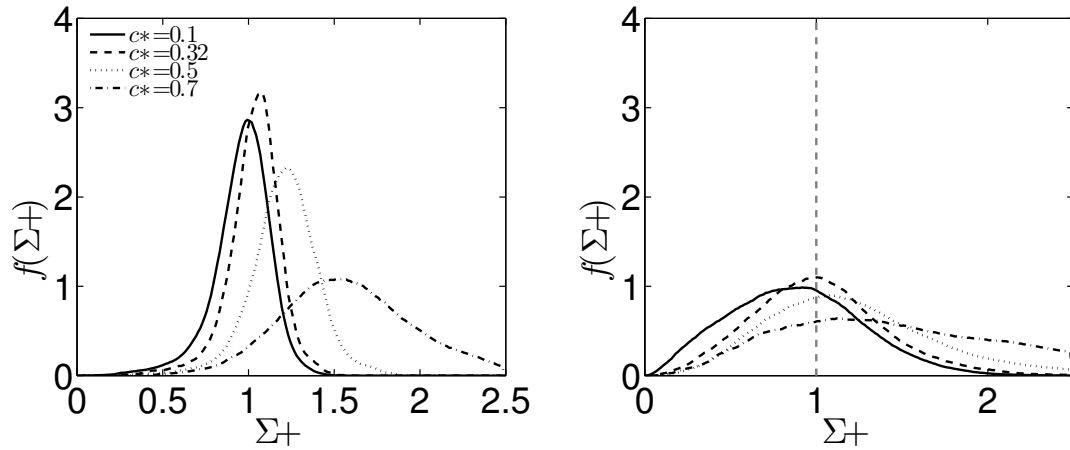


Figure 5.14: Pdfs of generalized FSD for case A (left) and case C (right).

Figures 5.15-5.18 show the pdfs of surface displacement speed, curvature, tangential strain, and stretch for case A (left) and case C (right) as calculated on different c -isosurfaces. Figures 5.19-5.26 show scatter plots of relevant surface quantities in order to help explain the behaviour of the pdfs.

For case A the displacement speed pdf for $c^* = 0.1$ peaks around 1 with a mean almost equal to unity (1.12) and a small standard deviation. This indicates that the flame front propagates towards the reactants at a speed almost equal to the laminar flame speed. For larger c^* values the pdfs spread out and shift towards higher mean values as expected, in agreement with 1-step chemistry DNS [132].

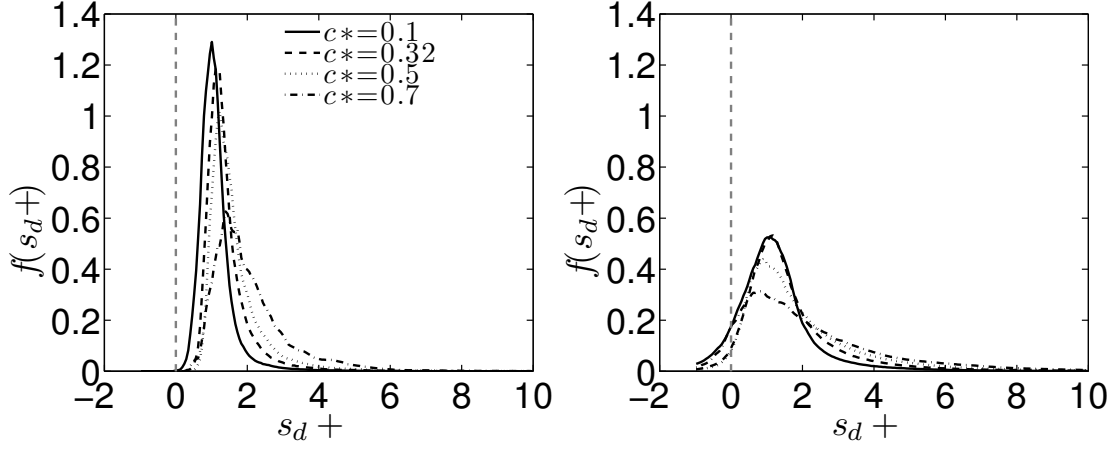


Figure 5.15: Displacement speed pdfs for case A (left) and case C (right).

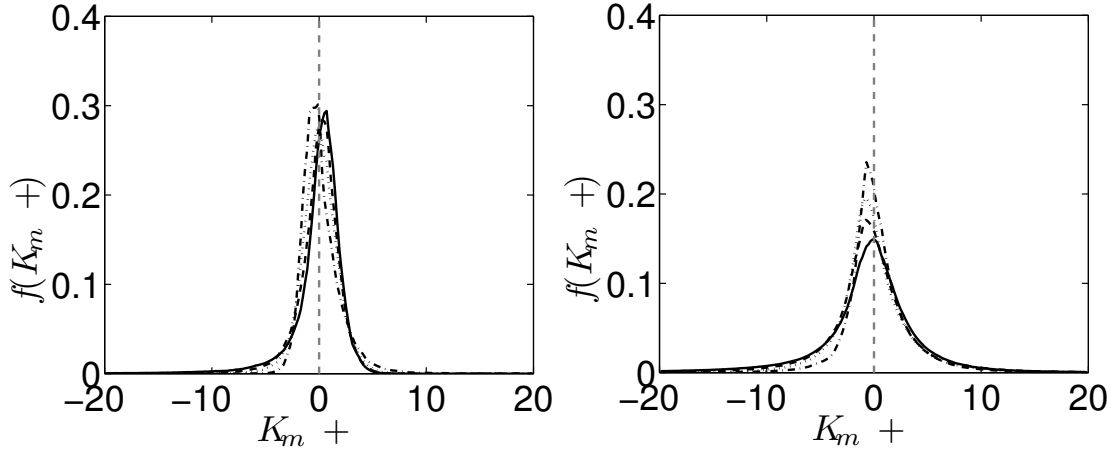


Figure 5.16: Curvature pdfs for case A (left) and case C (right). Lines as in Fig. 5.15.

For case C, the flame front is propagating towards the reactants with a speed of about 28 % higher than the laminar flame speed. An important difference in this case is the occurrence of negative displacement speeds with non-zero probability. This was also observed in 1-step chemistry DNS [132, 133]. The displacement speed can be decomposed as [132, 133]:

$$s_d = s_r + s_n + s_t + s_v \quad (5.7)$$

where s_r , s_n , s_t and s_v denote the contributions to the displacement speed of

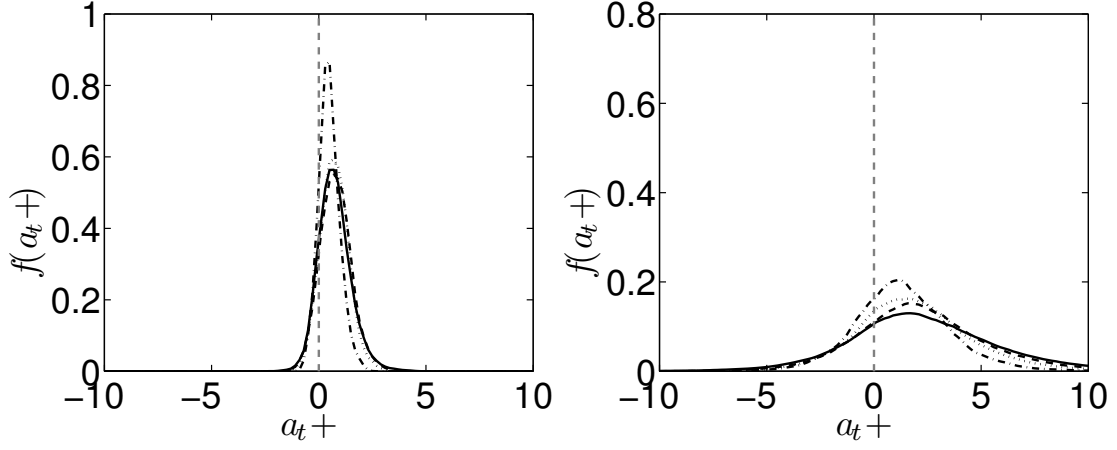


Figure 5.17: Tangential strain rate pdfs for case A (left) and case C (right). Lines as in Fig. 5.15.

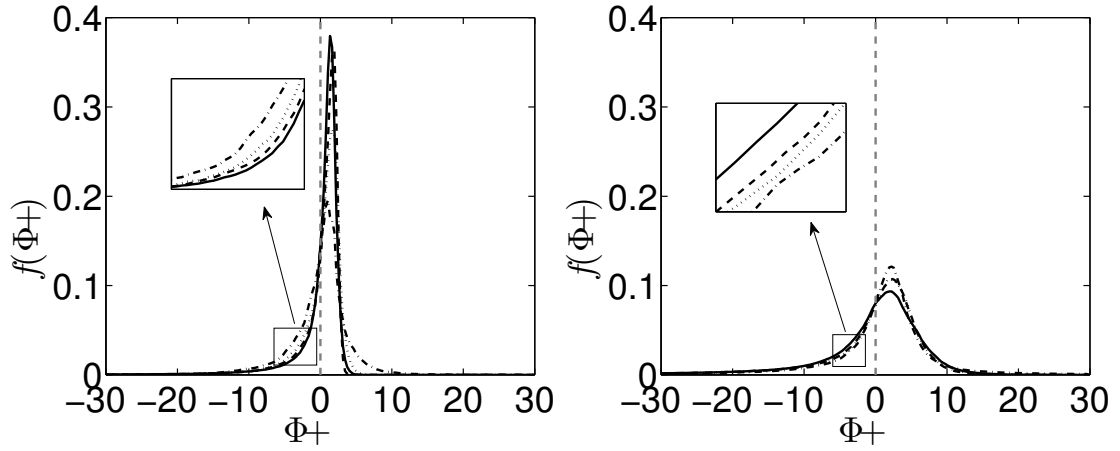


Figure 5.18: Stretch rate pdfs for case A (left) and case C (right). Lines as in Fig. 5.15.

reaction, normal heat diffusion, tangential heat diffusion, and species diffusion respectively. For the cases in this study the contribution due to species diffusion s_v was found to be negligible. The tangential heat diffusion term s_t is equal to $s_t = -\lambda K_m / (\rho C_p)$ [132, 133], i.e. it is proportional to the curvature. The negative displacement speed occurs in regions of high positive curvature where the contribution of the tangential diffusion term s_t exceeds the contributions of the

reaction and the normal diffusion terms [132, 133]. This can be seen more clearly in Figs. 5.19 and 5.20. These figures show the variation of the displacement speed on the $c=0.32$ iso-surface, with curvature and strain. It is clear that the displacement speed does not show any significant correlation with strain, but there is a strong correlation with curvature. Since curvature is the main variable affecting the displacement speed, one may see from Fig. 5.19 that for case C negative displacement speeds occur at regions with high positive curvatures as theory suggests [132, 133].

Negative displacement speeds are not observed for case A due to the lower turbulence level, and hence the lower positive curvatures attained. This is also supported by comparing the curvature pdfs of the two cases shown in Fig. 5.16. The curvature pdfs for both cases are Gaussian-like consistent with previous DNS studies both in 2D with skeletal chemistry and in 3D with 1-step chemistry [125], [132]. For case A, the curvature pdfs peak around 0 and have in general smaller standard deviations than for case C as one may see from Table 5.2. This means that the probability of having high positive curvatures for case C is larger than for case A, supporting the non-zero probability of having negative displacement speeds. On the reactant side the pdfs show a slight skewness towards negative curvature values for both cases, with the mean curvature being negative. The skewness shifts to positive curvature values as we move towards the products, since the mean displacement speed is higher. As a result, one would expect surface area to be produced in the reactants and to be destroyed in the products. Comparison of the stretch pdfs in Fig. 5.18 shows that this indeed happens for case A, since there is a higher probability of negative stretch values as one moves towards the reactant side. At the same time the mean value of stretch shifts from positive values in the reactant side, to negative values in the product side, confirming the above arguments. A different behaviour is observed though for case C: the probability of having negative stretch values in the products is less than the probability of having negative stretch in the reactants. Also, as one may see from Table 5.2, the mean stretch in the reactants shifts from near 0 negative values to positive values in the products, suggesting that flame area is on average produced in the product side instead. This can be attributed to the intense turbulence for case C, which (1) causes extinction of the leading

flame front elements for $c < 0.1$ as one may see from Figs. 5.10 and 5.11, and (2) causes significant flame-flame interaction for $c < 0.1$ which also destroys flame surface area. Flame elements close to the product side however, interact with less intense turbulence and are thus less likely to extinguish or experience flame-flame interaction.

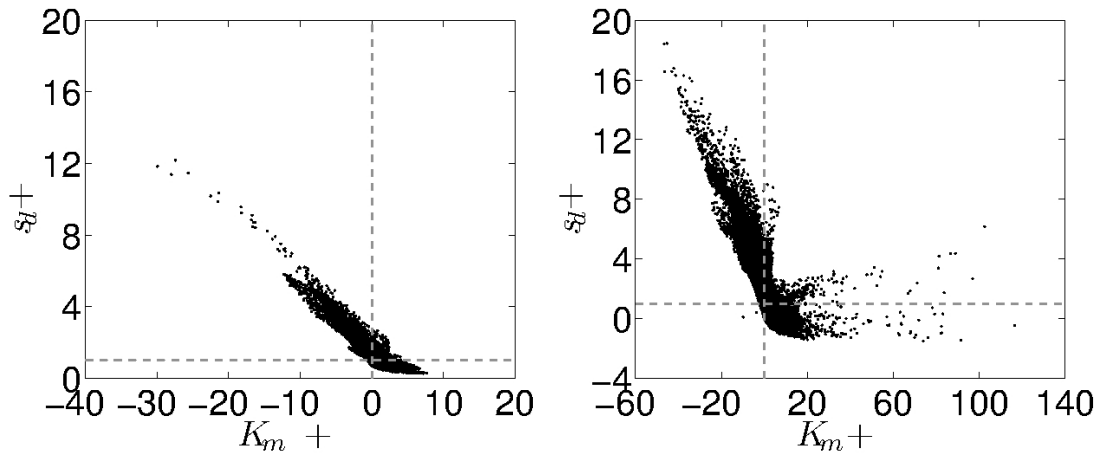


Figure 5.19: Displacement speed against curvature for cases A (left) at $t/t_{fl}=4.0$, and case C (right) at $t/t_{fl}=2.0$, for $c^*=0.32$.

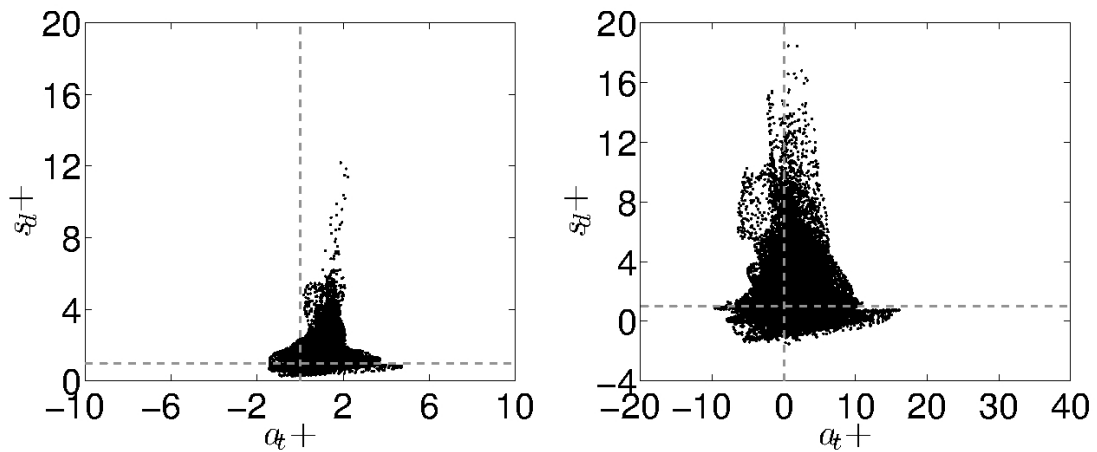


Figure 5.20: Displacement speed against tangential strain rate for case A (left) at $t/t_{fl}=4.0$, and case C (right) at $t/t_{fl}=2.0$, for $c^*=0.32$.

Another important point is that for negative curvatures s_d can be as much as 10 times larger than the laminar flame speed s_l . This is owing to increased heat

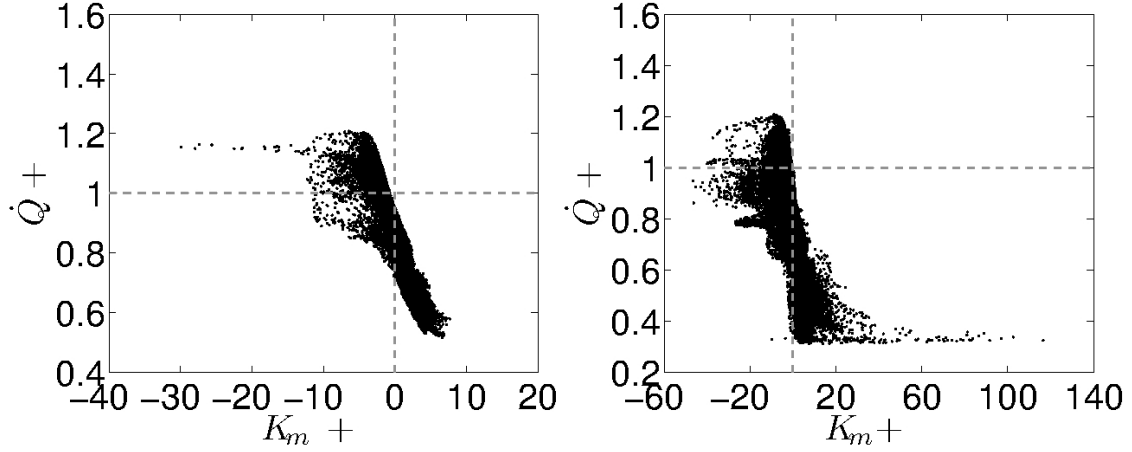


Figure 5.21: Heat release against curvature for case A (left) at $t/t_{fl}=4.0$, and case C (right) at $t/t_{fl}=2.0$, for $c^*=0.32$.

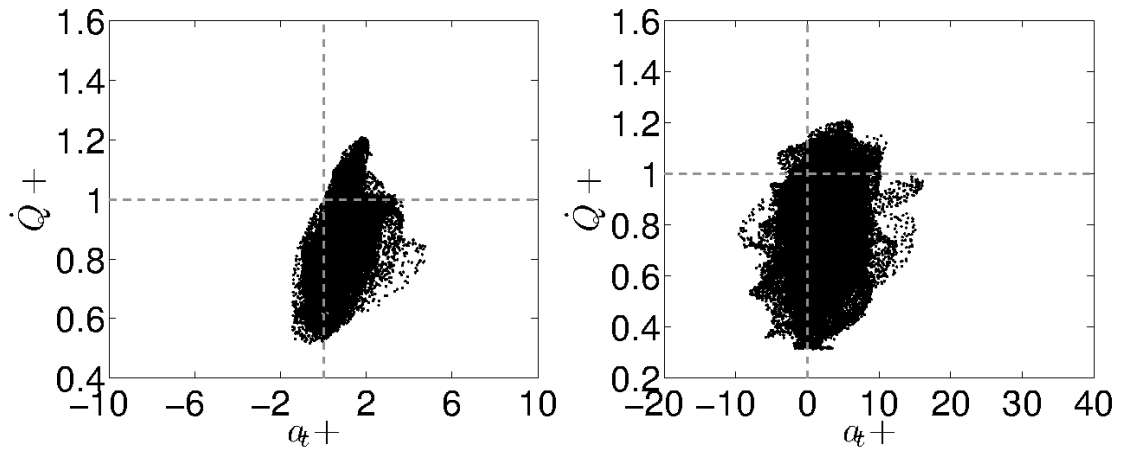


Figure 5.22: Heat release rate against tangential strain rate for case A (left) at $t/t_{fl}=4.0$, and case C (right) at $t/t_{fl}=2.0$, for $c^*=0.32$.

release rate in these regions as one may see from Figs. 5.21 and 5.22. Although there is some correlation of the heat release rate with strain, the correlation with curvature is much stronger in contrast to 2D detailed chemistry hydrogen DNS studies [20, 21]. Heat release rate is maximised in regions of negative curvature with the value being around 20% larger than than maximum laminar flame value. This increase though is too modest to explain the large displacement speeds observed in negatively curved regions, suggesting that the positive contribution

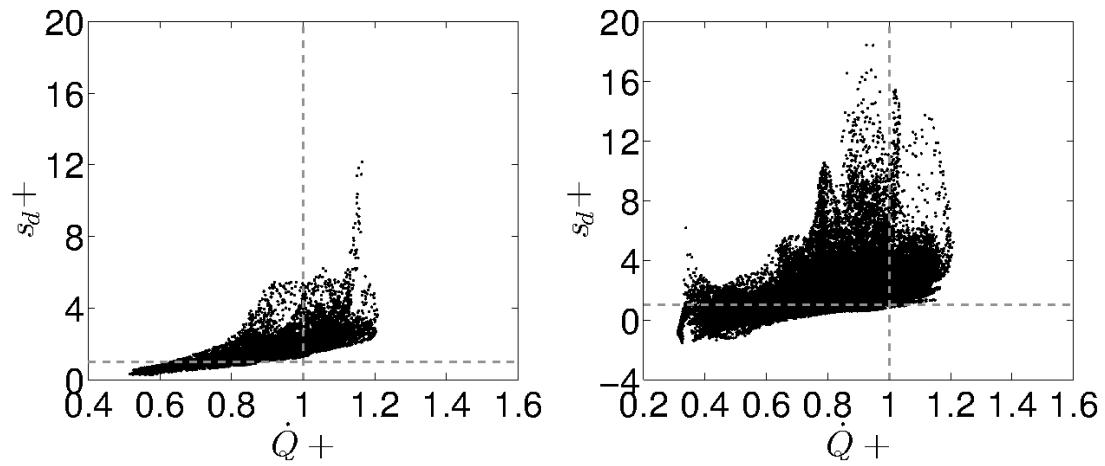


Figure 5.23: Displacement speed against heat release rate for case A (left) at $t/t_{fl}=4.0$, and case C (right) at $t/t_{fl}=2.0$, for $c^*=0.32$.

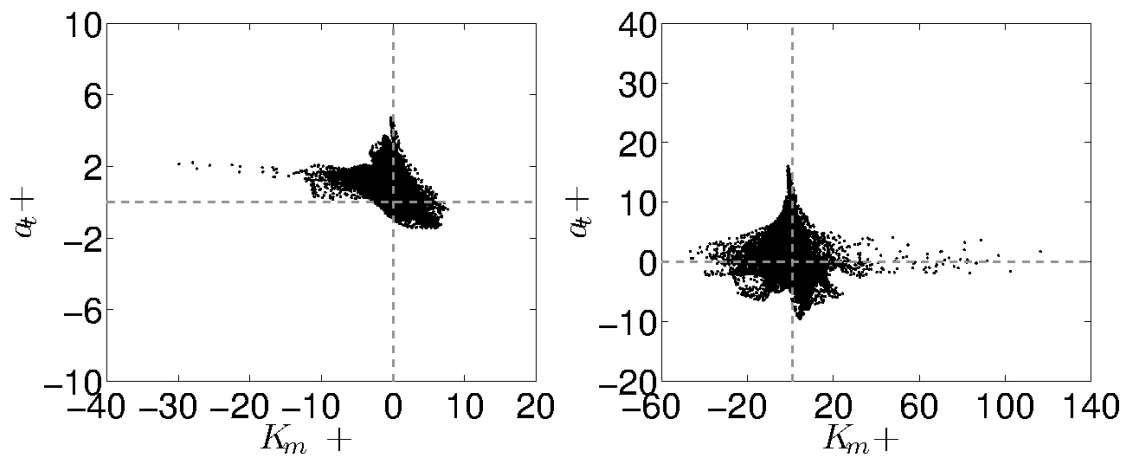


Figure 5.24: Tangential strain rate against curvature for case A (left) at $t/t_{fl}=4.0$, and case C (right) at $t/t_{fl}=2.0$, for $c^*=0.32$.

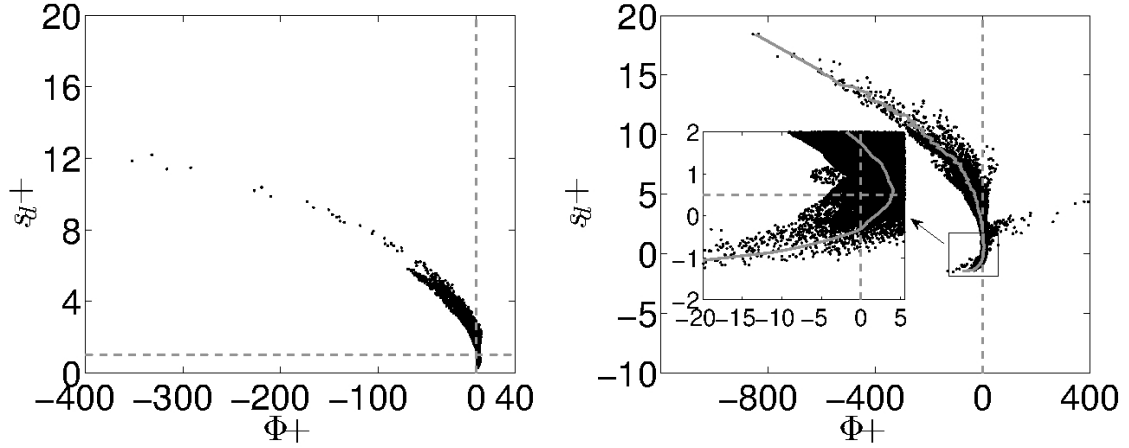


Figure 5.25: Displacement speed against stretch rate for case A (left) at $t/t_{fl}=4.0$, and case C (right) at $t/t_{fl}=2.0$, for $c^*=0.32$. Grey continuous line shows the conditional average for case C.

of the tangential heat diffusion term is also important. Another important point for case C is the fact that for high positive curvatures the heat release rate is non-zero whereas the displacement speed is negative. This also justifies the aforementioned discussion in that tangential straining exceeds the contribution of the heat release. Figure 5.23 shows this more clearly where heat release rate is positively correlated with displacement speed.

Figure 5.17 shows the tangential strain rate pdfs. For both turbulence levels the pdfs are Gaussian-like. The mean strain remains relatively unchanged and positive as one moves towards the products, in agreement with previous studies in the literature [125],[132]. This result indicates that the probability of having positive strain is higher than the probability of having negative strain. In order to check the correlation between strain and curvature, Fig. 5.24 shows a scatter plot of the tangential strain rate against curvature. For case A, there is a weak negative correlation between strain and curvature, with negative strains appearing for positive curvatures. For case C no such correlation is observed although for both cases maximum straining occurs near zero curvatures.

Figure 5.25 shows the variation of displacement speed against flame stretch on the $c^*=0.32$ iso-surface. Also shown in grey continuous line for case C is the

conditional average, which helps to elucidate the variation of displacement speed with flame stretch rate and to understand the flame response to fluid dynamic stretch. For small curvature and strain rates, i.e for small stretch values, theory suggests that the variation of displacement speed with stretch is linear and given by [134, 135]:

$$\frac{s_d}{s_l} = 1 - Ma \frac{\Phi \delta}{s_l} \quad (5.8)$$

where Ma is the fuel's Markstein number. The Markstein number is essentially equal to $Ma = -\partial s_d^+ / \partial \Phi^+$. It is clear from Fig. 5.25 that: (a) the variation of displacement speed with stretch rate is not linear, and (b) there exist significantly large negative stretch rates [136] which are quite improbable. These results are consistent with the 2D DNS of methane-air combustion of Chen and Im [137]. Furthermore, as observed in [137], and noting the stretch rate pdf in Fig. 5.18, the majority of the flame experiences small stretch rate values. For small and positive stretch values, and for $s_d^+ > \simeq 1$, the relationship is indeed roughly linear as theory suggests, and the Markstein number is positive, suggesting a thermo-diffusively stable flame. For larger negative stretch rates and positive displacement speeds, the Ma number is observed to decrease. As explained in [137] for large positive displacement speeds and for large curvature values $Ma \sim -1/(\delta K_m)$. Since large positive displacement speeds occur at regions with large negative curvature (and large negative stretch rate), Ma is positive and decreases in accordance with the non-linear variation observed in Fig. 5.25.

From the inset in Fig. 5.25 for case C, it is observed that the Markstein number changes its sign at $s_d^+ \simeq 0.5$. Furthermore, the linear relation between s_d^+ and Φ^+ for positive stretch rates holds for $\Phi^+ < 5$. In the work of Mishra et al. [138] outwardly and inwardly propagating laminar flames with 1-step chemistry were computationally studied, and was concluded that the linear relationship holds for normalized stretch rates less than 0.1. The stretch rate was normalized in [138] using $\delta^0 = \lambda / (\rho C_p s_l)$. The value of 5 obtained in the present work translates to 0.32 when δ^0 is used for normalization. Furthermore, it was found [138] that the linear region can be extended up to a normalized stretch rate of 0.5 with

an error smaller than 5%. Thus, the linear region is extended up to $\Phi^+ < 5.25$ which is in agreement with the results of this study. For negative stretch rates, the linearity begins to deteriorate, since the Markstein number is observed to gradually change. Despite this, the relationship between s_d^+ and Φ^+ is observed to still be roughly linear for large negative stretch values spanning $-800 < \Phi^+ < -400$, for case C, and for smaller negative stretch rates spanning $-20 < \Phi^+ < 0$ as one can see from the inset of Fig. 5.25. Thus, the strongest non-linear variation of s_d^+ with Φ^+ is observed for medium value negative stretch rates, which was also observed in [138] for flames with $Le > 1$. These results suggest that the use of a linear relation in Eq. 5.6 to analyse or model premixed flames in large turbulence is limited and caution must be exercised.

5.7 Preferential diffusion

In order to understand the increased heat release rate in negatively curved regions, surface scatter plots of the species mass fractions and reaction rates and the correlations between Y_α and K_m , and Y_α and a_t , are analysed. For practical reasons, only a small sample of the correlations are shown here for case C in Figs. 5.26 and 5.27. Similar correlations were observed for case A.

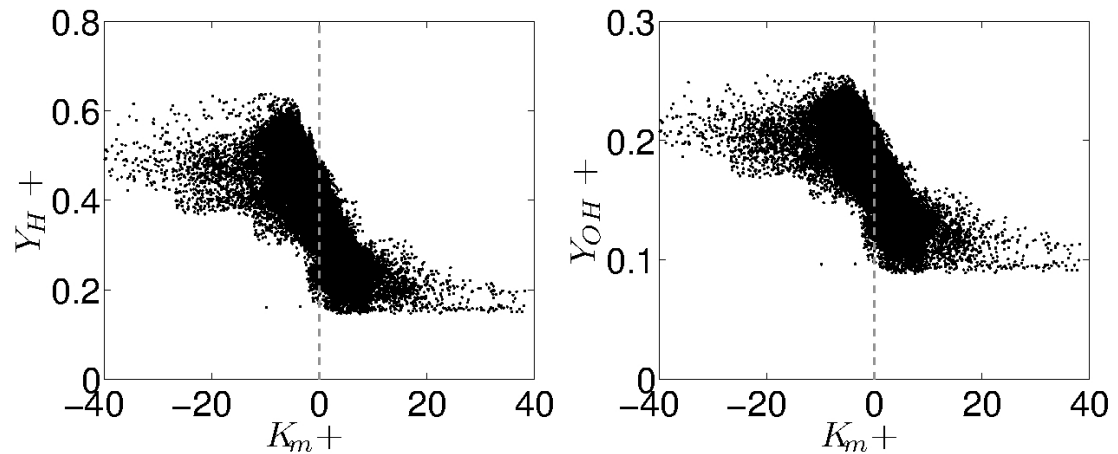


Figure 5.26: H and OH mass fractions against curvature for case C at $t/t_{fl}=2.0$, for $c^*=0.32$.

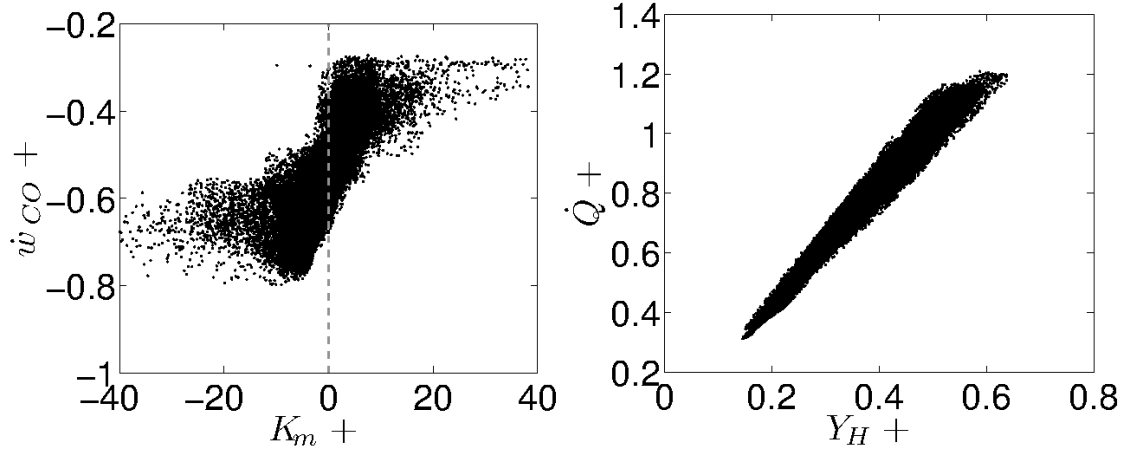


Figure 5.27: CO consumption rate against curvature, and heat release rate against H mass fraction for case C at $t/t_{fl}=2.0$, for $c^*=0.32$.

One may see from Fig. 5.26, that the mass fractions of the radicals H and OH exhibit strong negative correlations with curvature, and peak values are observed for negatively curved regions. Similar results were found to be true for the O radical also (not shown here). Furthermore, the majority of species showed comparatively weaker correlations with tangential strain rate. As one may see from Figs. 5.11 and 5.12, the radical species H, OH and O, all peak after the peak heat release rate. This means that their diffusion velocities for low c are negative, i.e. diffusion takes place from the product side to the reactant side. In the turbulent case, diffusing from the product side to the reactant side, these species are consequently focused in regions which are convex towards the products, i.e. with negative curvature, and are defocused in regions with positive curvature, which explains the observed negative correlations with curvature. A negative correlation with curvature for the H radical was also observed in the 2D methane DNS of Echekki and Chen [125], whose mass fraction also peaked towards the product side.

Furthermore, the large H concentration in regions with negative curvature increases the rate of the chain branching reaction $H + O_2 = O + OH$, producing more OH radicals. In particular, as one may see from Fig. 5.26, Y_{OH}^+ in the negatively curved regions is much larger than 0.23 which is the OH mass fraction for the laminar case on the same iso-surface i.e. $c^*=0.32$. Since the major con-

stituent in the fuel is CO, and the reaction $\text{OH} + \text{CO} = \text{H} + \text{CO}_2$ is the major CO consumption pathway, CO consumption is thus also enhanced in negatively curved regions due to the large OH concentrations there, as one may see from Fig. 5.27. This results in the observed large heat release rates at negative curvatures, since the above reaction is the biggest heat release rate provider. Figure 5.27, also shows that the H mass fraction is almost linearly correlated with the heat release rate justifying the above observation.

The molecular hydrogen H_2 , is found to have only a weak correlation with curvature in contrary to previous methane combustion DNS [125]. This is because as one may see from Fig. 5.11, the H_2 concentration is affected by the presence of water vapour in the fuel mixture [38]. This, results in strong reactive contributions affecting H_2 concentration, making it less curvature dependent. Species such as O_2 , H_2O , CO, HO_2 and HCO were found to correlate strongly with curvature also, in contrast to CO_2 which was found to peak in positive curvatures instead. This is attributed to the presence of CO_2 in the reactants, which causes a large positive convective contribution. As a result, since CO_2 production peaks well after the peak heat release zone primarily through the consumption of CO around $c=0.4$ (Fig.5.1), it is focused in positively curved regions increasing its concentration, and defocused in negatively curved regions reducing its concentration.

In general, the mass fraction of a species on the c^* iso-surface under turbulence, depends on the balance among reaction, diffusion and convection. Thus, an exact analysis of the contributions of reaction, convection and diffusion to the mass fraction balance equation on the flame surface, and its sensitivity to the choice of the c^* iso-surface is an entire subject on its own, and it is the subject of future work.

5.8 Heat release rate correlations

In this section we test how the commonly used flame observables for heat release rate imaging perform for the multi-component flame. This is of specific interest in the light of the subtle but important difference in the flame front structure and its response to curvature and strain rate induced by turbulence for multi-component fuel-air flames discussed above.

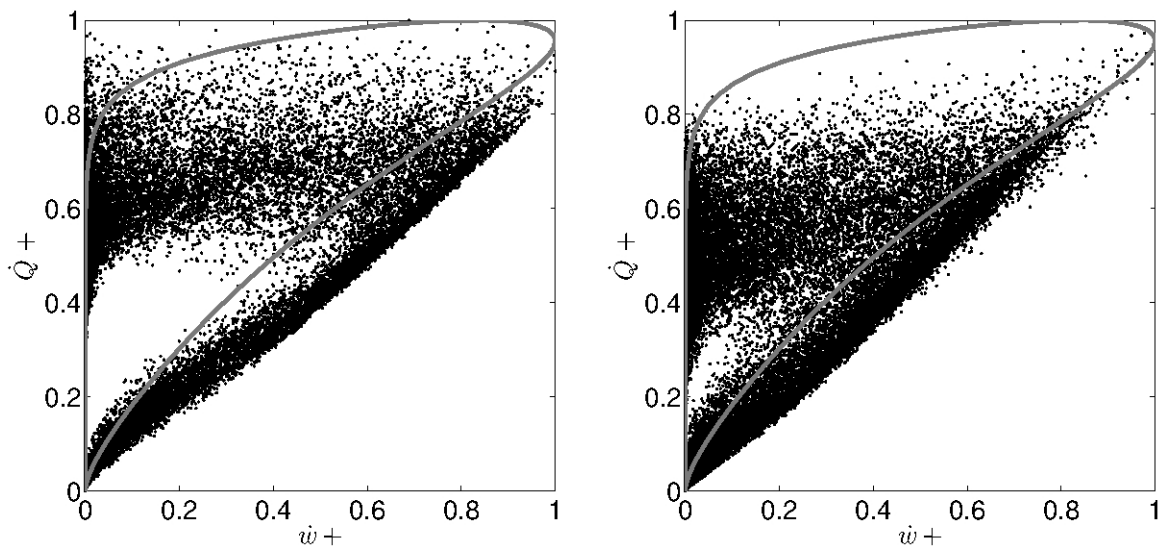


Figure 5.28: Heat release rate normalized by its instantaneous maximum value, against the forward rate of the reaction $\text{OH} + \text{CH}_2\text{O} = \text{HCO} + \text{H}_2\text{O}$, for case A (left) at $t/t_{fl}=4$, and case C (right) at $t/t_{fl}=2$. Grey lines show the laminar unstrained flame result using GRI-3.0.

The correlation of the heat release rate with the net rate of the reaction $\text{OH} + \text{CH}_2\text{O} = \text{HCO} + \text{H}_2\text{O}$, was found to be good both in theoretical and experimental studies [51, 52, 53], for methane [139, 140], ethylene [141] and for propane [142] flames. In a recent computational study however [55], the validity of this correlation was examined for a range of fuels including alcohols, unsaturated hydrocarbons, and aromatic. It was concluded that the above correlation does not hold well and alternative correlations were proposed. The correlation for multi-component fuel flames is still an open question.

Figure 5.28 shows the instantaneous heat release rate \dot{Q} against the forward rate of the reaction $\text{OH} + \text{CH}_2\text{O} = \text{HCO} + \text{H}_2\text{O}$ (the reverse rate is negligible in comparison). The normalization here is done based on the instantaneous maximum value as would be done in an experimental measurement. The correlation for the laminar flame computed using GRI-3.0 is also shown in Fig. 5.28 as solid grey lines. Two important conclusions can be drawn from this figure: (a) the poor correlation observed for the multi-component fuel flame is not because of the skeletal mechanism used and (b) the poor correlation in the turbulent case is not in fact a

manifestation of the turbulence itself, since the correlation for the laminar case is poor also. For both cases there is clearly no correlation between the heat release rate and the forward rate of the reaction $\text{OH} + \text{CH}_2\text{O} = \text{HCO} + \text{H}_2\text{O}$. This is a consequence of the mixture composition which suggests that the contribution of the above reaction to the heat release rate is not as important as it is in methane flames. Furthermore, as one may observe from Figs. 5.11 and 5.12, peak OH concentration occurs well behind the maximum heat release zone ($c = 0.32$), but CH_2O concentration peaks well before that in the preheat zone of the flame due to the rapid CH_4 consumption explained in section 5.5. In fact, the same poor correlation was found to hold between the product $[\text{OH}][\text{CH}_2\text{O}]$ only, i.e. neglecting any temperature dependence, and \dot{Q} . Consequently, alternative flame markers are required to image heat release rate in combustion involving this type of multi-component fuels.

Chapter 6

Heat release rate markers for premixed combustion

It was shown in the previous chapter that the commonly used HRR marker in laser diagnostics i.e. the forward rate of the reaction $\text{OH} + \text{CH}_2\text{O} = \text{HCO} + \text{H}_2\text{O}$ is inadequate for the multi-component fuels considered in this study. In this chapter, the validity of this flame marker is re-visited using two different methods to identify alternative HRR markers. The performance of the markers identified is then examined in turbulent combustion using DNS data of a methane flame, of a diluted methane flame, and of the multi-component flame.

6.1 DNS databases

The DNS databases involve freely propagating flames of an undiluted methane-air mixture (flame C in [143]), a diluted methane-air mixture (flame B in [143]), both having an equivalence ratio ϕ of 0.8, and an undiluted multi-component fuel-air mixture with $\phi=1.0$ (cases A and C in Table 5.1).

6.2 Analysis

The objective is to find suitable flame markers which correlate with the HRR preferably as much linearly as possible. In that respect, a series of laminar un-

strained premixed flame computations have been performed using the PREMIX code of the CHEMKIN package [96, 97], at $p=1$ atm and $T_r=800$ K. The computations have been performed both for methane-air and multi-component fuel-air mixtures (to match the DNS), and a mixture-averaged formulation was used for the species diffusivities. GRI-3.0 [73] is used in the computations since it is a well validated mechanism for methane combustion which is one of the fuels of interest. Furthermore, the skeletal mechanism derived in Chapter 2 from GRI-3.0, was shown to perform reasonably well against experimental flame speed and ignition delay data for multi-component fuel mixtures, thus justifying the use of GRI-3.0 in this study.

The first method of the analysis is to rank elementary reactions based on their fractional contribution to the total HRR, and then to investigate whether the highest ranking reactions show good correlations with the heat release rate. The second method is based on an error estimator function which can be used to directly evaluate the spatial correlation of the heat release rate with a scalar of our choice. These two methods are described below.

6.2.1 Fractional influence method

This method is based on identifying a reaction imparting the most fractional influence on the overall HRR. The heat released by a reaction r , \dot{q}_r , across the flame brush of an unstrained laminar premixed flame is given by:

$$\dot{q}_r = \int_x \dot{w}_r(x) \sum_{\alpha} h_{f,\alpha}^0 (\nu_{r,\alpha}'' - \nu_{r,\alpha}') dx \quad (6.1)$$

where \dot{w}_r is the net reaction rate of reaction r , $h_{f,\alpha}^0$ is the formation enthalpy of species α , and $\nu_{r,\alpha}''$ and $\nu_{r,\alpha}'$, are the stoichiometric coefficients of species α in reaction r in the products and reactants respectively. The standard state of 1 atm and 298.15 K is used for the calculation of the species formation enthalpies. Having calculated \dot{q}_r , each reaction is then ranked according to its fractional contribution to the total HRR, $f_{qr} = 100 \cdot |\dot{q}_r| / |\dot{Q}_t|$, where \dot{Q}_t is the total HRR across the flame brush:

$$\dot{Q}_t = \sum_r \dot{q}_r \quad (6.2)$$

Thus $\sum_r f_{qr} = 100$, and positive and negative values of f_{qr} respectively denote endothermic and exothermic reactions. This fraction is not the same as the one used in the earlier studies of Najm and his co-workers [51, 52, 53] and in [55], where a particular location inside a flame was considered. Although both of these methods are equally good, the integral method gives an overall measure to identify a reaction having the largest fractional influence on the total integrated heat release rate. The reaction identified thus, is then used to find chemical markers for the HRR, and the performance of these markers for turbulent conditions is evaluated using the DNS data described briefly in section 6.1.

6.2.2 Error estimator method

In this approach, an error measure $Z(v)$ for a variable v , which may be a reliable HRR marker is defined as:

$$Z(v) = \int_x \left(\frac{|\dot{Q}(x)|}{\max(|\dot{Q}(x)|)} - \frac{|v(x)|}{\max(|v(x)|)} \right)^2 dx \quad (6.3)$$

where v can be any variable of our choice such as the concentration of a species or the rate of a reaction. This error, Z , may then be ranked for every variable v using $Z^+ = 100 \cdot Z / \max(Z)$. It is clear that the function Z gives an estimate of the error associated with the variable v , normalised using its maximum value as in Eq. 6.3, and spatially matched normalised HRR. The choice of v is of course not unique, however for any given variable v the one which minimizes Z would imply the best correlation with the HRR. The mass density ρY_α of a species α , and the net rate of a reaction r , \dot{w}_r , are used for v to find good HRR markers associated with the concentration of a species and with the rate of a reaction respectively. In the case $v = \dot{w}_r$, this may not be an exact method since the rate of a reaction r may have both positive and negative parts thus contributing ambiguously to the error estimator Z . However, the top-correlating reactions when $v = \dot{w}_r$ were found to have either only positive or negative contributions across the flame brush, thus not influencing the above definition.

6.3 Methane fuel-air mixtures

Figures 6.1 and 6.2 show f_{qr} for the methane-air mixtures having $\phi=0.5$ and 1.0 respectively. Only the top 15 reactions are shown for convenience. For all conditions the major heat consuming reaction is the chain branching reaction $\text{H} + \text{O}_2 = \text{O} + \text{OH}$. For $\phi=0.5$ the major heat releasing reactions are $\text{OH} + \text{CO} = \text{H} + \text{CO}_2$ followed by $\text{O} + \text{CH}_3 = \text{H} + \text{CH}_2\text{O}$. For $\phi=1.0$ this balance is changed. It is important to note that the reaction $\text{O} + \text{CH}_3 = \text{H} + \text{CH}_2\text{O}$ was also found to have the largest fractional influence on the HRR in the study of Najm et al. [51], and also in the study of Gazi et al. [55] who used a more detailed mechanism [144]. What is noteworthy, is the fact that the reaction $\text{OH} + \text{CH}_2\text{O} = \text{HCO} + \text{H}_2\text{O}$ does not contribute largely to the HRR for $\phi=0.5$, and it does not even appear in the top 15 reactions for $\phi=1.0$ as one can see from Fig. 6.2. Furthermore, the relatively small contribution of the reaction $\text{OH} + \text{CH}_2\text{O} = \text{HCO} + \text{H}_2\text{O}$ to the HRR was also observed in [55]. The variation of $|\dot{Q}|^+ = |\dot{Q}|/\max(|\dot{Q}|)$ with the normalised net rates $\dot{w}_r^+ = \dot{w}_r/\max(\dot{w}_r)$, of the top three reactions is shown in Figs. 6.1 and 6.2 on the right. It is clear that a large fractional contribution of a reaction to the HRR does not automatically imply that this will have a good correlation with the HRR. For example the reaction $\text{OH} + \text{CO} = \text{H} + \text{CO}_2$ having the highest exothermic fractional influence for the $\phi=0.5$ flame, shows a poorer correlation than the reaction $\text{O} + \text{CH}_3 = \text{H} + \text{CH}_2\text{O}$ which has the second largest exothermic fractional influence. Similar arguments apply for the stoichiometric case also, and thus this method does not help to identify HRR markers.

Consequently, we use the error measure $Z(\rho Y_k)$, defined in Eq. 6.3. The results are shown in Figs. 6.3 and 6.4, where the error measure is normalised using $Z^+ = 100 \cdot Z/\max(Z)$ as noted earlier. Of all the species, in lean and stoichiometric flames, the HCO concentration minimizes Z^+ suggesting that this species is expected to have the best possible correlation with the HRR. Indeed one observes this in the corresponding figures on the right. This result for [HCO] is consistent with previous studies [51, 52, 53]. One also observes from Figs. 6.3 and 6.4 that as Z^+ increases the linearity of the correlation with the HRR becomes poorer, and overall these results help justifying the use of Eq. 6.3 for systematically

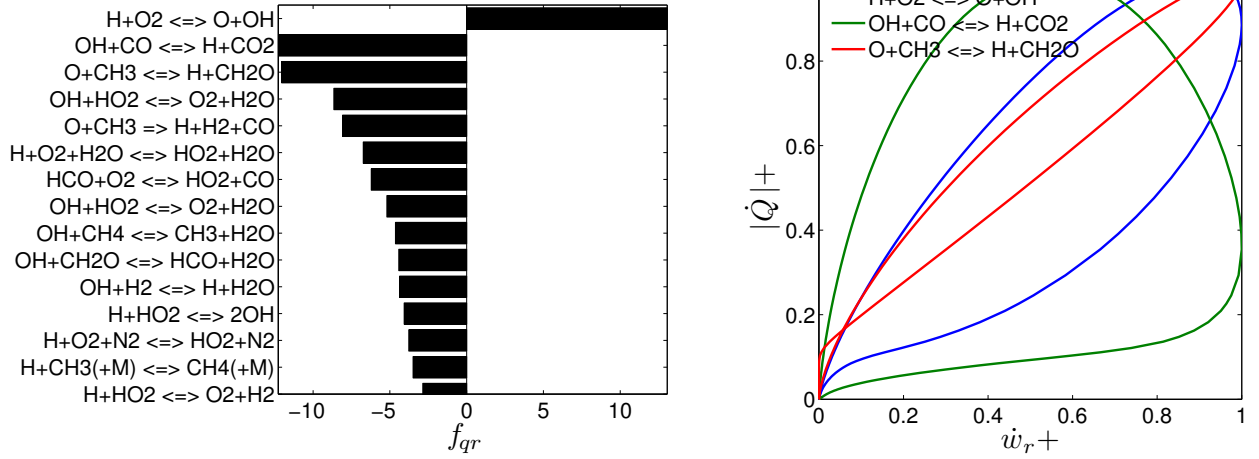


Figure 6.1: Methane-air, $\phi=0.5$, $T_r=800$ K, $p=1$ atm.

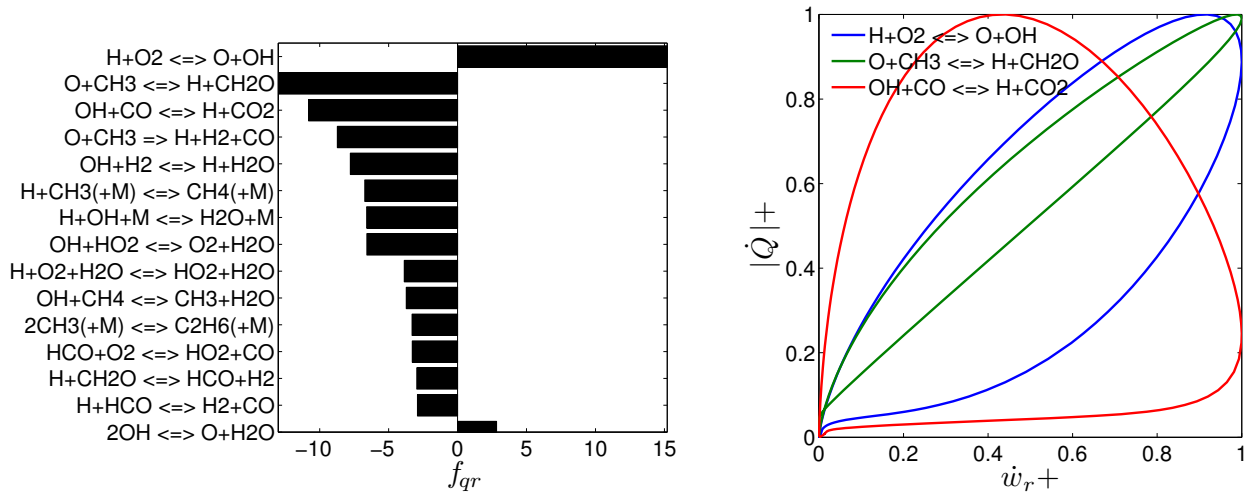


Figure 6.2: Methane-air, $\phi=1.0$, $T_r=800$ K, $p=1$ atm.

identifying heat release rate correlations.

As noted in the introduction, the signal to noise ratio for HCO in laser diagnostics is generally low, and thus alternative markers were proposed for the HRR. This proposition was based on the reactions which are thought to be responsible for the majority of HCO production [51, 52, 53], and one of these reactions is $\text{OH} + \text{CH}_2\text{O} = \text{HCO} + \text{H}_2\text{O}$. Thus measuring $[\text{OH}][\text{CH}_2\text{O}]$ which is proportional to the forward rate of this reaction, was expected to give an estimate of the HCO

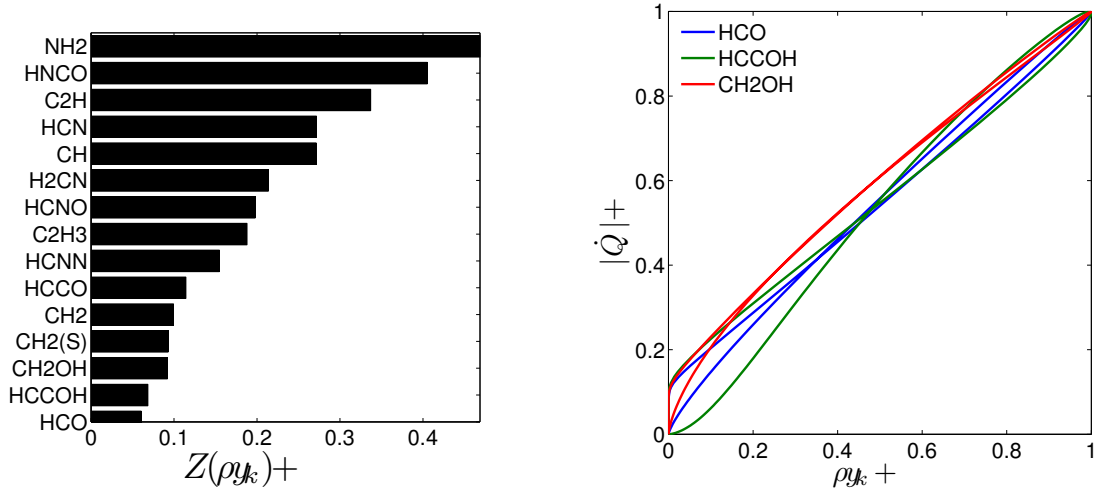


Figure 6.3: Methane-air, $\phi=0.5$, $T_r=800$ K, $p=1$ atm.

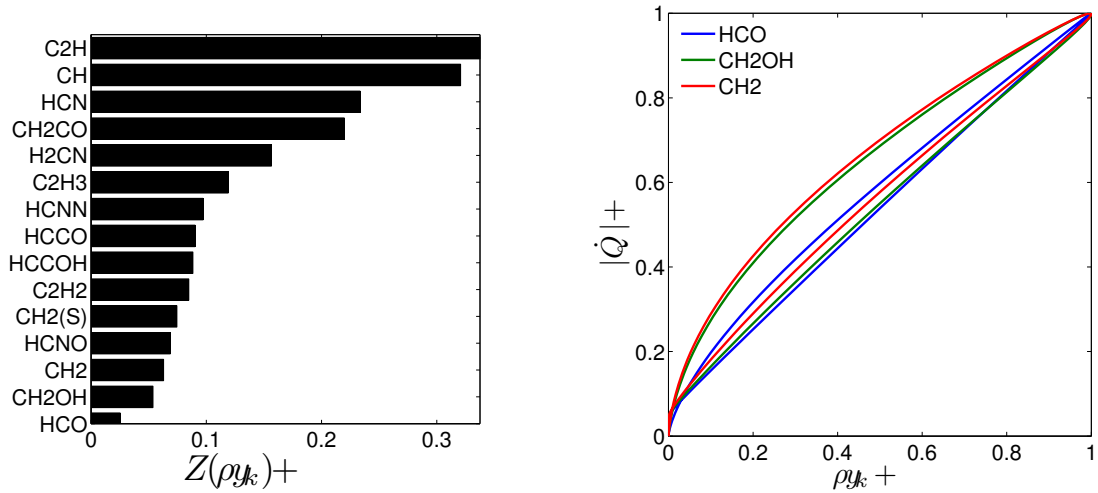


Figure 6.4: Methane-air, $\phi=1.0$, $T_r=800$ K, $p=1$ atm.

concentration and thus serve as a good marker for the heat release rate. In this study, this hypothesis is re-examined using $Z(\dot{w}_r)$. The results of this analysis are shown in Figs. 6.5 and 6.6. For the $\phi=0.5$ case, the chain-terminating reaction $\text{H} + \text{HO}_2 = \text{O}_2 + \text{H}_2$ has the minimum error as per Eq. 6.3, followed by the chain-carrying reaction $\text{H} + \text{HO}_2 = \text{O} + \text{H}_2\text{O}$. Both of these reactions are exothermic, and despite the fact that they do not contribute much to the overall HRR (see Fig. 6.1), they have good spatial correlations with the heat release rate.

Also shown in Fig. 6.5 for comparison, is the rate of $\text{OH} + \text{CH}_2\text{O} = \text{HCO} + \text{H}_2\text{O}$. This reaction has an overall larger error than the reactions $\text{H} + \text{HO}_2 = \text{O}_2 + \text{H}_2$ and $\text{H} + \text{HO}_2 = \text{O} + \text{H}_2\text{O}$. As one can see from Fig. 6.5 this error occurs for relatively low heat release rates where the correlation of this reaction is observed to be poorer relative to $\text{H} + \text{HO}_2 = \text{O}_2 + \text{H}_2$ and $\text{H} + \text{HO}_2 = \text{O} + \text{H}_2\text{O}$. For large heat release rates, the correlation of $\text{OH} + \text{CH}_2\text{O} = \text{HCO} + \text{H}_2\text{O}$ is observed to be better than either $\text{H} + \text{HO}_2 = \text{O}_2 + \text{H}_2$ and $\text{H} + \text{HO}_2 = \text{O} + \text{H}_2\text{O}$, however since $Z(\dot{w}_r)$ gives a measure of the spatial correlation across the whole of the flame brush this is smallest for $\text{H} + \text{HO}_2 = \text{O}_2 + \text{H}_2$ and $\text{H} + \text{HO}_2 = \text{O} + \text{H}_2\text{O}$, implying an overall better correlation with the HRR. Furthermore, the rate of the reaction $\text{OH} + \text{CH}_2\text{O} = \text{HCO} + \text{H}_2\text{O}$ shows a non-zero HRR for zero reaction rate, as one can see from Fig. 6.5 which is consistent with previous studies [51, 52, 53, 55]. Thus, the correlation based on this reaction cannot be used to identify local extinction. $\text{H} + \text{HO}_2 = \text{O}_2 + \text{H}_2$ and $\text{H} + \text{HO}_2 = \text{O} + \text{H}_2\text{O}$ on the other hand show zero HRR at zero rates, implying that these markers can capture local extinction as well if they can be identified using laser diagnostics. For the $\phi=1.0$ case, the values of Z^+ are altered significantly, with the endothermic reactions $\text{O} + \text{CH}_3\text{OH} = \text{OH} + \text{CH}_3\text{O}$ and $\text{O} + \text{CH}_4 = \text{OH} + \text{CH}_3$ having the smallest errors thus implying the best correlations with the HRR.

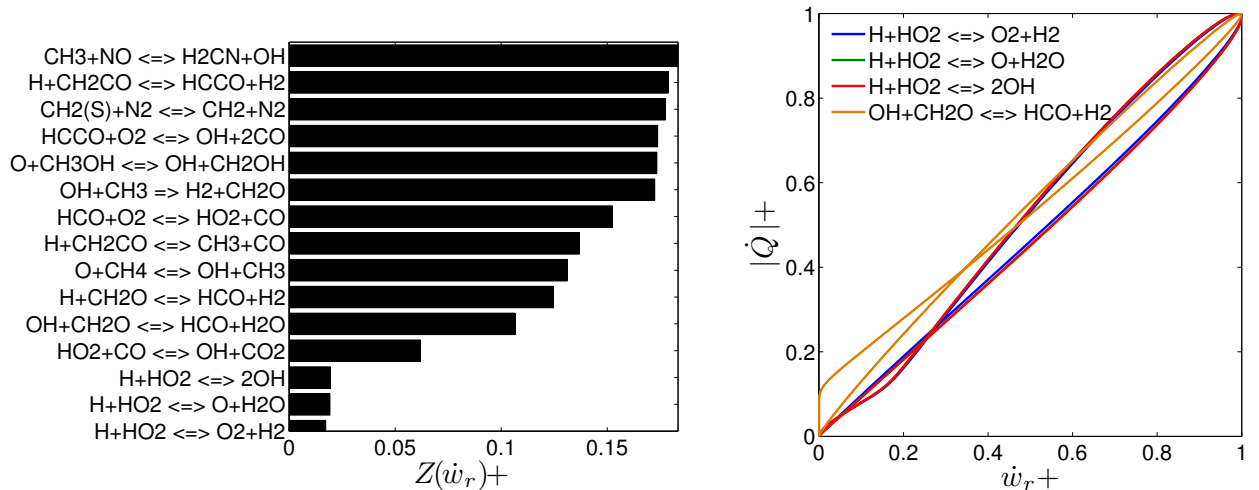


Figure 6.5: Methane-air, $\phi=0.5$, $T_r=800$ K, $p=1$ atm.

Therefore it is clear that HRR correlation is strongly dependent on the equiv-

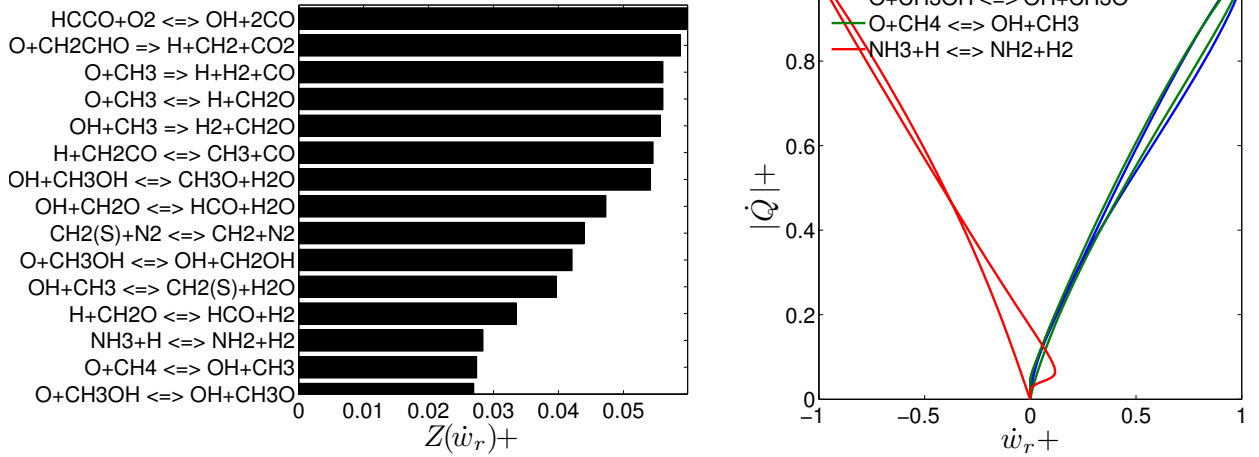


Figure 6.6: Methane-air, $\phi=1.0$, $T_r=800$ K, $p=1$ atm.

alence ratio. In the hope to find a reasonable correlation across ϕ , the ϕ -averaged error $\bar{Z} = \sum_{\phi} Z/N_{\phi}$ where N_{ϕ} is the total number of ϕ samples considered, can be used to extract the reaction with the best overall correlation across different stoichiometry. Towards this goal, and with lean combustion in mind, computations of laminar premixed flames for $0.5 \leq \phi \leq 1.0$ in steps of 0.1 have been conducted and \bar{Z} calculated for all reactions. In a similar manner to the analysis using Z , the reactions are ranked based on the value of \bar{Z} . The results are shown in Fig. 6.7, using the GRI-3.0 [73] and the San Diego [106] mechanisms. As noted in the introduction, the observed correlations depend on the chemical mechanism used. The use of the San Diego mechanism will help to elucidate this dependence and to see whether the same reactions showing the smallest \bar{Z} for GRI-3.0, also show the same trend for a different mechanism. Reactions ranking high in both mechanisms would thus imply possibly good HRR correlations for that particular reaction irrespective of the mechanism used. The results are shown in Fig. 6.7 on the right. Overall, \bar{Z} is generally larger for the San Diego mechanism implying reduced spatial HRR correlations for the same reaction. However, the reaction $\text{H} + \text{HO}_2 = \text{O}_2 + \text{H}_2$ ranks 1st and 4th using the GRI and San Diego mechanisms respectively, while the reaction $\text{H} + \text{HO}_2 = \text{O} + \text{H}_2\text{O}$ ranks 2nd and 1st. The reaction $\text{OH} + \text{CH}_2\text{O} = \text{HCO} + \text{H}_2\text{O}$ commonly used for the HRR marker, ranks 6th for GRI-3.0 and it does not even appear in the top 15 reactions for the San Diego

mechanism. The reactions $\text{O} + \text{CH}_4 = \text{OH} + \text{CH}_3$ and $\text{H} + \text{CH}_2\text{O} = \text{HCO} + \text{H}_2$ are found to rank high for both mechanisms.

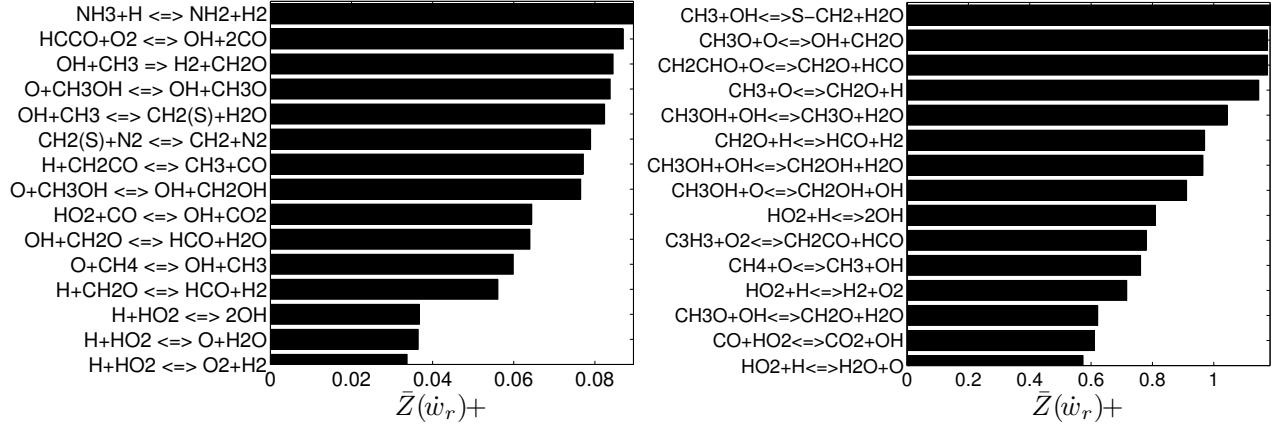


Figure 6.7: ϕ -averaged $Z(\dot{w}_r)^+$ across $\phi=0.5-1.0$ in steps of 0.1, using GRI-3.0 (left) and San Diego (right) mechanisms.

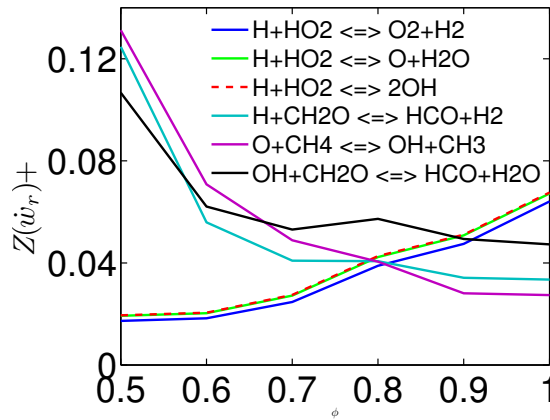


Figure 6.8: $Z(\dot{w}_r)^+$ of the top six reactions in Fig. 6.7 against ϕ .

To shed some light into the performance of these markers for different equivalence ratios, one can study the $Z^+(\dot{w}_r)$ variation with ϕ . This variation is shown in Fig. 6.8 for the top six reactions appearing in Fig. 6.7, using GRI-3.0 which shows the smaller Z . For lean mixtures, the reactions $\text{H} + \text{HO}_2 = \text{O}_2 + \text{H}_2$ and $\text{H} + \text{HO}_2 = \text{O} + \text{H}_2\text{O}$ have the smallest errors and thus the best correlations with the HRR. The reaction $\text{H} + \text{HO}_2 = 2\text{OH}$ shows almost the same variation in error

as the reaction $\text{H} + \text{HO}_2 = \text{O} + \text{H}_2\text{O}$. The reaction $\text{OH} + \text{CH}_2\text{O} = \text{HCO} + \text{H}_2\text{O}$ has a much larger error than either of the above two reactions, implying a reduced correlation. As stoichiometry is approached, the error associated with the reaction $\text{OH} + \text{CH}_2\text{O} = \text{HCO} + \text{H}_2\text{O}$ decreases, and for $0.8 \leq \phi \leq 1.0$ becomes smaller than the error associated with the above two reactions implying a better HRR correlation. However, at the same time the errors associated with the reactions $\text{O} + \text{CH}_4 = \text{OH} + \text{CH}_3$ and $\text{H} + \text{CH}_2\text{O} = \text{HCO} + \text{H}_2$ also decrease and become less than the error for $\text{OH} + \text{CH}_2\text{O} = \text{HCO} + \text{H}_2\text{O}$ when $\phi \geq 0.7$. Thus, these results suggest that for very lean mixtures the rate of the reactions $\text{H} + \text{HO}_2 = \text{O}_2 + \text{H}_2$ or $\text{H} + \text{HO}_2 = \text{O} + \text{H}_2\text{O}$, would serve as an un-ambiguous and good HRR marker, while for near-stoichiometric mixtures the rate of the reactions $\text{O} + \text{CH}_4 = \text{OH} + \text{CH}_3$ or $\text{H} + \text{CH}_2\text{O} = \text{HCO} + \text{H}_2$ seem a better choice. It is important to note at this point that the reaction $\text{OH} + \text{CH}_2\text{O} = \text{HCO} + \text{H}_2\text{O}$ was found not to be the primary source of formyl radicals in [55], which explains the increased error associated with this reaction observed in the current study. Instead, the reaction $\text{H} + \text{CH}_2\text{O} = \text{HCO} + \text{H}_2$ was found by [55] to be the major HCO formation path, which explains the relatively lower error associated with this reaction, since as already mentioned HCO correlates strongly with the HRR.

As already mentioned in the introduction, the derivation of HRR markers in past studies [51, 52, 53, 55] was primarily based on laminar flame computations. Thus the effect of turbulence on the proposed correlations was not examined, and it is important to note that reactions showing high correlations for the laminar flames may not necessarily show high correlations for the turbulent case also, due to the effects of curvature and strain rate induced by turbulence. It is well known that these effects can impart different levels of influence on different species because of the difference in their molecular diffusivities and Lewis numbers. For example the curvature can strongly affect the spatial variation of lighter species such as atomic hydrogen. Thus, the proposed correlations of this study are tested for turbulent flames using the DNS data described in section 6.1. Figure 6.9 shows a scatter plot of the HRR against the forward rates of reactions $\text{OH} + \text{CH}_2\text{O} = \text{HCO} + \text{H}_2\text{O}$ and $\text{H} + \text{CH}_2\text{O} = \text{HCO} + \text{H}_2$, for case C in Table 3.2. The reactions $\text{O} + \text{CH}_4 = \text{OH} + \text{CH}_3$ and $\text{H} + \text{HO}_2 = \text{O} + \text{H}_2\text{O}$ do not take place in the mechanism used for the DNS [109], hence these relationships

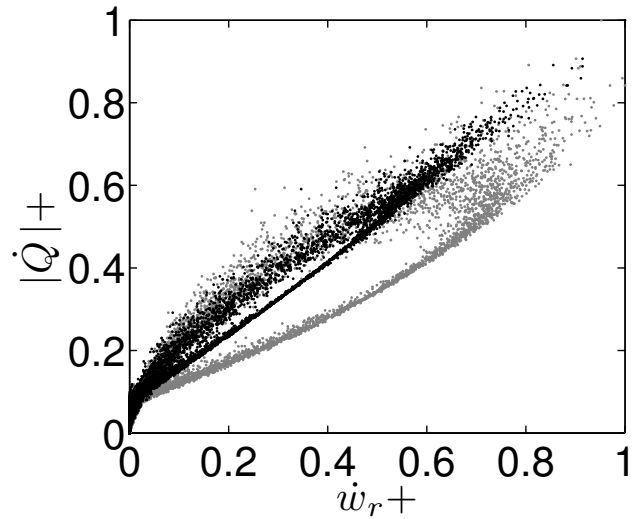


Figure 6.9: Scatter plot of heat release rate against the rates of $\text{OH} + \text{CH}_2\text{O} \Rightarrow \text{HCO} + \text{H}_2\text{O}$ (grey dots) and $\text{H} + \text{CH}_2\text{O} \Rightarrow \text{HCO} + \text{H}_2$ (black dots) for case C in [143], using the rate constants from Smooke's mechanism [109]

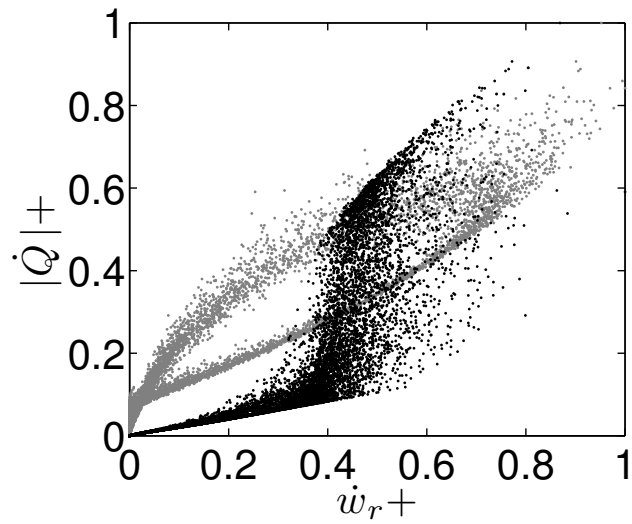


Figure 6.10: Scatter plot of heat release rate against the rates of $\text{OH} + \text{CH}_2\text{O} \Rightarrow \text{HCO} + \text{H}_2\text{O}$ (grey dots) and $\text{H} + \text{HO}_2 \Rightarrow \text{O}_2 + \text{H}_2$ (black dots) for case C in [143], using the rate constants from Smooke's mechanism [109].

cannot be tested. All quantities are normalised with respect to their instantaneous maximum values, and consistent with the results shown in Fig. 6.8, the reaction $\text{H} + \text{CH}_2\text{O} = \text{HCO} + \text{H}_2$ shows a clearly improved correlation with the HRR compared to the reaction $\text{OH} + \text{CH}_2\text{O} = \text{HCO} + \text{H}_2\text{O}$. In particular, the scatter is reduced significantly, and the linearity of the correlation is also improved. The results in Fig. 6.8 also show the reactions $\text{H} + \text{HO}_2 = \text{O}_2 + \text{H}_2$ and $\text{H} + \text{HO}_2 = 2\text{OH}$ to have smaller errors than the commonly used marker. Figure 6.10 shows the HRR against the rate of $\text{H} + \text{HO}_2 = \text{O}_2 + \text{H}_2$. Consistent with the results in Fig. 6.5, this reaction correlates better with the HRR in regions of low to intermediate HRR. At zero reaction rate, the HRR is observed to be zero as well, suggesting that this reaction may capture local extinction. Similar results were also observed to hold for $\text{H} + \text{HO}_2 = 2\text{OH}$. For intermediate to high HRR however, the commonly used marker seems to perform better, suggesting that in regions of intense HRR it is a more reliable marker than the H and HO_2 based marker.

In order to examine the influence of the chemical mechanism used in the DNS on the proposed HRR correlations, Fig. 6.12 shows the correlations of some of the top-correlating reactions using both GRI-3.0 [73] and Smooke’s mechanism as used in the DNS [109], for the stoichiometric case. It is clear that there is a large difference on the HRR correlation for the reaction $\text{H} + \text{HO}_2 \rightleftharpoons \text{O}_2 + \text{H}_2$, similar to the one observed with the DNS data. This suggests that the poor correlation observed in the DNS data for relatively large values of the HRR is due to the chemical mechanism used (Smooke’s mechanism) and not because of the correlation itself. Another important point is that the correlations of the other two reactions are relatively insensitive to the chemical mechanism used. This implies that the good correlation observed for $\text{H} + \text{CH}_2\text{O} \rightleftharpoons \text{HCO} + \text{H}_2$ is not biased in any way when using Smooke’s mechanism.

The performance of the marker $\text{H} + \text{CH}_2\text{O} = \text{HCO} + \text{H}_2$ is also evaluated using a mild combustion DNS database. This database, corresponding to case B in [143], involves a methane-air mixture diluted with combustion products, at a turbulence level of $u_{rms}/s_l=9.88$. The results are shown in Fig. 6.11. Both the commonly used marker and $\text{H} + \text{CH}_2\text{O} = \text{HCO} + \text{H}_2$ show a significant scatter across all HRR values, with the majority of the points however falling on an

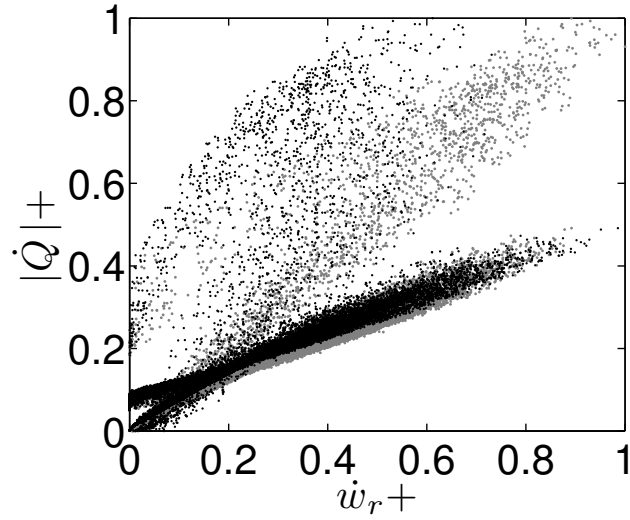


Figure 6.11: Scatter plot of heat release rate against the rates of $\text{OH} + \text{CH}_2\text{O} \Rightarrow \text{HCO} + \text{H}_2\text{O}$ (grey dots) and $\text{H} + \text{CH}_2\text{O} \Rightarrow \text{HCO} + \text{H}_2$ (black dots), for mild combustion case B in [143], using the rate constants from Smooke's mechanism [109].

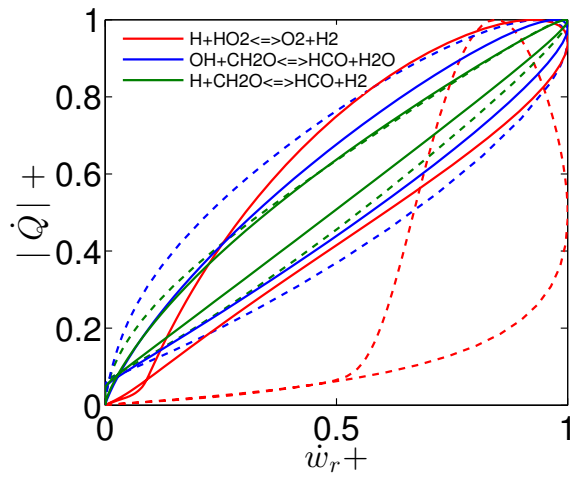


Figure 6.12: A comparison of the top HRR-correlating reactions using GRI-3.0 [73] (continuous lines) and Smooke [109] (dashed lines) mechanisms. The results are for a stoichiometric methane-air laminar flame.

almost straight line for both cases. In agreement with the results in Fig. 6.9, $\text{H} + \text{CH}_2\text{O} = \text{HCO} + \text{H}_2$ seems to be showing a relatively lower scatter suggesting that it may be a more reliable HRR marker, despite the chemical complexity of this fuel.

6.4 Multi-component fuel-air mixtures

In this section a similar analysis is carried out for a multi-component fuel mixture, as noted earlier. This fuel consists of $\text{CO}, \text{H}_2, \text{H}_2\text{O}, \text{CO}_2$ and CH_4 in the proportions given in Table 3.2. Figures 6.13 and 6.14 show f_{qr} for $\phi=0.5$ and 1.0 respectively, obtained using GRI-3.0. For both equivalence ratios the reaction $\text{OH} + \text{CO} = \text{H} + \text{CO}_2$ has the highest fractional influence followed by the recombination reaction $\text{H} + \text{O}_2 + \text{H}_2\text{O} = \text{HO}_2 + \text{H}_2\text{O}$. However, for both conditions the recombination reaction appears to have the best correlation with the HRR as one can see from the corresponding figures on the right, despite the fact that it contributes only about 10% to the total HRR, whereas the reaction $\text{OH} + \text{CO} = \text{H} + \text{CO}_2$ contributes in both cases by more than 30%.

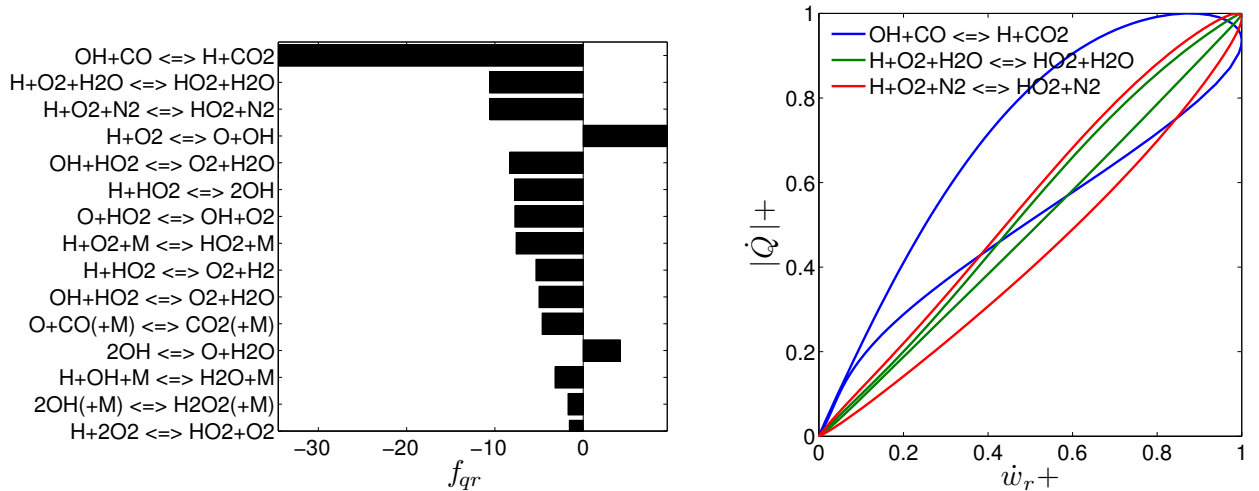


Figure 6.13: Multi-component fuel mixture, $\phi=0.5$, $T_r=800$ K, $p=1$ atm.

The results obtained using the error-estimator analysis are shown in Figs. 6.15 and 6.16, for the mass densities of various species. The error is minimum for the concentration of HCO only for the stoichiometric mixture. However, this

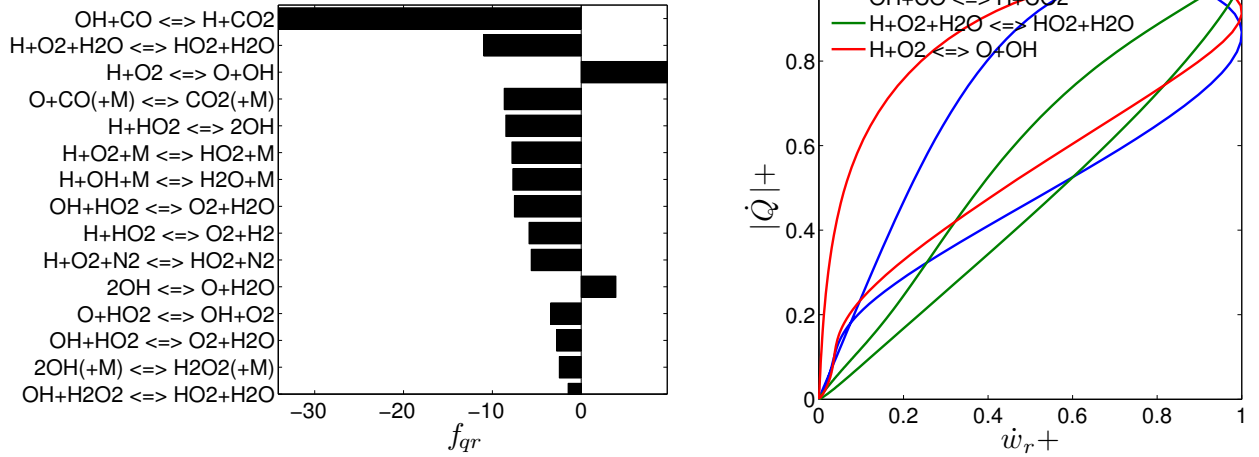


Figure 6.14: Multi-component fuel mixture, $\phi=1.0$, $T_r=800$ K, $p=1$ atm.

minimum error is observed to be significantly larger than the corresponding error for the stoichiometric methane-air mixture shown in Fig. 6.4. The influence of this increased error is reflected in the relatively poorer correlation with the HRR shown in Fig. 6.16. Thus, these results suggest that more than one species may be required for a good HRR correlation for the multi-component fuel-air mixture, although the carbon oxidation is expected to be through the methyl radical for this fuel mixture.

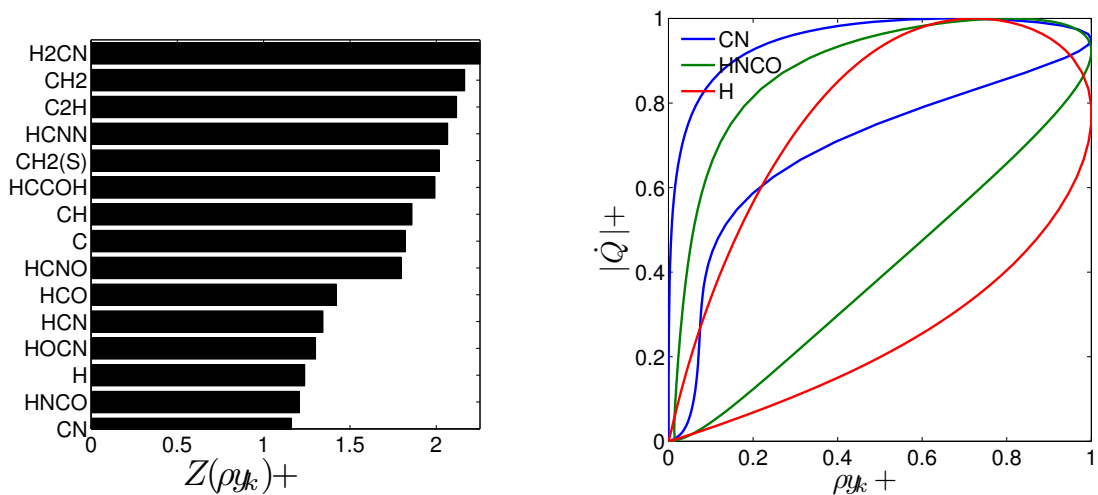


Figure 6.15: Multi-component fuel mixture, $\phi=0.5$, $T_r=800$ K, $p=1$ atm.

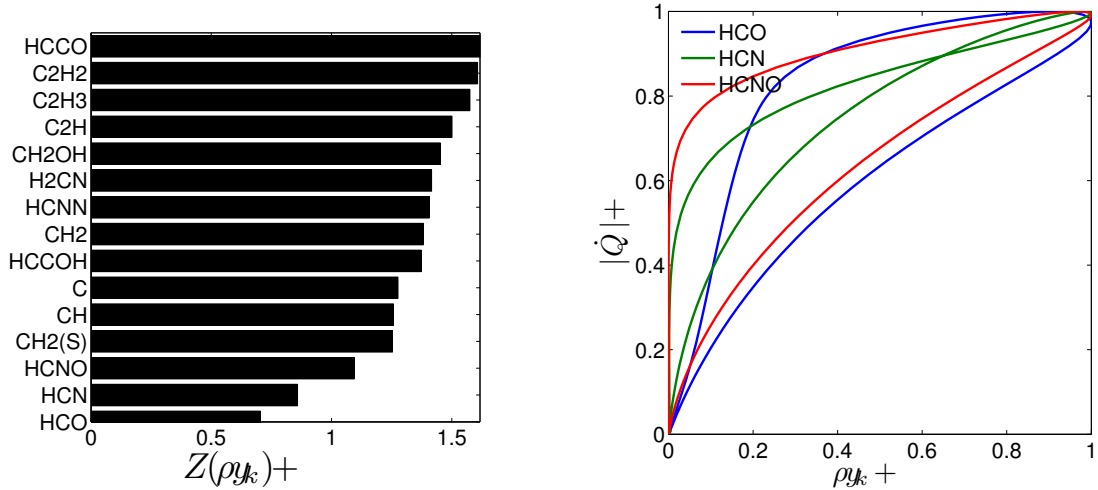


Figure 6.16: Multi-component fuel mixture, $\phi=1.0$, $T_r=800$ K, $p=1$ atm.

Figures 6.17 and 6.18 show $Z(\dot{w}_r)$ for $\phi=0.5$ and 1.0 respectively. For lean mixtures the reaction $\text{H} + \text{O}_2 + \text{H}_2\text{O} = \text{HO}_2 + \text{H}_2\text{O}$ gives the smallest error and the best HRR correlation among the top three reactions identified. At stoichiometric conditions this reaction is trumped by the reaction $\text{H} + \text{O}_2 + \text{M} = \text{HO}_2 + \text{M}$. It is important to note at this point that despite the fact that both of the above two reactions are third-body recombination reactions each one appears separately in the the GRI-3.0 dataset since the third body efficiency for H_2O in $\text{H} + \text{O}_2 + \text{M} = \text{HO}_2 + \text{M}$ is zero (see Eq. 6.5). For both equivalence ratios considered, the commonly used marker (rate of $\text{OH} + \text{CH}_2\text{O} = \text{HCO} + \text{H}_2$) does not appear in the top 15 reactions. This was also observed in the previous chapter where this commonly used correlation was tested.

Following a similar analysis as in the previous section, Fig. 6.19 shows \bar{Z} averaged across $0.5 \leq \phi \leq 1.0$ in steps of 0.1. This is done using both GRI-3.0 [73] and Li et al. [84] mechanisms. The third body recombination reaction $\text{H} + \text{O}_2 + \text{M} = \text{HO}_2 + \text{M}$ is found to rank 1st and 3rd using the GRI-3.0 and Li et al. mechanisms respectively, while the reaction $\text{O} + \text{HO}_2 = \text{OH} + \text{O}_2$ ranks 3rd and 1st respectively, indicating that these reactions are strong candidates to mark HRR. Overall though one may observe from Fig. 6.19, that the errors using the Li et al. mechanism are generally higher than using GRI-3.0, implying that the correlation for the same reaction is generally weaker. Thus, in order to

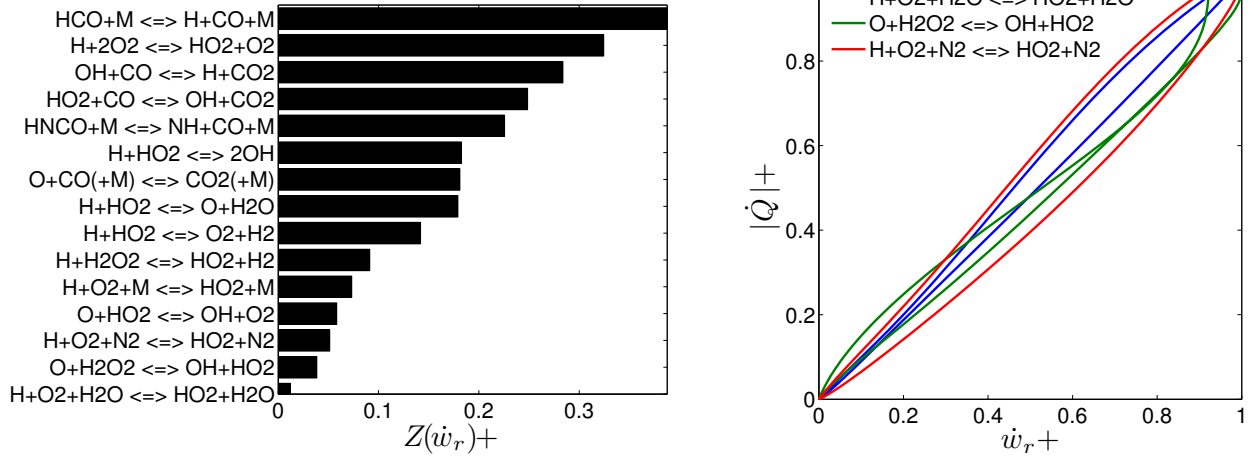


Figure 6.17: Multi-component fuel mixture, $\phi=0.5$, $T_r=800$ K, $p=1$ atm.

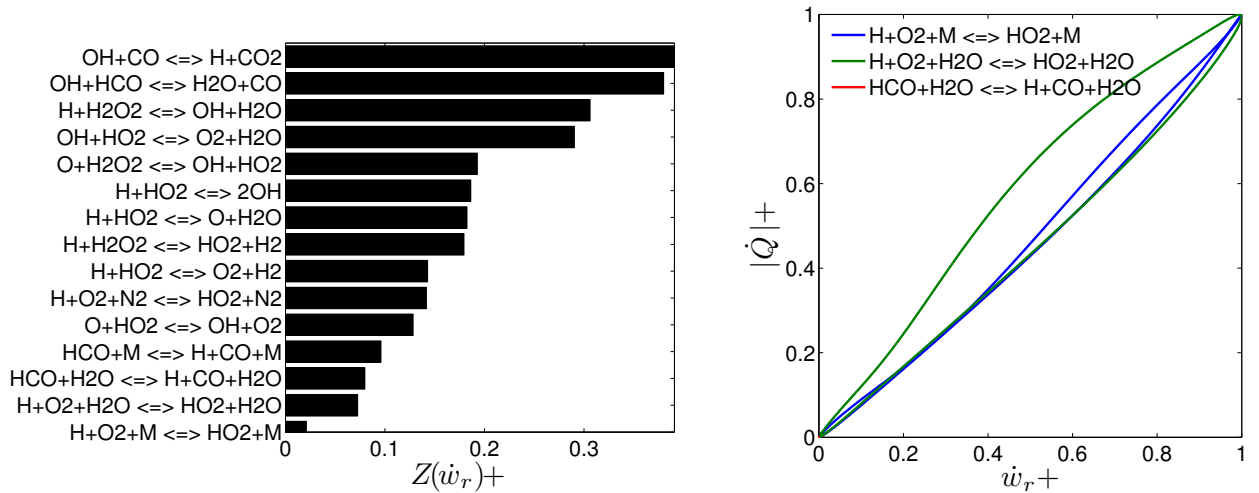


Figure 6.18: Multi-component fuel mixture, $\phi=1.0$, $T_r=800$ K, $p=1$ atm.

examine the error variation with the equivalence ratio, the top three reactions of Fig. 6.19 using GRI-3.0 are considered. The results are shown in Fig. 6.20. The reaction $O + HO_2 = OH + O_2$ has larger errors compared with the other two reactions. The recombination reaction $H + O_2 + H_2O = HO_2 + H_2O$ has a smaller error than the reaction $H + O_2 + M = HO_2 + M$ at lean conditions. This behaviour changes at $\phi \simeq 0.7$ indicating that for near-stoichiometric conditions the rate of the reaction $H + O_2 + M = HO_2 + M$ is a better marker for the HRR.

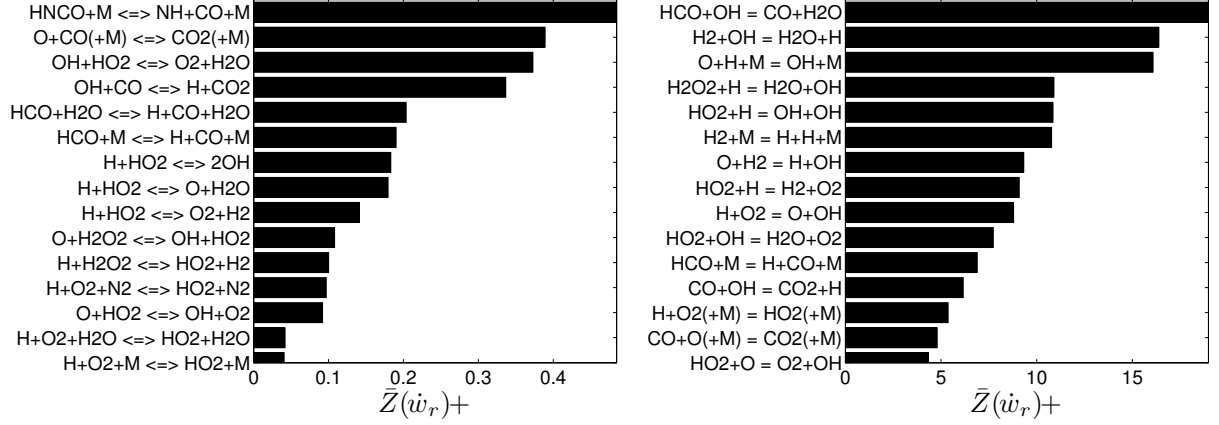


Figure 6.19: ϕ -averaged $Z(\dot{w}_r)$ across $\phi=0.5-1.0$ in steps of 0.1, using GRI-3.0 (left) and Li et al. (right) mechanisms.

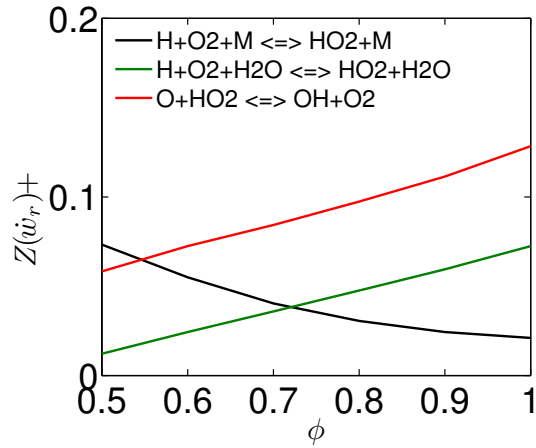


Figure 6.20: $Z(\dot{w}_r)^+$ of the top three reactions in Fig. 6.19 against ϕ .

The reverse rate of $\text{H} + \text{O}_2 + \text{M} = \text{HO}_2 + \text{M}$ is found to be negligible in comparison with the forward rate of this reaction, and thus the net rate is given by:

$$\dot{w}_r \simeq k_f[\text{H}][\text{O}_2] \sum_{\alpha} \eta_{\alpha}[c_{\alpha}] \quad (6.4)$$

where η_{α} is the third body efficiency of species α , and k_f is the forward rate of this reaction. Equation 6.4 suggests that the experimental estimation of this

rate requires in addition to $[H]$ and $[O_2]$, the concentrations of all species which have non-zero third body coefficients. This is of course impossible since there are $O(50)$ species present with non-zero third body coefficients. This issue can be alleviated by noting, as Eq. 6.3 suggests, that we are not in fact interested in the quantitative measurement of the rate of this reaction. We are rather interested in capturing a reasonably correct variation of the rate of this reaction across the flame brush, and how this correlates with the HRR as per Eq. 6.3. Rigorous analysis employing different species involved in the list of third body species for this reaction, revealed CO and CO_2 to primarily influence this variation. Thus, considering the third body efficiencies of these species only, taken from GRI-3.0, one can estimate this variation using:

$$\dot{w} \sim T^{-0.86} [H][O_2](0.75[CO] + 1.5[CO_2]) \quad (6.5)$$

Figure 6.21 shows the net rate of $H + O_2 + M = HO_2 + M$ and that using Eq. 6.5 normalised with respect to their corresponding maximum values. It is clear that Eq. 6.5 captures the variation of this rate across the flame brush very well, and as a result Eq. 6.5 is expected to show the same (good) correlation with the HRR. To validate these results, Fig. 6.22 shows scatter plots of the normalised HRR against the normalised rate of $OH + CH_2O = HCO + H_2$ and Eq. 6.5. The commonly used flame marker shows a poor correlation with the HRR, and it was shown in Chapter 5 that this is not a result of the turbulence-scalar interaction. The flame marker calculated from Eq. 6.5 on the other hand, shows an almost linear correlation with the HRR with minimal scatter, for both turbulence levels considered.

Figure 6.23 shows the normalised heat release rate against the rate of the reaction $OH + CH_2O = HCO + H_2$, and of $O + HO_2 = OH + O_2$ which is found to rank high in Fig. 6.19. Although this reaction shows a larger error in comparison with $H + O_2 + M = HO_2 + M$, it has no temperature dependence in both the GRI-3.0 and Li et al. datasets [84], and may thus be easier for laser diagnostics, but one need to image O and HO_2 . Consistent with the previous analysis which revealed the rate of $O + HO_2 = OH + O_2$ to have a larger error, it shows a poorer correlation with the HRR in comparison to the rate of the third body

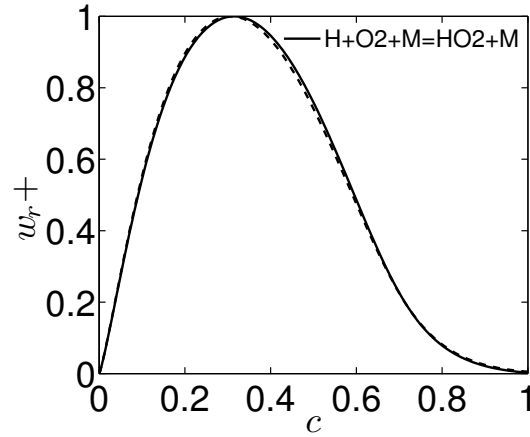


Figure 6.21: Normalised rate of $\text{H} + \text{O}_2 + \text{M} = \text{HO}_2 + \text{M}$ and Eq. 6.5 (dashed line) across the flame brush.

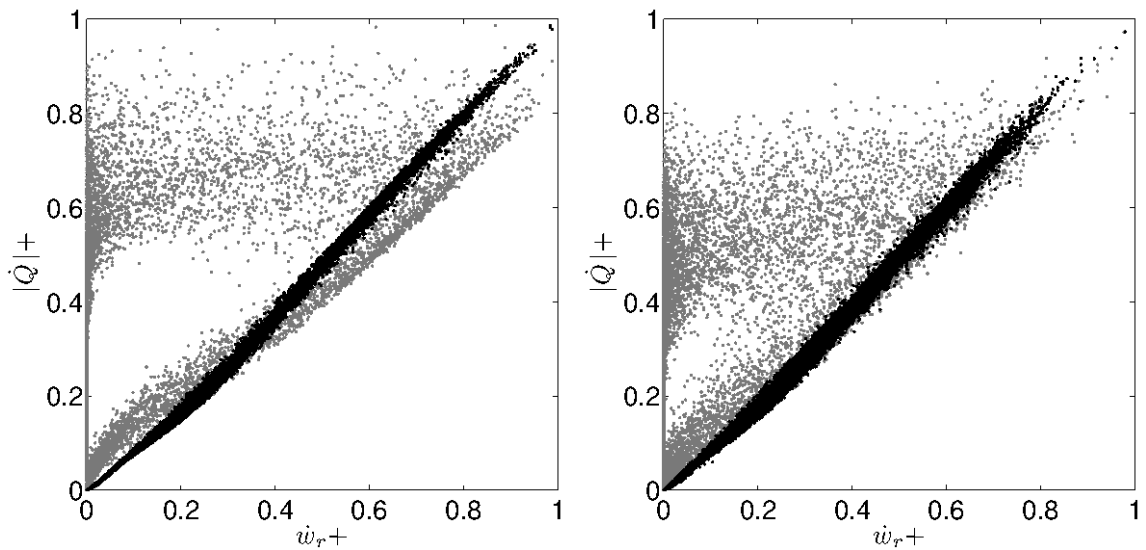


Figure 6.22: Scatter plot of heat release rate for case A (left), and case C (right), against the rate of $\text{OH} + \text{CH}_2\text{O} \Rightarrow \text{HCO} + \text{H}_2\text{O}$ (grey dots) and using Eq. 6.5 (black dots).

reaction. However, as one can see from Fig. 6.23, $\text{O} + \text{HO}_2 = \text{OH} + \text{O}_2$ also gives an improved correlation with the HRR compared to the commonly used flame markers. Furthermore, the results shown in Fig. 6.19 suggest that these proposed correlations will be improved for leaner mixtures, which are of practical

interest. The validity of these correlations for mixtures with higher H_2 levels and in non-premixed combustion is a subject of future work.

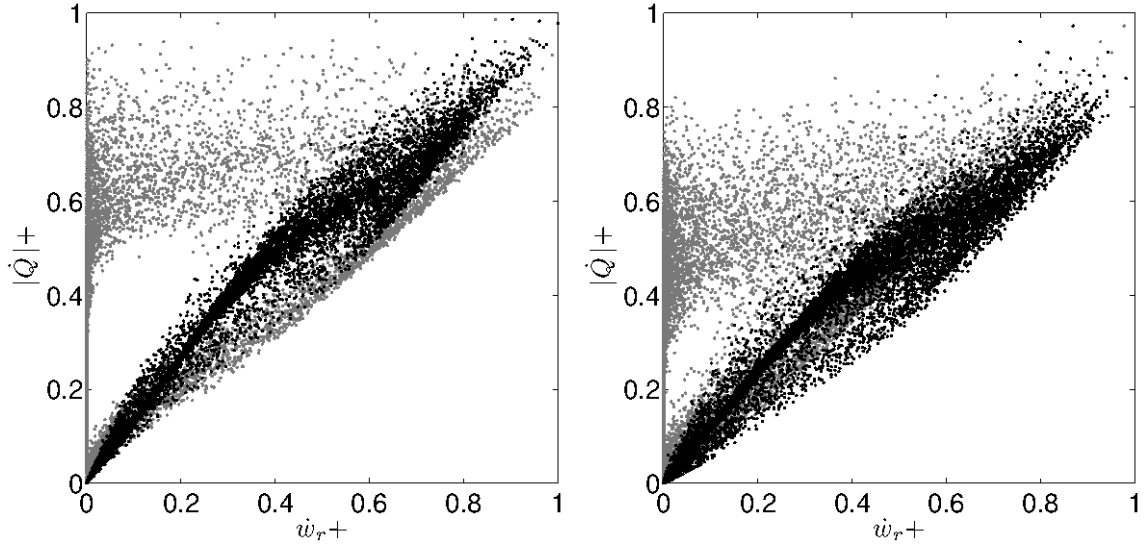


Figure 6.23: Scatter plot of heat release rate for case A (left) and case C (right), against the rate of $OH + CH_2O \Rightarrow HCO + H_2O$ (grey dots) and the rate of $O + HO_2 \Rightarrow OH + O_2$ (black dots).

Following a similar analysis to section 6.3 Fig. 6.24 shows the correlations of the proposed markers using both GRI-3.0 [73] and the skeletal mechanism of Nikolaou et al. [38]. It is clear that the correlations are relatively insensitive to the use of the skeletal mechanism. As a result, the skeletal mechanism does not in any way influence the good correlations observed with the DNS data in Figs. 6.22 and 6.23.

6.5 Proposed HRR markers

Table 6.1 shows a summary of all the previous analysis, essentially encapsulating the results shown in Figs. 6.7, 6.8, 6.19 and 6.20. Table 6.1 shows the range of equivalence ratios where each reaction has an improved correlation with the HRR as opposed to the commonly used marker. Also shown is the validation procedure (DNS, laminar) for the proposed correlations. It was shown in section 6.3, that the chemical mechanism used in the methane DNS introduces a bias in the HRR

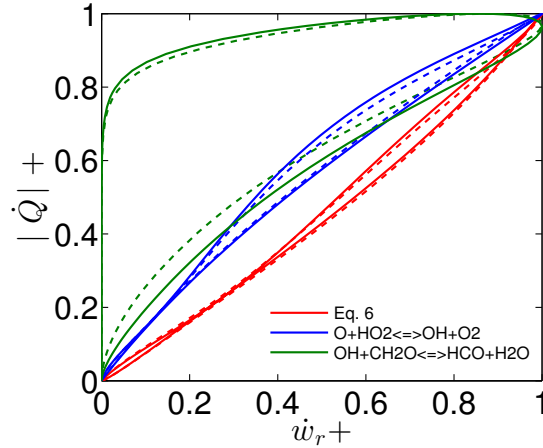


Figure 6.24: A comparison of the top HRR-correlating reactions using GRI-3.0 [73] (continuous lines) and Nikolaou et al. [38] (dashed lines) mechanisms.

correlation for the first three reactions. As a result, the DNS correlations for these reactions cannot be considered plausible. These reactions involving, H and HO₂, were however validated in the laminar case, and were shown to give improved correlations for $\phi \lesssim 0.9$ as per Fig. 6.7. For relatively lean to stoichiometric conditions, the reactions $\text{H} + \text{CH}_2\text{O} \rightleftharpoons \text{HCO} + \text{H}_2\text{O}$ and $\text{O} + \text{CH}_4 \rightleftharpoons \text{OH} + \text{CH}_3$ also give improved correlations with the HRR. For the multi-component fuel flame the third body reaction $\text{H} + \text{O}_2 + \text{M} \rightleftharpoons \text{HO}_2 + \text{M}$ from which Eq. 6.5 was derived, is observed to give very good HRR correlations for relatively lean to stoichiometric mixtures. Although the reaction $\text{O} + \text{HO}_2 \rightleftharpoons \text{OH} + \text{O}_2$ has a slightly poorer correlation with the HRR, laminar flame computations suggest it to perform better for very lean conditions.

It is important to note at this point that despite the drawbacks associated with the $[\text{OH}][\text{CH}_2\text{O}]$ correlation, it is widely used because it is easy to measure. Although the $[\text{OH}][\text{CH}_2\text{O}]$ correlation does not provide equally good quantitative results, it can still be used to mark locations of increased chemical activity. The alternative correlations proposed in this study provide improved quantitative correlations but require the simultaneous measurement of more than one species, some of which may be difficult to measure. These markers should thus be taken

Fuel	ϕ	Reaction	Validation
CH ₄	≤ 0.9	$\text{H} + \text{HO}_2 \rightleftharpoons \text{O}_2 + \text{H}_2$	Laminar
CH ₄	≤ 0.9	$\text{H} + \text{HO}_2 \rightleftharpoons \text{O} + \text{H}_2\text{O}$	Laminar
CH ₄	≤ 0.9	$\text{H} + \text{HO}_2 \rightleftharpoons 2\text{OH}$	Laminar
CH ₄	0.6-1.0	$\text{H} + \text{CH}_2\text{O} \rightleftharpoons \text{HCO} + \text{H}_2\text{O}$	DNS ($\phi=0.8$) [143]+Laminar
Dilluted-CH ₄	-	$\text{H} + \text{CH}_2\text{O} \rightleftharpoons \text{HCO} + \text{H}_2\text{O}$	DNS ($\phi=0.8$) [143]
CH ₄	0.7-1.0	$\text{O} + \text{CH}_4 \rightleftharpoons \text{OH} + \text{CH}_3$	Laminar
Multi-component	≥ 0.55	$\text{H} + \text{O}_2 + \text{M} \rightleftharpoons \text{HO}_2 + \text{M}$, Eq. (6.5)	DNS ($\phi=1.0$) +Laminar
Multi-component	≤ 0.55	$\text{O} + \text{HO}_2 \rightleftharpoons \text{OH} + \text{O}_2$	DNS ($\phi=1.0$) +Laminar

Table 6.1: The range of equivalence ratios where the respective reactions show improved correlations with the HRR (for the methane and diluted methane mixtures) as opposed to the commonly used marker, using GRI -3.0 [73]. The San Diego [106] and Li et al. [84] mechanisms were also used to confirm these results (see Figs. 6.7 and 6.19). For the multi-component fuel two alternative correlations are proposed.

as a guideline which will help in the future to develop the necessary techniques needed for the measurement of the associated species.

Chapter 7

Modelling

In this chapter, the performance of some commonly used mean reaction rate closures is evaluated against the multi-component fuel DNS data. This is done for the lowest (case A) and highest (case C) turbulence levels given in Table 5.1, both in the RANS and LES context. Details of these models can be found in the sections which follow.

7.1 RANS

In the context of reacting RANS simulations one is required to solve a transport equation for the mean progress variable \tilde{c} , in addition to the conservation equations for mass, momentum, and energy. For high Reynolds numbers, Re , this equation is [58]:

$$\frac{\partial \bar{\rho} \tilde{c}}{\partial t} + \frac{\partial \bar{\rho} \tilde{u}_i \tilde{c}}{\partial x_i} = - \frac{\partial \overline{\rho u_i'' c''}}{\partial x_i} + \overline{\dot{w}_c} \quad (7.1)$$

The above equation has two unclosed terms requiring modelling. These are the progress variable mean reaction rate, $\overline{\dot{w}_c}$, and the turbulent scalar flux, $\overline{\rho u_i'' c''}$. DNS databases are primarily used to derive and validate closures for the progress variable mean reaction rate, $\overline{\dot{w}_c}$, whether in RANS or LES context. As noted in the introduction, the future fuels are more likely to be multi-component including light and heavy gases, and accurate mean reaction rate closures are required for such fuels. In this section, a scalar dissipation rate model and five different

mean reaction rate closures are tested, details of which are given in the following sections.

7.1.1 SDR model

The scalar dissipation rate $N = D(\partial c / \partial x_i)(\partial c / \partial x_i)$, where D is the thermal diffusivity ($\lambda / (\rho C_p)$), is a very important quantity in the study of turbulent reacting flows as it characterizes the turbulent mixing. It is related directly to the heat release rate in both premixed and non-premixed flames, and is involved in flamelet, probability density function and conditional moment closure models of turbulent combustion. As a result, modelling of the mean scalar dissipation rate is of paramount importance. In the study of Swaminathan and Bray [145], a scalar dissipation rate model was developed, by deriving a transport equation for the mean scalar dissipation rate defined as $\tilde{\epsilon}_c = \overline{\rho D(\partial c'' / \partial x_i)(\partial c'' / \partial x_i)} / \bar{\rho}$. An order of magnitude analysis was then conducted in the limit of large Da and Re numbers. In this limit it is safe to assume that $\tilde{N} \simeq \tilde{\epsilon}_c$. The order of magnitude analysis showed that the dominant terms are the dilatation, strain, chemical reaction and dissipation: $T_2 + T_{32} + T_4 - D_2 \simeq 0$, using the same notation as in [145]. This was in contrast to earlier models where the dilatation term was ignored [146, 147, 148, 149]. Using these terms, a simple algebraic closure was proposed [145] for the mean scalar dissipation rate, which was validated at the time using a 2D skeletal chemistry DNS database [21], and a 3D single-step chemistry DNS database [150] with an overall good agreement. The model developed in [145], was based on the assumption that the scalar gradient preferentially aligns with the most compressive principal strain rate. In later studies [151, 130, 152], it was shown that the scalar gradient aligns preferentially with the most extensive principal strain rate in regions of intense heat release, implying that the contribution of turbulence-scalar interaction term, T_{32} , is a sink instead of being a source for scalar gradient generation. To account for this, a revised model for $\tilde{\epsilon}_c$ was proposed in a later study [153]. This model is:

$$\tilde{\epsilon}_{cm} \simeq \frac{1}{\beta'} \left[(2K_c^* - \tau C_4) \frac{s_l}{\delta_l} + C_3 \frac{\tilde{\epsilon}}{\bar{k}} \right] \tilde{c}(1 - \tilde{c}) \quad (7.2)$$

where $C_3=1.5\sqrt{\text{Ka}}/\sqrt{(1+\text{Ka})}$, $C_4=1.1/(1+\text{Ka})^{-0.4}$, and Ka is the Karlovitz number further details of which can be found in [58]. These two terms relate to the source and sink contributions from the turbulence-scalar interaction term, T_{32} . The constant $\beta'=6.7$, and K_c^* depends on the mixture and is obtained from a laminar unstrained flame calculation [153]. For the mixture considered here $K_c^*=0.66\tau$, where the heat release rate parameter is $\tau=(T_p - T_r)/T_r$. The model constant β' appears in the modelling of $(T_4 - D_2)$ appearing in the balance equation of $\tilde{\epsilon}_c$ [154]. In the limit of large Da and Re numbers, i.e. in the flamelet regime: $g=\tilde{c}''^2/\tilde{c}(1-\tilde{c}) \simeq 1$. As a result, the variance, \tilde{c}''^2 , can be estimated from $\tilde{c}(1-\tilde{c})$. β' is found to be a constant and equal to 6.7 in this regime. This may not be entirely valid when the flame thickens substantially at higher turbulence levels. Under such conditions $\tilde{c}(1-\tilde{c})$ over-estimates the progress variable variance significantly, and the value of β' requires to be increased to account for this effect. This can be seen in Fig. 7.1 showing the variation of g with \tilde{c} for the two flames. For both cases it is clear that $g \ll 1$. For case A $g_{max} \simeq 0.5$, and for case C $g_{max} \simeq 0.3$. As a result, for case A $\beta'=6.7$, while $\beta'=9.49$ was found to give improved results for case C.

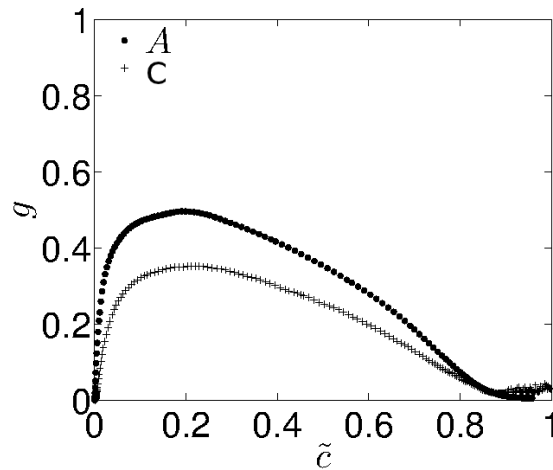


Figure 7.1: $g=\tilde{c}''^2/\tilde{c}(1-\tilde{c})$ for cases A and C. Note that g is much less than unity for both cases.

Figure 7.2 shows the prediction of the model in Eq. 7.2 against $\tilde{\epsilon}_c^+$ as obtained from the DNS for cases A and C respectively. Also shown is \tilde{N}^+ . These quantities

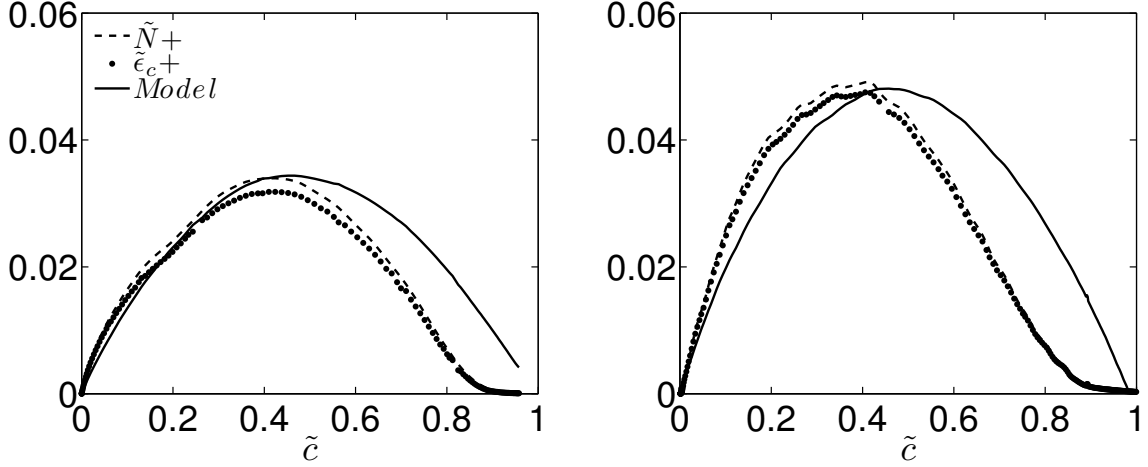


Figure 7.2: Scalar dissipation rate comparison with the model's prediction (Eq. 7.2) for cases A (left) and C (right) . Case A: $\beta=6.70$. Case C: $\beta=9.49$.

are normalized using the reactant values ρ_r , s_l and δ_l . It is clear that for both turbulence levels $\tilde{N}^+ \simeq \tilde{\epsilon}_c^+$. This shows that the high Re number assumption used in the model development is justified even for the multi-component fuel flame. For both cases Eq. 7.2 gives a good agreement with the DNS data especially in the range $0.0 \leq \tilde{c} \leq 0.5$. For higher \tilde{c} values the model slightly over-estimates the mean scalar dissipation rate. As one can observe from Fig. 7.1, this is owing to the larger over-estimation of the progress variable variance since g decreases for higher \tilde{c} . This behaviour results from the wider distribution of the heat release rate for the multi-component fuel flame in regions well after the location of peak heat release rate. Overall, this model gives a reasonable agreement with the DNS data despite the chemical complexity of the fuel mixture. It is important to remind ourselves at this point that the performance of this model in actual RANS also depends on the turbulence closure used. In particular, a $k - \epsilon$ model [155, 156] is usually used, and this will have a direct effect on the performance of the SDR model. DNS is useful in this regard in that the performance of Eq. 7.2 can be isolated from the turbulence closure used.

7.1.2 Reaction rate closures

In this section the performance of five different mean reaction rate models is examined using the DNS data. These are the Eddy Break Up (EBU) model [157, 158], the algebraic closure of Bray [159], the unstrained flamelet model [160], the generalized flame surface density (FSD) model [61, 62, 63, 64, 65], and a strained flamelet model [58]. These models are briefly described in the following sections.

(1) Eddy Break Up model (EBU) [157, 158]:

$$\overline{\dot{w}_c} = C_{ebu} \bar{\rho} \frac{\tilde{\epsilon}}{k} \tilde{c} (1 - \tilde{c}) \quad (7.3)$$

where C_{ebu} is the model constant usually of the order unity. In this study, $C_{ebu}=3.26$ for case A and 2.43 for case C. These values are found to give improved agreement with the DNS data.

(2) Algebraic closure of Bray [159]:

$$\overline{\dot{w}_c} = \frac{2}{2C_m - 1} \bar{\rho} \tilde{\epsilon}_{cm} \quad (7.4)$$

$$\overline{\dot{w}_c} = \frac{2}{2C_m - 1} \bar{\rho} \tilde{\epsilon}_c \quad (7.5)$$

where $C_m = \overline{c \dot{w}_c} / \overline{\dot{w}_c} = \int_0^1 \zeta w_c(\zeta) f(\zeta) d\zeta / \int_0^1 w_c(\zeta) f(\zeta) d\zeta$, ζ is the sample space variable for the progress variable, and $f(\zeta)$ is the burning mode pdf obtained using the progress variable gradient in the laminar unstrained flame. At this point it is perhaps important to emphasize that the above closure was derived [159] by assuming an infinitely thin flame front. This means that c can take the values 0 or 1 only. Consequently, the pdf is purely bimodal and has a zero burning mode contribution. This regime is known as flamelet combustion. As a result, $\overline{\dot{w}_c}=0$, consistent with the flame undergoing no reaction. A way around this problem was to relax the original assumptions made, and calculate C_m from a canonical flame configuration, such as a laminar unstrained flame. Thus the thinner a flame

is the better the above closure will be. The thicker a flame is, the lower the C_m value and the worst the agreement. In any case C_m should be larger than 0.5 to ensure a positive mean reaction rate. This implies that there is a limiting maximum flame width for which this model may be applied. This limit depends on the progress variable definition and on the mixture thermo-chemical conditions. For this flame C_m is found to be equal to 0.55. Thus in order to test the validity of this model, the mean reaction rate is calculated using both of the above equations and the models will henceforth be referred to as Bray-1 (Eq. 7.4) and Bray-2 (7.5). This will ensure that the scalar dissipation rate model is not in any way affecting the algebraic relationship itself.

(3) Unstrained flamelet model [160]:

$$\overline{\dot{w}_c} = \int_0^1 \dot{w}_{c,lam}(\zeta) f(\zeta) d\zeta \quad (7.6)$$

where ζ is the sample space variable for the progress variable c , and $f(\zeta)$ is a presumed progress variable pdf:

$$f(\zeta) = \frac{1 + \tau\zeta}{1 + \tau\tilde{c}} \tilde{f}(\zeta)$$

where $\tilde{f}(\zeta)$ is taken to be a β -function:

$$\tilde{f}(\zeta) = \frac{1}{C} \zeta^{a-1} (1 - \zeta)^{b-1}$$

and $C = \int_0^1 \zeta^{a-1} (1 - \zeta)^{b-1} d\zeta$, $a = \tilde{c}(1/g - 1)$, $b = (1 - \tilde{c})(1/g - 1)$. Comparisons of the β -pdf with the pdfs extracted from the DNS are discussed in the sections which follow.

(4) Generalized Flame Surface Density (FSD) model [61, 62, 63, 64, 65]:

In FSD modelling an algebraic closure is used for Σ , or a balance equation is solved [161, 162, 163, 164]. In the FSD approach the mean reaction rate, neglecting the contribution of diffusive effects, can be closed as:

$$\overline{\dot{w}_c} = \overline{\rho s_d}|_{c^*} \Sigma \simeq \rho_r s_l \Sigma \quad (7.7)$$

where $\Sigma = \overline{\chi}$ (here in the RANS context), and the bar in Eq. 7.7 denotes the average on a c^* iso-surface. An assumption commonly made is $\overline{\rho s_d}|_{c^*} \simeq \rho_r s_l$. In order to test this assumption for the multi-component fuel Fig. 7.3 shows pdfs of $\rho s_d^+ = \rho s_d / \rho_r s_l$ for different c^* iso-surfaces. Also shown in Table 7.1 is the mean and the standard deviation as extracted from the respective flame surface pdfs. The pdfs are Gaussian-like for both turbulence levels. For case C there is a wider spread of the pdfs and hence an increase in the standard deviation as one can see from Table 7.1. For case A the mean is found to be slightly less than unity for the majority of iso-surfaces considered, and for case C the mean is slightly larger. Nevertheless, in the regime where there is expected to be significant heat release i.e. for $0.1 < c < 0.6$ approximately (see Fig. 5.1 in Chapter 5), the mean is close to unity. Hence the assumption $\overline{\rho s_d}|_{c^*} \simeq \rho_r s_l$ seems to be well satisfied despite the chemical complexity of the fuel, and will thus be used to estimate the mean reaction rate as per Eq. 7.7.

Case A		
c^*	μ	σ
0.1	0.974	0.488
0.32	0.947	0.448
0.5	0.956	0.526
0.7	1.028	0.569
Case C		
c^*	μ	σ
0.1	1.060	1.128
0.32	1.127	1.038
0.5	1.135	1.086
0.7	1.234	1.196

Table 7.1: Mean μ and standard deviation σ calculated using the respective flame surface variable pdfs.

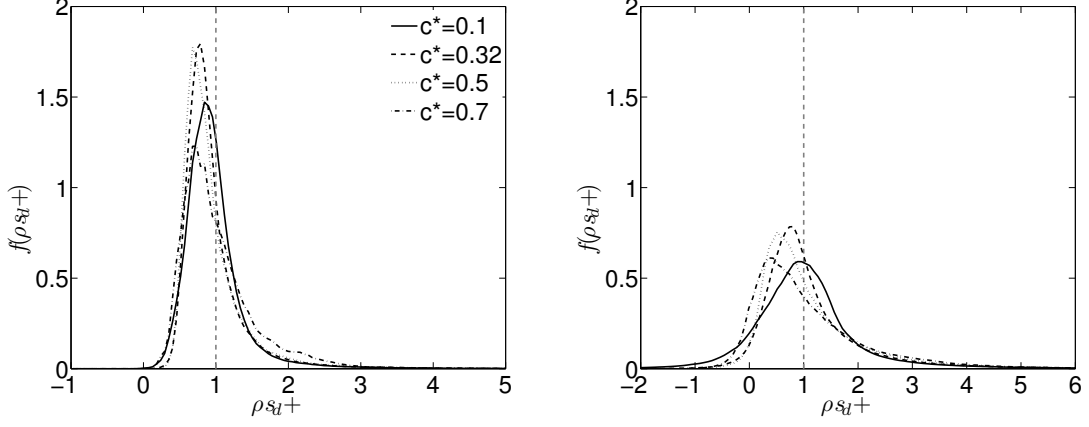


Figure 7.3: Density-weighted displacement speed pdfs, ρ_{sd}/ρ_{sl} , for case A (left) and case C (right).

(5) Strained flamelet model [58]:

$$\overline{\dot{w}_c} = \int_0^1 \int_0^{\psi_{max}} \dot{w}_{c,RTP}(\zeta, \psi) f(\psi|\zeta) f(\zeta) d\psi d\zeta \quad (7.8)$$

In the strained flamelet model the flame is assumed to be an ensemble of strained laminar flamelets. The flamelets are evaluated in the RTP (reactant to product) configuration for increasing strain rate values α . A table is then built $\dot{w}_{c,RTP}(\zeta, \psi)$, where ζ is the sample space variable for c , and ψ is the sample space variable for the strain rate α . The conditional pdf $f(\psi|\zeta)$ is assumed to be log-normal:

$$f(\psi|\zeta) = \frac{1}{(\psi|\zeta)\sigma\sqrt{2\pi}} e^{\frac{-1}{2\sigma^2} [\ln(\psi|\zeta) - \mu]^2}$$

and its shape at each point in the domain depends on the mean conditional scalar dissipation rate $\langle N|\zeta \rangle$. μ is calculated using the relationship: $\langle N|\zeta \rangle = e^{\mu + 0.5\sigma^2}$, and σ is taken to be 0.3 from [58]. The mean conditional scalar dissipation rate is estimated from the relationship [58]:

$$\langle N|\zeta \rangle \simeq \tilde{e}_{cm} N_{RTP}(\zeta) / \int_0^1 N_{RTP}(\zeta) \tilde{f}(\zeta) d\zeta.$$

It is important to note at this point that the variation of the scalar dissipation rate, N , with strain rate, α , in the RTP configuration is assumed to be independent of strain rate. This is a valid assumption in regions well away from extinction [58]. Further details of this model can be found in [58].

Figures 7.4 and 7.5 show the mean progress variable reaction rate estimated using the above five models against the DNS data for cases A and C respectively. The superscript + indicates quantities normalized using ρ_r , s_l and δ_l .

For case A, all models give a reasonable agreement with the DNS data. The EBU model shows the best overall agreement across the flame brush. The algebraic closure of Bray (Eq. 7.4) gives an excellent agreement for $0.6 \leq \tilde{c} \leq 1.0$ but slightly over-estimates the mean reaction rate for $\tilde{c} < 0.6$. If the same model but using Eq. 7.5 is used instead, the agreement becomes somewhat better for $\tilde{c} < 0.6$, but for $\tilde{c} > 0.6$ the mean reaction rate is slightly under-estimated. The discrepancies observed for this model are primarily owing to the finite flame thickness and the departure of the progress variable pdf from the bimodal shape which the model assumes. This is seen more clearly in Fig. 7.1: g is significantly less than unity for case A, indicating that even for the low turbulence level we are not in the flamelet regime. Nevertheless, the model still performs reasonably well. The unstrained flamelet model also shows a good agreement with the DNS data. The FSD model shows a reasonable agreement: it slightly over-estimates the mean reaction rate in the range $0 \leq \tilde{c} \leq 0.5$, while for $\tilde{c} > 0.5$ the mean reaction rate is under-estimated. This may be a result of the lack of straining effects in the model formulation, however excluding the strained flamelet model, straining effects are not included in either of the other models. For example, the unstrained flamelet model shows an improved agreement compared with the FSD model. The strained flamelet model on the other hand shows an excellent agreement for relatively low \tilde{c} values, while at high \tilde{c} values it under-estimates the mean reaction rate and collapses with the FSD model. For relatively low \tilde{c} values turbulence-scalar interaction is stronger and diffusive effects which are not accounted for in the FSD model become important. This may explain the slight over-estimation

when using Eq. 7.7, and in fact Re number effects can be incorporated into the modelled terms of the Σ balance equation to account for this [165].

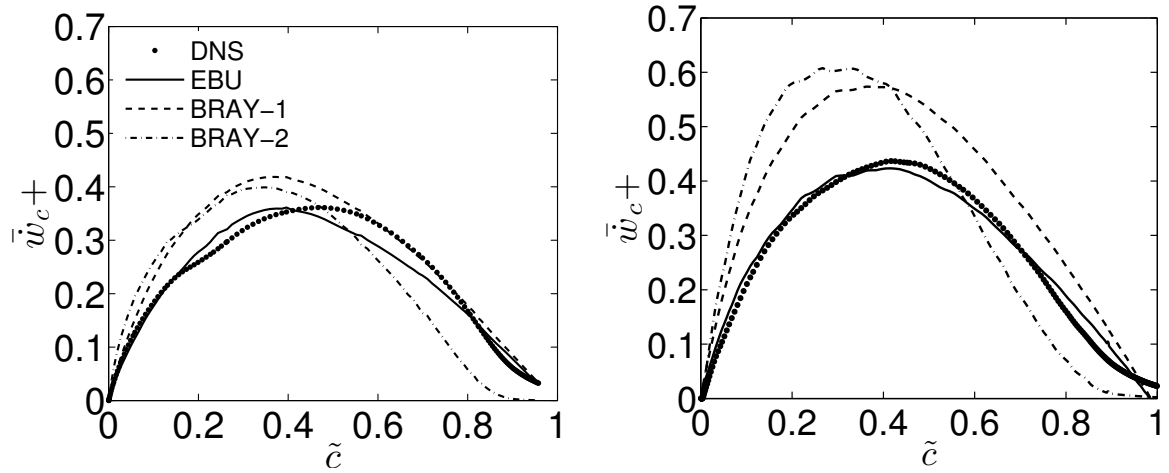


Figure 7.4: EBU model, and Bray's model using $\tilde{\epsilon}_{cm}$ (Bray-1) and $\tilde{\epsilon}_c$ (Bray-2). Case A (left) and case C (right). Case A: $C_{ebu}=3.26$. Case C: $C_{ebu}=2.43$.

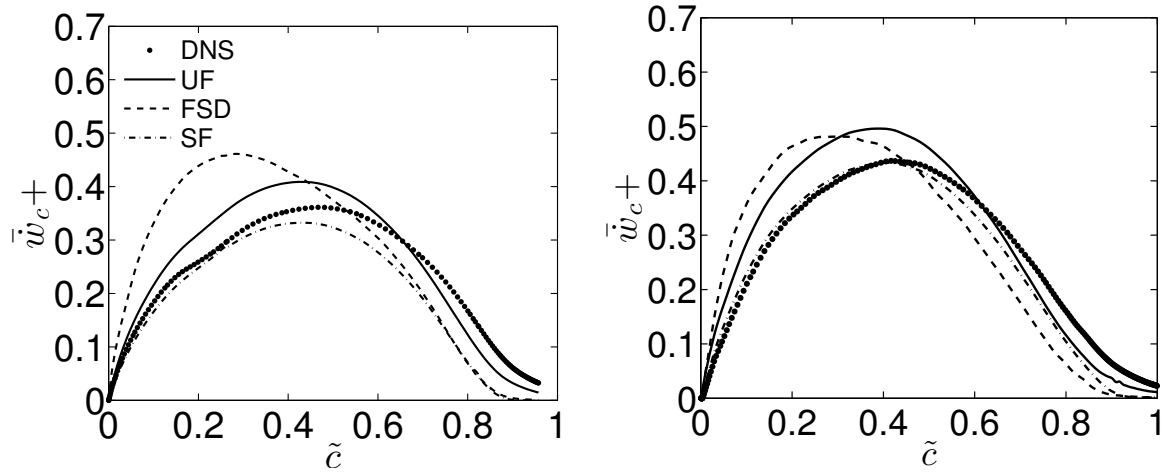


Figure 7.5: Unstrained flamelet model (UF), FSD model and strained flamelet model (SF). Case A (left) and case C (right).

For case C significant differences are observed between the models. The EBU model still gives overall the best agreement. However, this being a freely propa-

gating flame, it is subject to relatively low straining effects. Thus it is not certain how this model will perform for more highly strained configurations. The algebraic closure of Bray although captures well the trend in the mean reaction rate variation across the flame brush, does not perform equally well. Furthermore, the performance of this model is not much affected if the scalar dissipation rate as extracted from the DNS is used instead. This last point made serves to show that this is not a result of the scalar dissipation rate model used in the algebraic closure. It is rather a consequence of the algebraic relationship itself, which may not be valid at higher turbulence levels. As the turbulence level increases it is expected that the burning mode pdf contribution will also increase, with the progress variable pdf becoming less bimodal. With the burning mode pdf contribution increasing, the flame thickens substantially and the validity of Eq. 7.4 is reduced. This is also reflected in Fig.7.1 since g is essentially a measure of the departure from the flamelet regime. For case C, g is smaller than for case A and significantly less than unity, indicating a large departure from the flamelet regime. The unstrained flamelet model performs somewhat poorer compared to the low turbulence case, but still gives reasonable results. The FSD model in contrast to the Bray closure shows a much better agreement for the high turbulence case. This serves to justify the observations made in the previous paragraph regarding the diffusive effects, since these become less important for increasing Re number. The strained flamelet model is also observed to give an improved agreement with the DNS data. The choice of model to use however in a RANS or LES simulation, depends not only on the predictive ability of the model, but also on the ease of implementation. It is important to note that of all the models tested the most complex is the strained flamelet model, followed by the unstrained flamelet model.

7.1.3 c-pdfs model comparison

Many flamelet models like the unstrained flamelet model used in the previous section employ a presumed β -shaped pdf for the progress variable $\tilde{f}(c)$. The progress variable mean, \tilde{c} , and variance, $\widetilde{c''^2}$, are solved for in a RANS/LES simulation and used to estimate $\tilde{f}(c)$ at each point in the domain. Since the

DNS data in this study involve a multi-component fuel it becomes imperative to examine the validity of the β -pdf used in the models. Figures 7.6-7.10 show the prediction of the β -pdf against the pdfs extracted from the DNS in the range $0.1 < \tilde{c} < 0.9$. For $\tilde{c}=0.9$, the β -pdf gives an excellent agreement with the DNS data for both cases across the entire sample variable space. For $\tilde{c}=0.7$, there is some deviation from the DNS data: for both cases the β -pdf slightly over-estimates the burning mode pdf contribution in the range $0.1 < \zeta < 0.6$. At the same time it under-estimates the burning mode pdf contribution around the DNS mean value. For $\tilde{c}=0.5$, the β -pdf shows a good agreement at low ζ values only, and up to about $\zeta=0.2$. For $\zeta > 0.2$ a similar trend is observed as with the $\tilde{c}=0.7$ case. Similar trends are also observed for $\tilde{c}=0.1$ and 0.3. At this point it has to be emphasized that for this flame peak heat release occurs at $c=0.32$. As a result, the β -pdf over-estimates the burning mode pdf in the neighbourhood of the heat release range i.e. $0.1 < \zeta < 0.5$. At the same time it under-estimates the products contribution to the pdf. This helps to explain the slight over-prediction of the mean reaction rate seen in Fig.7.5 for $0.1 < \tilde{c} < 0.5$, and the slight under-prediction for $0.5 < \tilde{c} < 1.0$, when using the unstrained flamelet model. However, although the β -pdf does not accurately predict the actual progress variable pdf over the entire ζ space, the unstrained flamelet model still gives a good prediction of the mean reaction rate. This is so because the mean reaction rate is not as sensitive to the choice of $f(\zeta)$ but rather on the product $\dot{w}_{c,lam}(\zeta)f(\zeta)$. Thus the β -pdf requires to correctly predict the progress variable pdf in regions where there is significant heat release only.

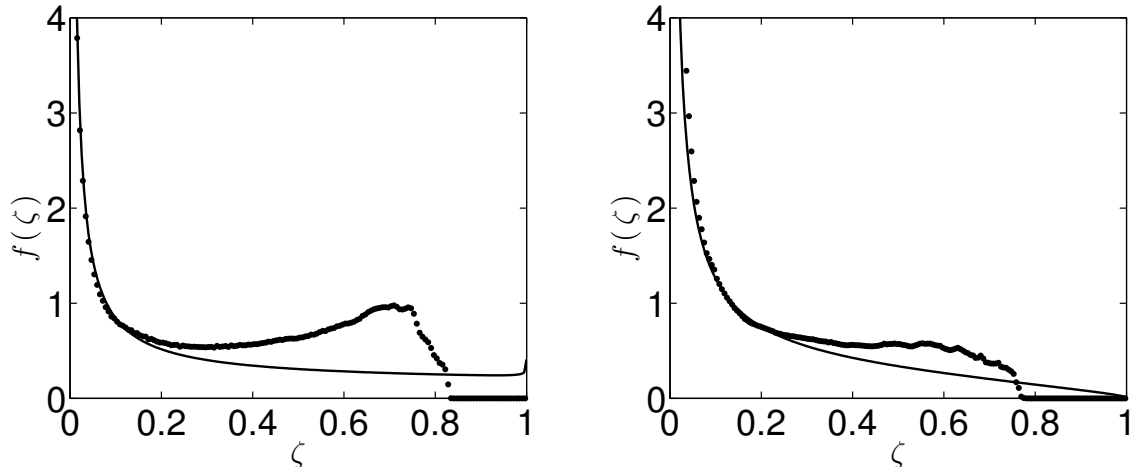


Figure 7.6: $\tilde{c}=0.1$ case A (left) and case C (right).

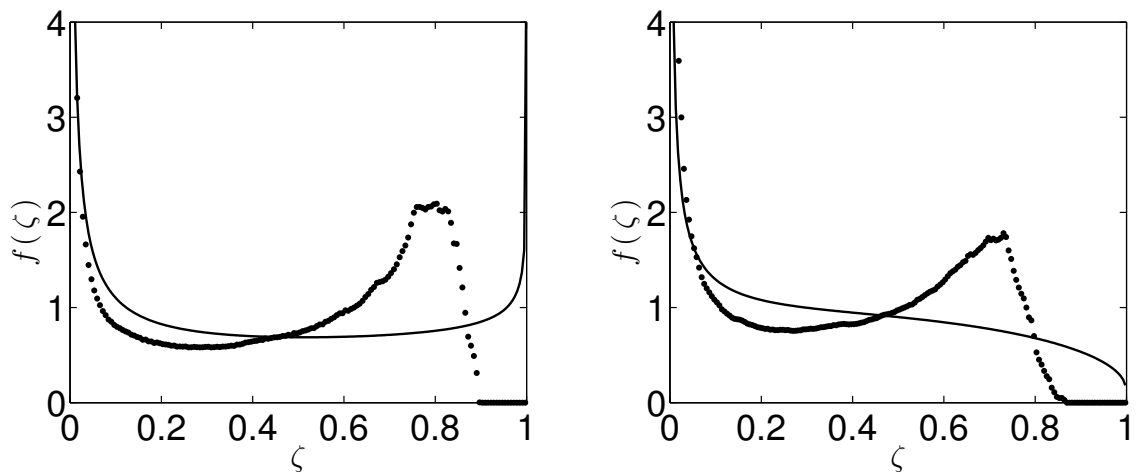


Figure 7.7: $\tilde{c}=0.3$ case A (left) and case C (right).

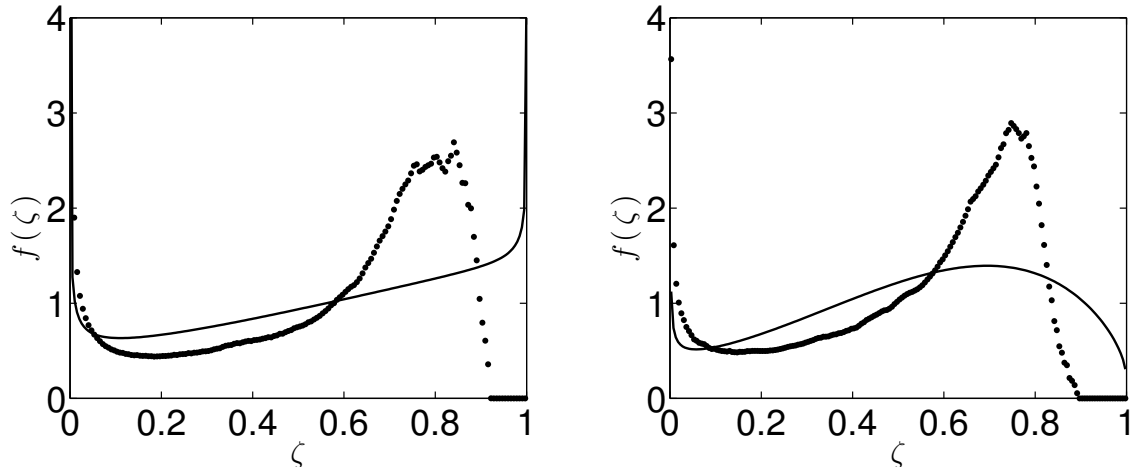


Figure 7.8: $\tilde{c}=0.5$ case A (left) and case C (right).

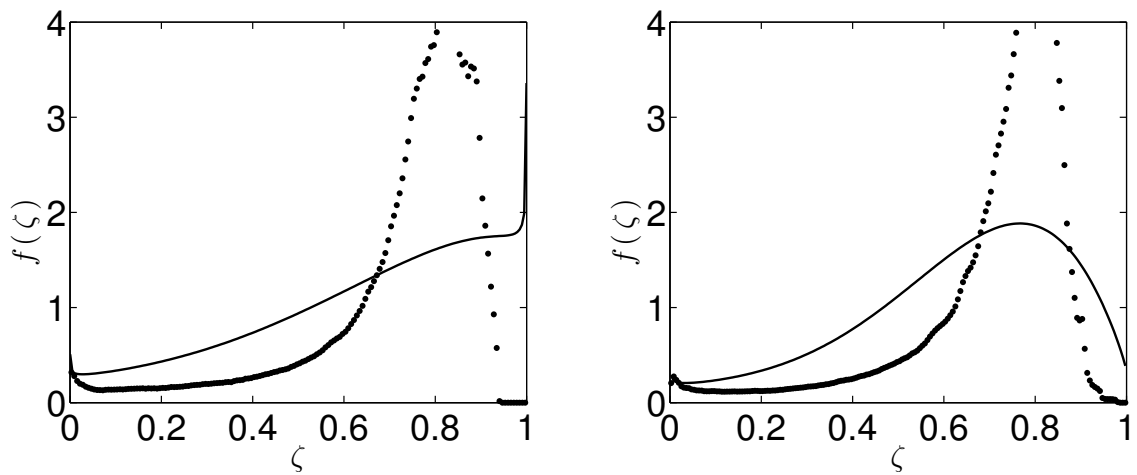


Figure 7.9: $\tilde{c}=0.7$ case A (left) and case C (right).

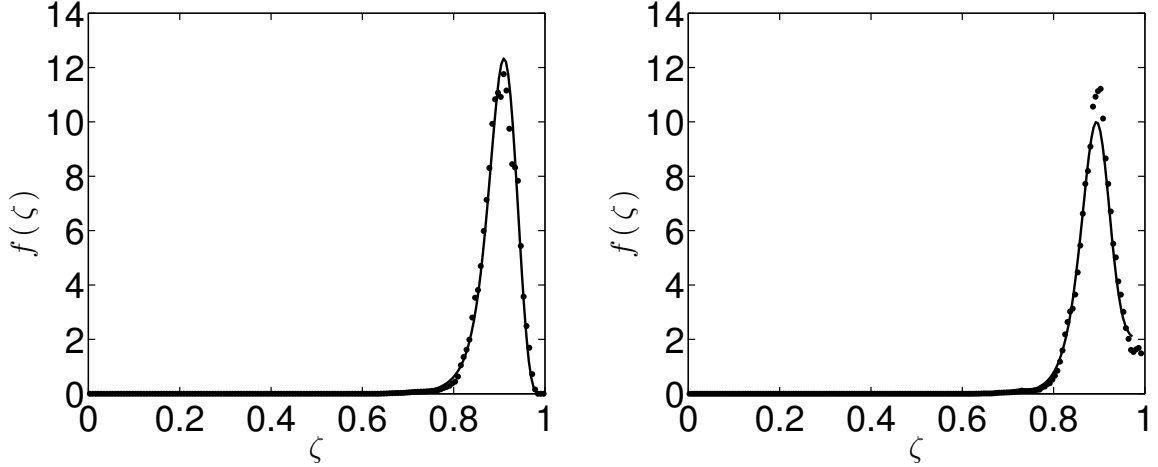


Figure 7.10: $\tilde{c}=0.9$ case A (left) and case C (right).

7.2 LES

In the previous section, various mean reaction rate closures were validated in the RANS context using the DNS data. The unstrained and strained flamelet models however, in actual RANS or LES, require the progress variable mean and its variance which are used to evaluate the β -pdf. Furthermore, the progress variable variance is strongly dependent on the SDR model used to close the equation. This is in contrast to the validation procedure in the previous section, where the actual mean and variance from the DNS are actually used. The FSD-based model also requires modelling or an additional balance equation to be solved for. These issues become more important in LES, because the filtered quantities vary with the filter size Δ and the filter type. The algebraic closure of Bray on the other hand relates directly to the SDR. Furthermore, it does not suffer explicitly from the sub-grid scale models used for the turbulent fluxes in the progress variable balance equation. The EBU model is the simplest, requiring only the mean progress variable. Thus, the algebraic closure of Bray and the EBU model, give perhaps the most plausible results when validated against DNS data. Thus, in this section the performance of an SDR model in the LES context is evaluated, along with the mean reaction rate closures using the Bray and the EBU models.

The filtered value of a quantity ϕ is calculated as:

$$\overline{\phi(\underline{x}, t)} = \int_{\underline{x}'} \phi(\underline{x} + \underline{x}', t) f(\underline{x}') d\underline{x}' \quad (7.9)$$

where f is a Gaussian filter of width Δ :

$$f(\underline{x}') = \left(\frac{6}{\pi \Delta^2} \right)^{\frac{3}{2}} e^{-\frac{6\underline{x}' \cdot \underline{x}'}{\Delta^2}} \quad (7.10)$$

The Favre-averaged filtered value of a variable, $\tilde{\phi}$, is then defined as:

$$\tilde{\phi}(\underline{x}, t) = \frac{1}{\bar{\rho}} \int_{\underline{x}'} \rho(\underline{x} + \underline{x}', t) \phi(\underline{x} + \underline{x}', t) f(\underline{x}') d\underline{x}' \quad (7.11)$$

The integration limits for \underline{x}' span $-0.75\Delta^+ \leq |\underline{x}'| \leq 0.75\Delta^+$ in each direction, where $\Delta^+ = \Delta/\delta_l$, and are sufficiently large to ensure that f drops to zero, thereby yielding a filter integral equal to one, thus not biasing the filtered variable values in any way. Since the flame is inherently unsteady, the entire computational domain serves as the sample volume. However, not all DNS grid points need to be filtered since adjacent grid points will have overlapping filters thus showing no significant difference in the filtered variable value. As a result, the spatial sample frequency is chosen so that for the minimum filter width considered, $\Delta^+ = 0.2$, there is a separation of exactly one Δ in each direction. Also, due diligence is made to ensure that sample points in the non-periodic direction are at least one Δ away from the boundaries. Time averaging of the filtered variables is done between $3 < t/t_{fl} < 5$ for case A and between $1 < t/t_{fl} < 4$ for case C.

Figure 7.11 shows instantaneous contours in the x, y plane for different z , of the progress variable filtered reaction rate $\overline{\dot{w}_c^+}$, normalized using the maximum laminar value. The results are shown for the highest turbulence level case i.e. case C, for filter widths of $\Delta^+ = 0.2, 1.0$ and 2.0 . Figure 7.11 shows that for small filter widths i.e. $\Delta^+ = 0.2$, the flame structure is very close to the actual DNS depicted in Fig. 5.10 of Chapter 5. The flame front is thin with reactive pockets forming along it interchanging with non-reactive regions. For $\Delta^+ = 1.0$ small-scale features of the flame front are smoothed out due to the action of the filter, and the maximum progress variable rate value reached drops. This is a result

of the increasing contribution of smaller progress variable reaction rates. For $\Delta^+=2.0$, the smoothing effects are more pronounced and the flame is very much thickened as opposed to smaller filter widths. This implies that the operating condition shifts to the left on the turbulent combustion diagram thus altering the turbulence-scalar interaction. Furthermore, the formation of reactive regions like the ones observed for $\Delta^+=0.2$ in the second row of figures behind and in front of the main flame front, are completely smoothed out. As a result these physical processes are lost in the filtering process and since in practical applications much larger filter widths are typically used, these results serve to show how different the flame structure can be even when using LES.

7.2.1 SDR model

In section 7.1.1 the performance of a scalar dissipation rate model (SDR) was validated against the DNS data in the RANS context. In LES, SDR modelling is also crucial but the subject has rarely been addressed. The performance of mean reaction rate closures requiring the progress variable variance, such as the unstrained and strained flamelet models, depend strongly on the SDR model used. The SDR model in Eq. 7.2 was extended for LES in [166]. This model reads:

$$\tilde{N} = \tilde{D} \frac{\partial \tilde{c}}{\partial x_i} \frac{\partial \tilde{c}}{\partial x_i} + (1 - e^{-\theta_5 \Delta^+}) \left[\frac{2K_c s_l}{\delta_l} + (C_3 - \tau C_4 \text{Da}_\Delta) \left(\frac{2u'_\Delta}{3\Delta} \right) \right] \frac{\tilde{c}(1 - \tilde{c})}{\beta_c} \quad (7.12)$$

where $\theta_5=0.75$, C_3 and C_4 are defined as in the RANS context but with the local Karlovitz number defined as $\text{Ka}_\Delta=(u'_\Delta/s_l)^{3/2}(\Delta^+)^{-1/2}$ instead. The local Damkohler number, Da_Δ , is given by $\text{Da}_\Delta=(\Delta/u'_\Delta)/(\delta_l/s_l)$, where u'_Δ is the rms speed in the local filter box defined as $u'_\Delta=\sqrt{(\widetilde{u_i u_i} - \tilde{u}_i^2)/3}$. The first term on the right-hand side of Eq. 7.12 is the contribution to the SDR from the resolved progress variable gradients and the second term represents the sub-grid scale contributions.

Figure 7.12 shows \tilde{N}^+ conditionally averaged in bins of c and time-averaged, calculated using Eq. 7.12 compared against the DNS data. This is done for four

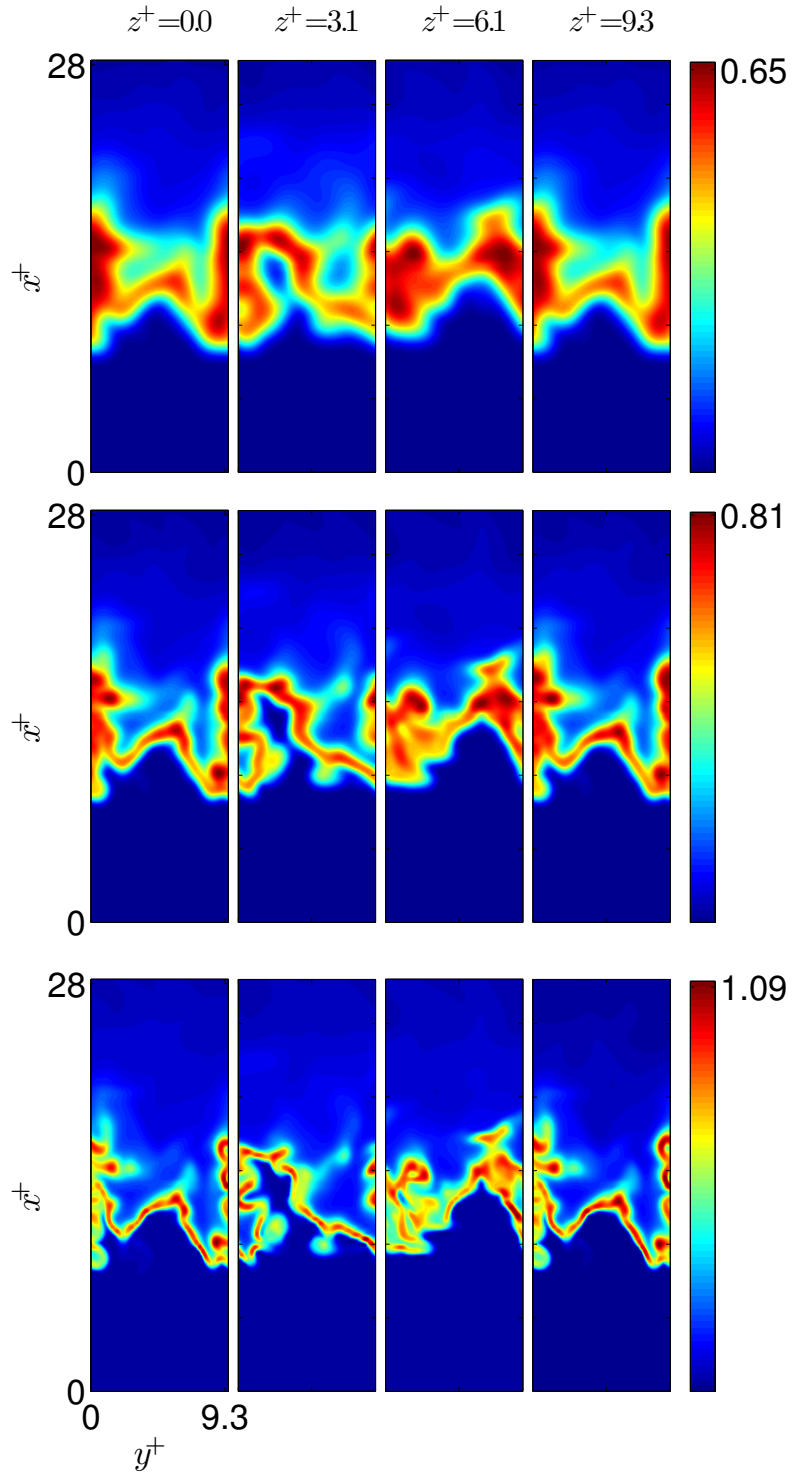


Figure 7.11: Progress variable filtered reaction rate $\overline{\dot{w}_c^+}$, normalized using the maximum laminar value, for case C at $t/t_{fl}=2.0$. Filter widths (bottom to top): $\Delta^+=0.2, 1.0$ and 2.0 .

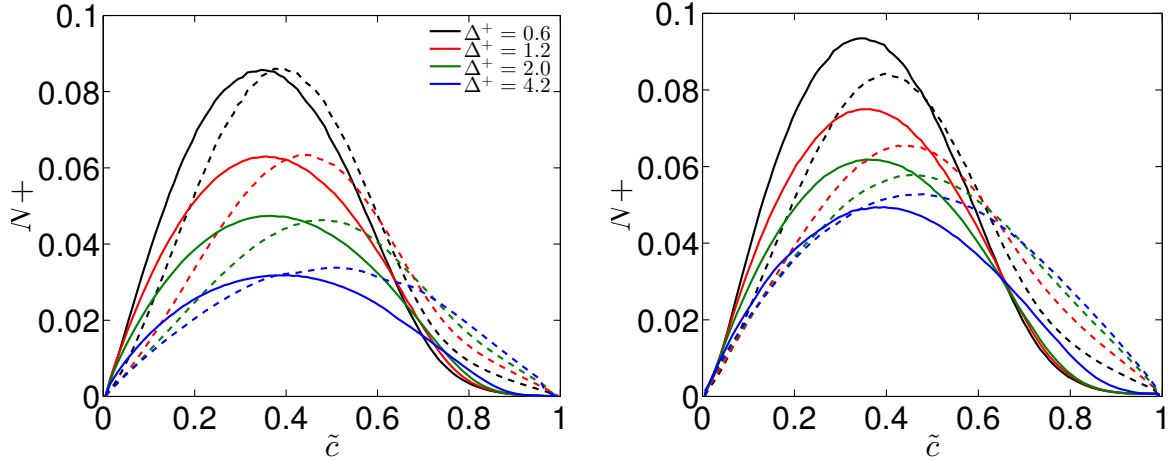


Figure 7.12: Scalar dissipation rate \tilde{N}^+ conditionally averaged in bins of \tilde{c} , and time-averaged, from the DNS (continuous lines) and estimated using Eq. 7.12 (dashed lines), for different filter widths Δ^+ , for cases A (left) and C (right). Case A: $\beta_c=9.4$. Case C: $\beta_c=7.5$.

filter widths, namely $\Delta^+=0.6, 1.2, 2.0$ and 4.2 . For low \tilde{c} values Eq. 7.12 slightly under-estimates the scalar dissipation rate, and for large \tilde{c} Eq. 7.12 slightly over-estimates the scalar dissipation rate. For increasing filter widths the over-estimation for large values of \tilde{c} increases, and the maximum conditional scalar dissipation rate estimated using Eq. 7.12 shifts to larger \tilde{c} values. This trend is observed for both cases and is related to the estimation of the sub-grid variance term $\tilde{c}(1-\tilde{c})/\beta_c$. For large filter widths the sub-grid scale contribution to \tilde{N} becomes more important, and the same applies for the progress variable variance. For large \tilde{c} values $\tilde{c}(1-\tilde{c})$ over-estimates the progress variable variance as in the RANS context discussed in section 7.1.1. This can be alleviated by having a filter size dependent β_c , however one can see from Fig. 7.12 that overall Eq. 7.12 gives reasonable agreement with the DNS data. The functional dependence of β_c on the filter size and turbulence level is a subject of future work.

7.2.2 Reaction rate closures

Figure 7.13 shows the conditionally averaged reaction rate using the algebraic closure of Bray (Eq. 7.4) against the DNS data. For both turbulence levels Eq. 7.4 over-estimates the mean reaction rate, with the over-estimation being stronger for small filter widths. This is not surprising since for small filter widths the progress variable pdfs deviate the most from the bimodal shape [166], which explains the associated over-prediction. For large filter widths, the progress variable pdfs are more bimodal-like [166], since the filtering is done over a larger domain including low and high c values. Since practical LES often use filter sizes much larger than the maximum used in this study, one would expect Eq. 7.4 to give better results for larger filter widths. Figure 7.14 shows the conditionally averaged reaction rate using the EBU model:

$$\bar{w}_c = C_{ebu} \bar{\rho} \frac{\Delta}{u'_{\Delta}} \tilde{c}(1 - \tilde{c}) \quad (7.13)$$

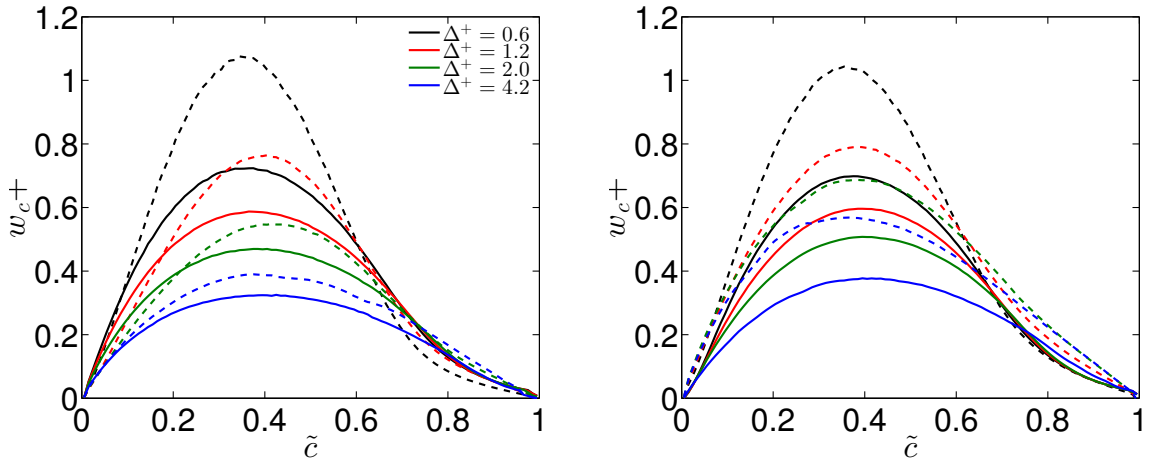


Figure 7.13: Mean reaction rate \bar{w}_c^+ conditionally averaged in bins of \tilde{c} , and time-averaged, from the DNS (continuous lines) and estimated using Eq. 7.4 (dashed lines) (and using \tilde{N} instead of \tilde{c}), for different filter widths Δ^+ , for cases A (left) and C (right). Case A: $\beta_c=9.4$. Case C: $\beta_c=7.5$.

In comparison to Bray's model Eq. 7.13 shows an overall better agreement with the DNS data. However, for large filter widths the difference with the DNS

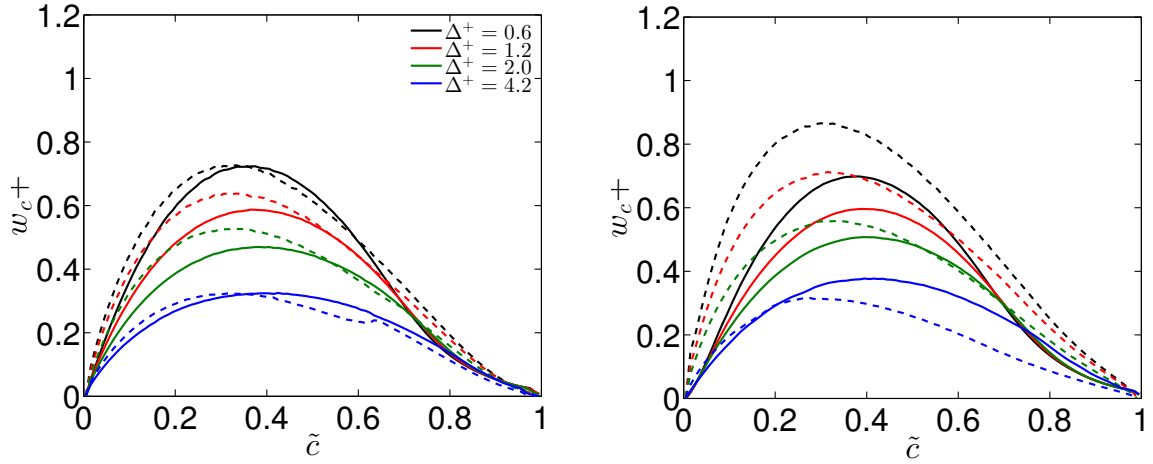


Figure 7.14: Mean reaction rate \bar{w}_c^+ conditionally averaged in bins of \tilde{c} , and time-averaged, from the DNS (continuous lines) and estimated using Eq. 7.13 (dashed lines), for different filter widths Δ^+ , for cases A (left) and C (right). Case A: $C_{ebu}=15.88$. Case C: $C_{ebu}=4.83$.

data is observed to increase which is in contrast with the results obtained using the algebraic closure of Bray. This suggests that Eq. 7.13 is more sensitive to the constant parameter's C_{ebu} variation with filter width than Eq. 7.13 is with the variation of β_c (used in the SDR model) with filter width. It thus uncertain how the EBU model will perform for larger filter widths.

Chapter 8

Concluding remarks

8.1 Conclusions

Three-dimensional direct numerical simulation of turbulent premixed combustion of a multi-component fuel involving CO, H₂, H₂O, CO₂ and CH₄ with air is performed. The simulations have been conducted using a 49-reaction 15-species skeletal mechanism, and a 5-step 9-species reduced mechanism, both developed in this study, for the chemical kinetics. To the author's knowledge these simulations are the first of their kind.

The skeletal and reduced mechanisms developed in this study, are extensively validated against experimental data of flame speeds and ignition delay times, for a range of thermo-chemical conditions in laminar flows. Furthermore, the DNS data are used to evaluate the performance of the reduced mechanism under turbulent conditions. It is shown that the reduced mechanism developed in this study, is able to reproduce the main statistics such as species mean mass fractions and mean heat release rate, but also the main flame surface statistics such as displacement speed and flame surface density probability density functions, at a significantly reduced computational cost. Thus, the chemical mechanisms developed can henceforth be used in future DNS and in LES during the design stage of industrial gas turbine combustors.

It is found that for the multi-component fuel flame heat is released over a wider temperature range, in contrast with the more traditional methane flame.

This arises from the existence of individual species reaction zones which do not overlap, either with each other or with the heat release zone, and resolution requirements for future DNS of such multi-component fuels should take care in resolving the minimum reaction zone thickness of all species present.

The ability of the commonly used flame markers for heat release rate visualization, namely the forward rate of the reaction $\text{OH} + \text{CH}_2\text{O} = \text{HCO} + \text{H}_2\text{O}$, is also examined for the multi-component fuel flame. It is found that this marker shows a poor correlation with the heat release rate. Alternative flame markers are thus proposed, developed based on an error-estimator function, both for the multi-component fuel flame and for the more commonly used methane flame. The DNS data are used to assess the performance of the proposed markers in turbulent conditions, and they are found to give improved correlations with the heat release rate. These markers will thus help experimentalists to develop the necessary laser imaging techniques for the more accurate visualization of heat release rate, which will enable after the design process an estimation of the performance of the combustor under practical operating conditions.

Different mean reaction rate closures for the multi-component fuel flame are evaluated both in the RANS and LES context. This was essential since the majority of mean reaction rate closures were developed using DNS data employing reduced chemistry schemes. It is found that although the majority of these closures give a good agreement with the DNS results, there exist significant differences between them, which become more pronounced with increasing turbulence level. Furthermore, it is observed that the models' constants depend strongly on the fuel composition and on the turbulence level, suggesting that further parametric studies using detailed chemistry DNS would be useful for further evaluation of these parameters.

8.2 Future work

- In Chapter 2 a reduced mechanism was developed for the combustion of low hydrogen and methane content multi-component fuels. A natural evolution of this work is to extend the range of applicability of the reduced mechanism to handle fuels with higher levels of hydrogen and methane, and to test these mechanisms

for non-premixed flames also.

- To conduct DNS using the skeletal and reduced mechanisms for non-premixed or partially premixed combustion.
- To use the reduced mechanism in LES and to compare with available and future experimental data.
- To examine the validity of the heat release rate markers proposed in Chapter 6 for fuels with different thermo-chemical conditions, and to compare with experimental data if possible.
- To conduct parametric DNS studies at different turbulence levels using the reduced mechanism for extensive evaluation of the mean reaction rate models' parameters, and in particular β , associated with the scalar dissipation rate model tested in Chapter 7.
- To conduct a more realistic swirling inflow DNS of the premixed multi-component fuel using the reduced mechanism.
- To post-process the DNS data in the context of emerging trends in reactive CFD such as Lattice-Boltzmann methods.

Appendix A

The range of conditions considered for the sensitivity analyses are given in Table A1. Two values for water content are considered. The raw sensitivity coefficients $k_i/s_l\partial s_l/\partial k_i$ are shown in Figs. A1 to A6 for CO/H₂/H₂O-air mixtures and in Figs. A7 to A12 for CO/CH₄/H₂O-air mixtures. If one were to conduct the sensitivity analyses for the ignition delays then the results would be very similar to those shown by [102] and thus they are not presented here.

p (atm)	T_r (K)	ϕ	f_{H_2}	f_{CH_4}	H ₂ O%
1	323	0.9	5/95	0	0
1	323	0.9	5/95	0	20
1	323	0.9	1	0	0
1	323	0.9	1	0	20
1	323	2	5/95	0	0
1	323	2	5/95	0	20
10	600	0.9	5/95	0	0
10	600	0.9	5/95	0	20
10	1000	0.9	5/95	0	0
10	1000	0.9	5/95	0	20
20	600	0.9	5/95	0	20
1	323	0.9	0	5/95	0
1	323	0.9	0	5/95	20
1	298	0.9	0	1	0
1	323	0.9	0	1	20
1	323	2	0	5/95	0
1	323	2	0	5/95	20
10	600	0.9	0	5/95	0
10	600	0.9	0	5/95	20
10	1000	0.9	0	5/95	0
10	1000	0.9	0	5/95	20
20	600	0.9	0	5/95	20

Table A1: Conditions for sensitivity analysis.

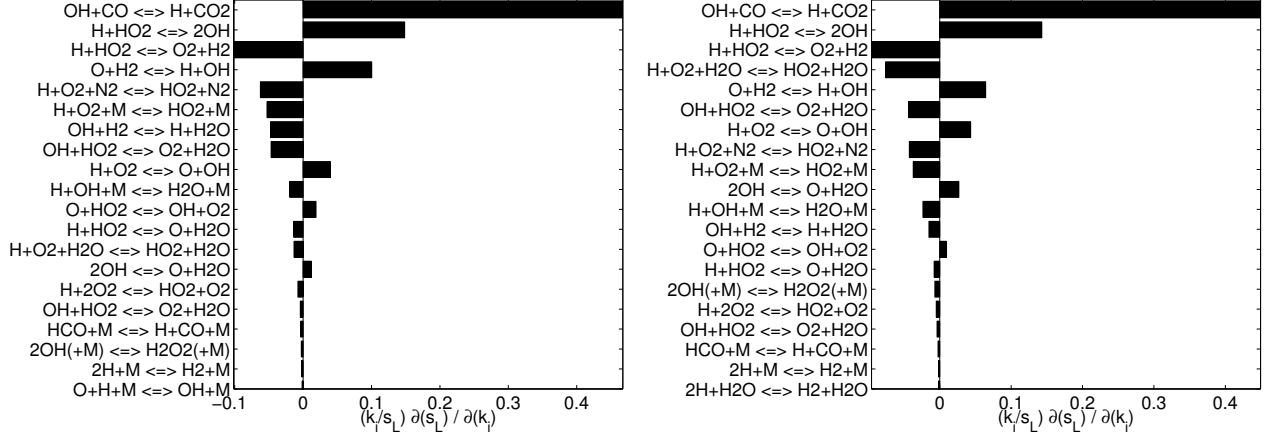


Fig. A 1: $T_r=323$ K, $p=1$ atm, $\phi=0.9$, $f_{H_2} = 5/95$ with $H_2O=0\%$ (left), 20% (right).

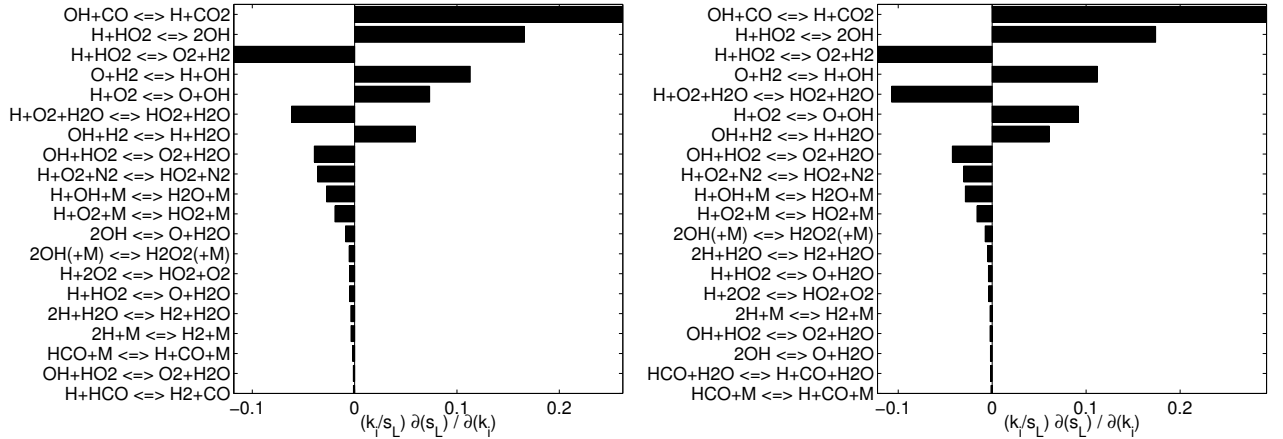


Fig. A 2: $T_r=323$ K, $p=1$ atm, $\phi=0.9$, $f_{H_2} = 1.0$ with $H_2O=0\%$ (left), 20% (right).

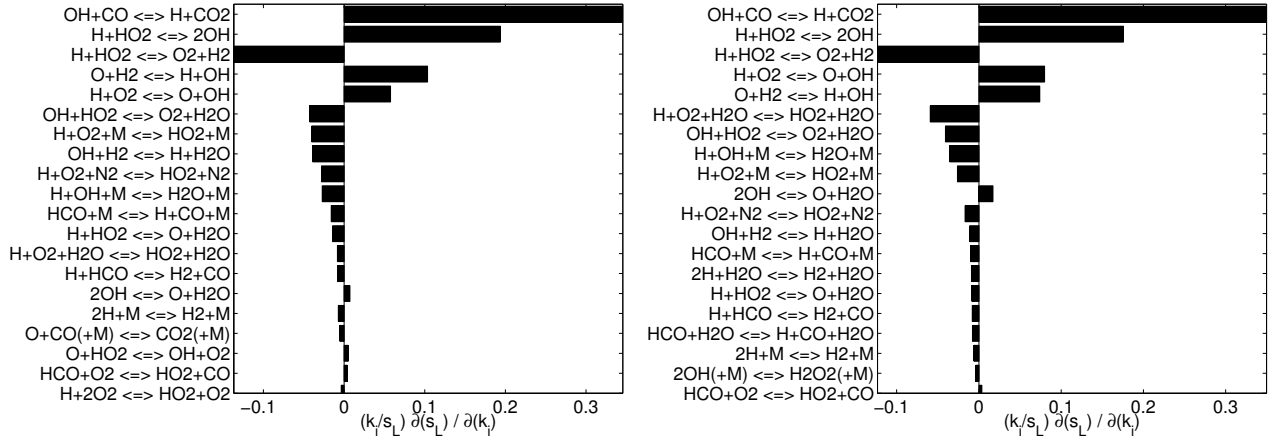


Fig. A 3: $T_r=323$ K, $p=1$ atm, $\phi=2.0$, $f_{H_2} = 5/95$ with $H_2O=0\%$ (left), 20% (right).

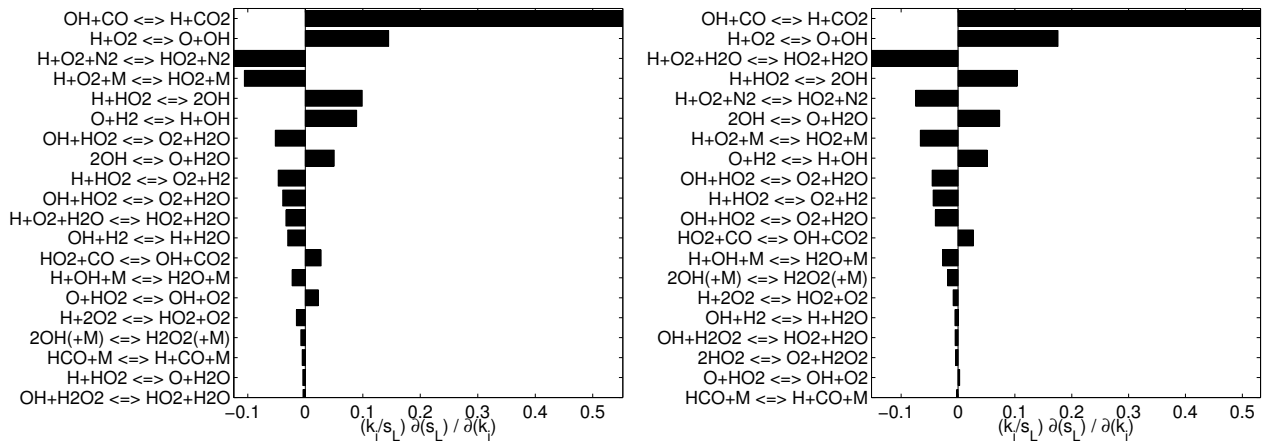


Fig. A 4: $T_r=600$ K, $p=10$ atm, $\phi=0.9$, $f_{H_2} = 5/95$ with $H_2O=0\%$ (left), 20% (right).

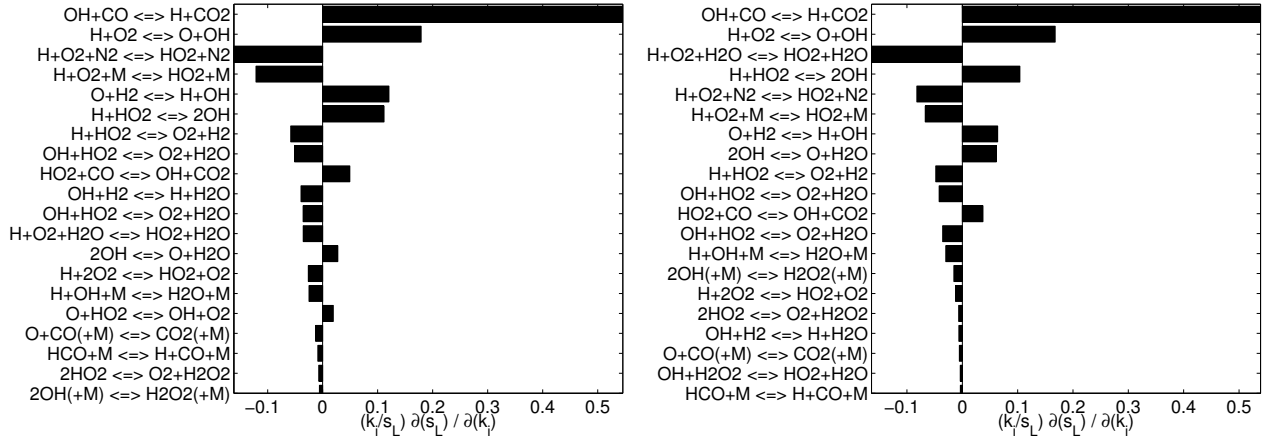


Fig. A 5: $T_r=1000$ K, $p=10$ atm, $\phi=0.9$, $f_{H_2} = 5/95$ with $H_2O=0\%$ (left), 20% (right).

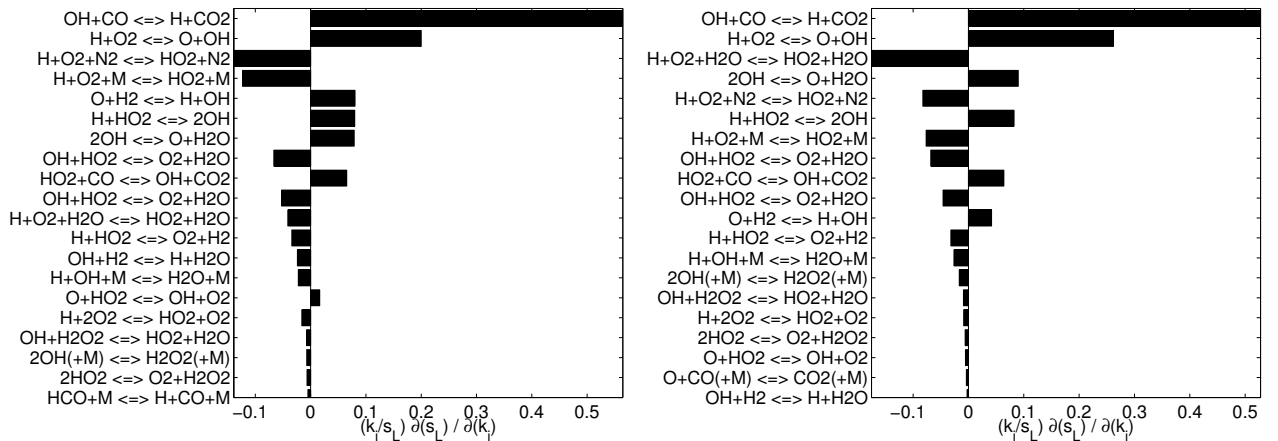


Fig. A 6: $T_r=600$ K, $p=20$ atm, $\phi=0.9$, $f_{H_2} = 5/95$ with $H_2O=0\%$ (left), 20% (right).

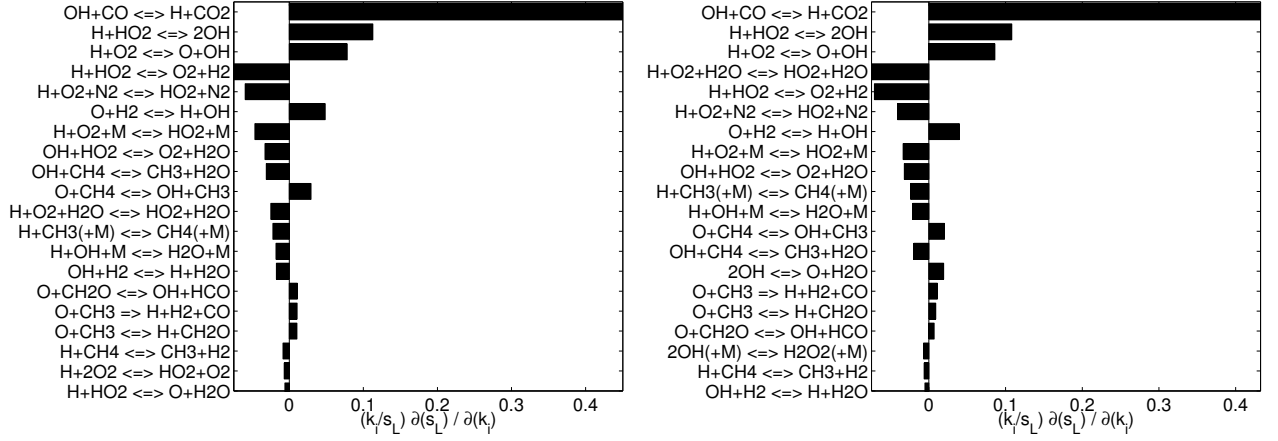


Fig. A 7: $T_r=323$ K, $p=1$ atm, $\phi=0.9$, $f_{CH_4} = 5/95$ with $H_2O=0\%$ (left), 20% (right).

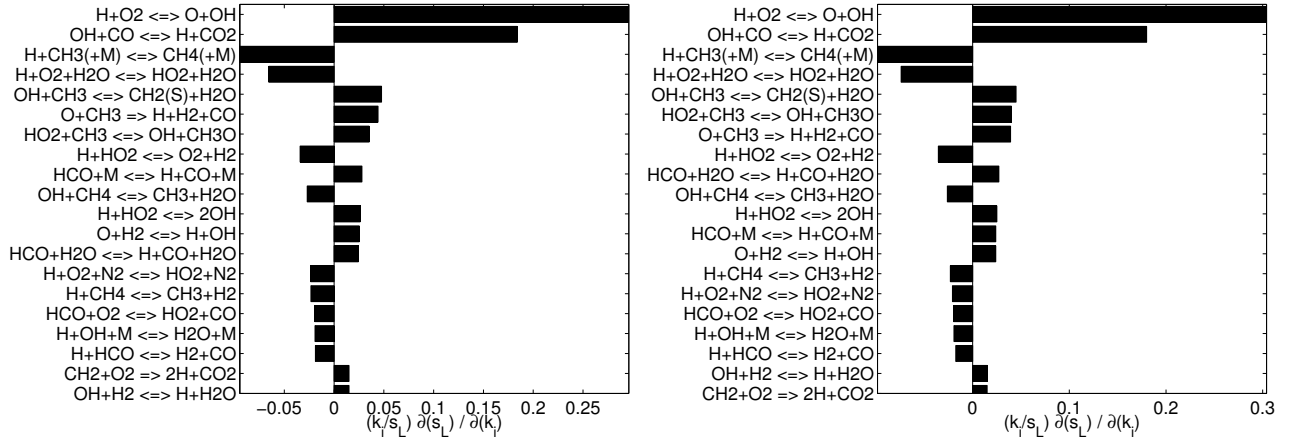


Fig. A 8: $T_r=323$ K, $p=1$ atm, $\phi=0.9$, $f_{CH_4} = 1.0$ with $H_2O=0\%$ (left), 20% (right).

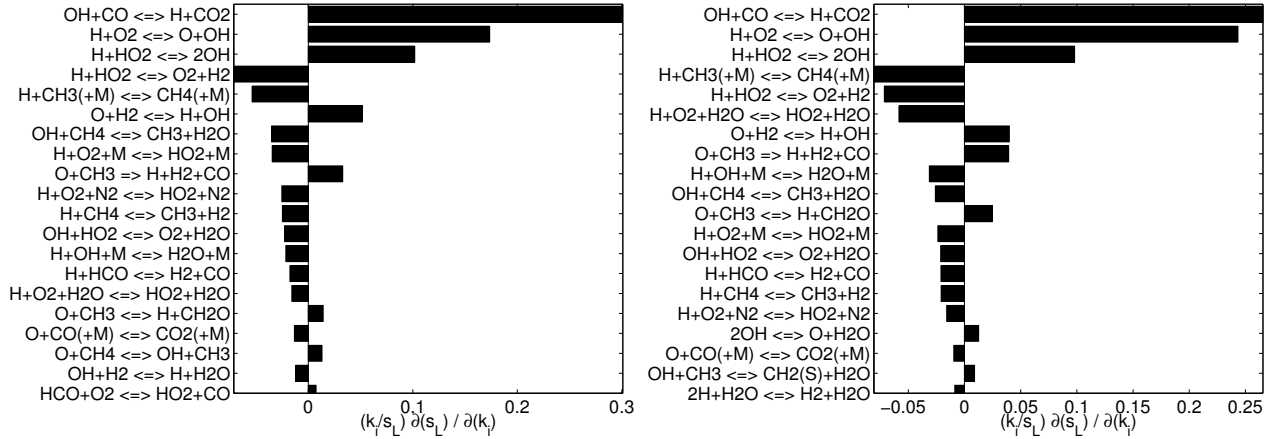


Fig. A 9: $T_r=323$ K, $p=1$ atm, $\phi=2.0$, $f_{CH_4} = 5/95$ with $H_2O=0\%$ (left), 20% (right).

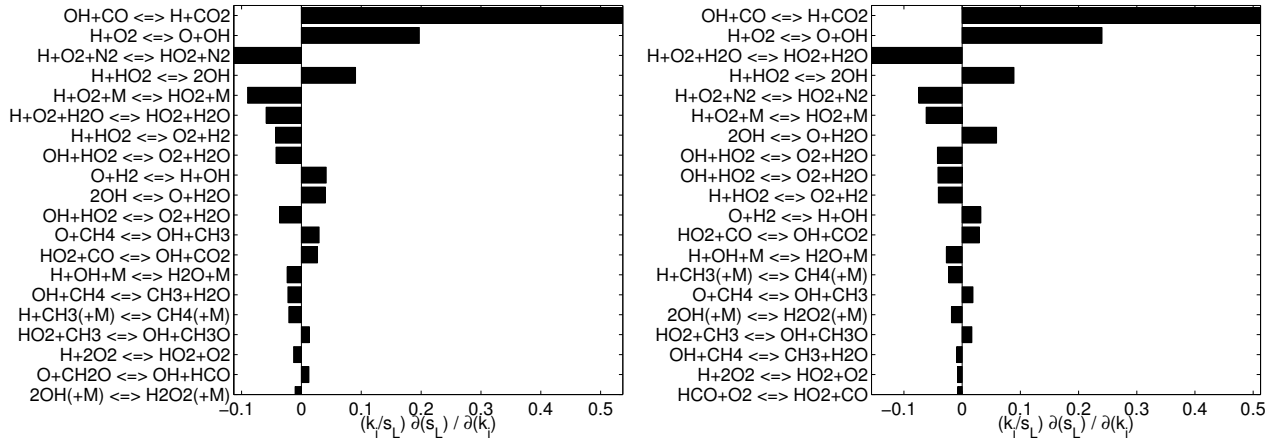


Fig. A 10: $T_r=600$ K, $p=10$ atm, $\phi=0.9$, $f_{CH_4} = 5/95$ with $H_2O=0\%$ (left), 20% (right).

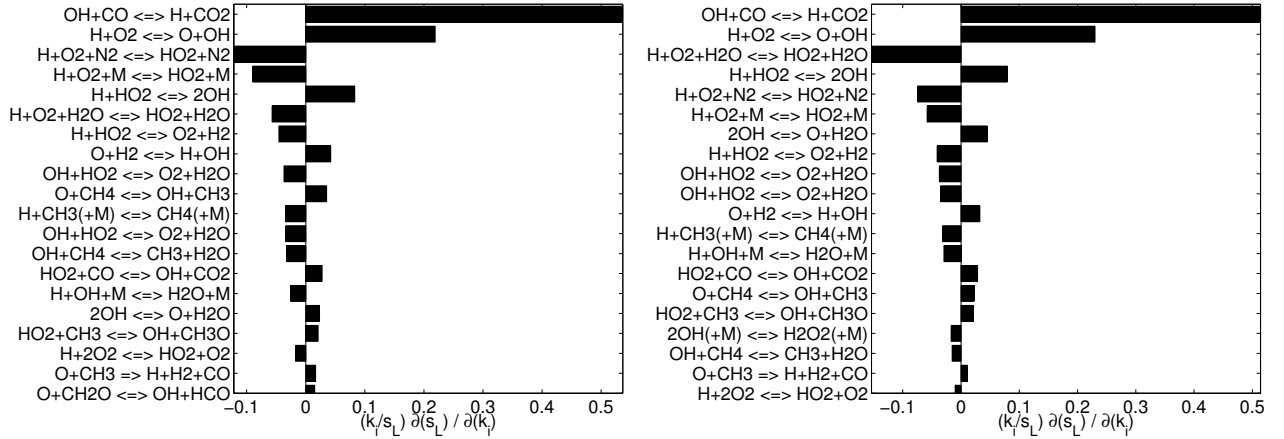


Fig. A 11: $T_r=1000$ K, $p=10$ atm, $\phi=0.9$, $f_{CH_4} = 5/95$ with $H_2O=0\%$ (left), 20% (right).

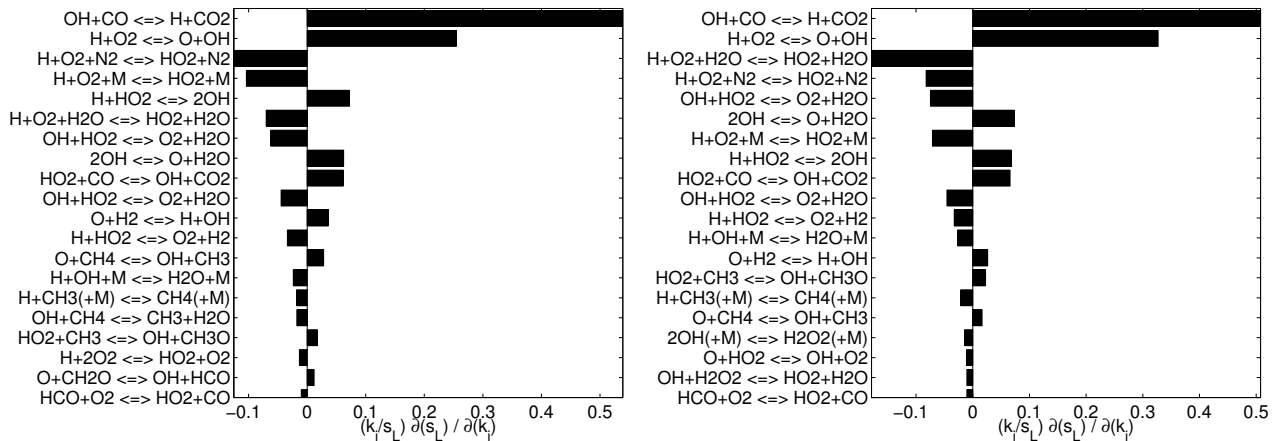


Fig. A 12: $T_r=600$ K, $p=20$ atm, $\phi=0.9$, $f_{CH_4} = 5/95$ with $H_2O=0\%$ (left), 20% (right).

Appendix B

Non steady-state species rates

The global net reaction rate, \dot{W}_k , for species k involved in the 5-step reduced mechanism is given below. The numbers inside the bracket refer to the elementary reaction in the skeletal set in Table 2.3.

$$\begin{aligned}\dot{W}_H = & \\ & -\dot{W}(1) + \dot{W}(2) + \dot{W}(3) - \dot{W}(5) - \dot{W}(6) - \dot{W}(7) - \dot{W}(8) - \dot{W}(9) - \dot{W}(10) - \dot{W}(11) - \\ & \dot{W}(12) - \dot{W}(15) - \dot{W}(20) - \dot{W}(23) - 2\dot{W}(25) - 2\dot{W}(26) - 2\dot{W}(27) - 2\dot{W}(28) - \\ & \dot{W}(29) - \dot{W}(31) + \dot{W}(32) - \dot{W}(35) + \dot{W}(38) + \dot{W}(39) + \dot{W}(40) + \dot{W}(43) + \dot{W}(44) - \\ & \dot{W}(46) - \dot{W}(47) - \dot{W}(48)\end{aligned}$$

$$\begin{aligned}\dot{W}_{O_2} = & \\ & -\dot{W}(1) - \dot{W}(5) - \dot{W}(6) - \dot{W}(7) - \dot{W}(8) - \dot{W}(9) - \dot{W}(10) + \dot{W}(12) + \dot{W}(13) + \\ & \dot{W}(14) + \dot{W}(16) + \dot{W}(17) + \dot{W}(18) + \dot{W}(30) - \dot{W}(37)\end{aligned}$$

$$\begin{aligned}\dot{W}_{H_2O} = & \\ & +\dot{W}(3) + \dot{W}(4) + \dot{W}(13) + \dot{W}(14) + \dot{W}(15) + \dot{W}(20) + \dot{W}(21) + \dot{W}(22) + \dot{W}(29) + \\ & \dot{W}(36) + \dot{W}(42) + \dot{W}(49)\end{aligned}$$

$$\dot{W}_{CO} =$$

$$-\dot{W}(32) - \dot{W}(33) - \dot{W}(34) + \dot{W}(35) + \dot{W}(36) + \dot{W}(37) + \dot{W}(38) + \dot{W}(39) + \dot{W}(44)$$

$$\dot{W}_{CO_2} =$$

$$\dot{W}(32) + \dot{W}(33) + \dot{W}(34) + \dot{W}(40)$$

$$\dot{W}_{H_2} =$$

$$-\dot{W}(2) - \dot{W}(3) + \dot{W}(12) + \dot{W}(23) + \dot{W}(25) + \dot{W}(26) + \dot{W}(27) + \dot{W}(28) + \dot{W}(35) + \dot{W}(44) + \dot{W}(47) + \dot{W}(48)$$

$$\dot{W}_{H_2O_2} =$$

$$\dot{W}(17) + \dot{W}(18) + \dot{W}(19) - \dot{W}(20) - \dot{W}(21) - \dot{W}(22) - \dot{W}(23) - \dot{W}(24)$$

$$\dot{W}_{CH_4} =$$

$$-\dot{W}(41) - \dot{W}(42) + \dot{W}(46) - \dot{W}(47)$$

References

- [1] T. Komori, N. Yamagami, and H. Hara. Design for blast furnace gas firing gas turbine. *Gas Turbine Engineering Section Power Systems Headquarters Mitsubishi Heavy Industries, Ltd. Industrial report*, 2004. www.mhi.co.jp/power/news/sec1/pdf/2004_nov_04b.pdf. 2, 65
- [2] K.H. Casleton, R.W. Breault, and G.A. Richards. System issues and trade-offs associated with syngas production and combustion. *Combust. Sci. Tech.*, 180:1013–1056, 2008. 2
- [3] M. Chaos and F.L. Dryer. Syngas combustion kinetics and applications. *Combust. Sci. Tech.*, 180:1053–1096, 2008. 2, 10, 11, 16
- [4] C.J. Sung and C.K. Law. Fundamental combustion properties of H₂/CO mixtures: Ignition and flame propagation at elevated pressures. *Combust. Sci. Tech.*, 180:1097–1116, 2008. 2, 11
- [5] D. Gielen. CO₂ removal in the iron and steel industry. *Energy Conver. Management*, 44:1027–1037, 2003. 2, 10
- [6] Department of Energy Report. Hydrogen from coal program: research, development, and demonstration plan for the period 2008 through 2016. U.S. Department of Energy. 2008. 2, 65
- [7] Department of Energy Report. Wabash river coal gasification re-powering project: a DOE assesment. U.S. Department of Energy National Energy Technology Laboratory. 2002. 2, 65

REFERENCES

- [8] O. Maustard. Report: Massachusetts Institute of Technology, Laboratory for energy and the environment (2005), an overview of coal based integrated gasification combined cycle technology. [2](#), [65](#)
- [9] O. Gicquel, L. Vervisch, G. Joncquet, B. Labegorre, and N. Darabiha. Combustion of residual steel gases: laminar flame analysis and turbulent flamelet modeling. *Fuel*, 82:983–991, 2003. [2](#)
- [10] U. Maas and S.B. Pope. Implementation of simplified chemical kinetics based on low-dimensional manifolds. *Proc. Combust. Inst.*, 24:719–729, 1992. [3](#)
- [11] B. Yang and S.B. Pope. Treating chemistry in combustion with detailed mechanisms-in situ adaptive tabulation in principal directions-premixed combustion ISAT. *Combust. Flame*, 112:85–112, 1998. [3](#)
- [12] N. Peters. Numerical and asymptotic analysis of systematically reduced reaction schemes for hydrocarbon flames. *Numerical simulation of combustion phenomena*, pages 90–109, 1985. Springer-Verlag. [3](#)
- [13] T. Lovas, D. Nilson, and F. Mauss. Automatic reduction procedure for chemical mechanisms applied to premixed methane/air flames. *Proc. Combust. Inst.*, 28:1809–1815, 2000. [3](#), [23](#)
- [14] A. Patel, S.C. Kong, and R.D. Reitz. Development and validation of a reduced reaction mechanism for HCCI engine simulations. *ASME*, 01-0558, 2004. [3](#)
- [15] H.S. Soyhan, P. Amneus, T. Lovas, D. Nilsson, P. Maigaard, F. Mauss, and C. Sorousbay. Automatic reduction of detailed chemical reaction mechanisms for autoignition under engine knock conditions. *J. Fuels and Lubricants, SAE Transactions*, 109:1435–1444, 2000. [3](#), [23](#)
- [16] Y.F. Tham, F. Bisetti, and J.Y. Chen. Development of a highly reduced mechanism for iso-octane HCCI combustion with targeted search algorithm. *Journal of Engineering for Gas Turbines and Power*, 130:042804, 2008. [3](#), [23](#), [24](#)

REFERENCES

- [17] H. Wang and M. Frenklach. Detailed reduction of reaction mechanisms for flame modelling. *Combust. Flame*, 87:365–370, 1991. [3](#)
- [18] P. Boivin, C. Jimenez, A.L. Sanchez, and F.A. Williams. A four-step reduced mechanism for syngas combustion. *Combust. Flame*, 158:1059–1063, 2011. [ix](#), [x](#), [xii](#), [4](#), [19](#), [24](#), [26](#), [27](#), [29](#), [32](#), [33](#), [50](#), [52](#)
- [19] W. Wang and B. Rogg. Reduced kinetic mechanisms and their numerical treatment I: wet-CO flames. *Combust. Flame*, 94:271–292, 1993. [4](#), [11](#), [12](#), [13](#), [14](#)
- [20] M. Baum, T.J. Poinso, and D.C. Haworth. Numerical simulation of turbulent premixed $H_2/O_2/N_2$ flames with detailed chemistry. *Proceedings of the Summer Program, Stanford Univ, NASA-Ames*, pages 345–366, 1992. [4](#), [5](#), [88](#), [116](#)
- [21] M. Baum, T.J. Poinso, D.C. Haworth, and N. Darabiha. Direct numerical simulation of $H_2/O_2/N_2$ flames with complex chemistry in two-dimensional turbulent flows. *J. Fluid Mech.*, 281:1–32, 1994. [4](#), [5](#), [88](#), [116](#), [149](#)
- [22] M. Lange, U. Riedel, and J. Warnatz. Parallel direct numerical simulation of turbulent reactive flows with detailed reaction schemes. *29th Proc. AIAA Fluid Dynamics Conference*, Paper 98-2979, 1998. [5](#)
- [23] J.H. Chen and H.G. Im. Stretch effects on the burning velocity of turbulent premixed hydrogen/air flames. *Proc. Combust. Inst.*, 28:211–218, 2002. [5](#)
- [24] H.G. Im and J.H. Chen. Preferential diffusion effects on the burning rate of interacting turbulent premixed hydrogen-air flames. *Combust. Flame*, 131:246–248, 2002. [5](#)
- [25] M. Tanahashi, Y. Fujimura, and T. Miyauchi. *First International Symposium on Turbulence and Shear Flows*, pages 59–64, 1999. [5](#), [64](#), [103](#)
- [26] S. Tanaka, M. Shimura, N. Fukushima, M. Tanahashi, and T. Miyauchi. Dns of turbulent swirling premixed flame in a micro gas turbine combustor. *Proc. Combust. Inst.*, 33:3293–3300, 2011. [5](#), [64](#)

REFERENCES

- [27] E.R. Hawkes, O. Chatakonda, H. Kolla, A.R. Kerstein, and J.H. Chen. A petascale direct numerical simulation study of the modelling of flame wrinkling for large-eddy simulations in intense turbulence. *Combust. Flame*, 159:2690–2703, 2012. [5](#)
- [28] I.R. Gran, T. Echehki, and J.H. Chen. Negative flame speed in an unsteady 2D premixed flame: A computational study. *Proc. Combust. Inst.*, 26:323–329, 1996. [5](#)
- [29] P. Domingo, L. Vervisch, S. Payet, and R. Hauguel. DNS of a premixed turbulent V flame and LES of a ducted flame using a FSD-PDF subgrid scale closure with FPI-tabulated chemistry. *Combust. Flame*, 143:566–586, 2005. [5](#)
- [30] J.H. Chen and T. Echehki. *Meeting of the Western States Section of the Combustion Institute, Livermore, CA, WSS/CI97S-055*, 1997. [5](#)
- [31] J.H. Chen, T. Echehki, and W. Kollmann. The mechanism of two-dimensional pocket formation in lean premixed methane-air flames with implications to turbulent combustion. *Combust. Flame*, 116:15–48, 1998. [5](#)
- [32] N. Peters, P. Terhoeven, J.H. Chen, and T. Echehki. Statistics of flame displacement speeds from computations of 2D unsteady methane-air flames. *Proc. Combust. Inst.*, 27:833–839, 1998. [5](#)
- [33] C.F. Kaminski, J. Hult, M. Alden, S. Lindenmaier, A. Dreizler, A. Maas, and M. Baum. Spark ignition of turbulent methane/air mixtures revealed by time-resolved planar laser-induced fluorescence and direct numerical simulations. *Proc. Combust. Inst.*, 28:399–405, 2000. [5](#)
- [34] J.B. Bell, M.S. Day, and J.F. Grcar. Numerical simulation of premixed turbulent methane combustion. *Proc. Combust. Inst.*, 29:1987–1993, 2002. [5](#), [103](#), [108](#)
- [35] R. Sankaran, E.R. Hawkes, J.H. Chen, T. Lu, and C.K. Law. Direct numerical simulations of turbulent lean premixed combustion. *J. Phys. Conf. Ser.*, 46:38–42, 2006. [5](#), [6](#), [64](#)

-
- [36] D. Thévenin, R. Hilbert, J. de Charentenay, and O. Gicquel. Three dimensional direct simulations of turbulent flames using realistic chemistry modelling. *IUTAM Symposium on turbulent mixing and combustion*, 70: 279–286, 2002. [5](#), [64](#)
- [37] E.R. Hawkes, R. Sankaran, J.C. Sutherland, and J.H. Chen. Scalar mixing in direct numerical simulations of temporally evolving plane jet flames with skeletal CO/H₂ kinetics. *Proc. Combust. Inst.*, 31:1633–1640, 2007. [5](#)
- [38] Z.M. Nikolaou, J.Y. Chen, and N. Swaminathan. A 5-step reduced mechanism for combustion of CO, H₂, H₂O, CH₄, CO₂ mixtures with low hydrogen/methane and high CO₂ content. *Combust. Flame*, 160:56–75, 2013. [xvii](#), [5](#), [77](#), [82](#), [86](#), [96](#), [97](#), [122](#), [145](#), [146](#)
- [39] A.K. Das, K. Kumar, and C. Sung. Laminar flame speeds of moist syngas mixtures. *Combust. Flame*, 158:345–353, 2011. [ix](#), [5](#), [12](#), [14](#), [16](#), [28](#), [29](#), [86](#), [97](#)
- [40] D. Singh, N. Takayuki, T. Saad, and L. Qiao. An experimental and kinetic study of syngas/air combustion at elevated temperatures and the effect of water addition. *Fuel*, 94:448–456, 2012. [ix](#), [x](#), [5](#), [12](#), [14](#), [15](#), [28](#), [30](#), [32](#), [33](#), [34](#), [35](#), [36](#), [86](#), [96](#), [97](#)
- [41] E.R. Hawkes and J.H. Chen. Direct numerical simulation of hydrogen-enriched lean premixed methane-air flames. *Combust. Flame*, 138:242–258, 2004. [5](#)
- [42] S. Mahalingam, J.H. Chen, and L. Vervisch. Finite-rate chemistry and transient effects in direct numerical simulations of turbulent non-premixed flames. *Combust. Flame*, 102:285–297, 1995. [6](#)
- [43] C.S. Yoo, E.S. Richardson, R. Sankaran, and J.H. Chen. A DNS study on the stabilization mechanism of a turbulent lifted ethylene jet flame in highly-heated coflow. *Proc. Combust. Inst.*, 33:1619–1627, 2011. [6](#)

-
- [44] J.H. Chen. Petascale direct numerical simulation of turbulent combustion—fundamental insights towards predictive models. *Proc. Combust. Inst.*, 33:99–123, 2011. [6](#), [7](#), [9](#)
- [45] C.K. Westbrook, Y. Mizobuchi, T.J. Poinso, P.J. Smith, and J. Warnatz. Computational combustion. *Proc. Combust. Inst.*, 30:125–157, 2005. [6](#)
- [46] N. Chakraborty, G. Hartung, M. Katragadda, and C.F. Kaminski. Comparison of 2D and 3D density-weighted displacement speed statistics and implications for laser based measurements of flame displacement speed using direct numerical simulation data. *Combust. Flame*, 158:1372–1390, 2011. [6](#)
- [47] V. Hiremath, S.R. Lantz, H. Wang, and S.B. Pope. Large-scale parallel simulations of turbulent combustion using combined dimension reduction and tabulation of chemistry. *Proc. Combust. Inst.*, 34:205–215, 2013. [6](#)
- [48] N. Swaminathan, G. Xu, A.P. Dowling, and R. Balachandran. Heat release rate correlation and combustion noise in premixed flames. *J. Fluid Mech.*, 681:80–115, 2011. [7](#)
- [49] T.J. Poinso, A.C. Trouvé, D.P. Veynante, S.M. Candel, and E.J. Esposito. Vortex-driven acoustically coupled combustion instabilities. *J. Fluid Mech.*, 177:265–292, 1987. [7](#)
- [50] S.M. Candel. Combustion instabilities coupled by pressure waves and their active control. *Proc. Combust. Inst.*, 24:1277–1296, 1992. [7](#)
- [51] H.N. Najm, P.H. Paul, C.J. Mueller, and P.S. Wyckoff. On the adequacy of certain experimental observables as measurements of flame burning rate. *Combust. Flame*, 113:312–332, 1998. [7](#), [8](#), [123](#), [127](#), [128](#), [129](#), [131](#), [134](#)
- [52] P.H. Paul and H.N. Najm. Planar laser-induced fluorescence imaging of flame heat release rate. *Proc. Combust. Inst.*, 27:43–50, 1998. [7](#), [8](#), [123](#), [127](#), [128](#), [129](#), [131](#), [134](#)
- [53] P.H. Paul and H.N. Najm. A study of flame observables in premixed methane-air flames. *Combust. Sci. Tech.*, 140:369–403, 1998. [7](#), [8](#), [123](#), [127](#), [128](#), [129](#), [131](#), [134](#)

REFERENCES

- [54] M.D. Smooke, I.K. Puri, and K. Seshadri. A comparison between numerical calculations and experimental measurements of the structure of a counter-flow diffusion flame burning diluted methane in diluted air. *Proc. Combust. Inst.*, 21:1783–1792, 1988. [8](#)
- [55] A. Gazi, G. Viourlotakis, and G. Skevis. Assessment of chemical markers for heat release rate correlations in laminar premixed flames. *Combust. Sci. Tech.*, 185:1482–1508, 2013. [8](#), [123](#), [127](#), [128](#), [131](#), [134](#)
- [56] S. Bockle, J. Kazenwadel, T. Kunzelmann, D.I. Shin, C. Schulz, and J. Wolfrum. Simultaneous single-shot laser-based imaging of formaldehyde, OH and temperature in turbulent flames. *Proc. Combust. Inst.*, 28:279–289, 2000. [8](#)
- [57] K.N. Gabet, R.A. Patton, N. Jiang, W.R. Lempert, and J.A. Sutton. High-speed CH₂O PLIF imaging in turbulent flames using a pulse-burst laser system. *Appl. Phys. B*, 106:569–575, 2012. [8](#)
- [58] H. Kolla and N. Swaminathan. Strained flamelets for turbulent premixed flame I: Formulation and planar flame results. *Combust. Flame*, 157:943–954, 2010. [9](#), [148](#), [150](#), [152](#), [155](#), [156](#)
- [59] N. Swaminathan and K.N.C. Bray. *Turbulent premixed flames*. Cambridge University Press, Cambridge, UK, 2011. [9](#), [10](#)
- [60] N. Peters. The turbulent burning velocity for large-scale and small-scale turbulence. *J. Fluid Mech.*, 384:107–132, 1999. [9](#)
- [61] F.E. Marble and J.E. Broadwell. The coherent flame model for turbulent chemical reactions. *Tech.Rep. TRW-9-PU, Project Squid.*, 1977. [9](#), [152](#), [153](#)
- [62] S.B. Pope. The evolution of surfaces in turbulence. *Int. J. Eng. Sci.*, 26:445–469, 1988. [9](#), [152](#), [153](#)
- [63] S.M. Candel, E. Maistret, N. Darabiha, T. Poinso, D. Veynante, and F. Lacas. Experimental and numerical studies of turbulent ducted flames. *Marble Symposium*, pages 209–236, 1988. [9](#), [152](#), [153](#)

-
- [64] K.N.C. Bray, M. Champion, and P.A. Libby. The interaction between turbulence and chemistry in premixed turbulent flames. *In: Turbulent Reactive Flows, Lecture Notes in Engineering, Springer Verlag*, pages 541–563, 1989. [9](#), [152](#), [153](#)
- [65] M. Boger, D. Veynante, H. Boughanem, and A. Trouvé. Direct numerical simulation analysis of flame surface density concept for large eddy simulation of premixed combustion. *Proc. Combust. Inst.*, 27:917–925, 1998. [9](#), [71](#), [152](#), [153](#)
- [66] S.B. Pope. Pdf methods for turbulent reacting flows. *Progr. Energy Combust. Sc.*, 11:119–192, 1985. [9](#)
- [67] P. Lindstedt. Transported probability density function methods for premixed turbulent flames. *Turbulent Premixed Flames, N. Swaminathan and K.N.C Bray, Cambridge Univ. Press, UK, 1st Edition*, 2011. [9](#)
- [68] W.P. Jones and Y. Prasetyo. Probability density function modelling of premixed turbulent opposed jet flames. *Proc. Combust. Inst.*, 26:275–282, 1996. [9](#)
- [69] S. Amzin, N. Swaminathan, J.W. Rogerson, and J.H. Ken. Conditional moment closure for premixed flames. *Combust. Sci. Tech.*, 184:1743–1767, 2012. [9](#)
- [70] T.J. Poinso. Using direct numerical simulations to understand premixed turbulent combustion. *Proc. Combust. Inst.*, 26:219–232, 1996. [9](#)
- [71] R.A. Yetter, F.L. Dryer, and H. Rabitz. A comprehensive reaction mechanism for carbon monoxide/hydrogen/oxygen kinetics. *Combust. Sci. Tech.*, 79:97–128, 1991. [11](#)
- [72] T.J. Kim, R.A. Yetter, and F.L. Dryer. New results on moist CO oxidation: high pressure, high temperature experiments and comprehensive kinetic modelling. *Proc. Combust. Inst.*, 25:759–766, 1994. [11](#)

REFERENCES

- [73] G.P. Smith, D.M. Golden, M. Frenklach, N.W. Moriarty, B. Eiteneer, M. Goldenberg, C.T. Bowman, R.K. Hanson, S. Song, W.C. Gardiner, V.V. Lissianski, and Z. Qin. GRI Mech 3.0. http://www.me.berkeley.edu/gri_mech. xvii, xxi, 11, 13, 26, 28, 34, 56, 93, 126, 132, 136, 137, 140, 145, 146, 147
- [74] A.N. Mazas, B. Fiorina, D.A. Lacoste, and T. Schuller. Effects of water vapour addition on the laminar burning velocity of oxygen-enriched methane flames. *Combust. Flame*, 158:2428–2440, 2011. 12
- [75] M.P. Burke, F.L. Dryer, and Y. Ju. Assessment of kinetic modelling for lean $\text{H}_2/\text{CH}_4/\text{O}_2$ -diluent flames at high pressures. *Proc. Combust. Inst.*, 33: 905–912, 2011. 12, 19
- [76] M. Kuznetsov, R. Redlinger, W. Breitung, J. Grune, A. Friedrich, and N. Ichikawa. Laminar burning velocities of hydrogen-oxygen-steam mixtures at elevated temperatures and pressures. *Proc. Combust. Inst.*, 33: 895–903, 2011. 12
- [77] A.E. Lutz. A numerical study of thermal ignition. *Technical Report SAND88-8228*, Sandia National Laboratories, 1988. 12
- [78] T. Boushaki, Y. Dhue, L. Selle, B. Ferret, and T. Poinso. Effects of hydrogen and steam addition on laminar burning velocity of methane-air pre-mixed flame: Experimental and numerical analysis. *Int. J. Hydr. Energy*, 37:9412–9422, 2012. 12
- [79] Y. He, Z. Wang, L. Yang, R. Whiddon, Z. Li, J. Zhou, and K. Chen. Investigation of laminar flame speeds of typical syngas using laser based bunsen method and kinetic simulation. *Fuel*, 95:206–213, 2012. ix, 12, 28, 31
- [80] H. Wang, X. You, A.V. Joshi, S.G. Davis, A. Laskin, F. Egolfopoulos, and C.K. Law. USC Mech Version II. High-temperature combustion reaction model of $\text{H}_2/\text{CO}/\text{C}_1 - \text{C}_4$ compounds. http://ignis.usc.edu/USC_Mech_II.htm, 2007. 12

REFERENCES

- [81] S.S. Vasu, D.F. Davidson, and R.K. Hanson. Shock tube study of syngas ignition in rich CO₂ mixtures and determination of the rate of $H + O_2 + CO_2 = HO_2 + CO_2$. *Energy Fuels*, 25:990–997, 2011. [xii](#), [12](#), [28](#), [50](#), [53](#)
- [82] E.L. Petersen, D.M. Kalitan, A.B. Barrett, S.C. Reehal, J.D. Mertens, D.J. Beerer, R.L. Hack, and V.G. McDonell. New syngas/air ignition data at lower temperature and elevated pressure and comparison to current kinetics models. *Combust. Flame*, 149:244–247, 2007. [12](#)
- [83] R. Sivaramakrishnan, A. Comandini, R.S. Tranter, K. Brezinsky, S.G. Davis, and H. Wang. Combustion of CO/H₂ mixtures at elevated pressures. *Proc. Combust. Inst.*, 31:429–437, 2007. [12](#)
- [84] J. Li, Z. Zhao, A. Kazakov, M. Chaos, F.L. Dryer, and J.J. Scire Jr. A comprehensive kinetic mechanism for CO, CH₂O, and CH₃OH combustion. *Int. J. Chem. Kin.*, 39:109–136, 2007. [ix](#), [xxi](#), [13](#), [29](#), [140](#), [143](#), [147](#)
- [85] M.A. Cherian, P. Rhodes, R.J. Simpson, and G. Dixon-Lewis. Kinetic modelling of the oxidation of carbon monoxide in flames. *Proc. Combust. Inst.*, 18:385–396, 1981. [16](#)
- [86] S. Hongyan, S.I. Yang, G. Jomaas, and C.K. Law. High-pressure laminar flame speeds and kinetic modelling of carbon monoxide/hydrogen combustion. *Proc. Combust. Inst.*, 31:439–446, 2007. [x](#), [19](#), [28](#), [35](#), [36](#)
- [87] M.P. Burke, M. Chaos, F.L. Dryer, and Y. Ju. Negative pressure dependence of mass burning rates of H₂/CO/O₂-diluted flames at low flame temperatures. *Combust. Flame*, 157:618–631, 2010. [x](#), [19](#), [28](#), [35](#), [37](#)
- [88] A.K. Das, C.J. Sung, Y. Zhang, and G. Mittal. Ignition delay study of moist hydrogen/oxidizer mixtures using a rapid compression machine. *Int. J. Hydr. Energy*, 37:6901–6911, 2012. [19](#)
- [89] C.L. Rasmussen, J. Hansen, P. Marshall, and P. Glarborg. Experimental measurements and kinetic modeling of CO/H₂/O₂/NO_x conversion at high pressure. *Int. J. Chem. Kin.*, 40:454–480, 2008. [19](#)

REFERENCES

- [90] T. Turanyi, A.S. Tomlin, and M.J. Pilling. On the error of the quasi-steady-state approximation. *J. Phys. Chem.*, 97:163–172, 1993. [23](#)
- [91] J.Y. Chen. Automatic generation of reduced mechanisms and their applications to combustion modelling. *Transactions of the Aeronautical and Astronautical Society of the Republic of China*, 33:59–67, 2001. [23](#)
- [92] J. Warnatz, U. Maas, and R.W. Dibble. Combustion. *Third Edition*, Springer-Verlag, pages 86–88, 2001. [23](#)
- [93] C.J. Montgomery, C. Yang, A.R. Parkinson, and J.Y. Chen. Selecting the optimum quasi-steady state species for reduced chemical kinetic mechanisms using a genetic algorithm. *Combust. Flame*, 144:37–52, 2006. [23](#), [24](#), [75](#)
- [94] J.Y. Chen. Development of reduced mechanisms for numerical modelling of turbulent combustion. *Workshop on Numerical Aspects of Reduction in Chemical Kinetics, CERMICS-ENPC Cite Descartes-Champus sur Marne, France, September 2, 1997*. [24](#), [75](#)
- [95] J.Y. Chen and Y.F. Tham. Speedy solution of quasi-steady state species by combination of fixed-point iteration and matrix inversion. *Combust. Flame*, 153:634–646, 2008. [25](#)
- [96] R.J. Kee, J.F. Grcar, M.D. Smooke, and J.A. Miller. A Fortran program for modelling steady laminar one-dimensional premixed flames. *Tech. Rep. SAND85-8240 Sandia National Laboratories*, 1985. [xx](#), [26](#), [54](#), [64](#), [93](#), [126](#)
- [97] R.J. Kee, F.M. Rupley, and J.A. Miller. Chemkin-II: A Fortran chemical kinetics package for the analysis of gas phase chemical kinetics. *Sandia National Laboratories Report, SAND89-8009B*, 1992. [26](#), [64](#), [93](#), [126](#)
- [98] P. Boivin, C. Jimenez, A.L. Sanchez, and F.A. Williams. A four-step reduced mechanism for syngas combustion. *Combust. Flame*, 158:1059–1063, 2011. [26](#)

REFERENCES

- [99] C.M. Vagelopoulos and F.N. Egolfopoulos. Laminar flame speeds and extinction strain rates of mixtures of carbon monoxide with hydrogen, methane, and air. *Proc. Combust. Inst.*, 25:1317–1323, 1994. [ix](#), [28](#), [31](#), [32](#)
- [100] J. Natarajan, T. Lieuwen, and J. Seitzman. Laminar flame speeds of H₂ / CO mixtures: Effect of CO₂ dilution, preheat temperature, and pressure. *Combust. Flame*, 151:104–119, 2007. [x](#), [28](#), [32](#), [33](#), [34](#), [35](#)
- [101] O. Park, P.S. Veloo, N. Liu, and F.N. Egolfopoulos. Combustion characteristics of alternative gaseous fuels. *Proc. Combust. Inst.*, 33:887–894, 2011. [x](#), [28](#), [37](#), [38](#)
- [102] D.M. Kalitan, J.D. Mertens, M.W. Crofton, and E.L. Petersen. Ignition and oxidation of lean CO/H₂ fuel blends in air. *J. Prop. Power*, 23:1291–1303, 2007. [xii](#), [28](#), [50](#), [52](#), [172](#)
- [103] B. Ruscic, A.F. Wagner, L.B. Harding, R.L. Asher, D. Feller, D.A. Dixon, K.A. Peterson, Y. Song, X. Qian, C. Ng, J. Liu, W. Chen, and D.W. Schwenke. On the enthalpy of formation of hydroxyl radical and gas-phase bond dissociation energies of water and hydroxyl. *J. Phys. Chem. A*, 106: 2727, 2002. [31](#)
- [104] J.T Herbon, R.K. Hanson, D.M. Golden, and C.T. Bowman. A shock tube study of the enthalpy of formation of OH. *Proc. Combust. Inst.*, 29:1201, 2002. [31](#)
- [105] S.G. Davis, A.V. Joshi, H. Wang, and F. Egolfopoulos. An optimized kinetic model of H₂/CO combustion. *Proc. Combust. Inst.*, 30:1283–1292, 2005. [34](#)
- [106] P. Saxena and F.A. Williams. Testing a small detailed chemical-kinetic mechanism for the combustion of hydrogen and carbon monoxide. *Combust. Flame*, 145:316–323, 2006. [xxi](#), [34](#), [132](#), [147](#)
- [107] E.V. Gurentsov, O.G. Divakov, and A.V. Eremin. Ignition of multicomponent hydrocarbon/air mixtures behind shock waves. *High Temperature*, 40: 379–386, 2002. [xii](#), [50](#), [54](#)

-
- [108] R.S. Cant. SENG2 user guide. CUED-A-THERMO-TR67 *September*, 2012. [55](#), [56](#), [61](#)
- [109] M.D. Smooke and V. Giovangigli. Lecture Notes in Physics. *Springer-Verlag*, 384:1–29, 1991. [xvi](#), [xvii](#), [57](#), [58](#), [134](#), [135](#), [136](#), [137](#)
- [110] K.W. Thompson. Time dependent boundary conditions for hyperbolic systems. *J. Comput. Phys.*, 68:1–24, 1987. [63](#)
- [111] K.W. Thompson. Time dependent boundary conditions for hyperbolic systems, II. *J. Comput. Phys.*, 89:439–461, 1990. [63](#)
- [112] T.J. Poinso. Boundary conditions for direct simulations of compressible viscous flows. *J. Comput. Phys.*, 101:104–129, 1992. [63](#)
- [113] M. Baum, T. Poinso, and D. Thevenin. Accurate boundary conditions for multi-component reactive flows. *J. Comput. Phys.*, 116:247–261, 1995. [63](#)
- [114] J.C. Sutherland and C.A. Kennedy. Improved boundary conditions for viscous, reacting, compressible flows. *J. Comput. Phys.*, 191:502–524, 2003. [63](#)
- [115] C.S. Yoo, Y. Wang, A. Trouvé, and H.G. Im. Characteristic boundary conditions for direct simulations of turbulent counterflow flames. *Combust. Theory Modelling*, 9:617–646, 2005. [63](#)
- [116] C.S. Yoo and H.G. Im. Characteristic boundary conditions for simulations of compressible reacting flows with multi-dimensional, viscous and reaction effects. *Combust. Theory Modelling*, 2:259–286, 2007. [63](#)
- [117] C.A. Kennedy, M.H. Carpenter, and R.M. Lewis. Low-storage, explicit Runge-Kutta schemes for the compressible Navier-Stokes equations. *Appl. Numer. Math.*, 35:177–219, 2000. [63](#)
- [118] G.K. Batchelor. The theory of homogeneous turbulence. *Cambridge Univ. Press*, 1982. [63](#)

REFERENCES

- [119] S.M. Candel and T. Poinso. Flame stretch and the balance equation for the flame surface area. *Combust. Sci. Tech.*, 70:1–15, 1990. [71](#)
- [120] T. Poinso and D. Veynante. Theoretical and numerical combustion. *Edwards Inc., Philadelphia, PA, U.S.A., Second Edition*, 2005. [71](#)
- [121] Z.M. Nikolaou and N. Swaminathan. Direct numerical simulation of multi-component fuel combustion with detailed chemistry. *Combust. Flame*, Submitted October 2013. [86](#)
- [122] R. Hilbert, F. Tap, H. El-Rabii, and D. Thévenin. Impact of detailed chemistry and transport models on turbulent combustion simulations. *Progr. Energy Combust. Science*, 30:61–117, 2004. [88](#)
- [123] G. Comte-Bellot and S. Corrsin. The use of a contraction to improve the isotropy of grid-generated turbulence. *J. Fluid Mech.*, 25:657–682, 1966. [99](#)
- [124] W.K. George. The decay of homogeneous isotropic turbulence. *Phys. Fluids*, 4(7):1492–1509, 1992. [99](#)
- [125] T. Echekki and J.H. Chen. Unsteady strain rate and curvature effects in turbulent premixed methane-air flames. *Combust. Flame*, 106:184–202, 1996. [103](#), [114](#), [118](#), [121](#), [122](#)
- [126] M. Tanahashi, Y. Nada, Y. Ito, and T. Miyauchi. Local flame structure in the well-stirred reactor regime. *Proc. Combust. Inst.*, 29:2041–2049, 2002. [103](#)
- [127] N. Peters. Laminar flamelet concepts in turbulent combustion. *Proc. Combust. Inst.*, 21(1):1231–1250, 1988. [104](#)
- [128] A.Y. Poludnenko and E.S. Oran. The interaction of high speed turbulence with flames: global properties and internal flame structure. *Combust. Flame*, 157:995–1011, 2010. [110](#)
- [129] A.Y. Poludnenko and E.S. Oran. Turbulence and scalar gradient dynamics in premixed reacting flows. *40th AIAA Fluid Dyn. Conf. Chicago IL.*, AIAA-5027, 2010. [110](#)

REFERENCES

- [130] N. Chakraborty and N. Swaminathan. Influence of the Damkohler number on turbulence-scalar interaction in premixed flames I: physical insight. *Phys. Fluids*, 19:045103, 2007. [110](#), [149](#)
- [131] S.H. Kim and H. Pitsch. Scalar gradient and small-scale structure in turbulent premixed combustion. *Phys. Fluids*, 19:115, 2007. [110](#)
- [132] N. Chakraborty and R.S. Cant. Unsteady effects of strain rate and curvature on turbulent premixed flames in an inflow-outflow configuration. *Combust. Flame*, 137:129–147, 2004. [111](#), [112](#), [113](#), [114](#), [118](#)
- [133] N. Chakraborty. Comparison of displacement speed statistics of turbulent premixed flames in the regimes representing combustion in corrugated flamelets and thin reaction zones. *Phys. Fluids*, 19:105–109, 2007. [112](#), [113](#), [114](#)
- [134] J. Buckmaster and G. Ludford. Theory of laminar flames. *Cambridge University Press*, 1982. [119](#)
- [135] F.A. Williams. Combustion theory. *Benjamin Cummings, Menlo Park, CA*, 1985. [119](#)
- [136] S. Ruan, N. Swaminathan, and Y. Mizobuchi. Investigation of flame stretch in turbulent lifted jet flame. *Combust. Sci. Tech.*, Accepted October 2013. [119](#)
- [137] J.H. Chen and H.G. Im. Correlation of flame speed with stretch in turbulent premixed methane-air flames. *Proc. Combust. Inst.*, 27:819–826, 1998. [119](#)
- [138] D.P. Mishra, P.J. Paul, and H.S. Mukunda. Stretch effects extracted from inwardly and outwardly propagating spherical premixed flames. *Combust. Flame*, 97:35–47, 1994. [119](#), [120](#)
- [139] R.L. Gordon, A.R. Masri, and E. Mastorakos. Heat release rate as represented by $[\text{OH}][\text{CH}_2\text{O}]$ and its role in autoignition. *Combust. Theory Modelling*, 13:645–670, 2009. [123](#)

REFERENCES

- [140] C.M. Vagelopoulos and J.H. Frank. An experimental and numerical study on the adequacy of CH as a flame marker in premixed methane flames. *Proc. Combust. Inst.*, 30:241–249, 2004. [123](#)
- [141] B.O. Ayoola, R. Balachandran, J.H. Frank, E. Mastorakos, and C.F. Kaminski. Spatially resolved heat release rate measurements in turbulent premixed flames. *Combust. Flame*, 144:1–16, 2006. [123](#)
- [142] A. Fayoux, K. Zahringer, O. Gicquel, and J.C. Rolon. Experimental and numerical determination of heat release in counterflow premixed laminar flames. *Proc. Combust. Inst.*, 30:251–257, 2004. [123](#)
- [143] Y. Minamoto and N. Swaminathan. Scalar gradient behaviour in mild combustion. *Combust. Flame*, 2013. <http://dx.doi.org/10.1016/j.combustflame.2013.10.005>. [xvi](#), [xvii](#), [125](#), [135](#), [136](#), [137](#), [147](#)
- [144] G. Vourliotakis, G. Skevis, and M.A. Founti. A detailed kinetic modelling study of benzene oxidation and combustion in premixed flames and ideal reactors. *Energy Fuels*, 25:1950–1963, 2011. [128](#)
- [145] N. Swaminathan and K.N.C. Bray. Effect of dilatation on scalar dissipation in turbulent premixed flames. *Proc. Combust. Inst.*, 143:549–565, 2005. [149](#)
- [146] R. Borghi. Turbulent premixed combustion: further discussions on the scales of fluctuations. *Combust. Flame*, 80:304–312, 1990. [149](#)
- [147] T. Mantel and R. Borghi. A new model of premixed wrinkled flame propagation based on a scalar dissipation equation. *Combust. Flame*, 96:443–457, 1994. [149](#)
- [148] R. Borghi and D. Dutoya. On the scales of the fluctuations in turbulent combustion. *Proc. Combust. Inst.*, 17:235–244, 1978. [149](#)
- [149] A. Mura and R. Borghi. Towards an extended scalar dissipation equation for turbulent premixed combustion. *Combust. Flame*, 133:193–196, 2003. [149](#)

REFERENCES

- [150] C.J. Rutland and R.S. Cant. *Proceedings of the Summer Program, Center for Turbulence Research, NASA Ames / Stanford University, Stanford CA*, page 75, 1994. [149](#)
- [151] N. Swaminathan and R.W. Grout. Interaction of turbulence and scalar fields in premixed flames. *Phys. Fluids*, 18:045102, 2006. [149](#)
- [152] G. Hartung, J. Hult, C.F. Kaminski, J. Rogerson, and N. Swaminathan. Effect of heat release on turbulence and scalar-turbulence interaction in premixed combustion. *Phys. Fluids*, 20:035110, 2008. [149](#)
- [153] H. Kolla, J.W. Rogerson, N. Chakraborty, and N. Swaminathan. Scalar dissipation rate modelling and its validation. *Combust. Sci. Tech.*, 181: 518–535, 2009. [149](#), [150](#)
- [154] N. Swaminathan N. Chakraborty, J.W. Rogerson. A priori assessment of closures for scalar dissipation rate transport in turbulent premixed flames using direct numerical simulation. *Phys. Fluids*, 20:045106, 2008. [150](#)
- [155] W.P. Jones and B.E. Launder. The prediction of laminarization with a 2-equation model of turbulence. *Int. J. Heat and Mass Transf.*, 15:301, 1972. [151](#)
- [156] W.P. Jones and B.E. Launder. Calculation of low Re number phenomena with a 2-equation model of turbulence. *Int. J. Heat and Mass Transf.*, 16: 1119–1130, 1973. [151](#)
- [157] D.B. Spalding. Development of the eddy break up model of turbulent combustion. *Proc. Combust. Inst.*, 16:1657–1663, 1977. [152](#)
- [158] D.B. Spalding. Mixing and chemical reaction in steady confined turbulent flames. *Proc. Combust. Inst.*, 13:649–657, 1971. [152](#)
- [159] K.N.C. Bray and J.B. Moss. A unified statistical model of the premixed turbulent flame. *Acta Astronautica*, 4:291–319, 1977. [152](#)

REFERENCES

- [160] J.A. van Oijen and L.P.H. de Goey. Modelling of premixed laminar flames using flamelet-generated manifolds. *Combust. Sci. Tech.*, 161:113–137, 2000. [152](#), [153](#)
- [161] R.S. Cant, S.B. Pope, and K.N.C. Bray. Modelling of flamelet surface to volume ratio in turbulent premixed combustion. *Proc. Combust. Inst.*, 23(1):809–815, 1990. [153](#)
- [162] E.R. Hawkes and R.S. Cant. A flame surface density approach to large eddy simulation of premixed turbulent combustion. *Proc. Combust. Inst.*, 28:51–58, 2000. [153](#)
- [163] E.R. Hawkes and R.S. Cant. Implications of a flame surface density approach to large eddy simulation of premixed turbulent combustion. *Combust. Flame*, 126:1617–1629, 2001. [153](#)
- [164] N. Chakraborty and R.S. Cant. Direct numerical simulation analysis of the flame surface density transport equation in the context of large eddy simulation. *Proc. Combust. Inst.*, 32:1445–1453, 2009. [153](#)
- [165] N. Chakraborty and R.S. Cant. Turbulent Reynolds number dependence of flame surface density transport in the context of Reynolds Averaged Navier-Stokes Simulations. *Combust. Flame*, 157:943–954, 2010. [157](#)
- [166] T.D. Dunstan, Y. Minamoto, N. Chakraborty, and N. Swaminathan. Scalar dissipation rate modelling for large eddy simulation of turbulent premixed flames. *Proc. Combust. Inst.*, 34:1193–1201, 2013. [164](#), [167](#)